THE CURACAUTÍN ERUPTION OF LLAIMA VOLCANO, CHILE

by

Aaron Asdale Marshall

A dissertation

submitted in partial fulfillment

of the requirements for the degree of

Doctor of Philosophy in Geosciences

Boise State University

August 2022

BOISE STATE UNIVERSITY GRADUATE COLLEGE

DEFENSE COMMITTEE AND FINAL READING APPROVALS

of the dissertation submitted by

Aaron Asdale Marshall

Dissertation Title: The Curacautín Eruption of Llaima Volcano, Chile

Date of Final Oral Examination: 01 July 2022

The following individuals read and discussed the dissertation submitted by student Aaron Asdale Marshall, and they evaluated the student's presentation and response to questions during the final oral examination. They found that the student passed the final oral examination.

Brittany D. Brand, Ph.D.	Chair, Supervisory Committee
V. Dorsey Wanless, Ph.D.	Member, Supervisory Committee
Mark Schmitz, Ph.D.	Member, Supervisory Committee
Benjamin J. Andrews, Ph.D.	Member, Supervisory Committee
Michael Manga, Ph.D.	Member, Supervisory Committee

The final reading approval of the dissertation was granted by Brittany D. Brand, Ph.D., Chair of the Supervisory Committee. The dissertation was approved by the Graduate College.

DEDICATION

This dissertation is dedicated to my parents, Pam and Bill Hartman and Craig Marshall. Thank you for your constant support. Additionally, I dedicate this dissertation to my former teachers and advisors Lynsey LeMay, Chuck Bailey, and Brent Owens, who inspired me to pursue my passion for scientific research.

ACKNOWLEDGMENTS

I was able to complete this dissertation thanks to the guidance and patience of my committee. My advisor Brittany Brand provided me with constant support and help, and fundamentally changed me as a scientist. Mark Schmitz and Dorsey Wanless always challenged me and pushed me to discover answers to questions I already knew. Finally, my external committee members Michael Manga and Ben Andrews were a source of constant help and motivation, both of whom always made time on the evenings and weekends for my questions.

Graduate school is stressful, and I would not have been able to get through without the help of so many friends in the Boise State University Department of Geosciences. In no particular order, graduate school was made easier thanks to Emma McCully, Claire Harrigan, Robin Trayler, Carson MacPherson-Krutsky, Nick Pollock, Darin Schwartz, Buchanan Kerswell, Pedro Valdivia, Sean Carney, Katie Murenbeeld, Mike Mohr, Sylvana Bendaña, Jenna Narducci, Kerri Spuller, and Megan Maksimowicz. Thank you all for the research discussions, peer reviews, distractions, and trips to R Bar.

Finally, I am ever grateful to my partner Caitlin Manfredo for her patience over five years for all my late nights in the lab, months-long trips to the field, and weekends away for work. Thank you for your constant support and encouragement.

ABSTRACT

Mafic magmas are the most common magmas erupted on Earth and on rocky bodies in the Solar System. The low viscosity of mafic magmas results in eruptions that are primarily effusive to mildly explosive. Rarely, mafic magmas erupt as more violent, explosive events, and the causes of this transition in eruptive style are hotly debated. In this dissertation, I investigated the conditions in the conduit and shallow subsurface that generated the unusually explosive mafic, Curacautín eruption of Llaima volcano, Chile. The Curacautín ignimbrite (Ci) is a basaltic andesite ignimbrite consisting of four flow units of variable thicknesses. New ^{14}C dates for five Ci exposures returned ages of ~12.6 ka suggesting the Ci was generated in a single eruptive event. Using new methods for volume estimation, I calculated a volume of 4.0–4.5 km^3 DRE for the Ci. Pyroclast textures, including moderate vesicularities and high microlite number densities suggest rapid magma ascent rates prior to eruption. I calculated timescales of crystallization for Ci plagioclase microlites of <10 s to ~5 hrs using crystal size distribution (CSD) theory. To further test the rapid ascent hypothesis, I modeled plagioclase nucleation and growth rates of 6.1×10^5 cm^{-3} hr^{-1} and 27.4 μm hr^{-1} for the Ci. I used these rates to conduct Monte Carlo simulations for Ci plagioclase CSDs and calculated ascent rates from <1–6 m s^{-1}, further supporting the rapid ascent hypothesis. I was unable to produce the smallest size populations of plagioclase microlites. Finally, I observe textures consistent with the autobrecciation and welding of protopyroclasts prior to eruption. I call this newly recognized process fusing and suggest it records conduit conditions not previously

considered in mafic eruptions. Size-restricted broken plagioclase crystals record fragmentation and secondary, post-fragmentation crystallization. Both processes may explain our inability to produce the smallest size population of plagioclase within the model. These observations have important implications for how we interpret the deposits of explosive eruptions. This research supports other work that suggests rapid magma ascent is the primary driver for highly explosive mafic eruptions in the absence of external water. Because people are living on or near volcanoes that erupt mafic magmas in ever increasing numbers, it is paramount that we understand what causes these systems to transition in eruption style.

TABLE OF CONTENTS

LIST OF TABLES

LIST OF FIGURES

LIST OF ABBREVIATIONS

BCE	before common era
BND	bubble number density
BP	before present
BSE	back scattered electron
BSU	Boise State University
^{14}C	carbon-14
CE	common era
Ci	Curacautín ignimbrite
cm	centimeters
CSD	crystal size distribution
dP/dt	decompression rate
DRE	dense-rock equivalent
g	grams
GC	Graduate College
hr	hours
ka	kilo-annum
kg	kilograms
km	kilometers
m	meters
μm	microns

mm	millimeters
MND	microlite number density
MPa	megapascal
ppm	parts per million
s	seconds
TDC	Thesis and Dissertation Coordinator
VEI	Volcanic Explosivity Index
μCT	X-ray computed microtomography
XRF	X-ray fluorescence

CHAPTER 1: INTRODUCTION

Magmas erupt in a diverse spectrum of styles and intensities. Effusive eruptions (Fig. 1.1A) are characterized by low to no explosivity that produce lava flows or domes (e.g., Platz et al., 2012; Dzurisin et al., 2015; Wolpert et al., 2016). Conversely, explosive eruptions (Fig. 1.1B) generate ash and pyroclastic bombs that can be carried tens to hundreds of km from source (e.g., Walker et al., 1980; Vinkler et al., 2012; Brand et al., 2016). Explosive eruptions also pose a significant risk to surrounding communities due to the hazards associated with such eruptions, including caldera collapse, sector collapse, pyroclastic density currents, bomb dispersal, and lahars (see Sigurdsson et al., 2015 and references therein). It is therefore a goal of volcanology to understand the hazard implications associated with differing eruption styles.

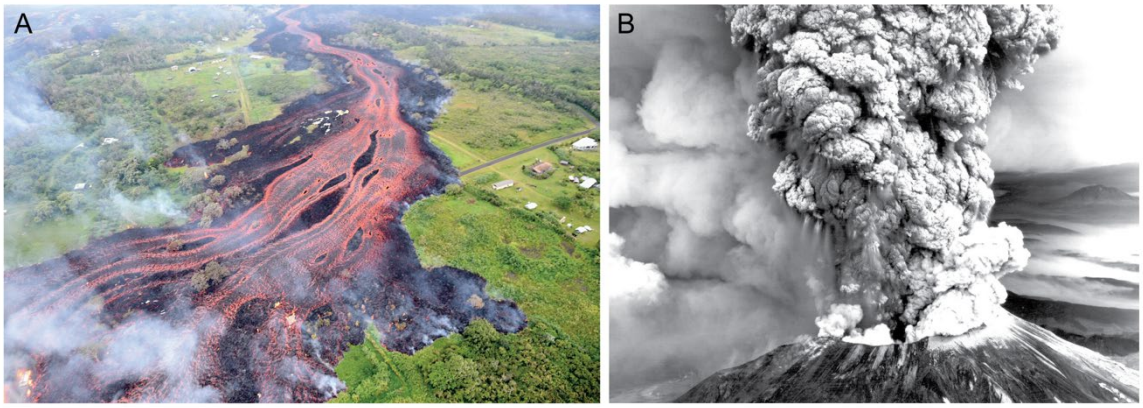

Figure 1.1 (A) Oblique aerial photograph of an effusive mafic lava flow from the 2018 Kilauea, HI eruption. (B) Aerial photograph facing the northeast of the high explosivity silicic 1980 eruption of Mount St. Helens, WA. Photo credit: United States Geological Survey.

While there are many intrinsic and extrinsic variables that influence eruption style, the strongest influence that governs eruption style is the type and amount of volatiles in and surrounding magmas. At depth, volatiles remain dissolved in magmas due to high confining pressures (P) acting upon the magma (Fig. 1.2). Magmas depressurize during ascent from depth towards the surface. At lower P, volatiles overcome the viscoelastic forces acting upon them, and bubbles nucleate and grow by diffusion, decompression, and coalescence. Early bubble nucleation may be facilitated by the presence of crystals in the magma that provide nucleation sites. Referred to as heterogeneous bubble nucleation, this process often leads to the development of permeability and subsequent degassing of the magma (Mangan and Sisson, 2000). Slowly ascending magmas facilitate degassing of the magma because of the time available for bubble nucleation and coalescence. Conversely, rapidly ascending magmas in the absence of pre-existing crystals suppresses bubble nucleation until shallow levels, resulting in late homogeneous bubble nucleation and no time for outgassing of the magma (Fig. 1.2). Such delayed, disequilibrium nucleation results in high explosivity eruptions (Mangan and Sisson, 2000).

Fragmentation is the dynamic transition of a magma with dispersed gas bubbles to a gas with dispersed magma droplets (pyroclasts) that occurs during explosive eruptions. Brittle failure theory shows us that magmas fragment when (1) the strain induced on a magma greatly exceeds the magma's ability to structurally relax, thereby driving the magma past the glass transition causing the melt to break as though it were a solid (Papale, 1999), or when (2) overpressure within bubbles acts to rupture the thin film of melt surrounding bubbles causing the magma to break as a non-Newtonian fluid (Zhang,

1999). Both models suggest bubbles must be out of equilibrium with their host magmas to fragment. Large stresses can be achieved by some combination of high melt viscosity, typically >10^6 Pa s (Namiki and Manga, 2008), crystallization (Arzilli et al., 2019), high strain rates (Papale, 1999), or bubble overpressure (Zhang, 1999).

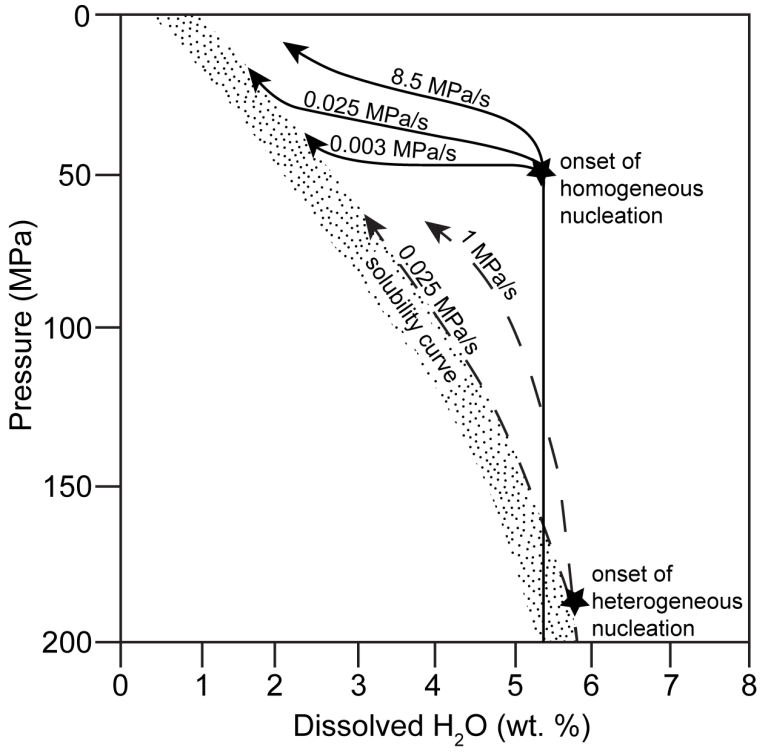

Figure 1.2 Results of decompression experiments by Mangan and Sisson (2000) meant to simulate delayed, disequilibrium degassing in a crystal-free rhyolite melt. Dashed curves represent degassing pathways for heterogeneous bubble nucleation and solid curves are pathways from homogeneous bubble nucleation. In natural systems, bubble nucleation is likely a combination of both heterogeneous and homogeneous nucleation (Mangan and Sisson, 2000).

Mafic magmas, those characterized by low weight % SiO_2, commonly erupt as low explosivity to effusive events. This is owing to their low melt viscosity which permits efficient bubble nucleation and segregation from the liquid magma, thus removing the volatile primer necessary for brittle fragmentation and higher explosivity eruptions through outgassing. Conversely, felsic magmas with high SiO_2-contents have

viscosities that are orders of magnitude higher than mafic magmas. This is due to their high Si-content that forms strong SiO_4 bonds that are difficult to break, resulting in increased the magma viscosity. Such high viscosities suppress bubble nucleation until shallow depths, resulting in delayed, homogeneous bubble nucleation and associated high bubble overpressure necessary for fragmentation. Experiments by Mangan and Sisson (2000) show that delayed, disequilibrium degassing results in homogenous bubble nucleation at shallow depths. Such densely packed and rapidly nucleated bubbles do not have time to grow and coalesce during magma ascent, thus resulting in bubble overpressure and brittle fragmentation.

Explosive silicic volcanism is a well-understood phenomenon. The same statement cannot be made for high explosivity mafic eruptions. This presents a substantial gap in our understanding of not just earth science, but the hazards associated with the most common type of volcanism on Earth (Parfitt, 2004). As populations continue to grow and developed lands expand, more people are living on or near volcanoes that erupt mafic magmas (Fig. 1.3). The work of Arzilli et al. (2019) shows any of these mafic volcanic centers has the potential to transition in eruption style from effusive to explosive activity. Therefore, understanding the causes of mafic explosive volcanism has implications for hazard forecasting and mitigation globally (Fig. 1.3).

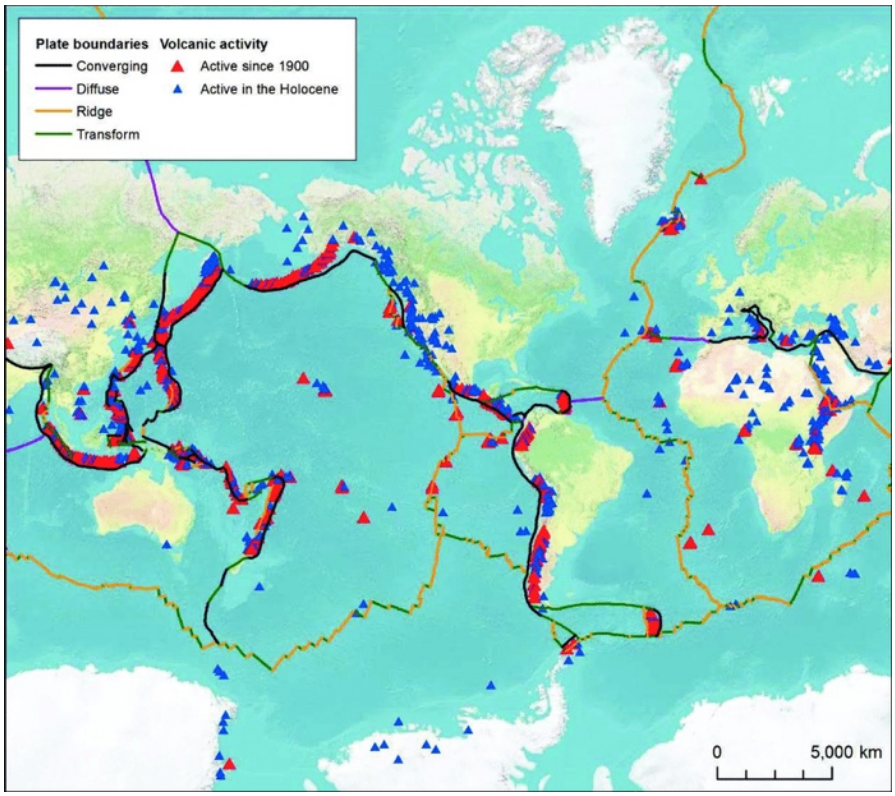

Figure 1.3 Map of the global distribution and status of Holocene volcanoes and plate boundaries (from Brown et al., 2015). Of the approximately 1500 volcanoes worldwide, around 80% erupt mafic magmas (Parfitt, 2004). Therefore, understanding what drives mafic explosive volcanism is critical for hazard forecasting and mitigation globally.

The goals of this dissertation are to (1) investigate and characterize the deposits of a voluminous mafic explosive eruption–the Curacautín eruption of Llaima volcano, Chile, (2) interpret and apply what we learn from the Curacautín eruption to improve our understanding of the conditions in the conduit and shallow subsurface that drive large-volume, mafic, explosive eruptions, and (3) offer a tool for others to use in evaluating the deposits of similar eruptions worldwide.

The contents of this dissertation are presented in four chapters written in a journal manuscript format. Chapter 2 is a comprehensive study of the deposit characteristics of the Curacautín eruption that I use to (1) improve our understanding of when and why the Curacautín eruption occurred, (2) revise the existing volume estimate of those deposits,

and (3) offer a conceptual model for the Curacautín eruption (Marshall et al., 2022a). In Chapter 3, I measure plagioclase crystal textures and calculate timescales of plagioclase crystallization and nucleation rates using crystal size distribution theory (Valdivia et al., 2022). Chapter 4 builds upon the work of Chapter 3 by expanding the calibration of the *SNGPlag* model of Befus and Andrews (2018) and Andrews and Befus (2020) for application to mafic magma compositions. I then numerically model plagioclase microlite nucleation and growth and compare the results to the natural textures measured in Chapter 3 to approximate decompression rates the Curacautín magma experienced prior to eruption. In Chapter 5 I propose a new conceptual model of conduit processes that created the unique textures observed in Curacautín pyroclasts and hypothesis those processes may occur at other mafic volcanoes. Together, the work presented here improves our understanding not just of the Curacautín eruption, but our understanding of mafic explosive volcanism and conduit processes at mafic volcanic centers around the world.

References

Andrews BJ, Befus KS (2020) Supersaturation Nucleation and Growth of Plagioclase: a numerical model of decompression-induced crystallization. Contrib Mineral Petrol 175:23. doi: 10.1007/s00410-020-1660-9

Arzilli F, La Spina G, Burton MR, Polacci, M, Le Gall N, Hartley ME, Di Genova D, Cai B, Vo NT, Bamber EC, Nonni S, Atwood R, Llewellin EW, Brooker RA, Mader HM, Lee PD (2019) Magma fragmentation in highly explosive basaltic eruptions induced by rapid crystallization. Nat Geosci 12:1023–1028. doi: 10.1038/s41561-019-0468-6

Befus KS, Andrews BJ (2018) Crystal nucleation and growth produced by continuous decompression of Pinatubo magma. Contrib Mineral Petrol 173:92. doi: 10.1007/s00410-018-1519-5

Brand BD, Bendaña S, Self S, Pollock N (2016) Topographic controls on pyroclastic density current dynamics: Insight from 18 May 1980 deposits at Mount St. Helens, Washington (USA). J Volcanol Geotherm Res 321:1–17. doi: 10.1016/j.jvolgeores.2016.04.018

Brown SK, Loughlin SC, Sparks RSJ, Vye-Brown C, Barclay J, Calder E, Cottrell E, Jolly G, Komorowski J-C, Mandeville C, Newhall C, Palma J, Potter S, Valentine G *in* Loughlin SC, Sparks S, Brown SK, Jenkins SF, Vye-Brown C, eds. (2015) Global Volcanic Hazards and Risk. Academic Press, p. 81–172. doi: 10.1017/CBO9781316276273

Dzurisin D, Moran SC, Lisowski M, Schilling SP, Anderson KR, Werner C (2015) The 2004 – 2008 dome-building eruption at Mount St. Helens, Washington: epilogue. Bull Volcanol 77(89). doi: 10.1007/s00445-015-0973-4

Mangan M, Sisson T (2000) Delayed, disequilibrium degassing in rhyolitic magma: decompression experiments and implications for explosive volcanism: Earth Planet Sci Lett 183:441–455

Marshall AA, Brand BD, Martínez V, Bowers JM, Walker M, Wanless VD, Andrews BJ, Manga M, Valdivia P, Giordano D (2022a) The mafic Curacautín ignimbrite of Llaima volcano, Chile. J Volcanol Geotherm Res 421:107418. doi: 10.1016/j.jvolgeores.2021.107418

Namiki A, Manga M (2008) Transition between fragmentation and permeable outgassing of low viscosity magmas. J Volcanol Geotherm Res 169:48–60. doi: 10.1016/j.jvolgeores.2007.07.020

Papale P (1999) Strain-induced magma fragmentation in explosive eruptions. Nature 397:425–428. doi: 10.1038/17109

Parfitt E (2004) A discussion of the mechanisms of explosive basaltic eruptions. J. Volcanol Geotherm Res 134:77–107. doi: 10.1016/j.jvolgeores.2004.01.002

Platz T, Cronin SJ, Procter JN, Neall VE, Foley SF (2012) Non-explosive, dome-forming eruptions at Mt. Taranaki, New Zealand. Geomorphology 136:15–30. doi: 10.1016/j.geomorph.2011.06.016

Sigurdsson H, Houghton B, McNutt SR, Rymer H, Stix J, eds. (2015) Encyclopedia of Volcanoes (2 ed.). Academic Press, 1421 p

Valdivia P, Marshall AA, Manga M, Brand BD, Huber C (2022) Mafic explosive volcanism at Llaima volcano: 3D X-ray microtomography reconstruction of pyroclasts to constrain shallow conduit processes. Bull Volcanol 48(2). doi: 10.1007/s00445-021-01415-8

Vinkler AP, Cashman K, Giordano G, Groppelli G (2012) Evolution of the mafic Villa Senni caldera-forming eruption at Colli Albani volcano, Itlay, indicated by textural analysis of juvenile fragments. J Volcanol Geotherm Res 235–236:37–54. doi: 10.1016/j.jvolgeores.2012.03.006

Walker GPL (1980) The Taupo pumice: product of the most powerful known (ultraplinian) eruptions?. J Volcanol Geotherm Res 8:69–94

Wolpert RL, Ogburn SE, Calder ES (2016) The longevity of lava dome eruptions. J Geophys Res B: Solid Earth 121(2):676–686. doi:10.1002/2015JB012435

Zhang Y (1999) A criterion for the fragmentation of bubbly magma based on brittle failure theory. Nature 402:648–650. doi: 10.1038/45210

CHAPTER 2: THE MAFIC CURACAUTÍN IGNIMBRITE OF LLAIMA VOLCANO, CHILE

This chapter is a manuscript that is published by Elsevier in the Journal of Volcanology and Geothermal Research. The full citation is: Marshall AA, Brand BD, Martínez V, Bowers JM, Walker M, Wanless VD, Andrews BJ, Manga M, Valdivia P, Giordano G (2022a) The mafic Curacautín ignimbrite of Llaima volcano, Chile. J Volcanol Geotherm Res 421:107418. doi: 10.1016/j.jvolgeores.2021.107418.

2.1 Abstract

Mafic volcanism accounts for 80% of magmas erupted on Earth. Although the majority of these eruptions are effusive to Strombolian and fountain-fed, large explosive mafic eruptions do occur. This work uses the deposits and pyroclast textures from the 12.6 ka Curacautín ignimbrite eruption of Llaima volcano to constrain the conditions that drove this mafic explosive eruption and extrapolate the findings to provide insights into the conditions that promote large-volume, mafic explosive volcanism elsewhere. The Curacautín ignimbrite (Ci) consists of four massive coarse ash to lapilli tuff flow units; Unit 1 is at least 30 m thick in proximal exposures, and Units 2–4 range from 1 to 4 m thick. New ^{14}C dates and field observations suggest the Ci is the result of a single eruptive episode at ~12.6 ka. A lack of fall deposits and presence of abundant clast agglutination suggests the Ci eruption was a boil over event. We estimate the proximal Ci

tephra volume to be between 6 and 9 km^3 (equivalent to 4.0–4.5 km^3 DRE), which is less than previous estimates. Even with our lower estimate, the Ci is still larger than the Masaya Triple Layer, Pucón ignimbrite, Tarawera 1886, and Etna 122 BCE mafic eruptions.

Average vesicularities of pyroclasts range from 43 to 71%, and all but one exposure have vesicularities ≤56%. Average phenocryst content is ≤1–3%, but plagioclase microlite crystallinities are between 29 and 44%, with volumetric number densities between 8.21×10^6 and 1.84×10^7 mm^{-3}. Such high microlite content suggests high disequilibrium resulting from rapid magma ascent and decompression. We interpret that the combination of rapid ascent and increased magma viscosity due to the crystallization of microlites caused gases to remain coupled with the Ci magma. This, in combination with ash textures, suggests the Ci eruption explosivity was driven by brittle fragmentation. Assuming that mass eruption rates exceeded 2.0×10^8 kg s^{-1} to produce complete column collapse, we estimate an eruption duration of ~15–17 h. This study further supports the interpretation that extensive microlite nucleation from rapid ascent can lead to large mafic explosive eruptions.

2.2 Introduction

Mafic volcanism constitutes more than 80% of volcanic activity on Earth (Parfitt, 1994). These eruptions are primarily effusive to mildly explosive (Strombolian) owing to low melt viscosities that facilitate efficient segregation of gas from the melt and inhibits fragmentation. However, larger-volume, explosive mafic eruptions do occur. Well-documented cases include the 122 BC eruption of Etna volcano, Italy (Coltelli et al.,

1998; Houghton et al., 2004; Sable et al., 2006), the 1707 Hoei eruption from Mt. Fuji, Japan (Miyaji et al., 2011), the 1886 eruption of Tarawera volcano, New Zealand (Houghton et al., 2004; Sable et al., 2006; Sable et al., 2009), and the Fontana lapilli basalt, San Antonio tephra, and Masaya Triple Layer eruptions of Masaya volcano, Nicaragua (Constantini et al., 2009; Constantini et al., 2010; Bamber et al., 2020; Pérez et al., 2020). The latter produced scoria fall deposits. Rarer still are ignimbrite-forming mafic eruptions such as the large-volume tephritic ignimbrites of Colli Albani volcano, Italy (Giordano et al., 2006; Freda et al., 2011; Vinkler et al., 2012), the Lican ignimbrite of Villaricca volcano, Chile (Lohmar et al., 2007), the La Garrotxa volcanic field, Spain (Martí et al., 2017), and ignimbrites from Nakadake, Aso volcano (Miyabuchi et al., 2006) and Fuji volcano, Japan (Yamamoto et al., 2005). The processes that generate these uncommon eruptions remain enigmatic because their behavior seemingly contradicts accepted volcanic conventions about the processes that lead to fragmentation (e.g., Papale, 1999). Therefore, investigating the deposits of mafic explosive and ignimbrite-forming eruptions may help improve our understanding of the conditions that promote these rare, yet devastating, events.

Much of our understanding of explosive eruptions comes from analyses of their eruptive products (Houghton and Gonnermann, 2008). Investigations of deposit distribution and granulometry can reveal fragmentation mechanism (Heiken and Wohletz, 1985), depositional processes (Branney and Kokelaar, 2002), and environmental conditions at the time of the eruption (White and Valentine, 2016). Vesicle textural studies in 2D (Shea et al., 2010), 3D (Degruyter et al., 2010; Giachetti et al., 2011; Baker et al., 2012a; Carey et al., 2013), and 4D (Baker et al., 2012b) inform the state of

magmatic volatiles prior to and during an eruption. Similar studies of microlites yield insights into magma decompression and ascent rates (Szramek et al., 2006; Szramek, 2016), undercooling and supersaturation (Hammer and Rutherford, 2002; La Spina et al., 2016; Befus and Andrews, 2018; Arzilli et al., 2019), and magma viscosity (Di Genova et al., 2020). These types of analyses are incorporated into models of volcano processes to improve our understanding of the magmatic and crustal conditions that drive explosive eruptions (Cashman and Giordano, 2014; Befus and Andrews, 2018; Moitra et al., 2018; Arzilli et al., 2019; Andrews and Befus, 2020).

The Curacautín ignimbrite (Ci) in southern Chile is a voluminous, mafic pyroclastic deposit generated by Llaima volcano in the late Pleistocene (Fig. 2.1, Naranjo and Moreno, 1991; Naranjo and Moreno, 2005; Lohmar, 2008). Naranjo and Moreno (1991) estimated a tephra volume of 24 km^3 (Naranjo and Moreno, 1991), making the Ci potentially one of the largest, yet least studied large-volume, mafic explosive eruptions. As such, the magmatic conditions that resulted in this explosive eruption are poorly constrained. The objectives of our study are to use the deposit distribution, stratigraphy, and ^{14}C dating to determine how many eruptive episodes are associated with the Ci, refine the volume estimate, and use pyroclast textures to investigate the conditions that drove the eruption(s). Finally, we offer a conceptual eruption model for the Ci.

2.2.2 Geologic background

2.2.2.1 Geologic setting

Llaima volcano (Fig. 2; 38°41’45 S, 71°43’54 W) is a Quaternary stratovolcano in the Southern Volcanic Zone of Chile. Llaima is positioned along the NE-SW trending

Liquiñe-Ofqui fault zone (Cembrano and Lara, 2009). With a volume of ~400 km^3 and a peak elevation of 3125 m (Naranjo and Moreno, 2005), Llaima is one of the largest Andean volcanoes (Völker et al., 2011). Llaima erupts approximately every seven years and has erupted 54 times since 1640 (Dzierma and Wehrmann, 2010) making it one of the most active Andean volcanoes as well. Modeling by Dzierma and Wehrmann (2010) predicts Llaima will have another VEI≥2 eruption within the next 20 years with a >90% probability.

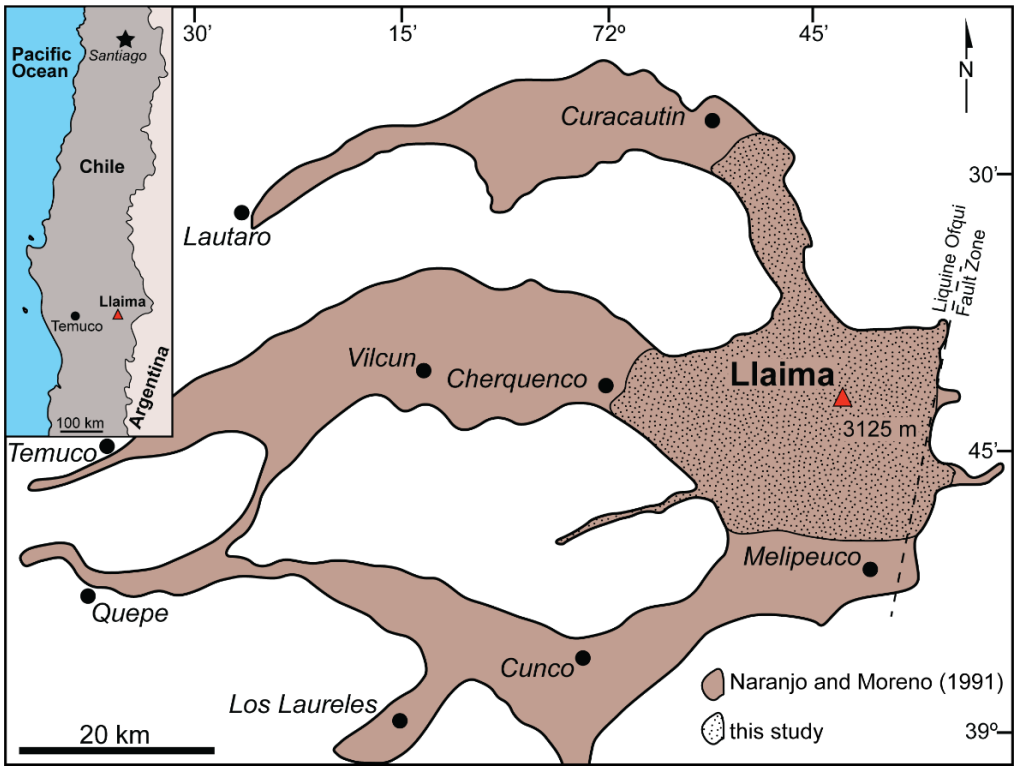

Figure 2.1 Original mapped extent of the Curacautín ignimbrite by Naranjo and Moreno (1991) and the approximate extent mapped in this study (stippled pattern). Red triangle represents the location of Llaima. Temuco is ~100 km west of Llaima.

2.2.2.2 Eruptive history

Llaima volcanism began ~185 ka with an ancestral shield volcano (Naranjo and Moreno, 1991). Ancestral deposits are poorly preserved due to heavy erosion during the Llanquihue glaciation (Stern, 2004; Lohmar et al., 2006). The onset of Llaima's postglacial activity is marked by the large-volume, mafic explosive eruption(s) that produced the extensive Ci (Naranjo and Moreno, 1991; Naranjo and Moreno, 2005; Lohmar, 2008). Previous carbon dates from the Ci stratigraphy suggest two eruptions, one at ~13.2 thousand years BP and another at ~12.6 thousand years BP (Naranjo and Moreno, 1991; Lohmar, 2008).

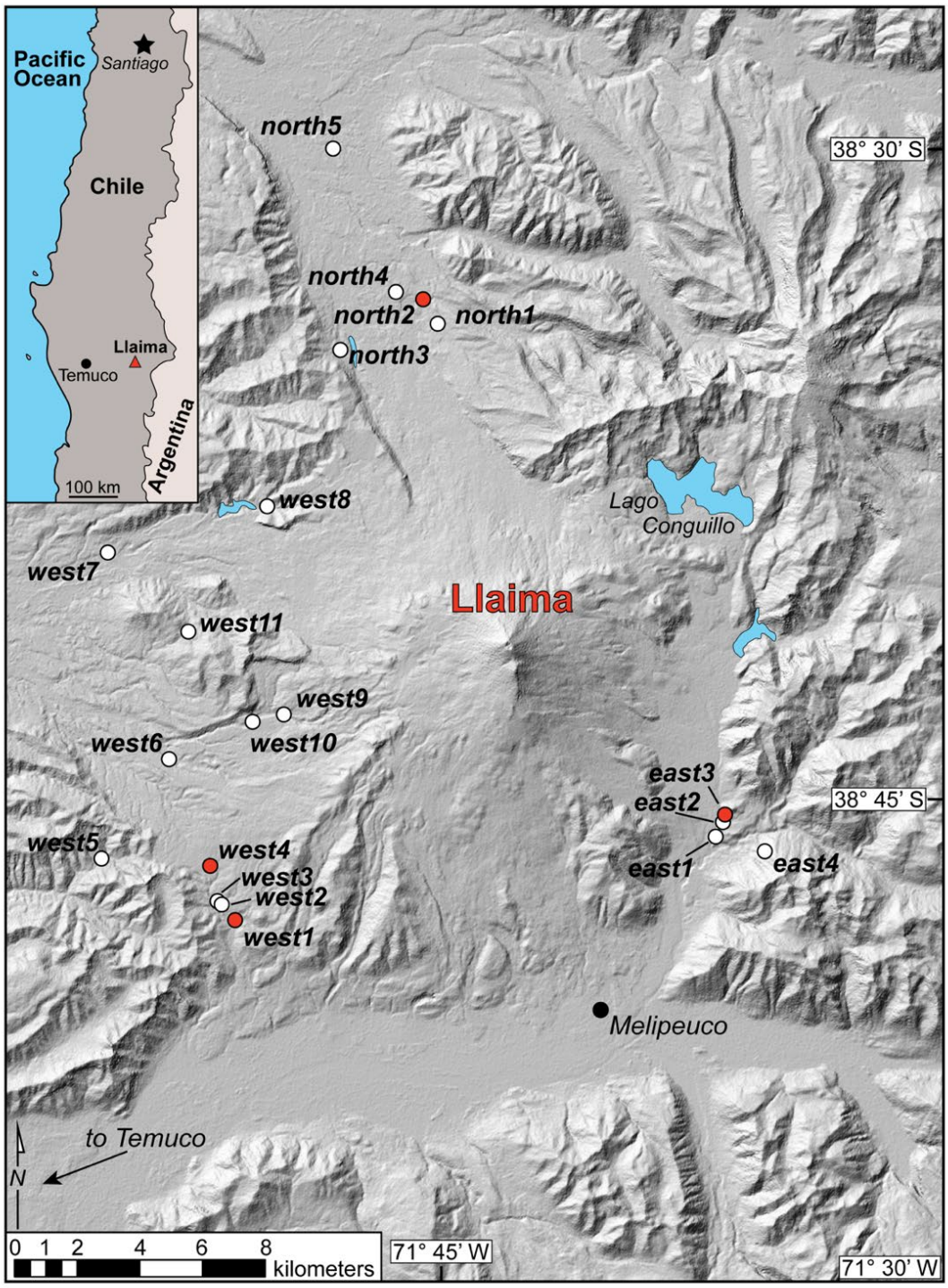

Figure 2.2 Shaded relief map of Llaima volcano. Sample locations investigated in this study are plotted as white circles. Red sample points represent locations where we collected charcoal for radiocarbon dating. Digital elevation model courtesy of http://www.ide.cl/index.php/imagenes-y-mapas-base.

The younger deposits overlying the Ci consist of reworked Ci material and paleosols. At 10.45 thousand years BP, Llaima produced a Plinian eruption of dacitic composition that is capped by surge deposits of the same eruption (Schindlbeck et al., 2014). The subsequent ten thousand years of deposits are composed of minor tephra falls, lava flows, and paleosols from Holocene cone building. Llaima's most recent eruption was a period of Strombolian explosions from 2008–2009 that generated tephra fall and minor lava flows (Ruth et al., 2016; Franco et al., 2019).

2.2.2.3 Why study the Curacautín ignimbrite?

The Ci is understudied despite its potential to provide insights into mafic explosive volcanism. Naranjo and Moreno (1991) hypothesize that the 13.2 thousand years BP eruption formed an 8 km wide now buried caldera, but no clear field evidence exists to support this interpretation. Their tephra volume estimate of 24 km^3 is calculated by assuming an average thickness of 10 m for 2,200 km^2 of deposits (Naranjo and Moreno, 1991). This estimate is a reasonable first order approximation, but applying new methods permits a more rigorous calculation of the eruptive volume. Naranjo and Moreno (1991) and Lohmar (2008) suggest the Ci was emplaced by two distinct eruptions based on ^{14}C ages of 13.2 thousand years BP and 12.6 thousand years BP; however, field evidence to support the time interval between two eruptions requires further investigation. Finally, the magmatic conditions that cause the explosive the Ci eruption have yet to be fully explored.

2.3 Methods

2.3.1 Field methods

We mapped the Ci to the north, east, and west of Llaima volcano (southern deposits are not exposed, Fig. 2.2). We measured stratigraphic sections at each outcrop to correlate deposits from one region to another. We collected samples for granulometry, pyroclast densities, textural analysis, and compositional analyses vertically for each stratigraphic section. We closely examined stratigraphic features to identify evidence indicative of a break in deposition, such as paleosols, coignimbrite ash, truncated elutriation pipes, reworked deposits, and erosional horizons. We also collected charcoal where present for ^{14}C dating.

2.3.2 Granulometry and pyroclast density analyses

We collected 31 bulk samples of ignimbrite, which includes ash, pumice, and lithics. For each sample, we gathered 20–25 kg of deposit from a clean outcrop face for granulometry. Bulk samples were sieved to -3 phi ϕ (8 mm) in the field in 1ϕ intervals (ϕ scale of Wentworth, 1922). Fine fractions were brought back to the lab, dried for 24 hr at 100 °C, reweighed to correct for water weight, and sieved in 1ϕ intervals using a hammer actuated automatic sieve down to 4ϕ. The <0.063 mm (>4ϕ) fraction represents the smallest bin. The size of the five largest blocks for each sample was measured in the field. Percent blocks was measured by point counting outcrop images using the *ImageJ* software (Schneider et al., 2012). Componentry was counted for all grains >-3ϕ in the field; 300 grains for size fractions -2ϕ to 1ϕ were counted in the lab using a binocular microscope.

The densities of up to 100 lapilli-size pyroclasts for a subset of samples were measured following the methods of Houghton and Wilson (1989). We sprayed clasts with a waterproofing sealant that adds negligible mass to each clast. Clasts from each sample set representing the average density and one standard deviation above and below the average density were cut into thin sections for textural analysis.

Dense rock equivalent (DRE) density was measured using He-pycnometry at the University of Oregon and converted to vesicularity using

$$\varphi = 100 \cdot \frac{\rho_{DRE} - \rho_{clast}}{\rho_{DRE}}$$

where φ=vesicularity, ρ_{DRE}=DRE density, and ρ_{clast}=clast density (Houghton and Wilson, 1989).

2.3.3 Pyroclast textural analyses

For lapilli-size clasts, phenocryst contents of plagioclase, olivine, pyroxene, and FeTi oxides were measured by area counting thin section scans and correcting for sample vesicularity. We performed textural analysis using backscattered images in order to measure the area and number of plagioclase crystals. Backscattered images were collected on a FEI Teneo Field Emission Scanning Electron Microscope (FESEM) at the Boise State University Center for Materials Characterization using a beam current of 6.4 nA and 15 kV accelerating voltage. Plagioclase microlites were segmented as individual polygons in ImageJ (Schneider et al., 2012). Plagioclase area fraction (ϕ_{plag}) was calculated using

$$\phi_{plag} = \frac{A_{plag}}{A}$$

where A=the vesicle-free area and A_{plag}=the area of plagioclase (Hammer et al., 1999). Plagioclase number densities N_A were calculated by

$$N_A = \frac{n_{plag}}{A}$$

where n_{plag}=number of plagioclase crystals. The longest axis was measured in *ImageJ* and used to calculate mean crystal size S_m. The volumetric number density (N_V) was then calculated using

$$N_V = \frac{N_A}{S_m}$$

after Couch (2003). Only plagioclase microlite textures were measured because plagioclase is most sensitive to changes in pressure, temperature, and water content (Szramek et al., 2006) and, therefore, a suitable proxy for conduit processes.

2.3.4 Radiocarbon analyses

We collected charcoal where exposed for ^{14}C dating. Analyses were conducted at the Rafter Radiocarbon Laboratory of GNS Science, National Isotope Centre, New Zealand following standard procedures. Ages are reported in years BP. Calibration was done using SHCal13 (Hogg et al., 2013). One sample was collected in the east, three from the west, and two from the north (Fig. 2.2).

2.3.5 X-ray fluorescence

We collected whole-rock major and trace element chemistry to investigate if a geochemical fingerprint exists between different Ci units vertically through the stratigraphy and geographically around the edifice. We conducted X-ray fluorescence

(XRF) analyses using the ThermoARL AdvantXP+ sequential XRF spectrometer at the Washington State University Peter Hooper GeoAnalytical Laboratory. Juvenile material was chipped and hand-picked under a binocular microscope to remove xenoliths and phenocrysts. Picked material was ground to a fine powder using a tungsten carbide mill. Glass beads were created by fusing sample powder with a 10:1 mixture of lithium tetraborate and lithium metaborate flux. See Johnson et al. (1999) for complete methods.

2.3.6 Volume estimate

To revise the volume estimate of Naranjo and Moreno (1991), we used a modified version of the methods of Silleni et al. (2020). We first delineated a 0-m isopach that represents an approximation of the maximum depositional extent of the Ci. To do this, we created a 10-m evenly spaced point grid encompassing 176 km^2 of mapped Ci deposits from the Naranjo and Moreno (2005) geologic map using ESRI's ArcMap software. We did not use the ~2,200 km^2 of deposits originally mapped in Naranjo and Moreno (1991) because we were unable to corroborate this area of deposition with our mapping. The farthest distance we mapped the Ci in this study is ~25 km to the north. The hillslope angle where the Ci is deposited was calculated at each point within the fishnet (17,615 total points). Three hillslopes, 9°, 13.5°, and 17.5° degrees were chosen to represent the maximum Ci extent whereby we trace a 0-m isopach. We approximate deposit thinning by measuring the change in deposit thickness between outcrops to estimate the lateral extent of Ci deposition in valleys and drainages using measured stratigraphic sections of this study and those of Lohmar (2008). We note that we only have one outcrop where the base is exposed, and this thinning is therefore assumed to be a minimum estimate.

Simplified 5-m isopachs up to a maximum thickness of 35 m were manually traced based on measured sections and field observations.

2.4 The Curacautín ignimbrite

The Ci is exposed proximally (within ~30 km) to the north, east, and west of Llaima volcano. Naranjo and Moreno (1991) map the Ci throughout drainages to the S and SW of Llaima and as far west as the city of Temuco (Fig. 2.1); however, our field mapping did not locate any Ci exposures beyond those shown in Fig. 2.2. Therefore, we base our volume estimates on the known exposures mapped in our study and those of Naranjo and Moreno (2005).

The most complete section of the Ci is found on the east side of the modern-day edifice and contains four discernable units (outcrops east1, 2, and 3; Fig. 2.2). Exposures to the north and west share similar deposit characteristics to the flow units observed in the east. However, we do not find multiple flow units in these other exposures, which could be due to the lack of deposition of multiple flow units in other locations, amalgamation of flow unit contacts, or loss of data due to the incomplete and heavily eroded nature of those outcrops. As such, we use depositional characteristics, granulometry, pyroclast density, and pyroclast chemistry to try to correlate outcrops around the volcano. Sample locations and granulometric data are presented in Table 2.1.

2.4.1 Eastern stratigraphy

The most complete eruptive sequence is exposed in the eastern exposures (Fig. 2.3). Here, the Ci consists of four flow units of variable thicknesses. The lowest and

thickest unit is Unit 1. This unit is exposed and accessible at exposures east1, east2, and east3 (Fig. 2.2). Units 2, 3, and 4 are considerably thinner, and only accessible at exposure east3.

2.4.1.1 Unit 1

Unit 1 is at least 30 m thick (base not exposed). It consists of a massive, very poorly sorted, and matrix-supported lapilli tuff with no distinct grading patterns. Faint diffuse stratification is evident throughout (Fig. 2.3). The exposure on average contains 1% blocks of juvenile magma (scoria) and lithics, but some localized block concentrations can be up to 3%. Lapilli and ash sized grains at the base of east1 (Fig. 2.2) are composed of 78% scoria and 22% lithics; lithics include mafic lavas and lesser amounts of granite and crystals. Scoria concentrations are variable upsection between 74% and 77% and decrease to 71% near the top. Granitic lithic clasts (lapilli to fine blocks in size) within the ashy matrix are platey and subangular to angular. Mdϕ for bulk samples (pyroclasts + lithics) are variable between 0.0 and 1.1 with a sorting (σ) from 2.76 to 3.01 (Table 2.1; Fig. 2.4). Unit 1 slightly fines upsection (Fig. 2.4). There are 0.5–1 cm diameter degassing pipes in the upper 0.5 m that abruptly truncate at the contact with overlying Unit 2. The uppermost 3–6 cm contains a fine-grained ash with small spherical to ellipsoidal voids. The ash is capped with a thin (cm-thick) layer of spherical ash pellets typically 1–3 mm in diameter (Fig. 2.6).

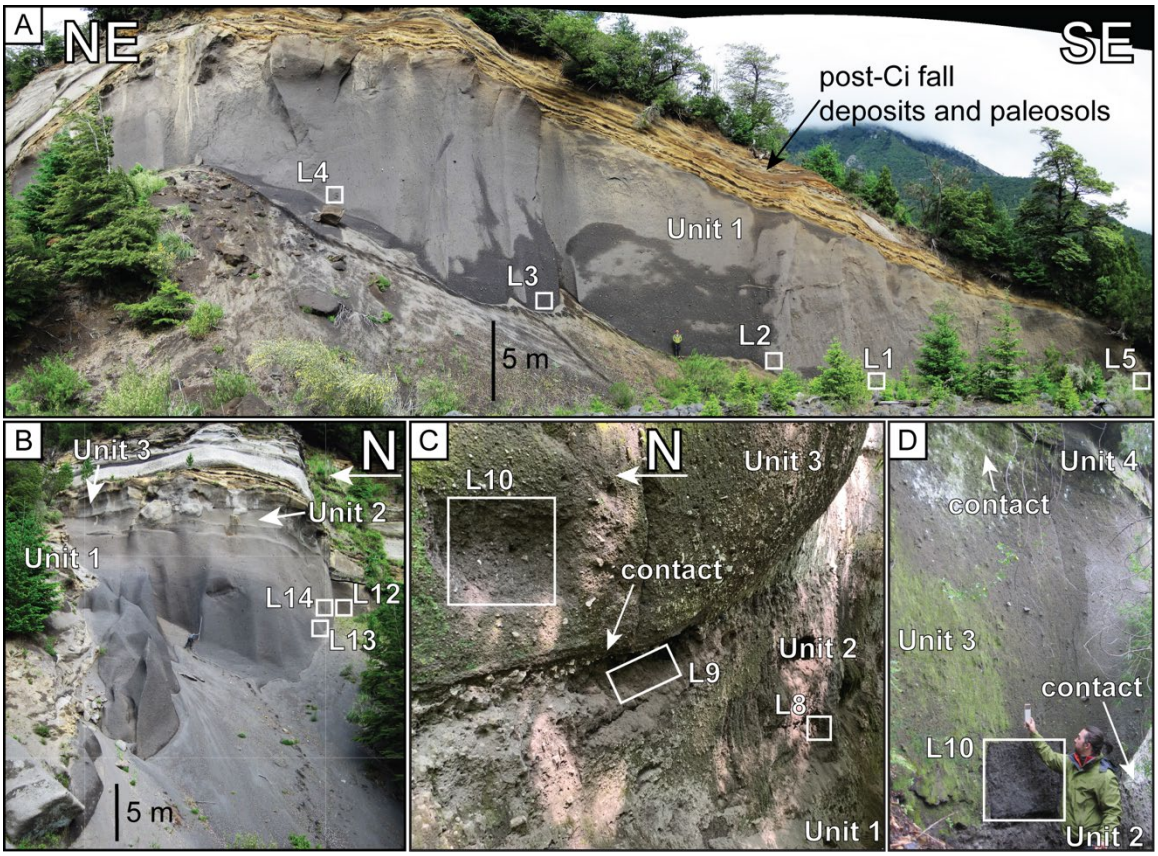

Figure 2.3 Outcrop photos from select exposures on the east. We sampled the entire stratigraphy by sampling laterally across three exposures. Sample locations are marked by white boxes. Cardinal directions are in bold white text. (A) Outcrop east1, which is the lowermost part of Unit 1. The base is not exposed. Unit 1 is the thickest flow Unit of the Ci. (B) Outcrop east2 approximately 200 m north of east1. The contact between Unit 1 and Units 2 and 3 is visible but inaccessible. (C) Outcrop east 3 approximately 50 m north of east2. Here we can access the contacts between all flow units. Charcoal collected from Unit 2 (L9) returned an age of 12,643±0.055 thousand years BP. (D) Outcrop east 3 showing the contact between Units 3 and 4.

Pyroclasts are subrounded, microvesicular, and often contain 1–5% of 1–5 mm diameter granitic and intermediate to mafic lithic inclusions, ≤2% phenocrysts of primarily plagioclase with lesser amounts of olivine, pyroxene, and Fe-Ti oxides, and 2–3 mm diameter crystal clots. Pyroclasts often exhibit agglomerate textures both in hand sample and in thin section (Fig. 2.7). Here, we use the term agglomerate to describe clasts

comprising multiple pyroclasts fused together. Pyroclast groundmass is highly crystalline and microlite-rich with little to no glass (Fig. 2.8A). Unit 1 has ϕ_{plag} between 0.36 and 0.44, N_A between 4.99×10^4 and 6.72×10^4 mm^{-2}, and N_V between 8.21×10^6 and 1.33×10^7 mm^{-3} (Table 2.2). The average plagioclase microlite length is 5–6 μm. There is no systematic trend in microlite volumetric number densities with stratigraphic level. Unit 1 pyroclast densities range from 0.63 and 2.62 g cm^{-3}; average pyroclast densities are between 1.21±0.23 g cm^{-3} and 1.39±0.30 g cm^{-3}; there is no systematic stratigraphic trend (Fig. 2.4). The DRE density is 2.76 g cm^{-3}. Vesicularity ranges between 50±11% and 56±8% with an average of 52% (Table 2.1).

Table 2.1 Curacautín granulometry and density data. Elevation is measured from the base of the exposure.

Sample	Northing	Easting	Outcrop	Unit	Elevation (m)	Mdϕ	Sorting (σ)	F2	F1	Average density (g cm-3)	Vesicularity (%)
L1	5705312	0271726	east1	1	1	0.00	3.00	16.59	56.19	1.32 ± 0.28	52 ± 10
L2	5705312	0271726	east1	1	3	0.00	2.99	16.84	56.82	1.35 ± 0.30	51 ± 11
L3	5705312	0271726	east1	1	7	1.10	3.01	21.60	63.02	1.21 ± 0.23	56 ± 8
L4	5705357	0271750	east1	1	14	0.75	2.75	23.12	72.49	1.31 ± 0.28	53 ± 10
L13s	5705515	0271804	east2	1	24.5	0.70	2.71	23.83	72.59	1.26 ± 0.25	54 ± 9
L14s	5705515	0271804	east2	1	25.5	0.25	2.76	18.98	68.12	1.39 ± 0.30	50 ± 11
L12	5705515	0271804	east2	1	28	0.50	2.59	18.58	67.71		
L6	5705558	0271863	east3	1	32	0.25	2.93	19.10	65.62	1.26 ± 0.27	54 ± 10

Sample	Northing	Easting	Outcrop	Unit	Elevation (m)	Mdϕ	Sorting (σ)	F2	F1	Average density (g cm-3)	Vesicularity (%)
L7	5705558	0271863	east3	2	32	0.25	1.78	6.94	70.52		
L8	5705558	0271863	east3	2	33	0.25	2.63	19.32	69.35	1.32 ± 0.32	52 ± 12
L10	5705558	0271863	east3	3	35	0.25	2.71	13.23	64.13	1.39 ± 0.37	50 ± 13
L18	5705558	0271863	east3	4	~39	0.25	2.25	13.24	70.66	1.41 ± 0.31	49 ± 11
L16	5711555	0256269	west11	unk	1	-1.00	2.20	4.50	50.72	1.58 ± 0.26	43 ± 10
L21	5705086	0272892	east4	unk	1	-1.75	2.02	2.20	36.14	1.35 ± 0.32	53 ± 13
L23	5709606	0253180	west9	unk	1	-1.75	2.30	4.24	37.87		
L24	5709266	0251805	west10	unk	1	-2.25	2.29	3.30	28.63	1.45 ± 0.40	50 ± 18
L25	5702880	0249719	west4	unk	1	-1.00	2.56	9.81	48.10	0.83 ± 0.25	71 ± 10

Sample	Northing	Easting	Outcrop	Unit	Elevation (m)	Mdϕ	Sorting (σ)	F2	F1	Average density (g cm-3)	Vesicularity (%)
L30	5701665	0250840	west2	unk	0.5	-0.50	2.72	12.80	57.30		
L31	5703025	0246533	west5	unk	0.5	0.40	2.28	15.12	73.73		
L34	5727122	0257641	north2	unk	0.5	-1.25	3.00	9.10	46.53	1.34 ± 0.24	52 ± 9
L35	5726337	0257848	north1	unk	1	-0.60	2.50	10.00	56.21	1.43 ± 0.25	49 ± 9
L36	5726337	0257848	north1	unk	5	-0.25	2.53	12.83	62.48	1.38 ± 0.25	50 ± 9
L37	5726337	0257848	north1	unk	~8	-0.50	2.42	10.39	61.14	1.34 ± 0.22	52 ± 8
L38	5726093	0254449	north3	unk	1	-0.50	2.21	7.23	59.74		
L39	5727546	0256997	north4	unk	0.5	-0.45	2.64	11.70	59.78	1.47 ± 0.24	47 ± 9
L40	5718323	0251676	west8	unk	1	-0.75	2.39	8.58	55.05		

Sample	Northing	Easting	Outcrop	Unit	Elevation (m)	Mdϕ	Sorting (σ)	F2	F1	Average density (g cm-3)	Vesicularity (%)
L41	5716247	0245296	west7	unk	<0.5	-0.20	2.49	11.09	61.87		
L42	5700831	0251158	west1	unk	1	-0.40	2.77	11.65	58.20		
L43	5701758	0250698	west3	unk	0.5	0.25	2.94	14.61	64.87		
L44	5701758	0250698	west3	unk	1	0.35	2.68	14.65	68.29		
L45	5707924	0248529	west6	unk	1	-1.00	2.78	12.55	49.03		

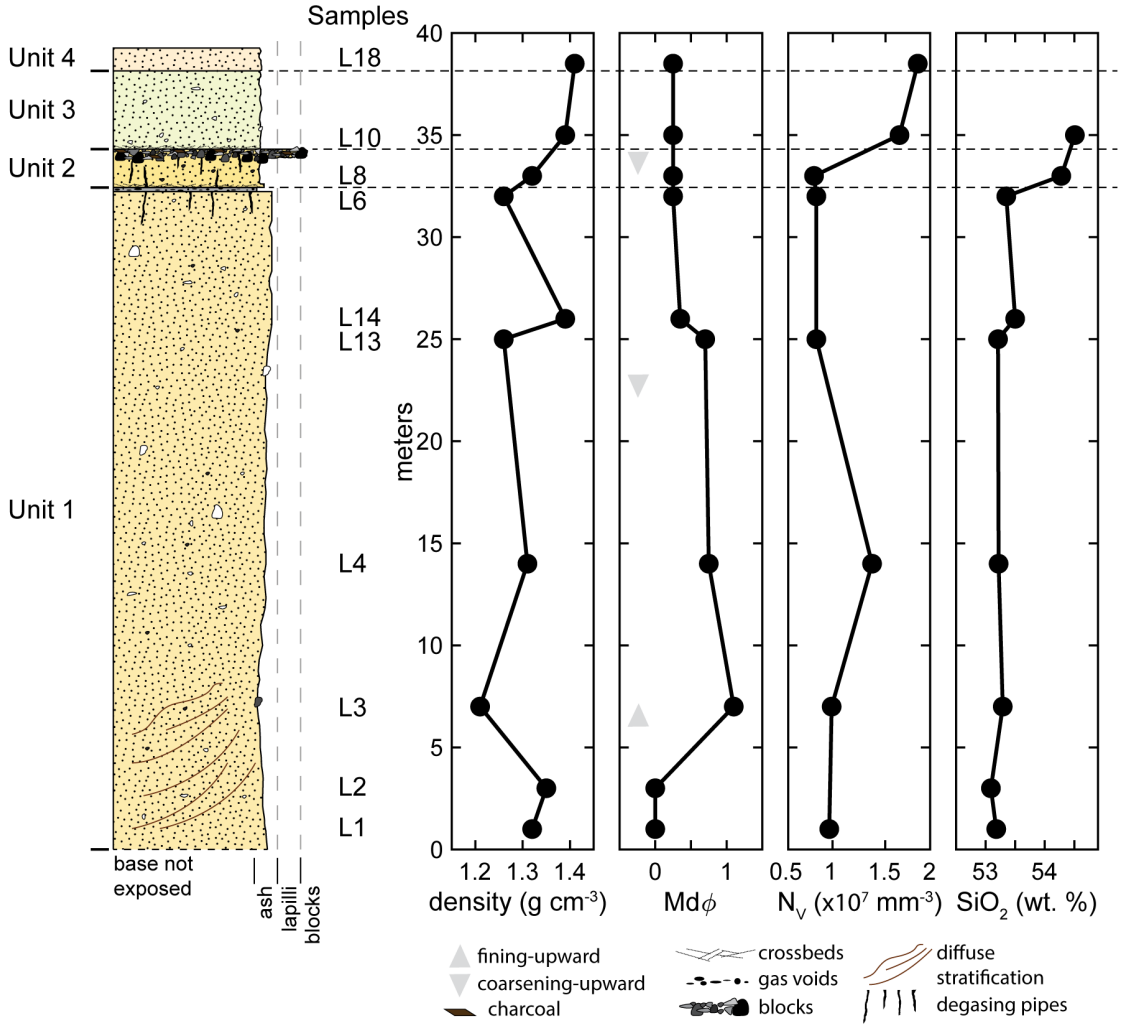

Figure 2.4 Stratigraphic column of the eastern Ci stratigraphy across exposures east1, east2, and east3. Plotted alongside the column are the Ci density (g cm^{-3}), Mdϕ, plagioclase N_V (mm^{-3}), and SiO_2-content to visualize stratigraphic variability. Juvenile densities are highly variable across all units. Unit 1 grain size data fine upwards before slightly coarsening again near the top. Units 2, 3, and 4 have the same Mdϕ. N_V are variable in Unit 1 and steadily increase in overlying units. SiO_2-content is homogenous in Unit 1 and becomes more evolved in Units 2 and 3. Chemistry was not collected for Unit 4.

Major and trace element chemistry is provided in Table 2.3. There are no systematic trends in Unit 1 major element contents stratigraphically or spatially. Unit 1 SiO_2-content ranges from 53.09–53.50 wt. % (Fig. 2.4) and MgO-content ranges from

4.11 to 4.30 wt. % (Fig. 2.9). Similarly, FeO-content is between 11.15 and 11.46 wt. %. Total alkalis (Na_2O+K_2O) range from 4.05 to 4.34 wt. %. CaO/Al_2O_3 ratios for Unit 1 range from 0.52 to 0.53. Unit 1 has an average Ba concentration of 198 ppm and La concentrations between 3.27 and 9.21 ppm (Fig. 2.10). Ce concentrations range from 14.85 to 21.57 ppm. Sr increases upsection throughout east1, east2, and east3 from 415 to 420 ppm before decreasing back to 414 ppm. Ni and Cr concentrations exhibit little variability from 10.39–13.96 ppm and 8.32–10.99 ppm, respectively. Additional trace element data is listed in Table 2.3.

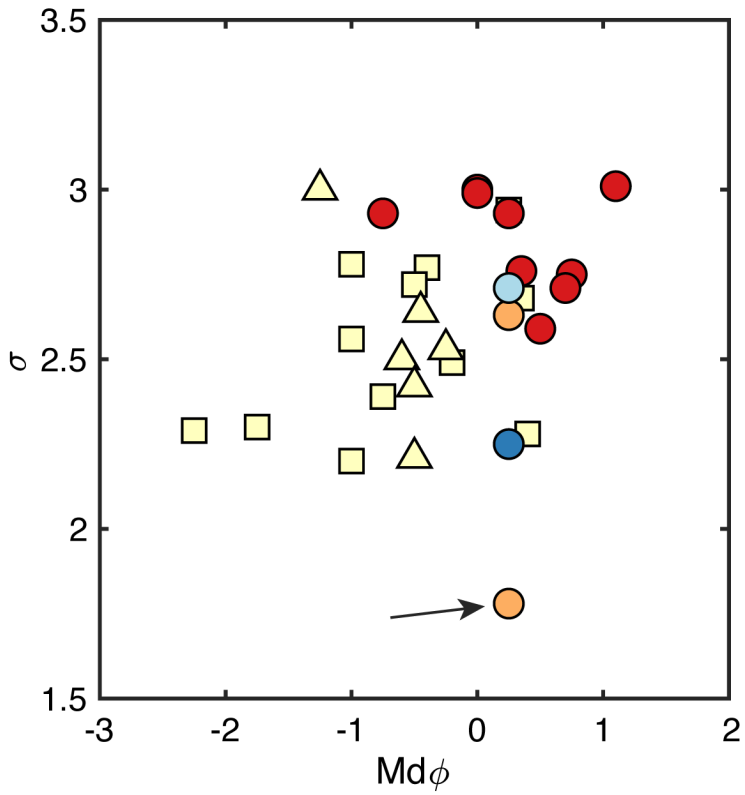

Figure 2.5 Ci Mdϕ versus sorting (σ). σ is calculated using the equation of Folk and Ward (1957). Most Ci deposits are very poorly sorted coarse ash tuffs and lapilli tuffs. The arrow points to the cross-bedded basal zone of Unit 2 and is the only poorly sorted sample. Due to a lack of contacts in the north and west, we are unable to differentiate between flow units.

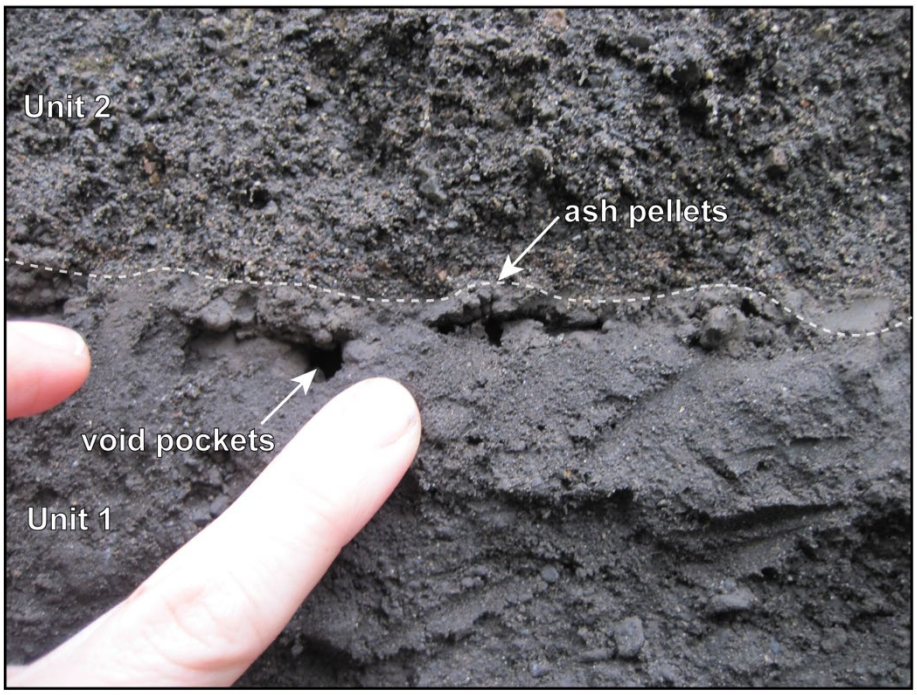

Figure 2.6 Contact between Units 1 and 2 at east3–the dashed white line indicates the contact. There are ellipsoidal void pockets in a fine-grained ash capped with ash pellets.

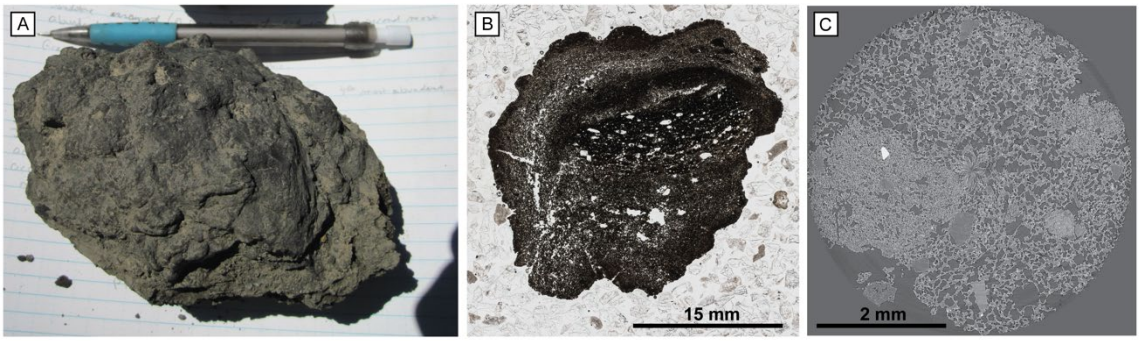

Figure 2.7 Examples of clast agglutination in Ci pyroclasts at multiple scales. (A) Small, agglutinated block from outcrop west9. (B) Thin section scan from outcrop north2. Evidence for clast agglutination is common in all exposures. (C) X-ray computed tomography (XRT) slice of a pyroclast from east2 exhibiting small-scale agglutination. See Valdivia et al. (2021) for XRT details.

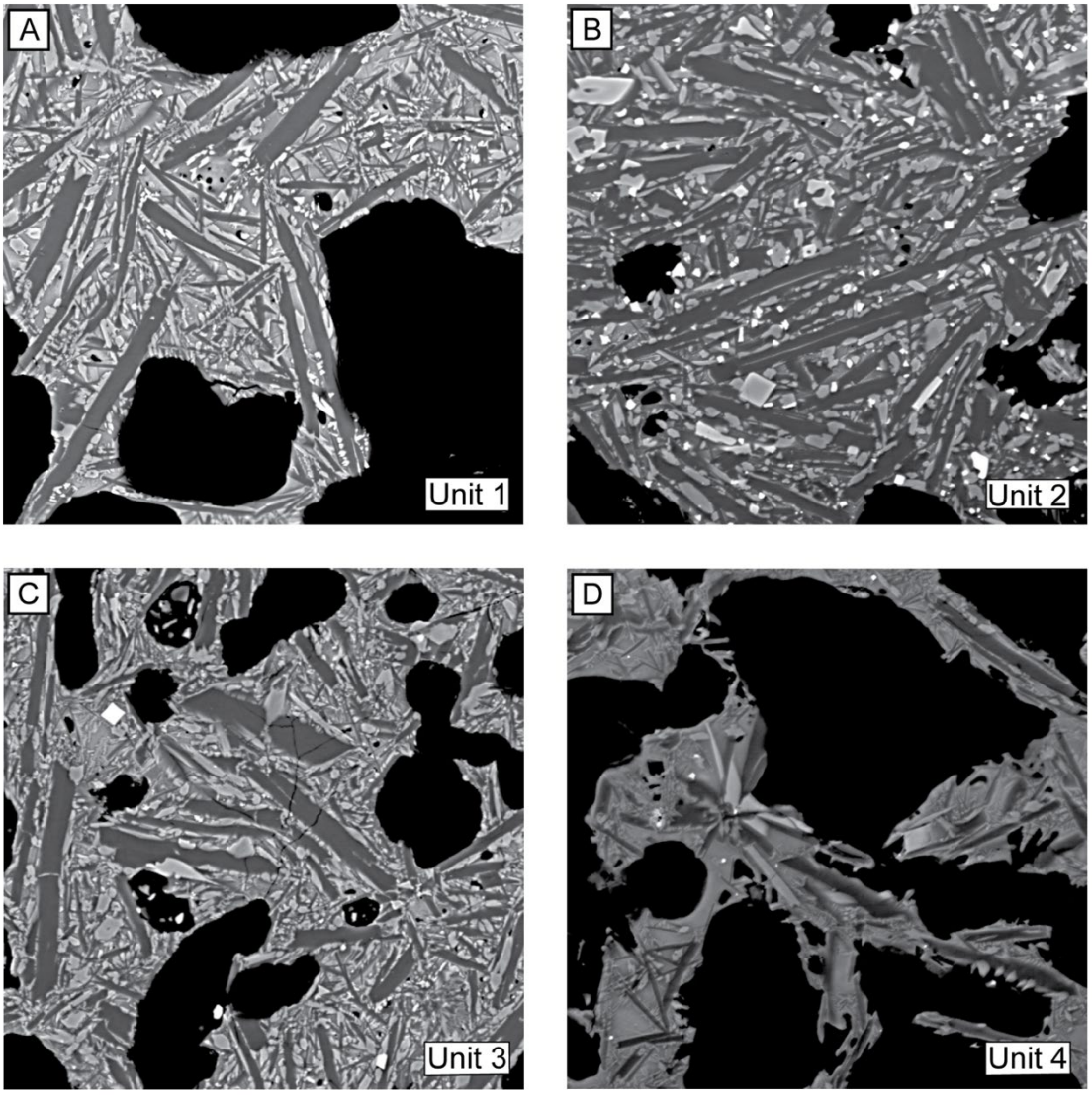

Figure 2.8 Backscattered electron images of Ci pyroclasts from flow units in the east. (A) Unit 1; (B) Unit 2; (C) Unit 3; (D) Unit 4. The horizontal field width of each image is 100 μm.

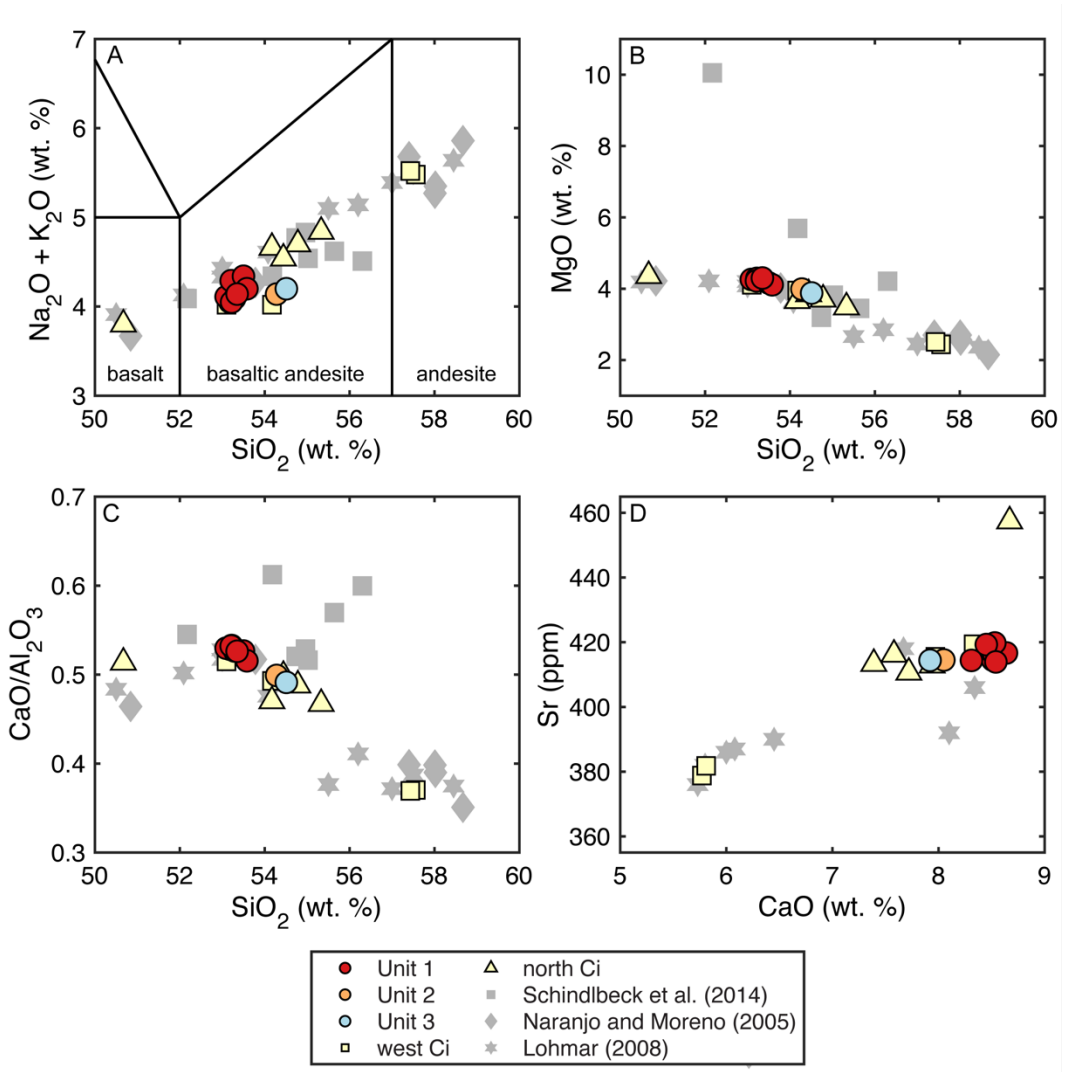

Figure 2.9 Whole-rock major element geochemistry. (A) Total alkali-silica diagram. (B) SiO_2 versus MgO Harker diagram. (C) SiO_2 versus CaO/Al_2O_3 Harker diagram. (D) CaO versus Sr diagram. Ci datasets of Naranjo and Moreno (2005), Lohmar (2008), and Schindlbeck et al. (2014) are plotted for comparison. The east stratigraphic section is where we observe the most complete stratigraphy for the Ci. However, the compositional range of the north and west exposures exceeds that of the eastern deposits.

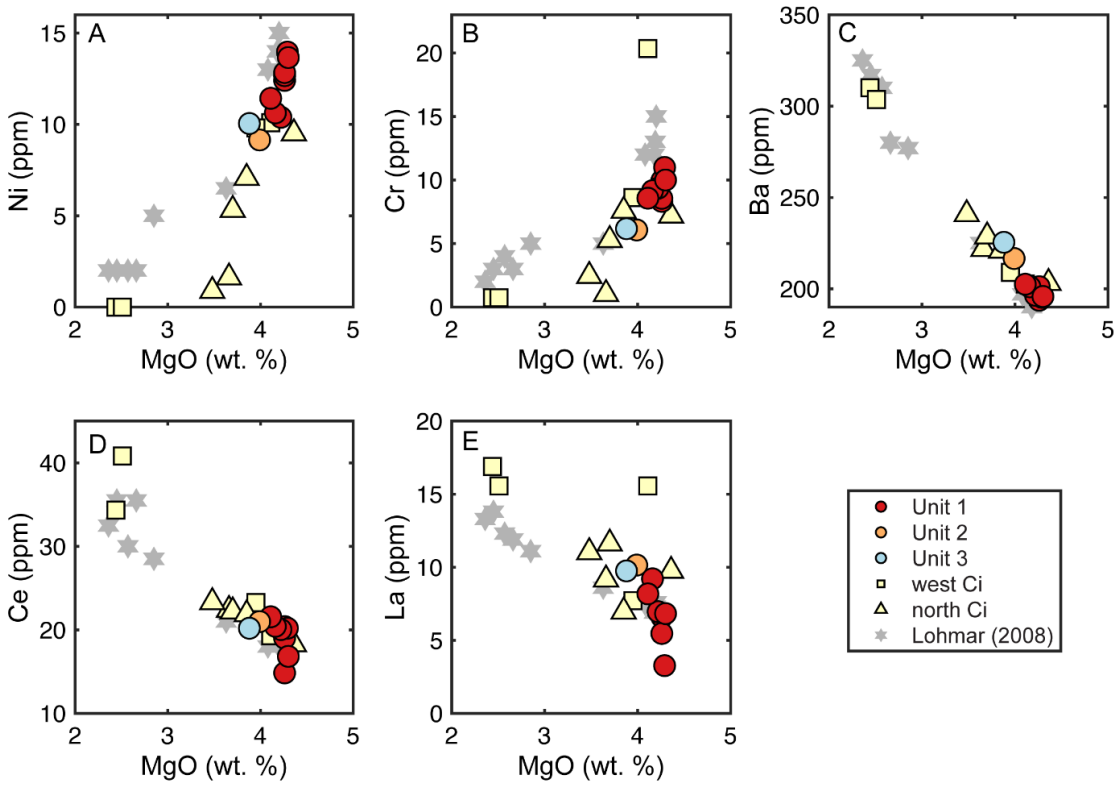

Figure 2.10 Select whole-rock Ci trace element geochemistry. (A) MgO versus Ni; (B) MgO versus Cr; (C) MgO versus Ba; (D) MgO versus Ce; (E) MgO versus La.

2.4.1.3 Unit 2

The contact between Unit 1 and Unit 2 is sharp (Fig. 2.3B). Unit 2 is ~1.5 m thick and begins with a 3–12 cm thick basal zone of poorly sorted, cross-stratified, medium to coarse lapilli pyroclasts and lithic ash that pinches and swells across the exposure (Fig. 2.6). Degassing pipes are prominent on fresh surfaces through this basal layer. The ash layer grades into a massive, very poorly sorted, matrix-supported lapilli tuff. The matrix of this unit is more indurated than Unit 1. The massive section of Unit 2 has a Mdϕ of 0.3, a σ of 2.63, and is reversely graded in the upper 15 cm to a lens of clast-supported coarse lapilli pyroclasts and fine blocks (Fig. 2.4). Charcoal collected from the clast-

supported layer (sample L8) returned a ^{14}C age of 12.643±0.055 thousand years BP (Table 2.4). Unit 2 componentry includes 77% juvenile pyroclasts and 23% lithics of primarily mafics and lesser amounts of granodiorite and free phenocrysts.

Pyroclasts are subrounded, microvesicular, and contain ≤2% lithic inclusions of mafic lavas and granitic rocks. Like in Unit 1 pyroclasts, the matrix is composed almost entirely of microlites (Fig. 2.8) but contains only ~3.5% phenocrysts of plagioclase and lesser amounts of olivine, pyroxene, and Fe-Ti oxides. There is little to no glass (Fig. 2.8B). Pyroclasts exhibit agglomerated textures. Unit 2 has a ϕ_{plag} of 0.42, N_A of 5.08×10^4 mm^{-2}, and an N_V of 7.95×10^6 mm^{-3} (Table 2.2). The average plagioclase microlite length is 7 μm. The average density of Unit 2 juveniles is 1.32±0.32 g cm^{-3} with a similar variability of total measured densities (0.62–2.25 g cm^{-3}). Unit 2 has a slightly higher DRE density of 2.78 g cm^{-3}. Pyroclasts have an average vesicularity of 52±12% (Table 2.1).

Only one sample was measured for Chemistry in Unit 2. This sample has SiO_2, MgO, and FeO contents of 54.28, 3.99, and 11.08 wt. %, respectively (Fig. 2.4; Table 2.3). The total alkali content is 4.14 wt. % while CaO/Al_2O_3 is 0.50 in Unit 2 (Fig. 2.9). Ba, Ce, and La concentrations increase to 217, 10.15, and 20.99 ppm in Unit 2. In contrast, Sr, Ni, and Cr decrease to 415, 9.15, and 6.07 ppm (Fig. 2.10, Table 2.3).

Table 2.2 Plagioclase microlite textures. All pyroclasts are from the eastern stratigraphic section. Three analyses were conducted for all samples except L3 and L13. The theoretical calculation of mean crystal size S_m from equation (1) of Blundy and Cashman (2008) is included to show the disagreement between this method and our measured S_m.

Unit	Unit 1					Unit 2	Unit 3	Unit 4
Sample	L1	L3	L4	L13	L6	L8	L10	L18
ϕ_{plag}	0.39	0.42	0.36	0.42	0.44	0.42	0.36	0.29
S_m (μm)	6.1	5.5	5.1	6.1	6.4	6.5	4.7	4.1
N_A (mm^{-2})	5.56E4	5.29E4	6.72E4	4.99E4	5.25E4	5.08E4	7.07E4	7.32E4
N_V (mm^{-3})	9.72E6	9.55E6	1.33E7	8.21E6	8.21E6	7.95E6	1.66E7	1.84E7
S_m (μm)*	2.7	2.8	2.4	2.9	2.9	2.9	2.2	2.0
N_V (mm^{-3})+	2.22E7	1.87E7	2.89E7	1.72E7	1.82E7	1.78E7	3.60E7	3.73E7
n_{plag}	1,113	437	1,737	437	985	1,307	1,796	1,180
error&	3%		2%		3%	3%	2%	3%

2.4.1.3 Unit 3

The contact between Unit 2 and Unit 3 is sharp (Fig. 2.3C and 2.3D). Unit 3 is ~4.2 m thick. The lowest 3–5 cm is cross-stratified and similar in appearance to the basal layer of Unit 2. This basal layer grades into a very poorly sorted and indurated massive lapilli tuff. Unit 3 contains ~24% lithics. Unlike other Ci units, Unit 3 lithics are dominated by 48% granite and leucogranite lithics with lesser amounts of mafics and free crystals. The Mdϕ is 0.3 with a σ of 2.71 (Table 2.1).

Juvenile pyroclasts are microvesicular, subrounded, have granitic to mafic lithic inclusions, and contain ~3% phenocrysts of plagioclase, olivine, and pyroxene. Similar to other units, pyroclasts are often agglomerates, contain little to no glass, and are composed

of >90% microlites of plagioclase, clinopyroxene, olivine, and Fe-Ti oxides. Unit 3 has a ϕ_{plag} of 0.36, N_A of 7.07×10^4 mm^{-2}, and an N_V of 1.66×10^7 mm^{-3} (Fig. 2.8C, Table 2.2). The average measured plagioclase microlite length is 5 μm. Densities vary between 0.63 and 2.69 g cm^{-3} with an average density of 1.39±0.37 g cm^{-3} (Fig. 2.4). The average vesicularity is 50±13% (Table 2.1).

The composition of only one sample was measured for chemistry in Unit 3. This sample has the highest SiO_2 content of 54.51 wt. % (Fig. 2.4), lowest MgO content of 3.88 wt. %, and the lowest FeO content of 10.98 wt. % of all eastern Ci units sampled (Table 2.3). Total alkalis increase slightly from Unit 2 to 4.20 wt. % in Unit 3. The CaO/Al_2O_3 ratio is 0.49. Ba-content increases to 225.47 ppm, while La and Ce both decrease to 9.75 and 20.20 ppm, respectively. Sr slightly decreases further to 414.42 ppm in Unit 3. Ni and Cr both increase from Unit 2 to Unit 3 to 10.05 and 6.17 ppm but are still lower than their Unit 1 averages of 12.25 and 9.36 ppm, respectively (Fig. 2.10).

2.4.1.4 Unit 4

The contact between Unit 3 and Unit 4 is sharp (Fig. 2.3D). Unlike Units 2 and 3, no coarse ash layer exists at the Unit 4 base (Fig. 2.4). Unit 4 is ~1.1 m thick, massive, very poorly sorted, and indurated. Juvenile content is 74%. Hydrothermally altered lithics make up 51% of lithic material, with lesser amounts of granite, mafics, and free crystals. Unit 4 has a Mdϕ of 0.25 with a σ of 2.25 (Table 2.1).

Table 2.3 Whole-rock major and trace element geochemistry. Major elements are reported as wt. % and trace elements are reported as ppm. FeO = total Fe.

Sample	L1	L2	L3	L4	L13	L14	L12	L6	L8	L10	L16	L23	L43	L44	L34	L35	L36	L37	L39
Unit	1	1	1	1	1	1	1	1	2	3	unk	unk	unk	unk	unk	unk	unk	unk	unk
SiO_2	53.18	53.09	53.29	53.22	53.21	53.50	53.58	53.35	54.28	54.51	53.10	54.17	57.56	57.43	54.17	54.78	54.44	50.67	55.33
TiO_2	1.45	1.47	1.47	1.47	1.46	1.46	1.47	1.47	1.46	1.46	1.39	1.46	1.42	1.44	1.51	1.46	1.45	1.54	1.48
Al_2O_3	16.10	16.14	16.18	16.22	16.03	16.05	16.12	16.23	16.13	16.12	16.18	16.17	15.58	15.73	16.12	15.82	15.92	16.88	15.82
FeO	11.30	11.34	11.32	11.26	11.46	11.30	11.18	11.15	11.08	10.98	10.97	10.92	9.94	9.72	11.05	10.94	11.00	12.20	10.71
MnO	0.18	0.19	0.19	0.19	0.19	0.19	0.19	0.19	0.19	0.19	0.18	0.18	0.29	0.36	0.19	0.19	0.19	0.19	0.19
MgO	4.26	4.26	4.26	4.29	4.22	4.16	4.11	4.30	3.99	3.88	4.11	3.95	2.44	2.51	3.66	3.70	3.85	4.36	3.48
CaO	8.51	8.55	8.52	8.64	8.53	8.45	8.31	8.54	8.05	7.92	8.33	7.97	5.77	5.81	7.58	7.72	7.94	8.67	7.39
Na_2O	3.43	3.50	3.43	3.43	3.65	3.70	3.55	3.52	3.44	3.49	3.39	3.35	4.50	4.55	3.99	3.93	3.81	3.45	4.04
K_2O	0.62	0.61	0.66	0.62	0.64	0.64	0.65	0.62	0.70	0.71	0.63	0.67	0.98	0.97	0.67	0.77	0.73	0.35	0.80
P_2O_5	0.17	0.18	0.18	0.18	0.18	0.18	0.18	0.18	0.19	0.20	0.18	0.19	0.32	0.32	0.22	0.22	0.21	0.13	0.22
Tot.	*99.21*	*99.33*	*99.48*	*99.53*	*99.56*	*99.63*	*99.34*	*99.54*	*99.52*	*99.47*	*98.46*	*99.01*	*98.79*	*98.84*	*99.16*	*99.54*	*99.52*	*98.44*	*99.47*

Sample	L1	L2	L3	L4	L13	L14	L12	L6	L8	L10	L16	L23	L43	L44	L34	L35	L36	L37	L39
Ni	12.41	12.67	12.84	13.96	10.39	10.63	11.43	13.66	9.15	10.05	10.09	9.80	0.00	0.00	1.62	5.32	7.07	9.51	0.88
Cr	9.95	8.32	8.56	10.99	9.36	9.16	8.57	10.00	6.07	6.17	20.34	8.61	0.74	0.74	1.03	5.27	7.57	7.20	2.45
Sc	38.32	38.12	39.60	39.70	37.58	37.88	38.42	39.30	36.52	36.82	37.83	36.63	30.65	30.09	35.04	36.40	36.35	40.87	33.37
V	462.75	464.71	456.51	469.36	463.83	453.05	443.05	461.34	415.51	403.37	394.94	394.52	171.35	178.97	383.72	379.32	399.53	484.90	348.78
Ba	196.90	193.74	201.19	195.33	196.44	201.10	202.52	195.82	216.61	225.47	202.71	208.99	310.02	303.58	221.77	228.67	220.87	203.20	240.84
Rb	12.74	13.00	13.85	12.61	14.02	13.78	12.55	12.03	14.04	15.21	14.59	13.39	21.56	20.27	15.12	15.87	15.69	8.02	17.04
Sr	414.49	415.40	416.31	416.69	419.78	419.29	414.39	413.92	414.52	414.42	419.39	415.50	378.80	381.15	416.21	410.65	412.85	457.42	413.36
Zr	70.62	70.59	73.33	70.29	72.28	73.40	74.47	71.48	78.90	80.99	76.34	79.50	130.36	129.68	86.78	86.19	82.09	74.04	88.54
Y	23.34	23.27	24.48	23.86	23.18	23.18	24.43	22.97	25.27	24.48	24.06	25.74	36.16	36.20	26.31	26.30	25.55	22.39	27.00
Nb	2.27	2.08	2.49	2.28	1.47	1.67	2.56	1.78	2.49	2.69	1.57	2.38	2.90	3.50	2.11	1.82	1.67	1.57	1.81
Ga	19.01	19.50	20.00	20.49	18.91	19.45	19.60	20.10	18.91	20.00	19.06	20.89	21.12	20.54	20.24	18.96	19.40	20.34	19.99
Cu	187.74	201.56	176.51	229.48	134.26	88.25	69.54	124.44	99.50	166.26	171.89	87.22	53.84	61.51	61.54	101.95	94.37	206.58	53.80
Zn	98.70	96.33	97.71	97.81	100.06	96.73	96.33	96.72	100.40	104.77	96.78	98.31	115.79	116.57	104.47	101.16	101.88	102.31	104.27
Pb	6.60	5.64	6.37	6.63	6.86	7.35	8.27	7.62	8.86	9.75	7.45	8.51	11.10	11.48	7.06	8.77	8.45	6.66	7.94

Sample	L1	L2	L3	L4	L13	L14	L12	L6	L8	L10	L16	L23	L43	L44	L34	L35	L36	L37	L39
La	6.60	6.63	5.47	3.27	6.96	9.21	8.18	6.83	10.15	9.75	9.31	7.72	16.90	15.56	9.16	11.62	6.97	9.75	11.03
Ce	19.01	14.85	20.40	20.20	20.04	20.43	21.57	16.83	20.99	20.20	19.31	23.27	34.34	40.83	22.39	22.21	21.87	18.28	23.32
Th	0.00	0.59	2.29	1.39	1.42	1.37	1.28	0.79	2.29	1.09	1.32	2.38	2.01	2.22	0.88	1.43	0.29	0.74	1.62
Nd	11.92	11.48	15.52	14.36	13.28	14.26	15.66	11.78	15.02	16.42	13.57	13.86	20.93	20.88	15.09	15.46	13.71	12.25	14.65
U	1.08	2.57	1.29	1.98	2.35	1.67	0.89	0.59	1.59	1.09	1.42	0.50	2.70	1.33	1.32	0.64	1.18	1.57	2.60
Tot.	*1594.54*	*1601.06*	*1594.70*	*1650.66*	*1552.47*	*1501.86*	*1473.69*	*1528.02*	*1496.79*	*1569.00*	*1541.97*	*1457.70*	*1361.27*	*1375.09*	*1431.86*	*1478.01*	*1477.34*	*1687.59*	*1413.30*

Table 2.4 Curacautín ignimbrite radiocarbon analyses. Age reported in years BP. σ is the error. The ^{14}C ages reported in this study are reported as defined by Stuiver and Polach (1977). Naranjo and Moreno (1991) do not report calibration information. Lohmar (2008) ages were calibrated using CALIB 5.0 (Stuiver et al., 2005).

Sample	Latitude	Longitude	^{14}C	σ	Reference
L8	5705558	0271863	12,643	55	this study
L34	5727122	0257641	12,696	56	this study
L42	5700831	0251158	12,754	56	this study
L43	5701758	0250698	12,774	55	this study
L44	5701758	0250698	12,555	57	this study
261089-2A	5725200	0258800	12,760	130	Naranjo and Moreno (1991)
040487-7	5701900	0251000	13,200	150	Naranjo and Moreno (1991)
190190-1BC	5705800	0272000	13,260	200	Naranjo and Moreno (1991)
041189-1A	5736200	0253400	13,460	400	Naranjo and Moreno (1991)
LL24B	5709200	0246400	12,510	40	Lohmar (2008)
LL25	5739900	0249900	12,650	140	Lohmar (2008)
LL9-1	5702100	0250900	12,730	90	Lohmar (2008)
LL13	5736200	0253400	13,230	330	Lohmar (2008)

Similar to underlying units, pyroclasts are subrounded, microvesicular, and microlite-rich. Unit 4 has the lowest ϕ_{plag} of 0.29, a N_A of 7.32×10^4 mm^{-2}, and an N_V of 1.84×10^7 mm^{-3} (Table 2.2). The average measured plagioclase microlite length is 4 μm. Although microlite-rich, Unit 4 has a higher glass content than underlying units (Fig. 2.8D). Phenocryst content is ≤1%. Juvenile densities are variable between 0.35 and 2.29 g cm^{-3} with an average of 1.41±0.31 g cm^{-3}. Despite Unit 4 having some of the lowest

pyroclast densities in the entire eastern stratigraphic section, the average pyroclast density is the densest of all units (Fig. 2.4). Accordingly, Unit 4's average pyroclast vesicularity of 49±11% is the lowest of all Ci units (Table 2.1).

Due to the indurated nature of Unit 4 and the difficulty in sampling this unit, we were unable to collect pyroclasts large enough for XRF analysis.

2.4.2 Select western exposures

2.4.2.1 West9

West9 is the only location where the base of the Ci is exposed (Fig. 2.11A inset). The basal contact is with a lava and is sharp. The base contains a high concentration of coarse lapilli and fine blocks, is massive to diffusely stratified and matrix- to clast-supported. Blocks are predominately lithics and include granitic rocks and mafic to intermediate lavas. The exposure is ~25 m thick, dark gray, very poorly sorted, and matrix-supported. There are distinct zones of fine to medium blocks with local concentrations >25% (Fig. 2.11A). Lithic blocks are predominantly subangular to subrounded and composed of granitic rocks and mafic to intermediate lavas. Similarly, pyroclast blocks are subangular to subrounded, irregularly shaped agglomerates (Fig. 2.7), and dense. Pyroclasts contain ash- and lapilli-size lithic inclusions of granitic material and mafic lavas. Despite the high block content, these blocky zones are mostly matrix-supported. The matrix is composed of Ci ash similar to the block-poor regions (Fig. 2.11A) and decrease upsection to <1%. Faint diffuse stratification is evident throughout the exposure. Similar to Units 3 and 4 in the east, this exposure is indurated, but not welded. The exposure is overlain by paleosols and reworked Ci material.

Lapilli-size pyroclasts are subrounded, microvesicular and frothy to dense and glassy, and sometimes exhibit radial jointing or agglomerate textures. Lapilli-size, angular lithic inclusions of granitic material and mafics are common. Sample L23 collected here has a Mdϕ of -1.8 and a σ of 2.30 (Table 2.1). L23 is compositionally similar with respect to eastern samples (Table 2.3); with 54.17 wt. % SiO_2-content, 3.95 wt. % MgO, 10.92 wt. % FeO, 4.02 wt. % total alkalis, and a CaO/Al_2O_3 ratio of 0.49 (Fig. 2.9). Cr and Ni are 8.61 and 9.80 ppm, respectively (Fig. 2.10). Ce is 23.27 ppm, which is slightly higher than eastern exposures. La is 7.72 ppm. Ba is higher than Unit 1 samples at 209 ppm and Sr is 416 ppm.

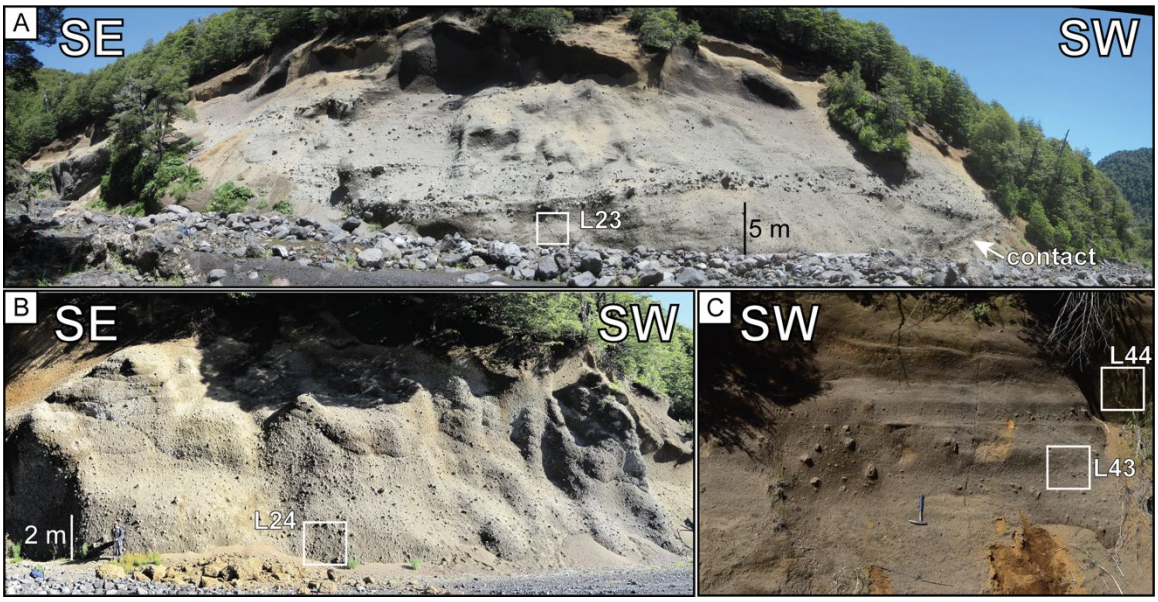

Figure 2.11 Select Ci exposures in the west. Sample locations are shown in white boxes. Cardinal directions are in bold white text. (A) Outcrop west9 is an ~25 m thick, indurated exposure where the base is exposed (white arrow). West9 has the highest concentration of blocks of any exposures in this study. The zones of blocks are matrix-supported, and the matrix is composed of Curacautín ash. (B) Outcrop west10 ~2 km southwest of west9 and located downstream in the same drainage. The base is not exposed here and the high concentration of blocks disappears. (C) Outcrop west3 where we collected ^{14}C ages of 12.774±0.057 thousand years BP (L43) and 12.555±0.055 thousand years BP (L44).

2.4.2.2 West10

West10 is ~1.5 km SW of west9 and in the same drainage (Fig. 2.2). Unlike west9, the base of west10 is not exposed. Here, the Ci is massive, very poorly sorted, and matrix-supported with little to no diffuse stratification (Fig. 2.11B). The exposure is ~12 m thick. In sharp contrast to nearby west9, there are little to no large lithic blocks in west10 either as clast-supported lenses or as dispersed material. Instead, blocks are primarily fine-grained in size, juvenile, display agglomerate textures, and have lithic inclusions of granitic material and mafic to intermediate lavas. Sample L24 collected here has a Mdϕ of -2.3 and a σ of 2.29 (Fig. 2.5, Table 2.1). Pyroclasts are phenocryst-poor, dense to frothy, and microvesicular, have an average density of 1.45±0.40 g cm^{-3}, and a corresponding vesicularity of 50±0.18%. No chemistry was collected on samples from this site.

2.4.2.3 West3

Here the Ci is ~1.5 m thick, brown, very poorly sorted, and matrix-supported (Fig. 2.11C). The base is not exposed and there is minor reworking at the top of the exposure. Blocks and coarse lapilli are locally concentrated, but otherwise the exposure is block-poor. The middle of this exposure has a 1–3 cm thick fine ash lens that both truncates one group of blocks while forming the base of a secondary group of blocks and coarse lapilli (Fig. 11C). The Ci is overlain by reworked material, soils, and vegetation. Samples collected below and above the thin ash layer have a Mdϕ of 0.25 and 0.35 and σ of 2.94 and 2.68, respectively (Table 1). This deposit is a coarse ash tuff. Charcoal collected from

L43 and L44 returned ^{14}C ages of 12.774±0.057 thousand years BP and 12.555±0.055 thousand years BP, respectively (Table 2.4).

West3 has the most evolved Ci compositions in this study (Table 2.3), with SiO_2 contents of 57.56 and 57.43 wt. % and MgO of 2.44 and 2.51 wt. % (Fig. 2.9). Their FeO content is also low compared to other locations at 9.94 and 9.72 wt. %. Accordingly, their total alkali contents of 5.48 and 5.52 wt. % are the highest of all samples. Both samples have a CaO/Al_2O_3 ratio of 0.37. L43 and L44 also exhibit elevated Ba, La, Ce compared to other samples, are depleted in Sr with respect to other samples, and have near undetectable and undetectable Cr and Ni content, respectively (Fig. 2.10). While these major and trace element data are unique in our dataset, they are similar to samples collected by Naranjo and Moreno (2005) and Lohmar (2008; Fig. 2.9).

2.4.3 Select northern exposures

2.4.3.1 North1

This exposure is ~12 m thick, beige to gray, massive, very poorly sorted, and matrix-supported (Fig. 2.12A). The base is not exposed and there is surficial reworking at the top of the deposit. The deposits are friable. Minor diffuse stratification is present near the top. The exposure has <1% blocks, but local concentrations can be >10%. Blocks are primarily subangular to subrounded lithics of intermediate lavas and lesser amounts of granitic material. Regions of high block concentration are matrix-supported and not laterally continuous. Juvenile blocks display agglomerate textures, are microporous, and contain lapilli-sized lithic inclusions of intermediate lavas to granitic material. A sharp contact with overlying reworked material and paleosols truncates gas elutriation pipes in

the upper 2–3 m. Gas elutriation pipes are evidence throughout the exposure (Fig. 2.12A).

Pyroclasts are subrounded, microvesicular, and contain lithic inclusions and rare crystal cumulates. Samples were collected at stratigraphic intervals of 1 m, 5 m, and as near to the top as possible (~8m, Table 2.1). The Mdϕ at the lowest point is -0.60, fines to -0.25, then coarsens to -0.50. The σ is similarly variable between 2.42 and 2.53. Pyroclast densities decrease upsection from 1.43±0.25 g cm^{-3} to 1.34±0.22 g cm^{-3} at the top. Accordingly, vesicularities increase from 49±9% at the base to 52±8% at the top (Table 2.1).

The base of north1 has SiO_2 and MgO content of 54.78 and 3.66 wt. %, respectively (Table 2.3). SiO_2 decreases to 50.67 wt. % upsection and is the least evolved sample we collected. MgO slightly increases upsection to 3.85 wt. %. FeO increases upsection from 10.94 to 12.20 wt. % while total alkalis decrease from 4.70 to 3.80 wt. %. CaO/Al_2O_3 increases slightly from 0.49 at the base to 0.51 near the top. Ba increases upsection while Sr and Ce decrease. Ni and Cr are low and variable (5.32–9.51 ppm and 5.27–7.57 ppm, respectively).

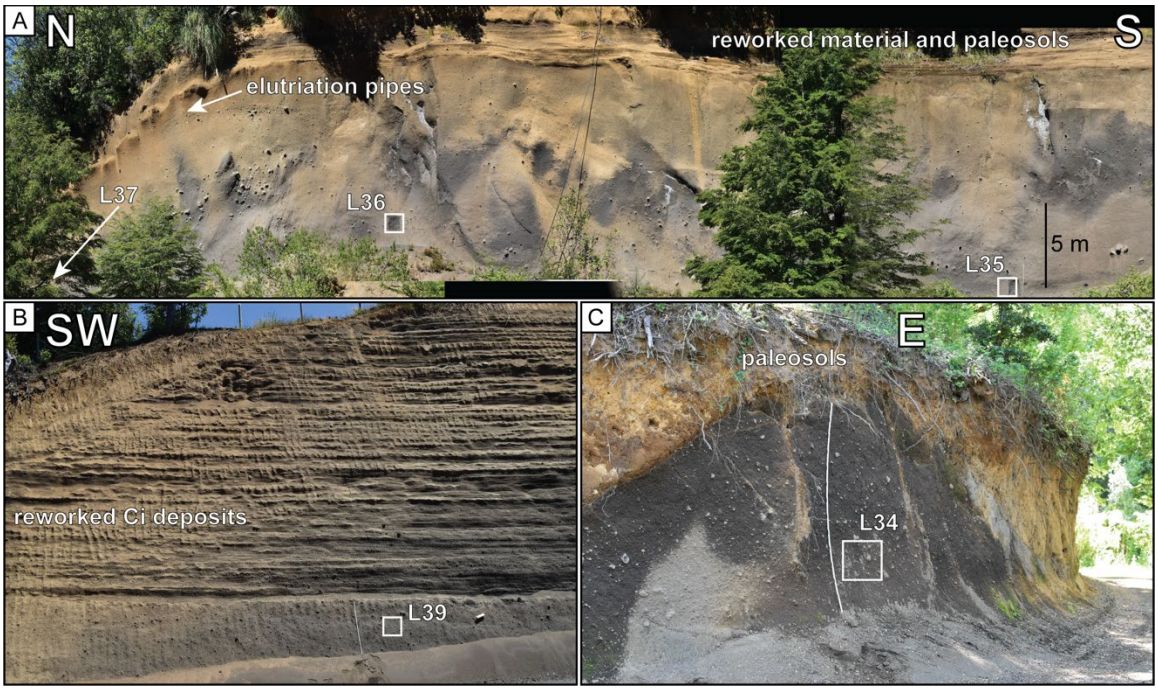

Figure 2.12 Select Ci exposures in the north. Sample locations are shown in white boxes. Cardinal directions are in bold white text. (A) North1 is the thickest exposure in the north. (B) Exposure north4 exhibiting extensive reworking of Ci material. White scale is 2 m. The dashed line marks the contact between the Ci and reworked Ci. (C) Exposure north2. Charcoal collected here returned a ^{14}C age of 12.696±0.056 thousand years BP.

2.4.3.2 North2

North2 is 2 m thick, dark gray, massive, very poorly sorted, and matrix supported (Fig. 2.12C). Like other exposures in the north, the base is not exposed. There are no blocks, visible structures, or depositional features. The top is in sharp contact with overlying paleosols. The exposure contains <1% mafic to intermediate lithics. The Mdϕ is -1.3 with a σ of 3.00 (Table 1). Charcoal collected from this exposure returned a ^{14}C age of 12.696±0.056 thousand years BP (Table 2.4).

Pyroclasts are subrounded, microvesicular, and contain rare lithic inclusions. Like other exposures, many pyroclasts display agglomerate textures (Fig. 2.7). The average

density is 1.34±0.24 g cm^{-3} and the vesicularity is 52±9% (Table 2.1). Here, the Ci is compositionally similar to other exposures, with 54.17 wt. % SiO_2, 3.66 wt. % MgO, 11.05 wt. % FeO, 4.66 wt. % total alkalis, and a CaO/Al_2O_3 ratio of 0.47 (Table 2.3). Ni and Cr are low (1.62 and 1.03, respectively) while Ba, Sr, and Ce are similar to other exposures (222, 416, and 22.39 ppm, respectively.

2.4.3.3 North4

Primary Ci deposits at north4 are up to 3 m thick, dark gray to brown, massive, very poorly sorted, and matrix supported (Fig. 2.12B). The base is not exposed, and the upper surface of the deposit is reworked. Approximately 10–12 m of reworked Ci material overlies the Ci. The exposure contains <1% blocks. The Mdϕ is -0.5 and the σ is 2.64 (Table 1). Juvenile pyroclasts are subrounded, phenocryst-poor, often agglomerates, and have an average density of 1.47±0.24 g cm^{-3}. Ash- to lapilli-sized lithic inclusions are common. The average vesicularity is 47±9%. Compositions are similar to other north exposures, with 55.33 wt. % SiO_2, 3.48 wt. % MgO, 10.71 wt. % FeO, 4.84 wt. % total alkalis, and a CaO/Al_2O_3 ratio of 0.47 (Table 2.3). At 0.88 and 2.45 ppm, Ni and Cr are lower than nearby north1 and north2. Ba and Ce are the highest in the north (241 and 23.32 ppm, respectively). Sr is 413 ppm and similar to other samples from the north.

2.5 Discussion

2.5.1 Correlating deposits regionally

The eastern stratigraphic section is the only location where we identified contacts between individual Ci flow units. Ci deposits in the north and west lack unit contacts, and

do not contain discernable granulometric, componentry, or depositional characteristics sufficient to correlate deposits with the four units exposed in the east outcrops.

Compositional similarity of the four eastern flow units and of north and west deposits is also unhelpful for unit correlation. Unit 1 is a basaltic andesite with minimal variability in composition with respect to stratigraphic level. Compositions evolve slightly in Units 2 and 3 (Fig. 2.4). However, this compositional shift is not a sufficient indicator for unit correlation because the entire XRF dataset compositionally spans from basalt to andesite (Fig. 2.9). Furthermore, Ci trace element data for Unit 1 are variable and slightly less evolved from Units 2 and 3. The spread of all analyses precludes the use of major and trace element chemistry as flow unit fingerprint regionally (Figs. 2.9, 2.10, Table 2.2), preventing geochemical correlation of units around the volcano. As such, we focus on the eastern stratigraphic section and regional ^{14}C dates to further interpret the Ci emplacement mechanisms and eruption sequence. We recognize that the eastern compositions and granulometry do not represent every Ci exposure. However, because we cannot correlate deposits in the north and west to specific flow units found in the east, and because the eastern stratigraphy has the most complete eruptive sequence, we chose to focus on the eastern stratigraphy to interpret the eruption.

2.5.2 Interpreting the eruption sequence

The dominant massive coarse ash tuff and massive lapilli tuff characteristics at all outcrops around Llaima suggest deposition from a concentrated pyroclastic density current (PDC) or series of currents (Branney and Kokelaar, 2002). Unit 1 exhibits some diffuse stratification (Fig. 2.3A), but is mostly massive, poorly sorted, and contains local

block concentrations, all of which are common characteristics of valley-ponded PDC deposits. We interpret the massive nature of the deposit and diffuse stratification to represent progressive aggradation from a concentrated pyroclastic current or series of closely spaced currents that resulted in indistinct flow boundaries. Diffuse stratification is likely the result of fluctuations in flow boundary zone shear conditions (Branney and Kokelaar, 2002).

The Unit 1 co-ignimbrite ash suggests a pause in between Unit 1 and Unit 2 deposition long enough to allow settling of the co-ignimbrite ash and pellets (Fig. 2.6). Ash pellets are indicative of environmental moisture at the time of settling (Van Eaton et al., 2012). Elutriation pipes in the upper 1–2 m of Unit 1 truncate at the co-ignimbrite ash. We interpret the elongated void pockets within the Unit 1 co-ignimbrite ash to represent ponded gas from the Unit 1 elutriation pipes (Fig. 2.6). This suggests degassing of the Unit 1 ignimbrite occurred following deposition of Unit 2 with the impermeable co-ignimbrite ash preventing further gas escape into the overlying deposit. The sharp contact, the preservation of ash pellets and gas pockets, and lack of reworking between Unit 1 and Unit 2 suggest a brief pause in deposition, perhaps no longer than hours to days.

The basal cross-stratified zone of Unit 2 also contains mm-thick, fines-depleted vertical pipes, interpreted as elutriation pipes. This suggests the basal cross-stratified region is a ground layer of the Unit 2 pyroclastic current, likely deposited by a more dilute PDC conditions associated with the current head (e.g., Scarpati et al., 2015); the overlying massive deposit indicative of deposition by a concentrated PDC. The same interpretation applies for the deposition of Units 3 and 4, although Unit 4 does not have a

ground layer. Similar to the contact between Units 1 and 2, the contacts between Units 2 and 3 and Units 3 and 4 are sharp, planar, and continuous with no reworking, incision, or soil horizon development. Therefore, the pauses between Unit 2 and 3 deposition and Unit 3 and 4 deposition are interpreted as similarly short as that between Units 1 and 2 (Fig. 2.4).

2.5.3 Is the Ci the result of two eruptions or one?

Naranjo and Moreno (1991) first proposed the Ci as the product of two eruptions separated by ~600 yrs based on radiocarbon analyses of ~13.2 thousand years BP and ~12.6 thousand years BP (Table 2.4). Lohmar (2008) also adopted the two-eruption model based on their radiocarbon analyses. Naranjo and Moreno (1991) recovered a ^{14}C age of 13,260±200 years BP from the Ci along the Trufulful River in the east that corresponds to our Unit 1. The five radiocarbon dates collected in this study are between 12.774 ± 0.057 and 12.555±0.055 thousand years BP. We did not find any samples in the 13.2–13.8 thousand years BP range (Table 2.4). We conclude a break of ~600 years between Unit 1 and Unit 2 in the east is not evident, nor is a significant break in deposition evident in any exposure around the volcano. Based on the extent of our ^{14}C sampling area combined with our new radiocarbon ages, we suggest a single eruptive episode at ~12.6 thousand years BP produced the entire Ci.

2.5.4 Volume estimate

To reassess the Ci volume, we use the deposit extent in our study, the deposit extent mapped in the earlier work of Naranjo and Moreno (2005), and a range of

maximum slopes of deposition to refine the volume calculation. Hill slopes of max Ci deposition are between 0° and 62.5° with an average of 8.9±8.7° (1σ). Approximately 46% of all points (8,033) are shallower than 5° and 71% are below 10° (12,424). These data are similar to the Campanian (Silleni et al., 2020) and Taupo (Wilson and Walker, 1985) ignimbrites. We use 0-m isopachs of 9° (average), 13.5° (+0.5σ), and 17.5° (+1σ) to estimate three volumes for the Ci (Fig. 2.13). We estimate multiple 0-m isopachs to quantify the sensitivity of our estimate with respect to the depositional slope.

The areas encompassed by the 9°, 13.5°, and 17.5° 0-m isopachs are 896 km^2, 963 km^2, and 981 km^2, respectively (Fig. 2.14). Integrating the region under the area versus thickness curves yields tephra volume estimates of 7.60 km^3, 8.33 km^3, and 8.58 km^3. Using an average vesicularity of 52%, the calculated DRE volumes are 3.95 km^3, 4.33 km^3, and 4.46 km^3.

We calculated a fourth volume estimate using the 13.5° slope and encompassing a region approximate to that of Naranjo and Moreno (1991) (Fig. 2.1). An 8 km diameter circular area was removed to represent a caldera as hypothesized by Naranjo and Moreno (1991). The area of this estimate is 1,625 km^2. Using the same 52% vesicularity, the calculated tephra volume is 10.02 km^3 and the DRE is 5.21 km^3.

Naranjo and Moreno (1991) map the Ci up to 100 km west of Llaima (Fig. 2.1), but do not provide location data for exposures. During our mapping we did not locate any exposures >30 km from Llaima. Additionally, the base of the Ci is only exposed at one location in this study (Fig. 2.10A). Our volume estimates are based on outer-caldera deposits only. No fall deposits for the Curacautín eruption have ever been found. Therefore, the volume estimates herein should be considered minimum estimates.

Because our 9° average maximum slope of deposition is similar to that of Wilson and Walker (1985) and Silleni et al. (2020), the tephra volume estimate 7.60 km^3, or 3.95 km^3 DRE is most reasonable.

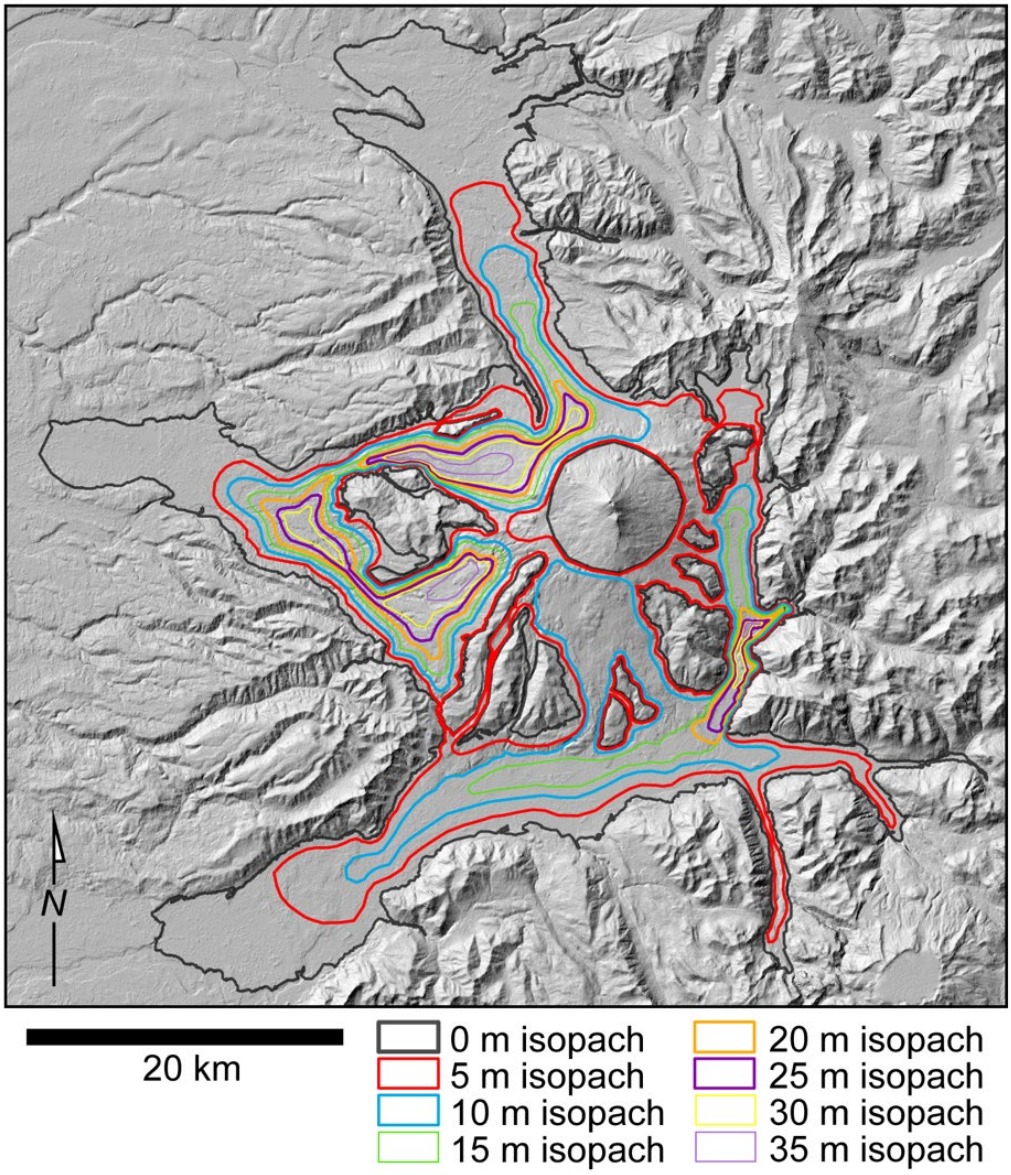

Figure 2.13 Isopach map of the Ci volume estimate with a 0-m isopach of 9°. Isopachs are drawn based on measured stratigraphic sections of this study and Lohmar (2008), field observations, and extrapolation of observations and slope data. An 8 km wide region representing a caldera as hypothesized by Naranjo and Moreno (1991) was removed from the volume estimate.

Our reported volume estimates have the following limitations. Because we did not have borehole data in the region, we could not approximate Ci thickness in areas where no surface exposures exist. Additionally, because we were not able to locate Ci deposits beyond ~30 km, we were limited in how far we could reasonably approximate runout. We restricted our isopachs to 5 m rather than precise isopachs such as 1 m due to our limited data, which includes stratigraphic sections of this study and those of Lohmar (2008). Finally, because we only found the base of the Ci in one exposure, our deposit thinning estimate is a minimum, and our volume estimate should only be considered a first order approximation.

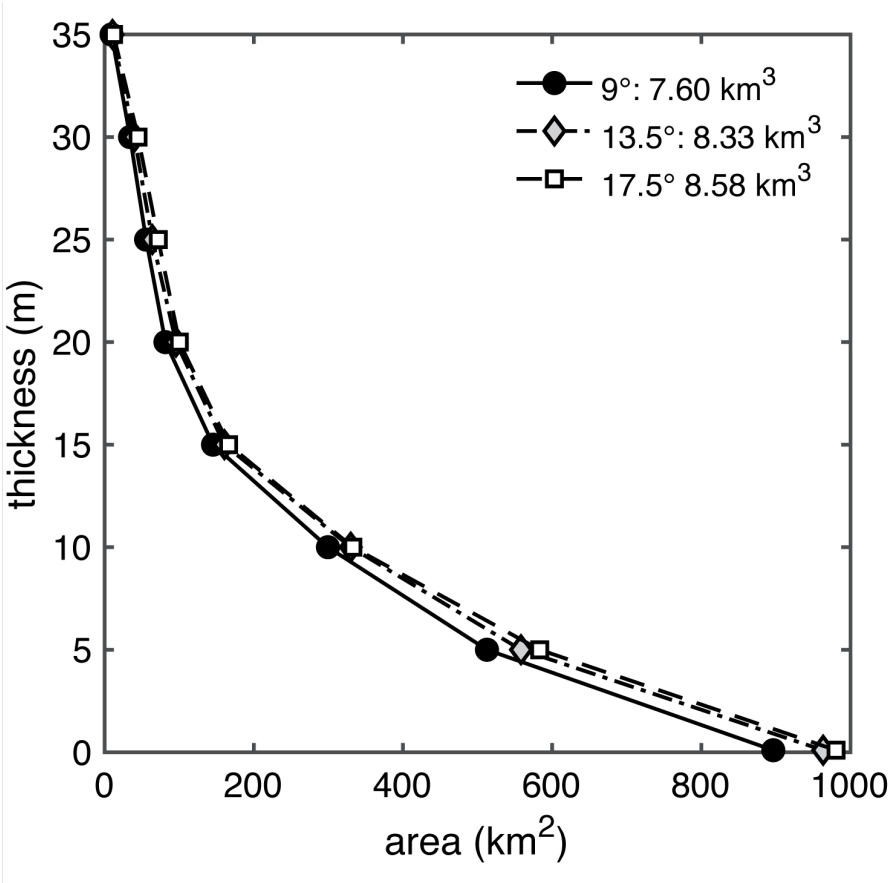

Figure 2.14 The Ci volume estimate in this study based on the isopach tracing method. The tephra volume is the integration of the area under the curve. Values reported for each degree are tephra and not DRE.

2.5.5 What were the magmatic conditions that drove the eruption?

The two most likely mechanisms to generate highly explosive mafic eruptions are rapid magma ascent rates combined with fast crystallization during ascent (e.g., Arzilli et al., 2019; Bamber et al., 2020) and magma-water interaction (e.g., Ross and White, 2005). Rapid ascent rates generate high degrees of undercooling and disequilibrium that can induce extensive and rapid microlite crystallization, thus increasing magma viscosity and trapping magmatic volatiles necessary for brittle fragmentation. Conversely, magma-water interaction involves the efficient transfer and release of thermal energy from a magma to a water source which drives explosivity (Zimanowski et al., 2015). Distinguishing between magmatic or phreatomagmatic fragmentation involves scrutiny of deposit characteristics and pyroclast textures. For example, pyroclasts of well-documented mafic explosive eruptions attributed to rapid magma ascent have characteristically high microlite contents that are evidence of high undercooling (Sable et al., 2006; Sable et al., 2009; Vinkler et al., 2012; Bamber et al., 2020); the deposits of magma-water interaction have high proportions of fines (>4ϕ) due to high fragmentation efficiency, and blocky ash grains (e.g., Walker, 1981; De Rita et al., 2002). Below we offer an interpretation for the primary fragmentation mechanism that drove the Ci eruption based on field observations and laboratory analyses.

Unlike the deposits of phreatomagmatic eruptions, Ci exposures are mostly homogenous and lack any depositional features common to wet eruptions such as soft sediment deformation, low-angle cross strata, palagonite, and sideromelane (Figs. 2.3, 2.11, 2.12). Agglutinated clasts are common in Ci exposures (Fig. 2.7) and suggestive of temperatures higher than those observed in phreatomagmatic eruptions. Ash pellets

preserved within the Unit 1 thin co-ignimbrite ash (Fig. 2.6) are conspicuous but may well be a product of atmospheric moisture rather than magma-water interaction (White and Valentine, 2016). In addition, the Mdϕ and fines content of the Ci (average Mdϕ of -0.27 and an average σ of 2.60; Table 2.1) are not consistent with similar mafic ignimbrites associated with magma-water interaction. Specifically, the Ci contains 73% moderately vesiculated ash on average, with only 13.2–19.8% total mass being fine ash, although we do note that Unit 1 is slightly fines-enriched. This is in contrast to the more typical 85-95% low vesicularity ash found in mafic ignimbrite-forming eruptions driven by magma-water interaction (e.g., Heiken and Wohletz, 1985; De Rita et al., 2002; Giordano et al., 2002; Miyabuchi et al., 2006).

We also investigated ash grains using scanning electron microscopy to look for surface features consistent with magma-water interaction (blocky grains, surface fractures, and adhering dust; Heiken and Wohletz, 1985; Büttner et al., 1999; Miyabuchi et al., 2006). Many ash particles are blocky to vesicular, but we do not see cracking or fine ash adhered to surfaces. Componentry analysis of Ci ash reveals a high relative proportion of scoria to lithics (22–29%), which indicates a lower amount of conduit margin breakage in the subsurface. We do note that approximately 51% of Unit 4 lithics are hydrothermally altered, which may suggest the latter stage of the Ci eruption interacted with some form of external water similar to the waning stages of the 122 Etna (Sable et al., 2006) and Tarawera 1886 (Houghton et al., 2004) eruptions. However, the high concentration of hydrothermally altered lithics may alternatively be a result of the conduit excavating a hydrothermally altered region of Llaima and not an influence of external water.

The only evidence that magma-water interaction may have played a role are the pervasive inclusions of country rock within pyroclasts. Inclusions are dominated by mafic lavas, and thus are likely excavated from Llaima's ancestral shield volcano lavas within 500–1000 m of the surface, where we might expect there to be sufficient groundwater (depth based on geologic map, Naranjo and Moreno, 2005). Indeed, wall rock brecciation is common in phreatomagmatic eruptions (see White et al., 2011); thus, phreatic activity or magma-water interaction along the conduit margins is a plausible explanation for the brecciation and injection of wall rock into the ascending magma. However, the agglomerate textures suggest clast fusing in the conduit post injection of wall rock, which is unexpected in phreatomagmatic eruptions due to the rapid lowering of temperatures. Therefore, our observations of Ci grain size, ash textures, componentry, inclusion of wall rock material within pyroclasts, and evidence for ash fusing suggest that, while magma-water interaction may have played some role in the eruption, it was not the driving mechanism that led to the Ci explosive conditions. Instead, we turn to the microlites for evidence of the conditions that promoted strong explosivity.

The interplay of bubbles and crystals during magma ascent has a considerable influence on eruption style. Microlites are particularly important as they can both facilitate degassing by creating new sites for bubble nucleation or suppress gas escape by increasing bulk viscosity and bubble network tortuosity (e.g., Vona et al., 2011; Moitra et al., 2018; Arzilli et al., 2019). For example, Sparks (1978) found that a critical vesicularity of ~75% for magmatic fragmentation in crystal-free magmas. In contrast, Arzilli et al. (2019) show the requirements for Plinian basaltic eruptions are temperatures <1100 °C, syn-eruptive crystal contents of more than 30%, and a bulk viscosity of 10^5 Pa

s. Experiments by Lindoo et al. (2017) show that the vesicularity of permeability onset in basaltic andesites is reached at vesicularities ≤56% when crystallization is greater than ~20%. This implies that at 20% crystallization, permeability is enhanced, and thus gas escape through a permeable magma could be a prevailing process. However, this was clearly not the case for the Curacautín magma

Many microlite morphologies observed in Ci pyroclasts, such as acicular, swallowtail, and skeletal, are associated with disequilibrium crystallization conditions and hence rapid growth (e.g., Hammer and Rutherford, 2002; Szramek et al., 2006; Shea and Hammer, 2013). Plagioclase microlite fractions in Ci pyroclasts (Fig. 2.8) are 0.29–0.44 (Table 2.2), well above the ~20% total crystallinity necessary to drop vesicularity of permeability onset to ≤56%. Plagioclase ϕ_{plag} and N_A textures are consistent with nucleation-dominated crystallization (Blundy and Cashman, 2008) and are suggestive of rapid magma ascent (Fig. 2.15). An analysis of plagioclase crystal size distributions (CSDs) suggests the population and size distribution of Ci plagioclase formed in seconds to hours, further supporting a rapid ascent hypothesis (Valdivia et al., 2021).

Ci vesicularities are between 43±10% and 71±10% and, as such, are within the critical vesicularity range for magmatic fragmentation of a crystal-bearing melt (e.g., Arzilli et al., 2019) (Fig. 2.4). Our microlite and vesicularity data are therefore most consistent with those observed in brittle fragmentation of a basaltic andesite magma. Further, Valdivia et al. (2021) found that 99% of the Ci vesicle network is largely interconnected but convoluted with high values of tortuosity. Additionally, they show that permeabilities of Ci pyroclasts calculated from 3D X-ray computed microtomography analyses by are $0.3–6.3\times10^{-12}$ m^2. These permeabilities are slightly

lower than those of other basaltic explosive eruptions (Colombier et al., 2021), and suggest that even though permeability was established, the Curacautín magma was unable to efficiently lose gas, resulting in a coupling of the gas to the magma. Using the bubble number density meter of Toramaru (2006), Valdivia et al. (2021) estimated a decompression rate for the Curacautín magma of 1.4 MPa s^{-1}. This rate is similar to the rates of 1.5 and 2.0 MPa s^{-1} calculated for the 1886 Tarawera and Etna 122 BC eruptions, respectively (Shea, 2017). Additionally, Valdivia et al. (2021) calculated a minimum overpressure of 5 MPa necessary to fragment the Curacautín magma, suggesting that rapid ascent could have generated the overpressure needed to fragment the microlite-bearing magma.

Comparing the Ci magmatic conditions to similar eruptions lends further insight into the conditions that produce explosive basaltic volcanism. The critical vesicularity of 30% necessary for brittle fragmentation of mafic magmas assumes crystallization must occur for mafic explosive volcanism (Arzilli et al., 2019). However, there are examples of mafic systems that erupt explosively but produce relatively glassy pyroclasts (e.g., Constantini et al., 2010; Bamber et al., 2020). The Fontana lapilli basalt is interpreted to be the result of rapid decompression, but not attributed to microlite crystallization and a subsequent rheological shift in the magma (Constantini et al., 2010). Instead, that eruption appears to be the result of phreatomagmatism and late decompression-induced homogeneous bubble nucleation from rapid ascent. Eruption temperatures are estimated at 1100 °C, which are likely too hot for extensive microlite crystallization by the time of eruption. Therefore, the rapid quenching from magma-water interaction and high temperatures are expected to produce relatively glass-rich pyroclasts (Fig. 2.15).

Similarly, the Masaya Triple Layer eruption (Bamber et al., 2020) contains both microlite-rich and microlite-poor pyroclasts but have a 50–80% glass matrix (Fig. 2.15). However, Masaya microlite N_V are at most only one order of magnitude different from those measured in the Ci and are comparable to N_V calculated in other explosive mafic eruptions (e.g., Etna, Tarawera; Sable et al., 2006; Sable et al., 2009). Additionally, Masaya microlite S_m are approximately half the size of those measured for the Ci. This may suggest that crystallization of the Ci magma began deeper in the conduit and would explain why Masaya has a high N_V but still high glass content. The deviation between our microlite calculations and those of similar eruptions may results from a range of microlite shapes and sizes that nevertheless produce a similar rheological shift to enable brittle behavior.

Our proposed model of rapid ascent of a partially degassed basaltic andesite magma contrasts with recent work by Ruth et al. (2016) that posits that the 2008 Strombolian activity at Llaima is the result of repeated injection of mafic magma batches, crystal mush remobilization, and extensive vesiculation. They calculated depths of magma storage between 1–4 km with recharge magmas rising from 14 km depth. Schindlbeck et al. (2014) calculated depths of Ci storage at ~18 km. Rapid ascent from greater depths would result in higher degrees of undercooling as the magma nears the surface, resulting in a faster rheological shift that locked up the Ci magma and inhibited degassing (Valdivia et al., 2021). The 2008 Strombolian eruption, by comparison, was passively degassing from a semi-shallow crystal mush zone that upon repeated addition of deeper magmas, unlocked trapped gases that triggered rapid ascent and subsequent Strombolian activity. We speculate that Llaima's varying degrees of explosivity may

reflect ranges in the depths from which the erupted magmas originated, suggesting that the size of magma injection may have an important control on the intensity of explosivity from Llaima.

To summarize, lithic entrainment within pyroclasts and the presence of hydrothermally altered accidentals suggest magma-water interaction may have played some role in the Curacautín eruption. However, the microlite textures, vesicle network properties, and evidence for pyroclast fusing in the conduit suggest that undercooling-induced crystallization, resulting from rapid magma ascent, resulted in both an increase in the Ci bulk magma viscosity and coupling of the gas to the magma, allowing the magma to reach the threshold necessary for brittle fragmentation of a crystal-bearing melt. Though we have not experimentally quantified the Ci ascent rate here, plagioclase microlite textures are on the order of magnitude of similar mafic explosive eruptions (Sable et al., 2006; Sable et al., 2009; Vinkler et al., 2012; Bamber et al., 2020).

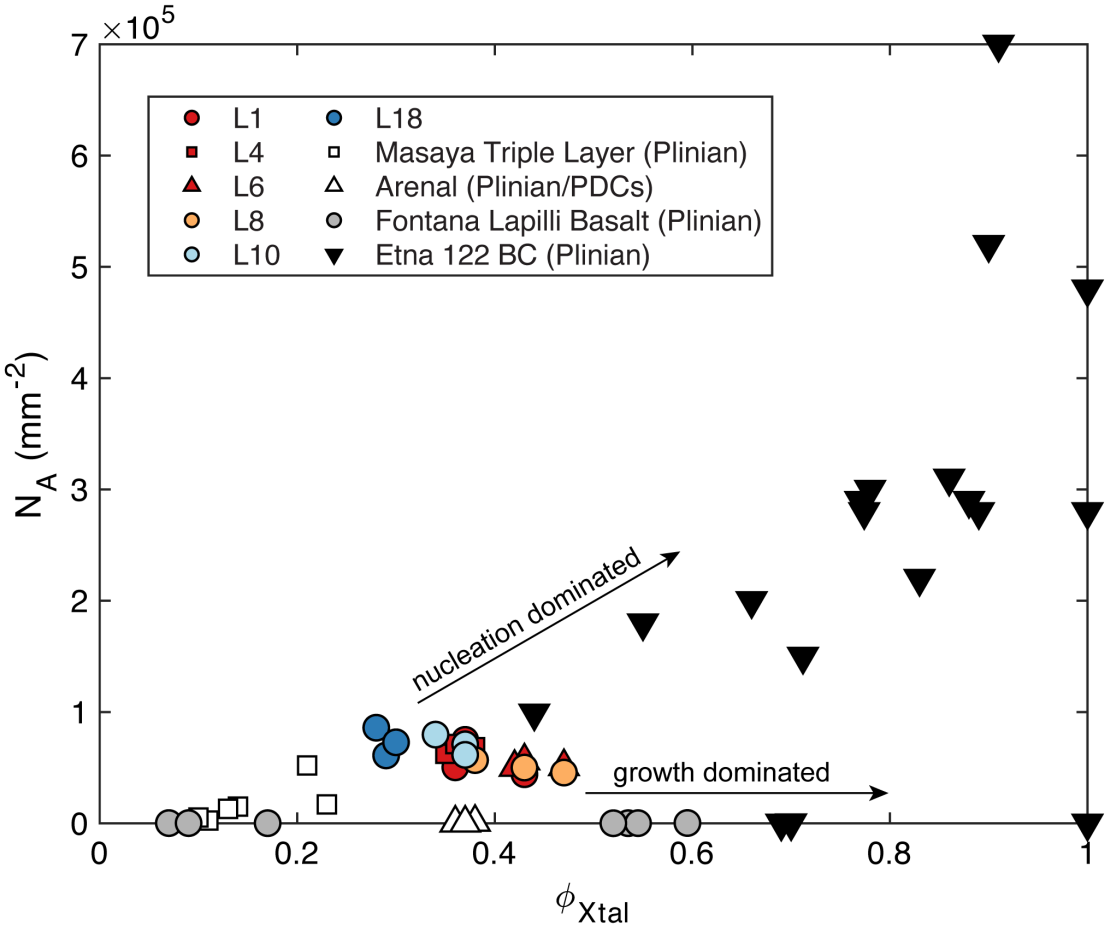

Figure 2.15 Crystal fraction (ϕ_{Xtal}) versus area number density N_A (mm^{-2}) for the Ci (this study), Masaya Triple Layer (Bamber et al., 2020), Etna 122 BC (Sable et al., 2006), mafic Plinian and PDC deposits of Arenal volcano (Szramek et al., 2006), and the Fontana Lapilli Basalt (Constantini et al., 2010). Constantini et al. (2010) report a range of values for ϕ_{Xtal} and the median of those ranges are plotted here. Only plagioclase ϕ and N_A are reported for the Ci. Other notable mafic explosive eruptions include the 1886 eruption of Tarawera volcano, New Zealand. Pyroclasts of that eruption contain 85–99% microlites, dominated by 57% plagioclase, 40% clinopyroxene, 2% olivine, and <1% FeTi oxides (Sable et al., 2009). The 2001 hydromagmatic to Strombolian and ash explosions eruption of Etna volcano produced N_A from 10^3–10^5 and glass contents of 12.6–76.1% (Taddeucci et al., 2004). An interesting observation is that high N_A, while typically associated with mafic explosive activity, is not always a necessity of high explosivity mafic eruptions. High N_A are typically attributed to undercooling from rapid ascent that drives disequilibrium crystallization (Arzilli et al., 2019), but these data highlight that such conditions are not always preserved in the pyroclast record. However, Ci plagioclase number densities are consistent with nucleation-dominated crystallization (Blundy and Cashman, 2008), a process attributed to high undercooling.

2.5.6 Conceptual eruption model

The observed high microlite crystallinity, disequilibrium microlite morphologies, and moderate vesicularities are consistent with magmatic fragmentation of a rapidly ascending and partially degassed melt (Lindoo et al., 2017; Moitra et al., 2018; Arzilli et al., 2019). Polylobate bubbles shaped by the high microlite content suggest bubble nucleation and degassing occurred due to a combination of rapid decompression and new nucleation sites created during microlite crystallization. The resulting increase in viscosity and bubble overpressure would likely have been sufficient to fragment the bulk magma brittlely.

Juvenile pyroclast vesicularities, bubble textures, and microlite textures are similar between Units 1, 2, and 3, suggesting similar conditions in ascent rate and fragmentation mechanisms. Unit 4, the thinnest of the Ci Units, has lower vesicularities and higher bulk densities relative to underlying units (Fig. 2.4). Unit 4 also has the lowest plagioclase microlite content, suggesting a decrease in decompression rate that allowed the ascending magma to maintain a lesser degree of undercooling or supersaturation, enabling enhanced degassing. This unit likely represents the waning stage of the eruption.

The Curacautín eruption paused for hours to days at the end of Unit 1, which allowed a fine-grained co-ignimbrite ash to deposit. Atmospheric moisture likely promoted the formation of massive ash pellets that cap the co-ignimbrite ash. Due to the lack of fine-grained laminae coating the ash pellets, they were likely deposited after the passing of the ash-rich Unit 1 pyroclastic current wake, thus not accreting fine ash to form accretionary lapilli (Brown et al., 2010). Degassing of Unit 1 generated gas elutriation pipes in the upper 1–2 m and circular to elongated gas pockets (void spaces;

Fig. 2.6) within co-ignimbrite ash of Unit I. We interpret that most of Unit 1 degassing occurred following the deposition of Unit 2, whereby the coignimbrite ash acted as an impermeable layer that trapped escaping gas from Unit 1. The sharp contacts, lack of reworking, evidence for primary ignimbrite deposits (e.g., elutriation pipes), and planar contacts between Units 1, 2, and 3 suggest a short-lived pause between deposition of ignimbrites. Unlike Unit 1, there are no ash pellets or a fine ash cap overlying Unit 2 or 3, suggesting subsequent currents deposited before co-ignimbrite ash could settle.

Different componentry for Units 2 and 3 may indicate a shift in vent location or fragmentation depth. For example, a higher concentration of granitic basement material in Unit 3 than Units 1, 2, and 4 could indicate fragmentation of bedrock deeper in the conduit or migration of the vent. The higher population of hydrothermally altered lithics in Unit 4 may indicate some interaction with external water or hydrothermally altered country rock.

Our minimum tephra volume estimate of 6.79–7.60 km^3 (Fig. 2.14) corresponds to a VEI5 Plinian eruption (Newhall and Self, 1982). There is no evidence that significant additional volume was deposited as a co-ignimbrite ash following the cessation of the eruption. The common image invoked by Plinian eruptions is a convecting column of ash and bombs towering tens of km into the atmosphere. The Ci, however, lacks any fall deposits and is composed entirely of valley-filling tuffs. Further, all Ci exposures contain agglutinated pyroclasts (Fig. 2.7), which suggest clasts were interacting with and impacting one another in the conduit before deposition. These observations suggest the Ci eruption was a boiling over event or collapsing low column that infilled valleys and

drainages around Llaima with the deposits of concentrated pyroclastic currents (e.g., Girodano and Dobran, 1994; Giordano and Doronzo, 2017; Smith et al., 2020).

Trolese et al. (2019) show that total collapse regimes that generate long runout PDCs (>20 km) result from a high amount of collapsing mass at low collapse heights. Due to their inability to entrain atmospheric air and cool down, these eruptions tend to be hot and result in deposit welding (Trolese et al., 2019). As noted above, the Ci lacks fall deposits, which we interpret to represent a collapse regime or boiling over event. However, the Ci is entirely nonwelded. The lack of welding is most likely due to the microlite rich and glass poor nature of the pyroclasts.

Based on our volume estimates, the Curacautín eruption cleared 1.1–1.2×10^{13} kg (0.97–1.1×10^{13} kg if using the linear regression of Wilson, 1991) of material from Llaima's reservoir. Modeling by Carey and Sigurdsson (1989) found that minimum mass eruption rates of 2.0×10^{8} kg s^{-1} are associated with large-volume pyroclastic current generation. Using our estimated erupted mass of 1.09–1.24×10^{13} kg and a minimum eruption rate for pyroclastic current generation of 2.0×10^{8} kg s^{-1}, we estimate a Curacautín eruption duration of ~15–17 hrs. We note that mass eruption rates are heavily dependent on parameters such as vent radius, shape, and eruption temperature (Trolese et al., 2019), and therefore these eruption durations are only first order approximations.

2.5.7 The caldera hypothesis

Naranjo and Moreno (1991) hypothesize the Ci eruption formed an 8-km diameter caldera due to the volume of material evacuated from the chamber and that Holocene deposits cover this caldera. Barometric measurements by Schindlbeck et al. (2014) place

the Ci melt residence at ~18 km depth corresponding to a roof aspect ratio (R) of ~2.25, where R is the ratio of reservoir depth to reservoir diameter. Roche and Druitt (2001) show that R values <1 are consistent with coherent caldera collapse while R values >1.4 are associated with incoherent caldera collapse. R values >2 may indicate caldera formation from incoherent faulting between the reservoir and surface, but Roche and Druitt (2001) stress this is not always the case because upward propagating faults may intersect at depth and cease their upward migration. One such case is the 1600 AD eruption of Huaynaputina, during which ~11 km^3 of DRE magma was erupted from reservoirs at ~20 km and ~6 km, and a volumetrically equivalent caldera did not form (Lavalleée et al., 2006). Therefore, we conclude there is not sufficient evidence corroborating the caldera-collapse hypothesis. Geophysical surveys capable of resolving subvolcanic features at depths of 20 km may be necessary to further explore the caldera model (e.g., Davy and Caldwell, 1998).

2.6 Conclusions

The Ci is an impressive example of the explosive endmember of mafic volcanism. We conducted extensive field and petrographic studies to develop a new conceptual eruption model for the Ci. Our field observations, including no evidence for a significant time break between flow units, and new ^{14}C data suggest the Curacautín eruption was a single event at ~12.6–12.7 thousand years BP. All juvenile clasts exhibit extensive microlite crystallization, polylobate vesicle networks, and moderate vesicularities that suggest this eruption was triggered by brittle magmatic fragmentation of a rapidly ascending, non-degassed, and highly viscous (relative to typical basaltic andesite

magmas) bulk magma. Using new detailed field observations and stratigraphic sections of Lohmar (2008) and this study, we estimate the minimum Ci tephra volume between 7.6 and 8.6 km^3 (DRE volume of 4.0–4.5 km^3) and a total mass of $0.97–1.2\times10^{13}$ kg. Our volume estimate and single eruption model allow us to estimate an eruption duration of ~15–17 hours. Despite the large volume, we did not find sufficient evidence to suggest the Curacautín eruption generated a volumetrically equivalent caldera. Our case study of the Ci supports a growing body of literature that suggests rapid ascent rates are one of the primary drivers for strongly explosive mafic eruptions (Houghton et al., 2004; Sable et al., 2006; Sable et al., 2009; Moitra et al., 2018; Arzilli et al., 2019; Bamber et al., 2020).

Future work is necessary to further constrain the conditions that promoted the explosive Ci eruption. The lack of fall deposits is peculiar and may be explained by an investigation of vent geometry. Further textural investigation of agglomerate textures and lithic inclusions are important for constraining processes within the conduit (e.g., magma-water interaction). More detailed whole-rock, trace element, and isotope studies are necessary to better resolve pre-eruptive conditions for the Ci. Comparison of Ci pyroclast textures with those created using high pressure-temperature decompression experiments of Ci melts could quantify decompression paths and the degree of Ci melt undercooling and plagioclase supersaturation (Shea and Hammer, 2013). Magma rheology experiments (e.g., Vona et al., 2011) could constrain the viscoelastic evolution of the Ci melt related to different temperatures and degrees of undercooling and would complement the decompression experiments with respect to textural comparison. Both the decompression experiments and rheology experiments could serve to extend numerical models of microlite nucleation and growth developed for silicic magmas (e.g., Andrews and Befus,

2020) to mafic compositions, providing additional quantitative insights into crystallization kinetics in mafic systems such as Llaima volcano

2.7 References

Andrews BJ, Befus KS (2020) Supersaturation Nucleation and Growth of Plagioclase: a numerical model of decompression-induced crystallization. Contrib Mineral Petrol 175:23. doi: 10.1007/s00410-020-1660-9

Arzilli F, La Spina G, Burton MR, Polacci, M, Le Gall N, Hartley ME, Di Genova D, Cai B, Vo NT, Bamber EC, Nonni S, Atwood R, Llewellin EW, Brooker RA, Mader HM, Lee PD (2019) Magma fragmentation in highly explosive basaltic eruptions induced by rapid crystallization. Nat Geosci 12:1023–1028. doi: 10.1038/s41561-019-0468-6

Baker DR, Mancini L, Polacci M, Higgins MD, Gualda GAR, Hill RJ, Rivers ML (2012a) An introduction to the application of X-ray microtomography to the three-dimensional study of igneous rocks. Lithos 148:262–276. doi: 10.1016/j.lithos.2012.06.008

Baker DR, Brun F, O'Shaughnessy C, Mancini L, Fife JL, Rivers M (2012b) A four-dimensional X-ray tomographic microscopy study of bubble growth in basaltic foam. Nat Commun 3:1135. doi: 10.1038/ncomms2134

Bamber EC, Arzilli F, Polacci M, Hartley ME, Fellowes J, Di Genova D, Chavarría D, Saballos JA, Burton MR (2020) Pre- and *syn*-eruptive conditions of a basaltic Plinian eruption at Masaya Volcano, Nicaragua: The Masaya Triple Layer (2.1 ka). J Volcanol Geotherm Res 392:1–16. doi: 10.1016/j.jvolgeores.2019.106761

Befus KS, Andrews BJ (2018) Crystal nucleation and growth produced by continuous decompression of Pinatubo magma. Contrib Mineral Petrol 173:92. doi: 10.1007/s00410-018-1519-5

Blundy J, Cashman KV (2008) Petrologic reconstruction of magmatic system variables and processes *in:* Minerals, Inclusions and Volcanic Processes. Rev Mineral Geochem 69:179–239

Branney MJ, Kokelaar P (2002) Pyroclastic density currents and the sedimentation of ignimbrites. Geological Society of London Memoir 27:1. doi: 10.1144/GSL.MEM.2003.027

Brown RJ, Branney MJ, Maher C, Dávila-Harris P (2010) Origin of accretionary lapilli with ground-hugging density currents: Evidence from pyroclastic couplets on Tenerife. Geol Soc Am Bull 122:305–320. doi: 10.1130/B26449.1

Büttner R, Dellino P, Zimanowski B (1999) Identifying magma-water interaction from the surface features of ash particles. Nature 401:688–690

Carey RJ, Manga M, Degruyter W, Gonnermann H, Swanson D, Houghton B, Orr T, Patrick M (2013) Convection in a volcanic conduit recorded by bubbles. Geology 41:395–398. doi: 10.1130/G33685.1

Carey S, Sigurdsson H (1989) The intensity of Plinian eruptions. Bull Volcanol 51:28–40

Cashman KV, Giordano G (2014) Calderas and magma reservoirs. J Volcanol Geotherm Res 288:28–45. doi: 10.1016/j.jvolgeores.2014.09.007

Cembrano J, Lara L (2009) The link between volcanism and tectonics in the southern volcanic zone of the Chilean Andes: A review. Tectonophysics 471:96–113. doi: 10.1016/j.tecto.2009.02.038

Colombier M, Vasseur J, Houghton BF, Cáceres F, Scheu B, Kueppers U, Dingwell DB (2021) Degassing and gas percolation in basaltic magmas. Earth Planet Sci Lett 573:117134. doi: 10.1016/j.epsl.2021.117134

Coltelli M, Del Carlo P, Vezzoli L (1998) Discovery of a Plinian basaltic eruption of Roman age at Etna volcano, Italy. Geology 26:1095–1098

Costantini L, Bonadonna C, Houghton BF, Wehrmann H (2009) New physical characterization of the Fontana Lapilli basaltic Plinian eruption, Nicaragua. Bull Volcanol 71:337–355. doi: 10.1007/s00445-008-0227-9

Costantini L, Houghton BF, Bonadonna C (2010) Constraints on eruption dynamics of basaltic explosive activity derived from chemical and microtextural study: The example of the Fontana Lapilli Plinian eruption, Nicaragua. J Volcanol Geotherm Res 189:207–224. doi: j.jvolgeores.2009.11.008

Couch S (2003) Experimental investigation of crystallization kinetics in a haplogranite system. Am Mineral 88:1471–1485

Davy BW, Caldwell TG (1998) Gravity, magnetic and seismic surveys of the caldera complex, Lake Taupo, North Island, New Zealand. J Volcanol Geotherm Res 81:69–89

De Rita D, Giordano G, Esposito A, Fabbri M, Rodani S (2002) Large volume phreatomagmatic ignimbrites from the Colli Albani volcano (Middle Pleistocene, Italy). J Volcanol Geotherm Res 118:77–98

Degruyter W, Burgisser A, Bachmann O, Malaspinas O (2010) Synchrotron X-ray microtomography and lattice Boltzmann simulations of gas flow through volcanic pumices. Geosphere 6:470–481. doi: 10.1130/GES00555.1

Di Genova D, Brooker RA, Mader HM, Drewitt JWE, Longo A, Deubener J, Neuville DR, Fanara S, Shebanova O, Anzellini S, Arzilli F, Bamber EC, Hennet L, La Spina G, Miyajima N (2020) In situ observation of nanolite growth in volcanic melt: A driving force for explosive eruptions. Sci Adv 6. doi: 10.1126/sciadv.abb0413

Dzierma Y, Wehrmann H (2010) Eruption time series statistically examined: Probabilities of future eruptions at Villarrica and Llaima Volcanoes, Southern Volcanic Zone, Chile. J Volcanol Geotherm Res 193:82–92. doi: 10.1016/j.jvolgeores.2010.03.009

Franco L, Palma JL, Lara LE, Gil-Cruz F, Cardona C, Basulato D, Martín, JS (2019) Eruptive sequence and seismic activity of Llaima volcano (Chile) during the 2007–2009 eruptive period: Inferences of the magmatic feeding system. J Volcanol Geotherm Res 379:90–105. doi: 10.1016j.jvolgeores.2019.04.014

Freda C, Gaeta M, Giaccio B, Marra F, Palladino DM, Scarlato P, Sottilli G (2011) CO_2-driven large mafic explosive eruptions: the Pozzolane Rosse case study from the Colli Albani Volcanic District (Italy). Bull Volcanol 73(3):241–256. doi: 10.1007/s00445-010-0406-3

Giachetti T, Burgisser A, Arbaret L, Druitt TH, Kelfoun K (2011) Quantitative textural analysis of Vulcanian pyroclasts (Montsererat) using multi-scale X-ray computed microtomography: comparison with results from 2D image analysis. Bull Volcanol 73:1295–1309. doi: 10.1007/s00445-011-0472-1

Giordano G, Dobran F (1994) Computer simulations of the Tuscolano Artemisio's second pyroclastic flow unit (Alban Hills, Latium, Italy). J Volcanol Geotherm Res 61(1–2):69–94

Giordano G, De Rita D, Cas R, Rodani S (2002) Valley pond and ignimbrite veneer deposits in the small-volume phreatomagmatic 'Peperino Albano' basic ignimbrite, Lago Albano maar, Colli Albani volcano, Italy: influence of topography. J Volcanol Geotherm Res 118:131–144

Giordano G, De Benedetti AA, Diana A, Dino G, Gaudioso F, Marasco F, Miceli M, Mollo S, Cas RAF, Funiciello R (2006) The Colli Albani mafic caldera (Rome, Italy): Stratigrapahy, structure and petrology. J Volcanol Geotherm Res 155:49–80. doi: 10.1016/j.jvolgeores.2006.02.009

Giordano G, Doronzo DM (2017) Sedimentation and mobility of PDCs: a reappraisal of ignimbrites' aspect ratio. Sci Rep 7(1):1–7. doi: 10.1038/s41598-017-04880-6

Hammer JE, Cashman KV, Hoblitt RP, Newman S (1999) Degassing and microlite crystallization during pre-climatic events of the 1991 eruption of Mt. Pinatubo, Philippines. Bull Volcanol 60:355–380

Hammer JE, Rutherford MJ (2002) An experimental study of the kinetics of decompression-induced crystallization in silicic melt. J Geophys Res 107:B1. doi: 10.1029/2001JB000281

Heiken G, Wohletz KH (1985) Volcanic Ash. Berkeley, University of California press, 246 p.

Hogg AG, Hua Q, Blackwell PG, Niu M, Buck CE, Guilderson TP, Heaton TJ, Palmer JG, Reimer PJ, Reimer RW, Turney CSM, Zimmerman SRH (2013) SHCal13 Southern Hemisphere Calibration, 0-50,000 Years cal BP. Radiocarbon 55(4):1889–1903. Doi: 10.2458/azu_js_rc.55.16783

Houghton BF, Gonnermann HM (2008) Basaltic explosive volcanism: Constraints from deposits and models. Chem Erde 68:117–140. doi: j.chemer.2008.04.002

Houghton BF, Wilson CJN, Del Carlo P, Coltelli M, Sable JE, Carey R (2004) The influence of conduit processes on changes in styles of basaltic Plinian eruptions: Tarawera 1886 and Etna 122 BC. J Volcanol Geotherm Res 137:1–14. doi: j.jvolgeores.2004.05.009

Houghton BF, Wilson CJN (1989) A vesicularity index for pyroclastic deposits. Bull Volcanol 51:451–462

Johnson DM, Hooper PR, Conrey RM (1999) XRF analysis of Rocks and Minerals for Major and Trace Elements on a Single Low Dilution Li-tetraborate Fused Bead. Adv X-Ray Anal 41:843–867

La Spina G, Burton M, de' Michieli Vitturi M, Arzilli F (2016) Role of syn-eruptive plagioclase disequilibrium crystallization in basaltic magma ascent dynamics. Nat Commun 7:13402. doi: 10.1038/ncomms13402

Lavallée Y, de Silva SL, Salas G, Byrnes JM (2006) Explosive volcanism (VEI 6) without caldera formation: insight from Huaynaputina volcano, southern Peru. Bull Volcanol 68:333–348. doi: 10.1007/s00445-005-0010-0

Lindoo A, Larsen JF, Chasmna KV, Oppenheimer J (2017) Crystal controls on permeability development and degassing in basaltic andesite magma. Geol. 45:831–834. doi: 10.1130/G39157.1

Lohmar S (2008) Petrologia de las ignimbritas Lican y Pucon (volcan Villarrica) y Curacautin (volcan Llaima) en los Andes del sur de Chile. Dissertation, University of Chile

Lohmar S, Parada MA, Robin C, Gerbe MC, Deniel C, Gourgaud A, Lopez-Escobar L, Moreno H, Naranjo JA (2006) Origin of postglacial 'mafic' ignimbrites at Llaima and Villarrica volcanoes (Southern Andes, Chile): assimilation of plutonic rocks as one of the triggering factors? Abstract, Simposio Sudamericano de Geología Isotópica (SSAGI), Punta del Este, Chile

Lohmar S, Robin C, Gourgaud A, Clavero J, Parada MA, Moreno H, Ersoy O, Lopez-Escobar L, Naranjo JA (2007) Evidence of magma-water interaction during the 13,800 years BP explosive cycle of the Licán Ignimbrite, Villarrica volcano (southern Chile). Rev Geol Chile 34:233–247.

Martí J, Planagumà LI, Geyer A, Aguirre-Díaz G, Pedrazzi D, Bolós X (2017) Basaltic ignimbrites in monogenetic volcanism: the example of La Garrotxa volcanic field. Bull Volcanol 79(33). doi:10.1007/s00445-017-1113-0

Miyabuchi Y, Watanabe K, aand Egawa Y (2006) Bomb-rich basaltic pyroclastic flow deposit from Nakadake, Aso Volcano, southwestern Japan. J Volcanol Geotherm Res 155:90–103. doi: 10.1016/j.jvolgeorest.2006.02.007

Miyaji N, Kan'no A, Kanamaru T, Mannen K (2011) High-resolution reconstruction of the Hoei eruption (AD 1707) of Fuji volcano, Japan. J Volcanol Geotherm Res 207:113–129. doi: 10.1016/j.jvolgeores.2011.06.013

Moitra P, Gonnermann HM, Houghton BF, Tiwary CS (2018) Fragmentation and Plinian eruption of crystallizing basaltic magma. Earth Planet. Sci. Lett. 500:97–104. doi: 10.1016/j.epsl.2018.08.003

Naranjo JA, Moreno H (1991) Actividad explosiva postglacial en el volcan Llaima, Andes del sur. Rev Geol Chile 18:69–80

Naranjo JA, Moreno H (2005) Geología del volcán Llaima, region de la Araucanía. Carta Geológica de Chile Scale 88:1–33

Newhall CG, Self S (1982) The Volcanic Explosivity Index (VEI): An Estimate of Explosive Magnitude for Historical Volcanism. J. Geophys. Res. 87:1231–1238

Papale P (1999) Strain-induced magma fragmentation in explosive eruptions. Nature 397:425–428. doi: 10.1038/17109

Parfitt E (2004) A discussion of the mechanisms of explosive basaltic eruptions. J. Volcanol Geotherm Res 134:77–107. doi: 10.1016/j.jvolgeores.2004.01.002

Pérez W, Freundt A, Kutterolf S, Schmincke H-U (2009) The Masaya Triple Layer: A 2100 year old basaltic multi-episodic Plinian eruption from the Masaya Caldera Complex (Nicaragua). J Volcanol Geotherm Res 179:191–205. doi: 10.1016/j.jvolgeores.2008.10.015

Roche O, Druitt TH (2001) Onset of caldera collapse during ignimbrite eruptions. Earth Planet. Sci. Lett. 191:191–202

Ross P-S, White JDL (2005) Mafic, large-volume, pyroclastic density current deposits from phreatomagmatic eruptions in the Ferrar large igneous province, Antarctica. Geology 113: 627–649. doi: 10.1086/449324

Ruth DCS, Cottrell E, Cortés JA, Kelley KA, Calder ES (2016) From Passive Degassing to Violent Strombolian Eruption: the Case of the 2008 Eruption of Llaima Volcano, Chile. J Petrol 57:1833–1864. doi: 10.1093/petrology/egw063

Sable J, Houghton B, Del Carlo P, Coltelli M (2006) Changing conditions of magma ascent and fragmentation during the Etna 122 BC basaltic Plinian eruption: evidence from clast microtextures. J Volcanol Geotherm Res 158:433–456. doi: 10.1016/j.jvolgeores.2006.07.006

Sable JE, Houghton BF, Wilson CJN, Carey RJ (2009) Eruption mechanisms during the climax of the Tarawera 1886 basaltic Plinian eruption inferred from microtextural characteristics of the deposits *in* Thordarson T, Self S, Larsen G, Rowland SK, Hoskuldsson A (eds) Studies in Volcanology: The Legacy of George Walker. Special Publications of IAVCEI 2:229–154. The Geological Society of London, London

Scarpati C, Sparice D, Perrotta A (2015) The ground layer of the Campanian Ignimbrite: an example of deposition from a dilute pyroclastic density current. Bull Volcanol 77(11):1–10. doi: 10.1007/s00445-015-0985-0

Schindlbeck JC, Freundt A, Kutterolf S (2014) Major changes in the post-glacial evolution of magmatic compositions and pre-eruptive conditions at Llaima volcano, Andean Southern Volcanic Zone, Chile. Bull Volcanol 76:830. doi: 10.1007/s00445-014-0830-x

Schneider CA, Rasband WS, Eliceiri KW (2012) NIH image to ImageJ: 25 years of image analysis. Nat Methods 9:671–675

Shea T (2017) Bubble nucleation in magmas: A dominantly heterogeneous process? J Volcanol Geotherm Res 343:155–170. doi: 10.1016/j.jvolgeores.2017.06.025

Shea T, Houghton BF, Gurioli L, Cashman KV, Hammer JE, Hobden BJ (2010) Textural studies of vesicles in volcanic rocks: An integrated methodology. J Volcanol Geotherm Res 190:271–289. doi: 10.1016/j.jvolgeores.2009.12.003

Shea T, Hammer JE (2013) Kinetics of cooling- and decompression-induced crystallization in hydrous mafic-intermediate magmas. J Volcanol Geotherm Res 260:127–145. doi: 10.1016/j.jvolgeores.2013.04.018

Silleni A, Giordano G, Isaia R, Ort MH (2020) Magnitude of the 39.8 ka Campanian Ignimbrite Eruption, Italy: a review and reassessment using an ignimbrite isopach map. Front. Earth Sci. doi: 10.3389/feart.2020.543399

Smith G, Rowley P, Williams R, Giordano G, Trolese M, Silleni A, Parsons DR, Capon S (2020) A bedform phase diagram for dense granular currents. Nat Commun 11(1):1–11. doi: 10.1038/s41467-020-16657-z

Stern CR (2004) Active Andean volcanism: its geologic and tectonic setting. Rev Geol Chile 31:161–206

Szramek L, Gardner JE, Larsen (2006) Degassing and microlite crystallization of basaltic andesite magma erupting at Arenal Volcano, Costa Rica. J Volcanol Geotherm Res 157:182–201. doi: 10.1016/j.jvolgeores.2006.03.039

Szramek L (2016) Mafic Plinian eruptions: Is fast ascent required?. J Geophys Res B: Solid Earth 121:7119–7136. doi: 10.1002/2016JB013208

Toramaru A (2006) BND (bubble number density) decompression rate meter for explosive volcanic eruptions. J Volcanol Geotherm Res 154:303–316. doi: 10.1016/j.jvolgeores.2006.03.027

Trolese M, Cerminara M, Ongaro TE, Giordano G (2019) The footprint of column collapse regimes on pyroclastic flow temperatures and plume heights. Nat Commun 10:2476. doi: 10.1038/s41467-019-10337-3

Valdivia Muńoz PA, Marshall AA, Brand BD, Manga M, Huber C (2021) Mafic explosive volcanism at Llaima volcano: 3D X-ray microtomography reconstruction of pyroclasts to constrain shallow conduit processes. Bull Volcanol. (*in revision*)

Van Eaton AR, Muirhead JD, Wilson CJN, Cimarelli C (2012) Growth of volcanic ash aggregates in the presence of liquid water and ice: an experimental approach. Bull Volcanol 74:1963–1984. doi: 10.1007/s00445-012-0634-9

Vinkler AP, Cashman K, Giordano G, Groppelli G (2012) Evolution of the mafic Villa Senni caldera-forming eruption at Colli Albani volcano, Italy, indicated by textural analysis of juvenile fragments. J Volcanol Geotherm Res 235–236:37–54. doi: 10.1016/j.jvolgeores.2012.03.006

Völker D, Kutterolf S, Wehrmann H (2011) Comparative mass balance of volcanic edifices at the southern volcanic zone of the Andes between 33°S and 46°S. J Volcanol Geotherm Res 205:114–129. doi: 10.1016/j.jvolgeores.2011.03.011

Vona A, Romano C, Dingwell DB, Giordano D (2011) The rheology of crystal-bearing basaltic magmas from Stromboli and Etna. Geochim Cosmochim Acta 75(11):3214–3236. doi: 10.1016/j.gca.2011.03.031

Walker GPL (1981) Characteristics of two phreatoplinian ashes, and their water-flushed origin. J Volcanol Geotherm Res 9:395–407

Walker GPL (1983) Ignimbrite types and ignimbrite problems. J Volcanol Geotherm Res 17:65–88. doi: 10.1016/0377-0273(83)90062-8

White JD, Ross PS (2011) Maar-diatreme volcanoes: A review. J Volcanol Geotherm Res 201(1–4):1–29. doi: 10.1016/j.jvolgeores.2011.01.010

White JDL, Valentine GA (2016) Magmatic versus phreatomagmatic fragmentation: Absence of evidence is not evidence of absence. Geosphere 12:1478–1488. doi: 10.1130/GES01337.1

Wilson CJN, Walker GPL (1985) The Taupo eruption, New Zealand 1. General aspects. Philos. Trans. R. Soc. London, Ser. A 314:199–228

Wilson CJN (1991) Ignimbrite morphology and the effects of erosion: A New Zealand case study. Bull Volcanol 53:635–644

Yamamoto T, Takada A, Ishizuka Y, Miyaji N, Tajima Y (2005) Basaltic pyroclastic flows of Fuji volcano, Japan: characteristics of the deposits and their origin. Bull Volcanol 67:622–633. doi:10.1007/s00445-004-0398-y

Zimanowski B, Büttner R, Dellino P, White JDL, Wohletz KH (2015) Magma-Water Interaction and Phreatomagmatic Fragmentation. Encyclopedia of Volcanoes 2 ed., p. 473–484

CHAPTER 3: CURACAUTÍN CRYSTAL SIZE DISTRIBUTION ANALYSIS

This chapter is part of a manuscript that is published by Springer in the Bulletin of Volcanology. The full citation is: Valdivia P, Marshall AA, Brand BD, Manga M, Huber C (2022) Mafic explosive volcanism at Llaima Volcano: 3D x-ray microtomography reconstruction of pyroclasts to constrain shallow conduit processes. Bull Volcanol 84(2). doi: 10.1007/s00445-021-01415-8.

3.1 Introduction

Magma decompression paths influence the style of volcanic eruptions (Waters et al., 2015; Moitra et al., 2018; Barth et al., 2019). As a magma ascends from the chamber up the conduit, decompression induces variable degrees of crystallization (Arzilli et al., 2019; Murch and Cole, 2019; Andrews and Befus, 2020; Bamber et al., 2020), viscosity and rheological evolution (Vona et al., 2011), and bubble nucleation (Shea, 2017). The solubility of H_2O and CO_2 further impact the evolution of the magma and eruption style. For example, the lower solubility of CO_2 drives the initial exsolution of bubbles that initiate magma ascent (Cashman, 2004), while H_2O exsolution in the shallow subsurface promotes crystallization by raising the melt liquidus temperature, thus increasing melt undercooling. Undercooling (ΔT), or supersaturation, is the difference between the liquidus temperature and pressure of a phase and the actual crystallization pressure and temperature (Fig. 3.1, Befus and Andrews, 2018). Over time *t*, this results in variable

rates of crystal nucleation and growth. At low $\Delta T/\Delta t$, crystal growth dominates resulting in larger euhedral to tabular crystals and low volumetric number densities (e.g., Szramek et al., 2006). Conversely, at high $\Delta T/\Delta t$, crystal nucleation dominates in response to supersaturation resulting in the rapid formation of small acicular, hopper, and skeletal crystals at high volumetric number densities (Shea and Hammer, 2013). Frozen crystal textures in pyroclasts thus detail the complex magma history from the chamber through the conduit prior to eruption.

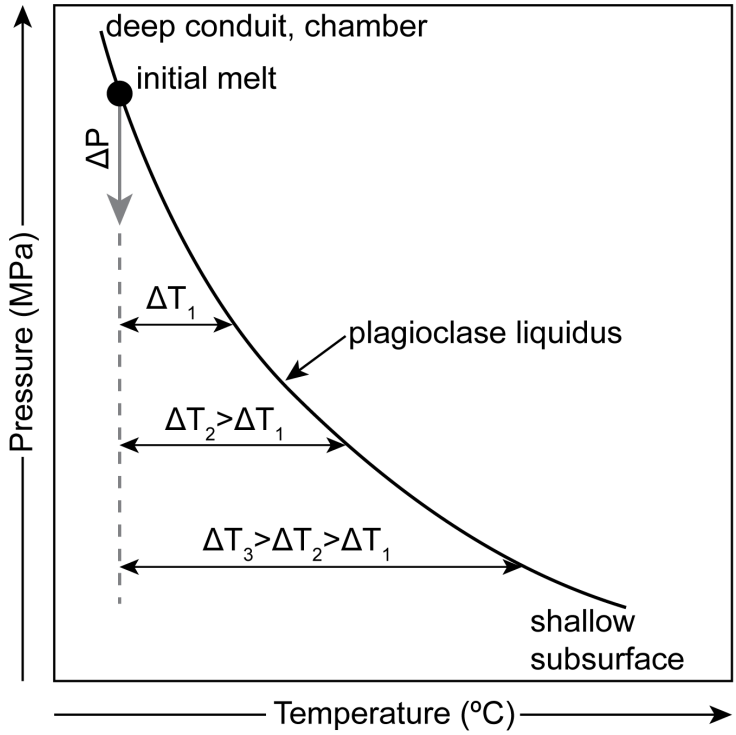

Figure 3.1. Simplified pressure-temperature schematic diagram of plagioclase undercooling (ΔT). The black curve is the theoretical plagioclase liquidus curve. The gray dashed line represents a change in pressure ΔP that results in variable degrees of undercooling ΔT (supersaturation) depending on how large ΔP is. The larger ΔP, the larger ΔT (shown as three arrows denoted as ΔT_1, ΔT_2, ΔT_3). Modified from Befus and Andrews (2018).

Marshall et al. (2022) hypothesized the Curacautín ignimbrite (Ci) melt ascended rapidly in the shallow subsurface based on high plagioclase microlite number densities. They propose that rapid ascent increased the viscosity of the Ci melt, trapping the magmatic volatiles necessary for brittle fragmentation. However, their work does not include a quantitative investigation of the Ci microlite textures. In this chapter, we conduct a crystal size distribution analysis of plagioclase microlites from Marshall et al. (2022) and calculate timescales of plagioclase crystallization for the Ci using experimentally determined growth rates. The results of my CSDs allow us to approximate crystallization times in the shallow subsurface prior to the Ci eruption.

3.1.1 Crystal size distributions

Crystal size distributions (CSDs) record a time-integrated history of magma decompression (Marsh, 1988; Cashman and Marsh, 1988). Log-linear trends in CSDs are interpreted as evidence for continuous crystal nucleation, growth, and decompression, while CSDs with kinks record a change in crystal nucleation or growth rates, reflecting a change in the decompression path history (Murch and Cole, 2019; Bamber et al., 2020). CSDs have also been used to differentiate between differing styles of volcanism (Murch and Cole, 2019). However, the interpretation of CSDs have limitations. Andrews and Befus (2020) note interpretations of CSDs require independent knowledge of nucleation and growth rates to calculate decompression rates. Additionally, interpretations of CSDs typically necessitate the assumption that nucleation and growth rates are constant, which is certainly not representative of conditions in nature. For the purposes of this work, however, nucleation and growth are assumed to be constant.

3.2 Methods

3.2.1 Textural analyses

Backscattered electron (BSE) images were collected on a Teneo FEI Field Emission Scanning Electron Microscope (FESEM) at the Boise State University Center for Materials Characterization a beam current of 6.4 nA and 15 kV accelerating voltage. BSE images were segmented and measured manually in ImageJ (Schneider et al., 2012) for calculation of microlite textures. Microlite area fraction (ϕ_X) was calculated using

$$\phi_X = \frac{A_X}{A}$$

where A_X=the area of the mineral phase and A=the vesicle-free area (Hammer et al., 1999). Glass content was calculated by

$$\phi_{glass} = 1 - \phi_{plag} - \phi_{feti} - \phi_{anh}$$

where ϕ_{plag}=plagioclase area fraction, ϕ_{feti}=FeTi oxide area fraction, and ϕ_{anh}=anhedral area fraction. Olivine and pyroxene were not differentiated because of the difficulty in reliably segmenting them from one another in BSE images. I calculated area number densities N_A by

$$N_A = \frac{n_X}{A}$$

where n_X=number of crystals of a given mineral phase. Mean crystal size S_m was measured directly in ImageJ. The volumetric number density (N_V) was calculated by

$$N_V = \frac{N_A}{S_m}$$

after Cashman (1992).

In order to calculate CSDs, microlites need to be assigned a crystal habit that describes their shape based on their short, intermediate, and long axes (S:I:L). We

obtained crystal habits using the stereological conversion program CSDslice v. 5 (Morgan and Jerram, 2006). Because of their acicular nature in two dimensions, we measured >250 plagioclase microlites per pyroclast to ensure correct determination of crystal habit (Morgan and Jerram, 2006). Crystal habits calculated from CSDslice v. 5 were used as inputs for CSDcorrections v. 1.6 (Higgins, 2000) to generate CSD plots. Microlites do not exhibit a preferential orientation and thus no fabric was factored into the CSD calculations. The crystal roundness was set to 0.1, and we used a shape geometry of parallepolid for stereological conversions. Five bins per decade were selected, with empty bins being excluded from the CSDs. Images were corrected for sample vesicularity measured in ImageJ.

Crystallization times τ can be calculated from CSDs by

$$k = \frac{-1}{G\tau}$$

where k is the slope of the CSD linear regression and G is the microlite growth rate (Cashman, 1988). We calculated τ using growth rates of 10^{-4} mm s^{-1} (Arzilli et al., 2019), 2×10^{-5} mm s^{-1} (Arzilli et al., 2015), 10^{-6} mm s^{-1} (Shea and Hammer, 2013), and 10^{-7} mm s^{-1} (Arzilli et al., 2015) to investigate the variability of fast versus slow crystallization (after Bamber et al., 2020). The y-intercept $n°$ of CSD linear regressions is the nucleation density (mm^{-4}). Cashman and Marsh (1988) showed that the nucleation rate J can be calculated by

$$J = n°G$$

where G is the mean linear growth rate.

3.3 Results

3.3.1 2D microlite morphologies

Plagioclase microlite morphologies are predominantly acicular to tabular, but incidences exist of skeletal, swallowtail, and rarely spherical (Fig. 3.2). Olivine and pyroxene are primarily euhedral to tabular, but often exhibit hopper morphologies. Pyroxenes are sometimes present as dendritic chains. FeTi oxides are tabular or blocky. Microlites do not exhibit a preferential orientation.

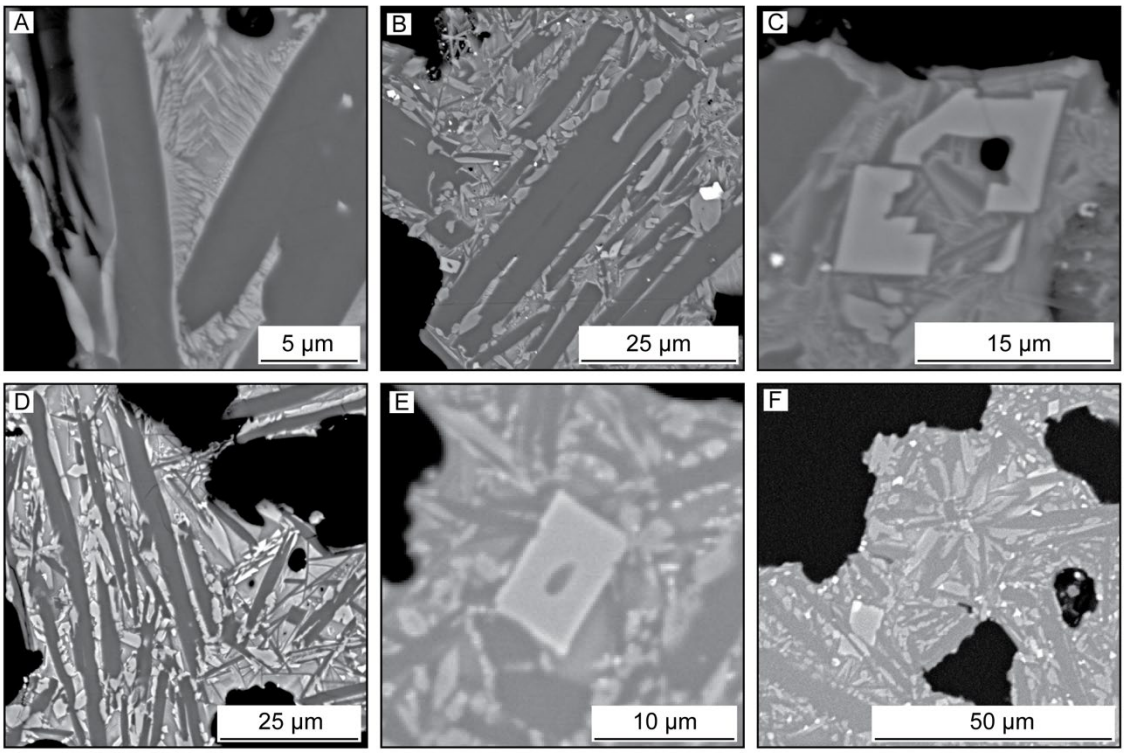

Figure 3.2. Examples of Ci microlite textures. (A) Dendritic anhedral microlites nucleated on plagioclase crystals. (B) Tabular plagioclase microlites and a swallowtail plagioclase microphenocryst. (C) Broken anhedral hopper microlite. (D) Acicular plagioclase microlites as small as ~5 µm. (E) Anhedral hopper microlite. (F) Spherical microlite cluster. The most common microlites are tabular and acicular plagioclase.

3.3.2 Textural analyses

Microlite textural measurements are available in Table 2.2. Unit 1 has a ϕ_{plag} between 0.36±0.02 and 0.44±0.03. Units 2, 3, and 4 have a ϕ_{plag} of 0.42±0.04, 0.36±0.02, and 0.29±0.01, respectively. Unit 1 ϕ_{anh} content is between 0.30±0.03 and 0.19±0.01. Units 2, 3, and 4 have ϕ_{anh} content of 0.27±0.02, 0.26±0.03, and 0.17±0.02, respectively. Unit 1 ϕ_{feti} is between 0.005±0.002 and 0.020±0.024; Units 2, 3, and 4 ϕ_{feti} are 0.010±0.002, 0.002±0.000, and 0.002±0.001, respectively. Unit 1 glass content is between 0.25±0.01 and 0.41±0.03. Units 2, 3, and 4 have glass contents of 0.30±0.06, 0.38±0.04, and 0.54±0.01, respectively.

Plagioclase microlite textures (Fig. 2.15) were calculated by Marshall et al. (2022a) and available in Table 2.2. Unit 1 plagioclase N_A are variable from 4.99–6.72×10^4 mm^{-2} and N_V range from 0.821–1.33×10^7 mm^{-3}. Characteristic crystal sizes (S_m) range from 5.1–6.4 μm. Unit 2 plagioclase N_A, N_V, and S_m are 5.08×10^4 mm^{-2}, 0.795×10^7 mm^{-3}, and 6.5 μm, respectively. Unit 3 plagioclase N_A, N_V, and S_m are 7.07×10^4 mm^{-2}, 1.66×10^7 mm^{-3}, and 4.7 μm, respectively. Unit 4 plagioclase N_A, N_V, and S_m are 7.32×10^4 mm^{-2}, 1.84×10^7 mm^{-3}, and 4.1 μm, respectively. S_m was measured directly in *ImageJ* and not calculated from N_A.

3.3.3 Plagioclase crystal size distributions

Plagioclase microlite habits are available in Fig. 3.3. Unit 1 plagioclase have tabular to rectangular prism habits and S:I:L axes between 1:6:10 and 1:8:10 (R^2=0.68–0.83). Units 2 and 3 have rectangular prism habits and S:I:L axes of 1:6:10 (R^2=0.80 and

0.85, respectively). Unit 4 plagioclase have a tabular habit and S:I:L axes of 1:6:10 (R^2=0.86).

All Ci CSDs are concave up (Fig. 3.4). Unit 1 has the highest number of bins and Unit 4 has the least. We identified two size populations of microlites based on linear regression fitting. The first regression is fit to the smallest crystal size population (segment A) and produces the steepest slopes (Fig. 3.4). The second regression is fit to the largest crystal size population (segment B) and creates shallower slopes. The *y*-intercept n° is the nucleation density (mm^{-4}). All CSDs exhibit a downturn at the smallest size bins (Fig. 3.4). Because our data were collected at 1500–2000x magnifications, these downturns likely reflect the reduced probability of intercepting small crystals and not inadequate image resolution (Cashman, 1998; Marsh, 1998). Data from downturns are not included in segment A regressions.

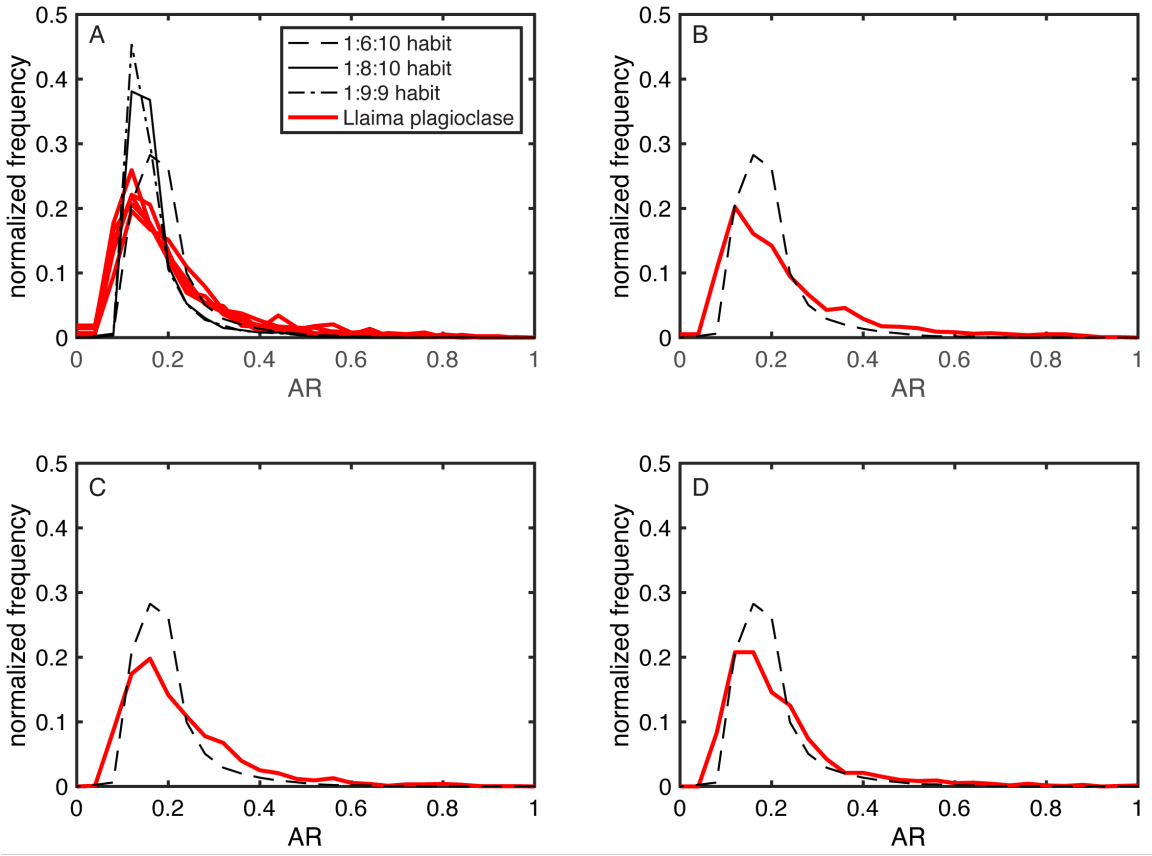

Figure 3.3 Ci plagioclase microlite habits for (A) Unit 1, (B) Unit 2, (C) Unit 3, and (D) Unit 4. AR=aspect ratio.

The results of the CSD analyses are in Table 3.1. Unit 1 average crystallization times τ for segment A are 2–4 s and 8–18 s for segment B for G=1×10^{-3} mm s^{-1} (Arzilli et al., 2019); Unit 1 τ for segment A are 1.7–3.7 min and 7.0–14.9 min for segment B for G=2.0×10^{-5} mm s^{-1} (Arzilli et al., 2015); Unit 1 τ for segment A are 3.4–7.4 min segment B are 0.2–0.5 hr for G=1.0×10^{-5} mm s^{-1} (Shea and Hammer, 2013); and Unit 1 τ for segment A are 0.6–1.2 hr and are 2.3–5.0 hr for segment B for G=1.0×10^{-6} mm s^{-1} (Arzilli et al., 2015). Unit 2 τ are between 4 s and 1.0 hr for segment A and 11 s and 2.9 hr for segment B for G=1×10^{-3}–1.0×10^{-6} mm s^{-1}. Unit 3 τ are between 3 s and 0.8 hr for segment A and 8 s and 2.2 hr for segment B for G=1×10^{-3}–1.0×10^{-6} mm s^{-1}. Unit 4 τ are

between 2 s and 0.7 hr for segment A and 10 s and 2.7 hr for segment B for G=1×10^{-3}–1.0×10^{-6} mm s^{-1}.

Unit 1 average plagioclase population densities (n°, y-intercept of CSDs) are between 21.91 and 23.56 mm^{-4} for segment A and between 16.21 and 18.44 mm^{-4} for segment B. Unit 2 has an average n° of 22.20 mm^{-4} for segment A and 18.91 mm^{-4} for segment B. Unit 3 has an average n° of 23.16 mm^{-4} for segment A and 19.83 mm^{-4} for segment B. Unit 4 has an average n° of 23.31 mm^{-4} for segment A and 18.73 mm^{-4} for segment B.

Nucleation rates J for Units 1–4 are between 1.46×10^{-2} mm^{-3}s^{-1} and 2.40×10^{-2} mm^{-3}s^{-1} using G=1.0×10^{-3} mm s^{-1} (Arzilli et al., 2019). J are between 2.92×10^{-4} mm^{-3}s^{-1} and 4.81×10^{-4} mm^{-3}s^{-1} using G=2.0×10^{-5} mm s^{-1} (Arzilli et al., 2015). J are between 1.46×10^{-4} mm^{-3}s^{-1} and 2.40×10^{-4} mm^{-3}s^{-1} using G=1.0×10^{-5} mm s^{-1} (Shea and Hammer, 2013). J are between 1.46×10^{-5} mm^{-3}s^{-1} and 2.40×10^{-5} mm^{-3}s^{-1} using G=1.0×10^{-6} mm s^{-1} (Arzilli et al., 2015).

Table 3.1 Results of plagioclase CSD analyses. Four values of τ_c are provided using different experimentally derived growth rates. Letter in parentheses for samples is the CSD segment. Multiple *J* and τ values correspond to their respective *G* values (footnotes). Note that the units for τ vary for different *G*. Three images were analyzed per sample, and their average was used for CSDs, timescale calculations, and nucleation rate calculations.

Sample	Unit	n^o (mm^{-4})	k (mm^{-1})	τ_c^1 (s)	J ($mm^{-3}s^{-1}$)	τ_c^2 (m)	J ($mm^{-3}s^{-1}$)	τ_c^3 (m)	J ($mm^{-3}s^{-1}$)	τ_c^4 (hr)	J ($mm^{-3}s^{-1}$)
L1 (A)	1	22.87	-383.33	3	2.29×10^{-2}	2.2	4.57×10^{-4}	4.4	2.29×10^{-4}	0.7	2.29×10^{-5}
L1 (B)	1	16.21	-60.89	18	1.62×10^{-2}	14.9	3.24×10^{-4}	29.7	1.62×10^{-4}	5.0	1.62×10^{-5}
L4 (A)	1	23.56	-500.72	2	2.36×10^{-2}	1.7	4.71×10^{-4}	3.4	2.36×10^{-4}	0.6	2.36×10^{-5}
L4 (B)	1	18.44	-126.23	8	1.87×10^{-2}	7.0	3.69×10^{-4}	14.1	1.87×10^{-4}	2.4	1.87×10^{-5}
L6 (A)	1	21.91	-235.04	4	2.19×10^{-2}	3.7	4.38×10^{-4}	7.4	2.19×10^{-4}	1.2	2.19×10^{-5}
L6 (B)	1	17.88	-70.93	14	1.79×10^{-2}	12.0	3.58×10^{-4}	24.0	1.79×10^{-4}	4.0	1.79×10^{-5}
L8 (A)	2	22.20	-270.18	4	2.22×10^{-2}	3.1	4.44×10^{-4}	6.2	2.22×10^{-4}	1.0	2.22×10^{-5}
L8 (B)	2	18.91	-95.06	11	1.89×10^{-2}	8.8	3.78×10^{-4}	17.6	1.89×10^{-4}	2.9	1.89×10^{-5}
L10 (A)	3	23.16	-337.44	3	2.31×10^{-2}	2.5	4.63×10^{-4}	5.0	2.31×10^{-4}	0.8	2.31×10^{-5}

Sample	Unit	n^o (mm^{-4})	k (mm^{-1})	τ_c^1 (s)	J ($mm^{-3}s^{-1}$)	τ_c^2 (m)	J ($mm^{-3}s^{-1}$)	τ_c^3 (m)	J ($mm^{-3}s^{-1}$)	τ_c^4 (hr)	J ($mm^{-3}s^{-1}$)
L10 (B)	3	19.83	-133.52	8	1.98×10^{-2}	6.7	3.97×10^{-4}	13.4	1.98×10^{-4}	2.2	1.98×10^{-5}
L18 (A)	4	23.64	-450.49	2	2.33×10^{-2}	2.0	4.66×10^{-4}	4.0	2.33×10^{-4}	0.7	2.33×10^{-5}
L18 (B)	4	18.73	-101.97	10	1.87×10^{-2}	8.2	3.57×10^{-4}	16.4	1.87×10^{-4}	2.7	1.87×10^{-5}

[1]$G=10^{-4}$ mm s^{-1} (Arzilli et al., 2019). [2]$G=2\times10^{-5}$ mm s^{-1} (Arzilli et al., 2015). [3]$G=10^{-6}$ mm s^{-1} (Shea and Hammer, 2013) .[4]$G=10^{-7}$ mm s^{-1} (Arzilli et al., 2015)

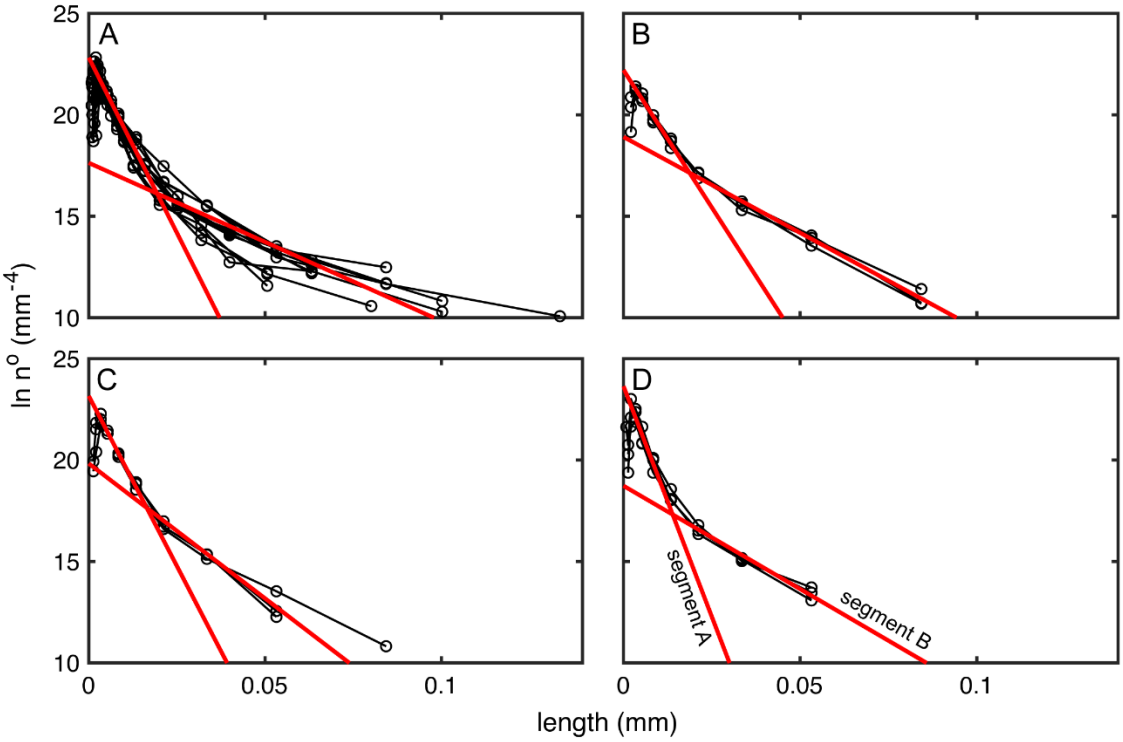

Figure 3.4 Ci CSDs for (A) Unit 1, (B) Unit 2, (C) Unit 3, and (D) Unit 4. I analyzed three pyroclasts for Unit 1, and one pyroclast each for Units 2, 3, and 4. All CSDs are concave up, and best fit linear regressions reflect at least two crystal nucleation events (e.g., Murch and Cole, 2019; Bamber et al., 2020). Regressions in (A) are the average of all Unit 1 samples. Segment A reflects syn-eruptive crystallization and segment B reflects crystallization deeper in the conduit. Down turns at the smallest microlite sizes are not calculated into segment A regressions (see body text for details).

3.4 Discussion

3.4.1 Crystallization times inferred from CSDs

CSDs are useful in identifying changing decompression pathways in the subsurface. For example, CSDs that form a straight line reflect continuous decompression while concave up CSDs reflect differing depths and rates of crystallization (Marsh, 1998). In the shallow subsurface, nucleation-dominated crystallization is driven by high decompression rates (Arzilli et al., 2019). Conversely, larger microlites and phenocrysts

form deeper in the conduit where they have time to grow during their ascent to the surface.

The two segments in our CSDs (Fig. 3.4) identified from separate linear regressions indicate a change in decompression pathways during ascent of the Ci magma (e.g., Murch and Cole, 2019; Bamber et al., 2020). Segment A is reflective of shallow, rapid decompression or syn-eruptive crystallization where nucleation-dominated crystallization prevails (Geschwind and Rutherford, 1995; Hammer et al., 1999; Blundy and Cashman, 2008). Segment B is representative of larger crystal sizes that nucleated deeper in the conduit. However, 85–93% of Ci plagioclase microlites are <10 μm, suggesting that even though a subpopulation of microlites crystallized deeper in the conduit, most plagioclase crystals had little time to grow. Therefore, we interpret that Ci CSDs are reflective of primarily shallow-conduit conditions.

The Ci bulk rock composition spans from basalt to andesite (50.67–57.56 wt. % SiO_2, Marshall et al., [2022]) with an average SiO_2 concentration of 54.05 wt. %, 1–2% pre-eruptive H_2O content. Using the plagioclase liquid hygrometer of Lange et al. (2009), Schindlbeck et al. (2014) calculated a storage depth for the Ci magma of 18 km. The plagioclase growth rates (G) of 10^{-4}–10^{-7} mm s^{-1} (Shea and Hammer, 2013; Arzilli et al., 2015; Arzilli et al., 2019) are suitable growth rates for my calculations as they were experimentally derived under similar compositions and water contents as the Ci. Bamber et al. (2020) determined that G values of 10^{-4} mm s^{-1} (Arzilli et al., 2019) and 2×10^{-5} mm s^{-1} (Arzilli et al., 2015) are most appropriate for crystallization in the conduit, while 10^{-6} mm s^{-1} (Shea and Hammer, 2013) and 10^{-7} mm s^{-1} (Arzilli et al., 2015) are appropriate for

phenocrysts or larger microlites crystallizing within the magma chamber. Below, we follow this same paradigm for the Ci.

Segment A τ indicate the Ci reached such high microlite crystallinities on the order of seconds to minutes (Table 3.1). Such rapid crystallization could only result from high degrees of undercooling (e.g., Arzilli et al., 2019) as there is no evidence that magma-water interaction played a significant role in the Ci eruption (Marshall et al., 2022). High degrees of undercooling are further reflected in the dominantly acicular to hopper microlite textures, which form under disequilibrium crystallization conditions (Shea and Hammer, 2013). Accordingly, J scales with τ because they are both a function of G. The maximum calculated τ of 5 hrs comes from the segment B regression for the base of Unit 1 and is reflective of the onset of magma migration to the surface. Despite being the lowest τ, 5 hrs is a rapid time for ascent from storage depths of 18 km (Schindlbeck et al., 2014). Because the Ci phenocryst population is ≤1–3% (Marshall et al., 2022), we imaged microlite populations at 1500–2000x magnification to fully resolve the smallest size population. Therefore, our CSDs reflect conditions from syn-eruptive and shallow crystallization to the deep conduit and not the magma chamber.

Ci microlite textures and CSDs indicate varying degrees of microlite nucleation, decompression rate, and ascent dynamics between the four units identified by Marshall et al. (2022). There is a general increase in segment A n° and J from Unit 1 into Units 2, 3, and 4 suggesting the ascent rates of later eruptive episodes increased along with nucleation rates. This is corroborated by the increased τ and can be explained by the high ΔT expected in the shallow conduit for high intensity mafic explosive eruptions (Arzilli et al., 2019; Bamber et al., 2020). There are no systematic trends in segment B n°, J, and τ

between units and likely reflect similar early crystallization depths and/or conditions for all erupted products. The lack of a high volume percent of phenocrysts reflects higher chamber temperatures and low to no ΔT. We therefore propose that Ci microlite textures reflect mid- to shallow conduit conditions and syn-eruptive crystallization, likely following the onset of bubble nucleation, rather than conditions in the magma chamber. The results of our CSD analyses for the Ci provide further support in a growing field of literature that suggests rapid magma ascent is necessary for high intensity, mafic explosive volcanism (Houghton et al., 2004; Sable et al., 2006; Sable et al., 2009; Moitra et al., 2018; Arzilli et al., 2019).

3.5 Conclusions

Ci textures are the result of disequilibrium crystallization in response to rapid magma ascent. All Ci CSDs are concave up with slight downturns at the finest size distribution of microlites. Concave up CSDs represent a change in magma ascent rates. We fit regressions to two CSD segments: segment A is fit to the smallest size population of microlites (excluding downturns) and represents syn-eruptive and shallow crystallization, while segment B is fit to larger microlites and microphenocrysts and represents deeper crystallization. Regressions were fit based on their R^2 values. Using experimentally derived growth rates G suitable for the Ci along with CSD regression slopes, we calculated crystallization times τ for segment A of 2 s to 1.2 hr. Segment B τ are 8 s to 5.0 hr. Segment A τ increase from Unit 1 into Units 2, 3, and 4, suggesting a general increase in ascent rate throughout the Ci eruption. Conversely, there are no systematic trends in segment B n°, J, and τ. Future work to confirm the results of Ci

CSD analyses should be in the form of high *P-T* decompression experiments or numerical modeling.

3.6 References

Andrews BJ, Befus KS (2020) Supersaturation Nucleation and Growth of Plagioclase: a numerical model of decompression-induced crystallization. Contrib Mineral Petrol 175:23. doi: 10.1007/s00410-020-1660-9

Arzilli F, Agostini C, Landi P, Fortunati A, Mancini L, Carroll M (2015) Plagioclase nucleation and growth kinetics in a hydrous basaltic melt by decompression experiments. Contrib Mineral Petrol 170:55. doi: 10.1007/s00410-015-1205-9

Arzilli F, La Spina G, Burton MR, Polacci, M, Le Gall N, Hartley ME, Di Genova D, Cai B, Vo NT, Bamber EC, Nonni S, Atwood R, Llewellin EW, Brooker RA, Mader HM, Lee PD (2019) Magma fragmentation in highly explosive basaltic eruptions induced by rapid crystallization. Nat Geosci 12:1023–1028. doi: 10.1038/s41561-019-0468-6

Bamber EC, Arzilli F, Polacci M, Hartley ME, Fellowes J, Di Genova D, Chavarría D, Saballos JA, Burton MR (2020) Pre- and *syn*-eruptive conditions of a basaltic Plinian eruption at Masaya Volcano, Nicaragua: The Masaya Triple Layer (2.1 ka). J Volcanol Geotherm Res 392:1–16. doi: 10.1016/j.jvolgeores.2019.106761

Barth A, Newcombe M, Plank T, Gonnermann H, Hajimirza S, Soto GJ, Saballos A, Hauri E (2019) Magma decompression rate correlates with explosivity at basaltic volcanoes – Constraints from water diffusion in olivine. J Volcanol Geotherm Res 387:106665. doi: 10.1016/j.jvolgeores.2019.106664

Befus KS, Andrews BJ (2018) Crystal nucleation and growth produced by continuous decompression of Pinatubo magma. Contrib Mineral Petrol 173:92. doi: 10.1007/s00410-018-1519-5

Blundy J, Cashman KV (2008) Petrologic reconstruction of magmatic system variables and processes *in:* Minerals, Inclusions and Volcanic Processes. Rev Mineral Geochem 69:179–239

Cashman KV (1998) Crystallization of Mount St. Helens 1980–1986 dacite: a quantitative textural approach. Bull Volcanol 50:194–209

Cashman KV (1992) Groundmass crystallization of Mount St. Helens dacite 1980–1986: a tool for interpreting shallow magmatic processes. Contrib Mineral Petrol 109:431–449

Cashman KV (2004) Volatile Controls on Magma Ascent and Eruption *in* Sparks RSJ, Hawkesworth CJ, eds., The State of the Planet: Frontiers and Challenges in Geophysics. Geophysical Monograph Series 150:109–124

Cashman KV, Marsh BD (1988) Crystal size distribution (CSD) in rocks and the kinetics and dynamics of crystallization II. Makaopuhi lava lake. Contrib Mineral Petrol 99:292–305

Geschwind C-H, Rutherford MJ (1995) Crystallization of microlites during magma ascent: the fluid mechanics of 1980–1986 eruptions at Mount St. Helens. Bull Volcanol 57:356–370

Hammer JE, Cashman KV, Hoblitt RP, Newman S (1999) Degassing and microlite crystallization during pre-climatic events of the 1991 eruption of Mt. Pinatubo, Philippines. Bull Volcanol 60:355–380

Higgins MD (2000) Measurement of crystal size distributions. Am Mineral 85:1105–1116

Higgins MD (2002) Closure in crystal size distributions (CSD), verification of CSD calculations, and the significance of CSD fans. Am Mineral 87:171–175

Houghton BF, Wilson CJN, Del Carlo P, Coltelli M, Sable JE, Carey R (2004) The influence of conduit processes on changes in styles of basaltic Plinian eruptions: Tarawera 1886 and Etna 122 BC. J Volcanol Geotherm Res 137:1–14. doi: 10.1016/j.jvolgeores.2004.05.009

Lange RA, Frey HM, Hector J (2009) Aa thermodynamic model for the plagioclase-liquid hygrometer/thermometer. Am Mineral 94:494–506. doi: 10.2138/am.2009.3011

Marsh BD (1988) Crystal size distribution (CSD) in rocks and the kinetics and dynamics of crystallization: I. Theory. Contrib Mineral Petrol 99:277–291

Marsh BD (1998) On the interpretation of crystal size distributions in magmatic systems. J Petrol 39:553–599

Marshall AA, Brand BD, Martínez V, Bowers JM, Walker M, Wanless VD, Andrews BJ, Manga M, Valdivia P, Giordano D (2022) The mafic Curacautín ignimbrite of Llaima volcano, Chile. J Volcanol Geotherm Res 421:107418. doi: 10.1016/j.jvolgeores.2021.107418

Moitra P, Gonnermann HM, Houghton BF, Tiwary CS (2018) Fragmentation and Plinian eruption of crystallizing basaltic magma. Earth Planet. Sci. Lett. 500:97–104. doi: 10.1016/j.epsl.2018.08.003

Morgan DJ, Jerram DA (2006) On estimating crystal shape for crystal size distribution analysis. J Volcanol Geotherm Res 154:1–7. doi: 10.1016/j.jvolgeores.2005.09.016

Murch AP, Cole PD (2019) Using microlites to gain insights into ascent conditions of differing styles of volcanism at Soufrière Hills Volcano. J Volcanol Geotherm Res 384:221–231. doi: 10.1016/j.jvolgeores.2019.07.022

Naranjo JA, Moreno H (1991) Actividad explosiva postglacial en el volcan Llaima, Andes del sur. Rev Geol Chile 18:69–80

Sable J, Houghton B, Del Carlo P, Coltelli M (2006) Changing conditions of magma ascent and fragmentation during the Etna 122 BC basaltic Plinian eruption: evidence from clast microtextures. J Volcanol Geotherm Res 158:433–456. doi: 10.1016/j.jvolgeores.2006.07.006

Sable JE, Houghton BF, Wilson CJN, Carey RJ (2009) Eruption mechanisms during the climax of the Tarawera 1886 basaltic Plinian eruption inferred from microtextural characteristics of the deposits *in* Thordarson T, Self S, Larsen G, Rowland SK, Hoskuldsson A (eds) Studies in Volcanology: The Legacy of George Walker. Special Publications of IAVCEI 2:229–154. The Geological Society of London, London

Schindlbeck JC, Freundt A, Kutterolf S (2014) Major changes in the post-glacial evolution of magmatic compositions and pre-eruptive conditions at Llaima volcano, Andean Southern Volcanic Zone, Chile. Bull Volcanol 76:830. doi: 10.1007/s00445-014-0830-x

Schneider CA, Rasband WS, Eliceiri KW (2012) NIH image to ImageJ: 25 years of image analysis. Nat Methods 9:671–675

Shea T (2017) Bubble nucleation in magmas: A dominantly heterogeneous process? J Volcanol Geotherm Res 343:155–170. doi: 10.1016/j.jvolgeores.2017.06.025

Shea T, Hammer JE (2013) Kinetics of cooling- and decompression-induced crystallization in hydrous mafic-intermediate magmas. J Volcanol Geotherm Res 260:127–145. doi: 10.1016/j.jvolgeores.2013.04.018

Szramek L, Gardner JE, Larsen (2006) Degassing and microlite crystallization of basaltic andesite magma erupting at Arenal Volcano, Costa Rica. J Volcanol Geotherm Res 157:182–201. doi: 10.1016/j.jvolgeores.2006.03.039

Vona A, Romano C, Dingwell DB, Giordano D (2011) The rheology of crystal-bearing basaltic magmas from Stromboli and Etna. Geochim Cosmochim Acta 75:3214–3236. doi: 10.1016/j.gca.2011.03.031

Waters LE, Andrews BJ, Lange RA (2015) Rapid Crystallization of Plagioclase Phenocrysts in Silicic Melts during Fluid-saturated Ascent: Phase Equilibrium and Decompression Experiments. J Petrol 56:981–1006. doi: 10.1093/petrology/egv025

CHAPTER 4: SNGPLAG CALIBRATION AND CURACAUTÍN IGNIMBRITE CRYSTAL SIZE DISTRIBUTION MODELING

This chapter is a manuscript that is being submitted for publication in the journal Contributions to Mineralogy and Petrology.

4.1 Introduction

4.1.1 Investigating magma ascent rates

Eruption style is strongly affected by decompression rate (e.g., Eichelberger et al., 1986; Jaupart and Allegre, 1991; Burgisser and Gardner, 2005). As magmas ascend from depth, volatiles exsolve and crystals nucleate and grow in response to changes in pressure (P) and temperature (T). During rapid ascent, bubbles remain coupled to the magma resulting in explosive eruption (Eichelberger et al., 1986; Jaupart and Allegre, 1991). Conversely, during slow ascent, bubbles coalesce, resulting in sufficient permeability to degas the melt and thus removing the volatile primer necessary for explosivity and result in effusive eruption (Mangan and Sisson, 2000). Crystallization of microlites during decompression increases magma viscosity (Vona et al., 2011; La Spina et al., 2016; Vetere et al., 2021) and may act to either impede the ability of gas to decouple from the magma or enhance coalescence by pushing isolated vesicles together. As such, understanding the rate of magma decompression and therefore ascent rate is important for estimating eruption duration, intensity, and volcano hazards.

Several analytical and experimental methods exist for the investigation of magma decompression rate, each with their own strengths and weaknesses. Bubble and crystal textures provide a record of magma decompression or ascent path (Cashman and Marsh, 1988; Blundy and Cashman, 2008; Arzilli et al., 2019; Bamber et al., 2020; Marshall et al., 2022a; Valdivia et al., 2022), and thus rocks provide a valuable look into the subsurface evolution of a magma. Crystal size distributions (CSDs) of microlites can be used to approximate crystallization times when a crystal growth rate is assumed (Marsh, 1988; Cashman and Marsh, 1988; Murch and Cole, 2019; Bamber et al., 2020; Valdivia et al., 2022). Although CSDs can be easily measured and their slopes used for interpretation of changing ascent rates, the calculations may be skewed if post-fragmentation crystallization occurs. Additionally, CSDs assume a constant crystal growth rate. More robust investigations involve reproducing measured microlite textures by performing magma decompression experiments (Fig. 4.1), during which crystal textures evolve in response to an applied perturbation in P and/or T (Geschwind and Rutherford, 1995; Hammer and Rutherford, 2002; Hammer, 2004; Szramek et al., 2006; Castro and Dingwell, 2009; Andrews and Gardner, 2010; Brugger and Hammer, 2010; Shea and Hammer, 2013; Waters et al., 2015; Befus and Andrews, 2018). Decompression experiments are effective at approximating ascent rates by producing sufficient undercooling (ΔT) necessary to drive crystallization, but for the most part only produce time-averaged ascent rates that do not reflect possible changes in ascent rate as a magma nears the surface. Furthermore, conducting decompression experiments can be time-consuming, and their cost is subject to the fluctuating prices of the precious metals market. Mineral breakdown reaction rims (Rutherford and Hill, 1993; Browne and

Gardner, 2006) and compositional zoning (Waters et al., 2015) form in response to the pressure change imposed on a magma during ascent but are not always present on crystals. Melt embayments allow for diffusive modeling of elemental loss and thus ascent rates (Liu et al., 2007; Myers et al., 2016; Myers et al., 2018; Barth et al., 2019). Melt inclusions and embayments are, however, not perfect storage containers. Mineral fractures may result in leakage, and diffusion modeling cannot be conducted without knowledge of initial conditions and diffusive boundary conditions. Finally, geophysical observations can be used to monitor seismicity with depth in real time and allows researchers to track magma movement during an eruption (e.g., Moran et al., 2008; Thelen et al., 2008). Not all volcanoes, however, are equipped with extensive geophysical arrays that allow precision monitoring, and geophysical observations may not distinguish between different types of subsurface volcanic activity.

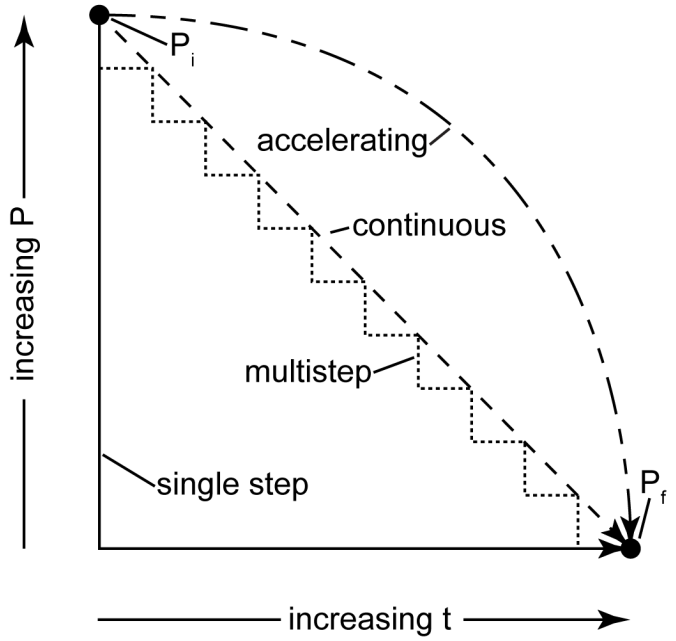

Figure 4.1. Schematic diagram of different decompression pathways. Single step experiments are subjected to a single perturbation in pressure and held at the new pressure until quenching (fragmentation). Continuous experiments undergo a continuous, uniform rate of decompression until quenching. Multistep experiments are subjected to different decompression events and pauses leading up to quenching. Accelerating experiments are subject to an increasing decompression rate over time. The crystal textures produced during decompression are quantified to compare with natural crystal textures to estimate natural decompression rates.

4.1.2 Existing numerical models for magma ascent rate

To circumvent some of the disadvantages of existing experimental and analytical methods for investigating ascent rates, numerical models exist that utilize observations easily collected from rocks. Toramaru (2006) developed a magma ascent rate meter as a function of bubble number density (BND) assuming a single homogeneous nucleation event and constant decompression. Although BNDs indeed reflect changes in volatile supersaturation and decompression, extensive coalescence, multiple nucleation events, highly tortuous bubble networks (e.g., Valdivia et al., 2022), or collapsed foam textures

are not representative of original BNDs and will skew ascent rate calculations. The model of Toramaru et al. (2008) uses microlite number densities (MND) to estimate ascent rates and only requires water and groundmass Si content at the point of microlite nucleation as additional inputs. However, as Murch and Cole (2019) point out, the model results of Toramaru et al. (2008) are highly influenced by the Si content input, and an error of only 5% in Si content can result in errors in ascent rate calculations as large as 500%. In addition, both models only produce time-averaged ascent rates rather than instantaneous rates over time, and therefore do not adequately model variable ascent rates such as occur in nature (e.g., Mastin and Ghiorso, 2000; Moran et al., 2008; Thelen et al., 2008).

4.1.3 SNGPlag

Supersaturation Nucleation and Growth of Plagioclase (SNGPlag) is an iterative forward model that calculates time-dependent plagioclase crystallization, the integral of nucleation and growth, within a constant magma composition for a specified pressure-temperature-time (*P*-*T*-*t*) path (Andrews and Befus, 2020). Comprehensive descriptions of the model can be found in Befus and Andrews (2018) and Andrews and Befus (2020) and are only summarized here. Specifically, the model tracks the numbers and sizes of plagioclase crystals within a 1 m^3 volume of magma. SNGPlag considers nucleation and growth as functions of plagioclase supersaturation ($\Delta\phi_{plag}$), defined as the difference between the equilibrium volume fraction of plagioclase as determined using MELTS (Gualda et al., 2012; Ghiorso and Gualda, 2015) and the modeled volume fraction. SNGPlag uses $\Delta\phi_{plag}$ rather than effective undercooling (ΔT_{eff}) as the former can be readily determined through time whereas ΔT_{eff} is only known at the onset of

decompression. Melt decompression and/or cooling act to increase $\Delta\phi_{plag}$. Nucleation and growth of plagioclase crystals in response to $\Delta\phi_{plag}$ drive the magma towards equilibrium, with the instantaneous nucleation and growth rates of plagioclase being functions of $\Delta\phi_{plag}$ (Befus and Andrews, 2018). SNGPlag allows nucleation and growth to be path-dependent and does not assume constant nucleation and growth rates (Andrews and Befus, 2020). SNGPlag can model multiple styles of decompression (e.g., linear, accelerating, paused) to investigate the style of decompression on plagioclase crystallization. In some scenarios, multiple decompression styles may be applied to the same experiment, such as a linear pathway that has a pause during decompression. While SNGPlag cannot provide a unique solution for natural samples, it can describe a limited range of likely decompression rates and paths (Andrews and Befus, 2020).

Previous versions of SNGPlag are calibrated for felsic compositions. Here, we extend the calibration of SNGPlag to include basaltic andesite compositions using the experimental results of Shea and Hammer (2013). We then apply an inverse implementation of SNGPlag to the 12.6 ka basaltic andesite Curacautín eruption of Llaima volcano, Chile (Marshall et al., 2022a; Valdivia et al., 2022) to estimate decompression rates necessary to generate ignimbrite-forming mafic eruptions. The results and application of our modeling can be applied to similar mafic volcanic centers to investigate the conditions that result in unusually explosive mafic eruptions.

4.1.4 The Curacautín eruption

The Curacautín eruption occurred at ca. 12.6 ka and resulted in the deposition of the extensive Curacautín ignimbrite (Ci) (Marshall et al., 2022a). The Ci is

a 4.0–4.5 km^3 (dense-rock equivalent) unconsolidated basaltic andesite ignimbrite exposed radially around Llaima that flowed up to 30 km from Llaima (Marshall et al., 2022a; Naranjo and Moreno, 2005), though others have mapped the Ci up to 100 km from source (Naranjo and Moreno, 1991). The Ci consists of four coarse ash to fine lapilli tuff flow units (Fig. 4.2) (Marshall et al., 2022a). Recent work by Marshall et al. (2022a) and Valdivia et al. (2022) suggests the Ci is the result of fragmentation of a rapidly ascending, non-degassed magma at a low fragmentation threshold. There is no evidence to suggest the explosivity of the Ci eruption was driven by magma-water interaction, though some evidence exists for localized phreatic activity (Marshall et al., 2022a, 2022b).

4.2 Methods

4.2.1 Calibration of SNGPlag for basaltic andesite compositions

Previously published versions of SNGPlag (Befus and Andrews, 2018; Andrews and Befus, 2020) use nucleation and growth rates determined experimentally for the 1991 Pinatubo dacite magma with a rhyolitic melt composition. Application of SNGPlag to the Curacautín eruption necessitates acquiring plagioclase nucleation (N_{plag}) and growth rates (G_{plag}) for a basaltic andesite magma. We used the results of single step decompression experiments conducted by Shea and Hammer (2013) on the Mascota basaltic andesite. Their study includes 11 experimental runs (Table 4.1) with P, T, H_2O, and compositional conditions reasonable for the Curacautín eruption (Lohmar, 2008; Schindlbeck et al., 2014). Importantly, they report the plagioclase crystallinities, maximum lengths, and

volumetric number densities for all runs, thereby enabling calculation of nucleation and growth rates.

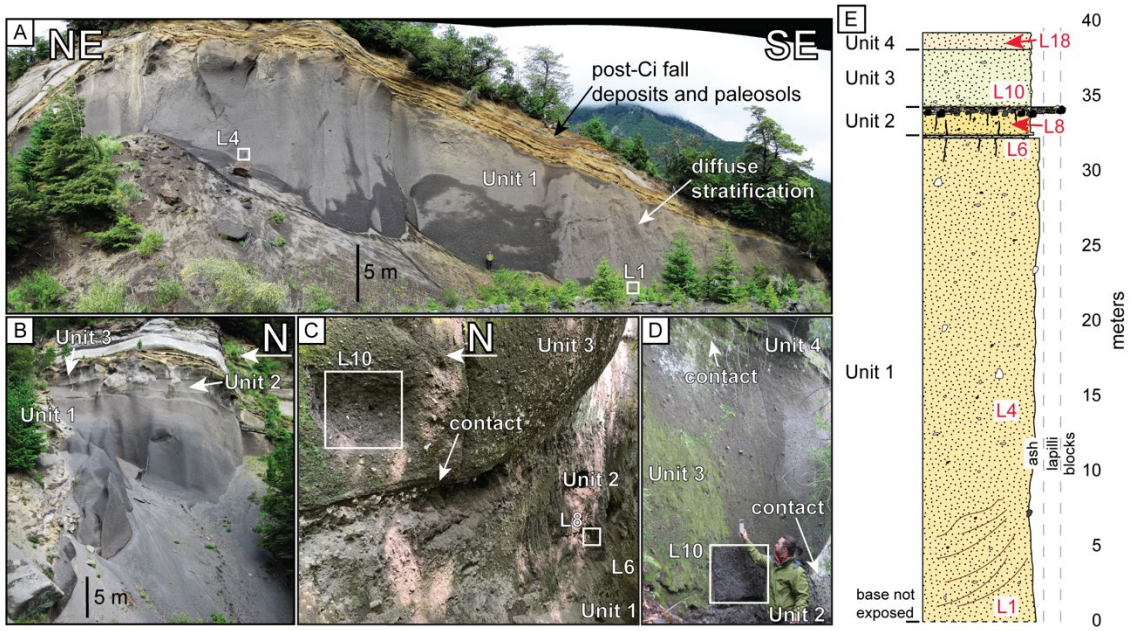

Figure 4.2. Curacautín flow units and eastern stratigraphy from Marshall et al. (2022a). Samples used for SNGPlag calibration and modeling come from these exposures. (A) Unit 1 where samples L1 and L4 were collected. (B) The contact between Units 1, 2, and 3 where samples. (C) Contacts between Units 1, 2, and 3 where samples L6, L8, and L10 were collected. (D) Contacts between Units 2, 3, and 4 where L8, L10, and L18 were collected. (E) The most complete section of Ci stratigraphy measured across the eastern outcrops in A, B, C, and D. Sample locations are provided. Sample locations in the stratigraphic column are in red.

Table 4.1 Experimental conditions of Shea and Hammer (2013) used for SNGPlag calibration. Initial pressure, P_i, for all runs was 150 MPa and all runs were isothermal, with T_i=T_f=1025 °C. ΔT_{eff} is reported as the initial plagioclase supersaturation immediately after decompression. Note that only two experiments were conducted to P_f<42 MPa.

Experiment	P_f (MPa)	t (hr)	ΔT_{eff} (°C)
SSD_52-12	100	12	52
SSD_82-12	65	12	82
SSD_112-12	42	12	112
SSD_52-24	100	24	52
SSD_82-24	65	24	82
SSD_112-24	42	24	112
SSD_52-48	100	48	52
SSD_82-48	65	48	82
SSD_112-48	42	48	112
SSD_137-48	22	48	137
SSD_155-48	10	48	155

4.2.2 Determination of instantaneous nucleation and growth rates of plagioclase

We adapted the existing SNGPlag code written in MATLAB to find N_{plag} and G_{plag} that best fit the experimental observations of Shea and Hammer (2013). Briefly, we assume that the N_{plag} and G_{plag} have functional forms that can be described as log-normal functions of $\Delta\phi_{plag}$; this functional form is used as variation of four different parameters can change the functional shape to virtually any arbitrary form (Befus and Andrews, 2018). We find the best fit for N_{plag} and G_{plag} by running SNGPlag for the known decompression experiments of Shea and Hammer (2013) across an 8-dimensional space (four dimensions for both N_{plag} and G_{plag}). This results in 100,000 possible combinations of N_{plag} and G_{plag}. N_{plag} and G_{plag} were modeled using the R2 high performance computing cluster at Boise State University. The best fit N_{plag} and G_{plag} are those that best recover the observed results of Shea and Hammer (2013). Run parameters were taken

from Shea and Hammer (2013) with each single-step run discretized into 2,500 *P-T-t* steps. N_{plag} and G_{plag} are calculated at each step as functions of $\Delta\phi_{plag}$ with the form

$$\frac{k}{x\sqrt{2\pi}} exp^{-\frac{(\ln x-\mu)^2}{2\sigma^2}}$$

Eq. 1

where $x=bexp^{1}\Delta\phi_{plag}$, $\Delta\phi_{plag}$= plagioclase supersaturation, and μ, σ, b, and k are fit parameters that describe the specific shape of curves that represent the mean, standard deviation, scaling with respect to $\Delta\phi_{plag}$, and its maximum value (Befus and Andrews 2018). The input ranges and best fit calibration parameters for N_{plag} and G_{plag} are provided in Table 4.2. Values for μ, σ, and k were randomly sampled from a selected range (Table 4.2). For our calibration, b was set to 1. SNGPlag accounts for volume interferences ϕ_{int} between crystals for a randomly distributed population of crystals by

$$\phi_{int} = 0.5(\phi_{app})^2$$

Eq. 2

where ϕ_{app} is the apparent crystallinity, which is the sum of all crystal sizes and numbers calculated at each step divided by the system volume (1 m^3). From this, we obtain the equation

$$\phi_{plag} = \phi_{app} - \phi_{int}$$

Eq. 3

where plagioclase crystallinity ϕ_{plag} is reported with overlapping crystals removed (Andrews and Befus, 2020). Finally, uncertainty in N_V and σ_{Nv} is determined by

$$\sigma_{N_V} = (SnN_V)^{-0.5}$$

Eq. 4

where *Sn* is the characteristic crystal size in a 1 mm^2 area (Andrews and Befus, 2020). Optimum values for G_{plag} and N_{plag} were determined using least squares optimization of the calibration data (Table 4.2).

During each step of SNGPlag, existing plagioclase grow, and new plagioclase nucleate based upon G_{plag}, N_{plag}, and $\Delta\phi_{plag}$. SNGPlag produces a plagioclase crystal number and size matrix that is binned and converted into cumulative CSDs. Because SNGPlag calculates volumetric number densities and size distributions by nucleating and growing plagioclase in a 1-m^3 model volume, we avoid the error that stereological conversions of 2D data produces. We chose to use a 1-m^3 model volume to effectively eliminate rounding errors and discrepancies that can occur in smaller volumes with less crystals.

Table 4.2 Plagioclase nucleation (N_{plag}) and growth (G_{plag}) rate calculation parameters. μ, σ, and b are fitting parameters with no units. k has units of m^{-3} s^{-1} for N_{plag} and um s^{-1} for G_{plag}.

Variable	N_{plag} range	optimum N_{plag}	G_{plag} range	optimum G_{plag}
μ	0.1–1.5	0.5398	0.1–1.5	0.5290
σ	0.5–2	0.5970	0.5–2	0.8770
b	1	1	1	1
k	10^9–10^{13}	6.0677×10^9	10^{-10}–10^{-5}	2.2003×10^{-8}

4.2.3 Modeling conditions

Modeling the Ci CSDs using the best fit N_{plag} and G_{plag} rates, requires realistic or plausible values for P_i, P_f, T, dP/dt, and volume fraction phenocrysts. Schindlbeck et al. (2014) calculated Ci crystallization temperatures of ~1,110±45 °C using the olivine- and clinopyroxene-liquid thermobarometer of Putirka (2008), water content of 1.4±0.32% using the plagioclase hygrometer of Lange et al. (2009), and storage pressures between

400 and 600 MPa corresponding to depths of up to 18 km, though work by Lohmar (2008) suggests that crystallization occurred at ≤7 km. Marshall et al. (2022a) measured phenocryst content of Curacautín pyroclasts from <1% to ~3.5%, and Lohmar (2008) measured up to 7% phenocrysts. Valdivia et al. (2022) estimated *dP/dT* for the Ci from 0.36 to 2.6 MPa s^{-1} using the bubble number density decompression rate meter of Toramaru (2006). Finally, experiments by Arzilli et al. (2019) found the conditions required for basaltic magmas to erupt as high explosivity events are temperatures <1100 °C, syn-eruptive crystal content ≥30%, and melt viscosities of 10^5 Pa s.

Our modeling consisted of 100,000 simulations with initial and final conditions selected in a random Monte Carlo scheme from a range of defined inputs (Table 4.3). We conducted experiments with P_i between 110 and 150 MPa based on a chamber depth of ~18 km (Schindlbeck et al., 2014). Starting phenocryst content was 5 vol. %. P_f was set to 10–40 MPa. All simulations were run at T=950–1050 °C; T_i and T_f were allowed to vary independently. We used average *dP/dt* of 1–1000 MPa hr^{-1} (0.0003–0.3 MPa s^{-1}). 40% of runs were linear decompressions, 30% accelerating, and 30% were two-step decompressions, whereby there was a pause following initial linear decompression and subsequent post-pause decompression was either linear or accelerating. A subset of experiments was declared to "fragment" at a pressure P_{frag} of 20–80 MPa during the simulations; these runs had *dP/dt* of 1–20 MPa hr^{-1} prior to fragmentation and increased to 30–400 MPa hr^{-1} following fragmentation. Runs that fragmented experienced cooling ΔT_{frag} of up to 60 °C, the upper bound suggested by Mastin and Ghiorso (2001) for adiabatic cooling of an erupting mixture of gas and ash.

4.2.4 Comparison of natural and modeled CSDs

In natural cumulative CSDs, we know the number of plagioclase crystals that are larger than each size bin. Using counting statistics, we can convert that size relationship into an uncertainty bound (σ_{CSD}) at each size, $\sigma_{CSD} = \sqrt{n_{bin}}$, where n_{bin} is the number of microlite counts per size bin. The upper and lower bounds then define an envelope for natural CSDs (Fig. 4.3). Therefore, with higher n_{bin}, our uncertainty becomes smaller. Our modeled CSDs therefore have an effective uncertainty of zero as the number of crystals that compose each size bin is in the billions. This is not to say the modeling here is perfect, but rather that uncertainty is orders of magnitude greater in measurements of the natural samples.

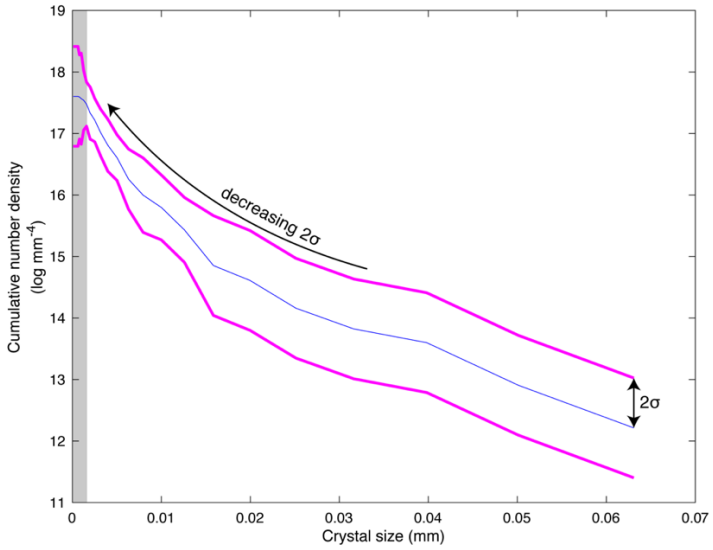

Figure 4.3. Example of how uncertainty is shown on our crystal size distribution (CSD) model runs (Appendix A). The blue line is the natural cumulative CSD and the pink lines are the 2σ error bounds calculated for each bin. Notice how 2σ decreases with smaller microlite sizes. This is a result of the higher number of microlites counted in the natural samples at these size ranges. The increase in 2σ near the y-intercept (gray field) results from a relative decrease in the number of smallest crystals counted in 2D measurements of the natural sample (Fig. 3.4) (Valdivia et al., 2022).

4.2.5 Modeling limitations

The experiments of Shea and Hammer (2013) were mostly quenched at higher pressures, with only two experiments decompressed to P_f of 22 and 10 MPa and ΔT>113 °C (Table 4.1). Those two experiments produced the highest plagioclase crystallinities of 34.8% and 46.1%, respectively. However, no experiments have been conducted at conditions where the melt viscosity should be highest. As such, our N_{plag} and G_{plag} for very high $\Delta\phi_{plag}$ are extrapolated, although we note that any decompression path other than single-step will have some crystallization prior to reaching lower P, and thus have a lower $\Delta\phi_{plag}$ than a single step run initially has at the same pressure. SNGPlag does not consider any unique conduit geometries or eruption style (e.g., dike geometry, ring faulting during eruption) that may impact late decompression or ascent dynamics. Shearing along conduit margins is not considered in this version of SNGPlag but has been shown to impact crystallization (Vetere et al., 2021). Finally, the only volatile species considered in our modeling is H_2O, although the presence of CO_2 or another volatile species should only affect the crystallization of plagioclase insofar as it reduces the partial pressure of H_2O.

Table 4.3 Parameters used for SNGPlag modeling for the Curacautín magma.

Parameter	Symbol	Values	Units
Initial pressure	P_i	110–150	MPa
Final pressure	P_f	10–50	MPa
Starting temperature	$T=T_i=T_f$	1000–1050	°C
Final temperature	$T=T_i=T_f$	1000–1050	°C
Decompression rate	dP/dt	5–250	MPa hr^{-1}
Pause depth	P_p	40–120	MPa
Pause duration	t	0.1–10	hr
Pre-pause decompression	dP/dt_{pre}	5–100	MPa hr^{-1}
Post-pause decompression	dP/dt_{post}	50–750	MPa hr^{-1}
Fragmentation level	P_{frag}	20–60	MPa
Phenocryst content		5	vol. %

4.3 Results

4.3.1 Instantaneous nucleation and growth rates of plagioclase

Instantaneous N_{plag} and G_{plag} curves have similar geometries (Fig. 4.4). The maximum N_{plag} of 6.1×10^5 cm^{-3} hr^{-1} is reached at $\Delta\phi_{plag}$=44 vol. %. The maximum G_{plag} of 27.4 μm hr^{-1} is reached at $\Delta\phi_{plag}$=29 vol. %. There is very little N_{plag} activity at $\Delta\phi_{plag}$<10%, but the G_{plag} of these early crystals is quite high. N_{plag} and G_{plag} beyond maximum $\Delta\phi_{plag}$ are extrapolated and may not be representative of nature.

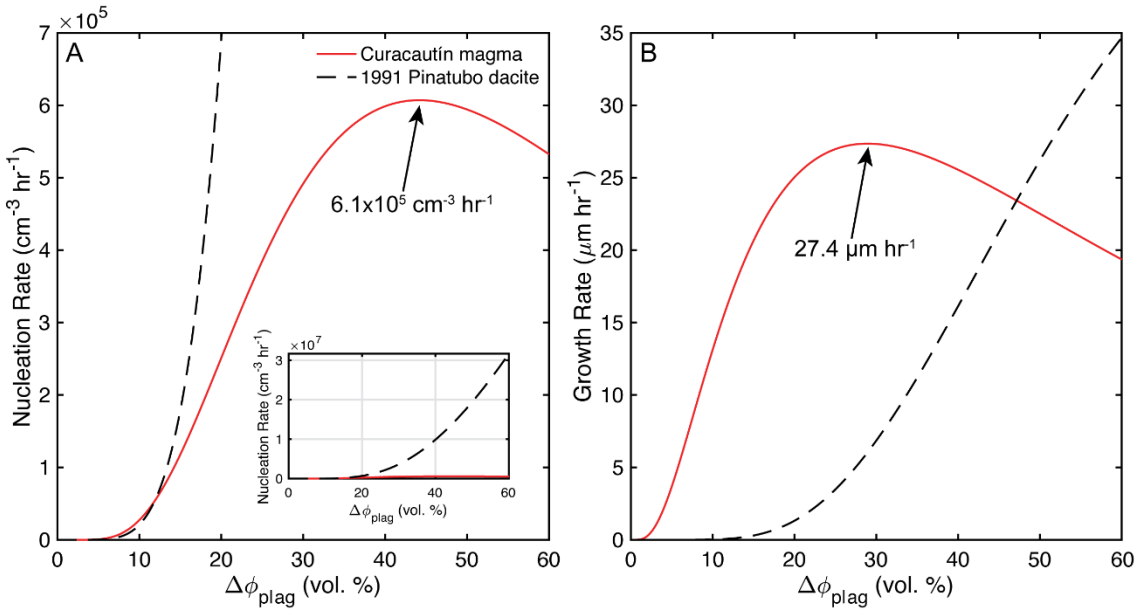

Figure 4.4. Modeled plagioclase nucleation (A) and growth (B) rate curves as a function of plagioclases supersaturation ($\Delta\phi_{plag}$) for the 12.6 ka basaltic andesite Curacautín eruption and the 1991 Pinatubo dacite eruption (Befus and Andrews, 2018). Inset of (A) is the demagnified Curacautín nucleation curve. Maximum nucleation and growth rates for the Curacautín magma are labeled on the plots.

4.3.2 Model results

The large parameter space over which we modeled the Curacautín eruption includes many runs that are physically unrealistic; we applied filters to remove those results. Our filters identified runs that begin and end >10 °C above the plagioclase liquidus and removes them. This reduced the number of model runs from 100,000 to 13,283 (Table 4.4). Because our decompression rates vary in an exponential fashion, it is not appropriate to compare them in linear space, so we report our average decompression rates as $\log_2$ values. For example, three decompression rates of 1, 9, and 80 MPa hr^{-1} would yield a linear average rate of 30 MPa hr^{-1}, but a more representative average rate is obtained in log space and yields 9 MPa hr^{-1}.

Average Unit 1 *dP/dt* are 53–93 MPa hr^{-1} for L1, 46–89 MPa hr^{-1} for L4, and 87–95 MPa hr^{-1} for L6 (Fig. 4.5). Average Unit 2 *dP/dt* are 62–93 MPa hr^{-1} (L8). Average Unit 3 *dP/dt* are the slowest at 6–55 MPa hr^{-1} (L10). Conversely, average Unit 4 *dP/dt* are the fastest at 104–141 MPa hr^{-1} (L18) (Table 4.4). Unit 1 average durations of decompression t_{avg} are between 1.40–4.08 hr for L1, 2.40–4.69 hr for L4, and 1.79–1.96 hr for L6. Unit 2 t_{avg} are between 1.69–2.02 hr (L8). Unit 3 t_{avg} are between 3.56–16.13 hr (L10). Unit 4 t_{avg} are between 0.87–0.96 hr (L18) (Table 4.4).

Table 4.4 Summary of 150,000 SNGPlag results. Three images for each sample were modeled. For each model run, SNGPlag generates a series of fits to the natural crystal size distributions (CDSs), denoted below as CSD fit. Fit f1 corresponds to the model runs that best fit the natural CSDs bins within 2σ (out of 31 total bins). Fit f2 is the second best fit and is determined by removing one bin from the total bins that fit. Fit f3 removes one additional bin.

sample	L1			L4			L6			L8			L10			L18		
unit	1									2			3			4		
Runs with Pi=110–150 MPA and Pf=10–50 MPa (n=100,000)																		
CSD fit	f1	f2	f3	f1	f2	f3	f1	f2	f3	f1	f2	f3	f1	f2	f3	f1	f2	f3
CSD bins	18/31	17/31	16/31	17/31	16/31	15/31	21/31	20/31	19/31	21/31	20/31	19/31	15/31	14/31	13/31	20/31	19/31	18/31
n	21	155	850	92	1,297	7,072	23	69	128	4	42	108	2	7	3,364	2	8	39
log2 dP/dtavg (1σ) (MPa hr-1)	6.31 (0.90)	6.11 (1.18)	5.09 (1.37)	5.93 (1.38)	5.09 (1.37)	4.90 (1.33)	6.06 (1.08)	6.15 (1.22)	6.09 (1.23)	5.82 (0.74)	6.01 (1.17)	6.08 (1.26)	2.69 (0.09)	3.55 (1.45)	5.29 (1.25)	6.69 (0.10)	6.86 (0.69)	6.89 (0.96)
median dP/dt (MPa hr-1)	90	77	32	65	35	29	64	80	77	59	65	81	6	7	41	104	110	151
range of dP/dt (MPa hr-1)	20–185	8–243	5–250	7–250	5–250	5–250	14–229	11–229	11–231	29–100	11–231	11–231	6–7	6–53	5–250	99–109	50–206	14–244

tavg (1σ) (hr)	1.40 (0.98)	1.88 (1.78)	4.08 (3.45)	2.40 (2.62)	4.26 (4.04)	4.69 (3.99)	1.79 (1.49)	1.92 (1.94)	1.96 (1.91)	1.69 (0.68)	1.95 (1.82)	2.02 (1.99)	16.13 (0.29)	11.22 (6.65)	3.56 (3.51)	0.87 (0.25)	0.89 (0.62)	0.96 (0.96)
Piavg (1σ) (MPa)	120.95 (7.24)	120.82 (7.00)	123.85 (9.34)	121.32 (7.52)	125.27 (9.66)	125.38 (10.18)	119.02 (5.88)	119.00 (5.32)	119.24 (5.80)	126.80 (9.95)	120.31 (6.90)	119.76 (6.10)	130.38 (13.34)	124.52 (9.41)	125.11 (10.36)	118.46 (2.73)	118.75 (4.81)	119.67 (5.68)
Pfavg (1σ) (MPa)	27.89 (10.44)	27.79 (11.28)	28.47 (11.38)	28.07 (11.00)	28.43 (11.39)	28.44 (11.46)	27.46 (12.49)	27.42 (12.68)	27.47 (12.02)	36.22 (13.04)	29.39 (11.82)	28.88 (12.02)	25.77 (21.86)	28.31 (11.92)	29.41 (11.64)	28.99 (22.33)	30.66 (11.78)	31.07 (11.53)
Runs with Pi=15–30 MPA and Pf=3–10 MPa (n=50,000)																		
CSD fit	f1	f2	f3	f1	f2	f3	f1	f2	f3	f1	f2	f3	f1	f2	f3	f1	f2	f3
CSD bins	18/31	17/31	16/31	17/31	16/31	15/31	21/31	20/31	19/31	20/31	19/31	18/31	14/31	13/31	12/31	20/31	19/31	18/31
n	19	188	586	51	1,252	6,665	29	82	155	55	168	291	4	8,607	19,364	22	46	127
log2 dP/dtavg (1σ) (MPa hr-1)	4.20 (1.02)	5.24 (1.42)	4.73 (1.64)	4.53 (1.25)	4.49 (1.68)	4.33 (1.58)	4.94 (1.29)	5.08 (1.45)	5.34 (1.46)	5.57 (1.47)	5.51 (1.40)	5.46 (1.39)	2.86 (0.49)	5.08 (1.64)	5.20 (1.53)	6.00 (0.86)	5.85 (1.09)	5.86 (1.24)
median dP/dt (MPa hr-1)	19	37	24	24	16	14	26	33	37	49	48	47	7	31	38	68	62	61

range of dP/dt (MPa hr-1)	6–94	6–245	5–246	5–163	5–254	5–316	7–181	5–211	5–242	7–234	5–245	5–247	5–11	5–344	5–344	19–211	11–211	6–245
tavg (1σ) (hr)	1.09 (0.64)	0.67 (0.64)	1.17 (1.15)	1.14 (1.04)	1.29 (1.07)	1.33 (1.06)	0.78 (0.63)	0.77 (0.82)	0.71 (0.76)	0.53 (0.57)	0.59 (0.71)	0.59 (0.68)	2.71 (1.16)	0.83 (0.86)	0.73 (0.80)	0.23 (0.11)	0.34 (0.31)	0.42 (0.49)
Piavg (1σ) (MPa)	23.02 (3.45)	22.89 (3.99)	23.91 (4.05)	24.56 (3.88)	23.56 (4.22)	23.37 (4.27)	23.37 (3.64)	22.89 (4.03)	22.98 (3.93)	21.96 (4.21)	22.92 (4.07)	22.83 (4.03)	25.44 (3.85)	22.45 (4.39)	22.25 (4.44)	20.96 (4.29)	22.27 (4.64)	22.88 (4.23)
Pfavg (1σ) (MPa)	6.06 (1.98)	6.40 (1.99)	6.35 (2.00)	6.13 (2.03)	6.31 (1.98)	6.35 (2.01)	6.20 (1.93)	6.39 (2.10)	6.23 (2.01)	6.13 (1.90)	6.44 (2.01)	6.47 (2.02)	7.18 (2.58)	6.48 (2.01)	6.49 (2.02)	7.05 (1.99)	6.78 (1.88)	6.67 (1.97)

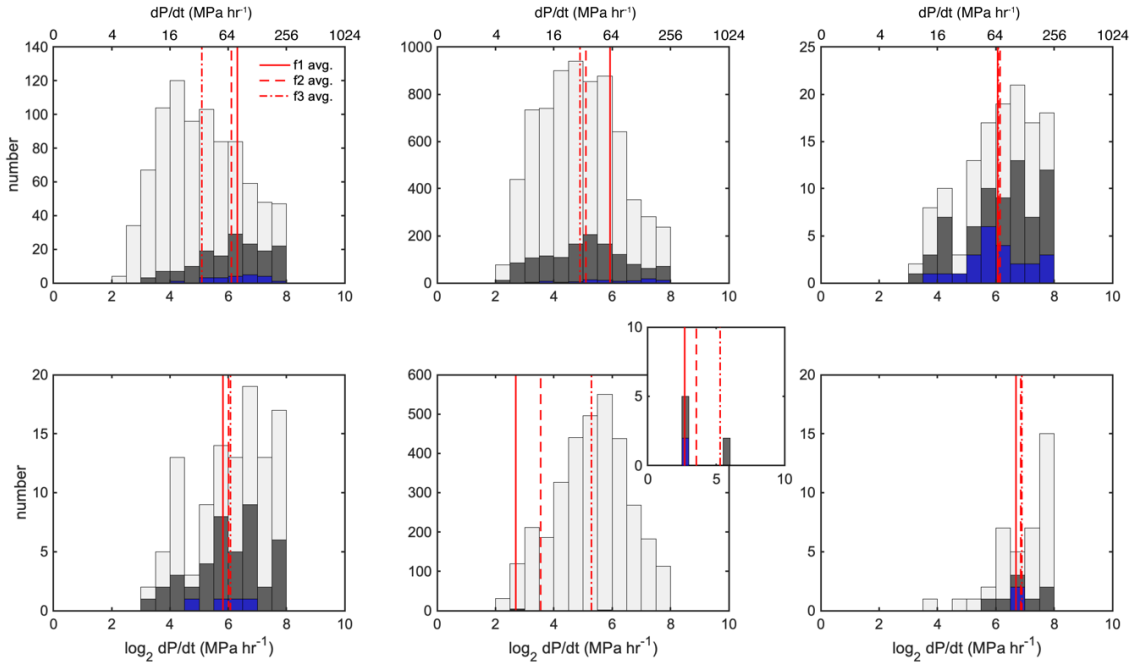

Figure 4.5. Histograms of Ci decompression rates plotted in linear space (top y-axis) and log2 space (bottom y axis) modeled using SNGPlag. Blue bars are f1 fits, dark gray are f2 fits, and light gray are f3 fits (see description in body text). Averages are shown as red lines. A) L1. B) L4. C) L3. D) L8. E) L10. Inset is zoomed in to f1 and f2 fits. Inset axes units are the same as the large plots. F) L18.

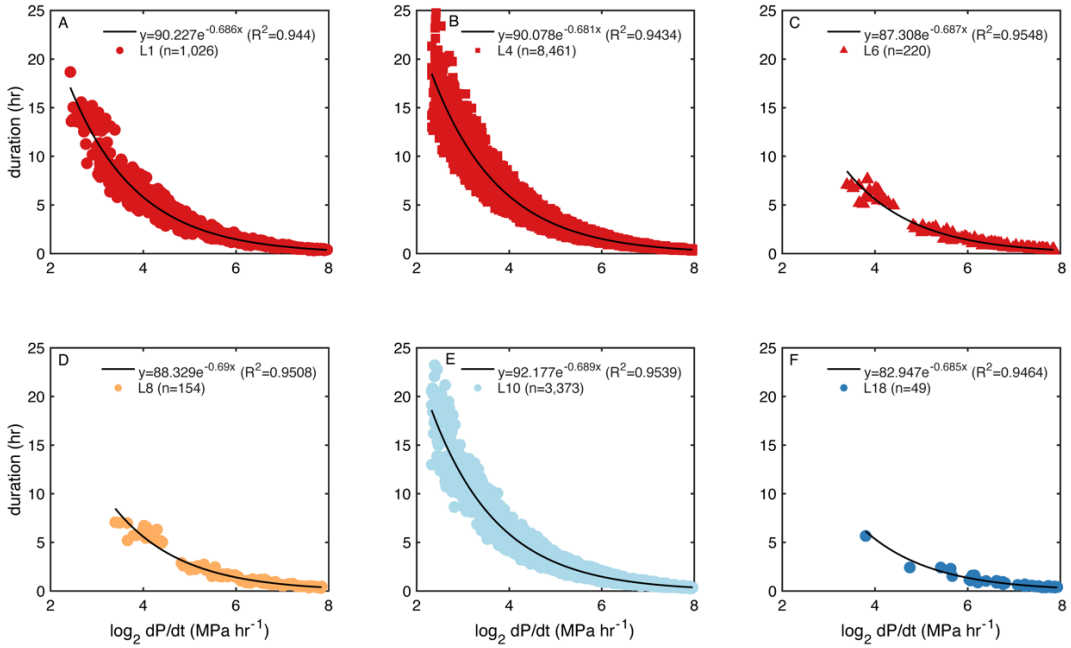

Figure 4.6. Plots of filtered log2 *dP/dt* (MPa hr^{-1}) versus duration of decompression (hr). (A) L1. (B) L4. (C) L6. (D) L8. (E) L10. (F) L18.

4.4 Discussion

4.4.1 Plagioclase nucleation and growth rates

N_{plag} and G_{plag} curves (Fig. 4.4) for the basaltic andesite Curacautín magma have similar shapes, but very different magnitudes, in comparison to those determined for the 1991 Pinatubo dacite (Befus and Andrews, 2018). The Curacautín magma reaches a maximum N_{plag}=6.1×10^5 cm^{-3} hr^{-1} at $\Delta\phi_{plag}$=44 vol. % which is an order of magnitude lower than the Pinatubo dacite at the same $\Delta\phi_{plag}$ (Fig. 4.4A). Conversely, the maximum Curacautín G_{plag} of 27.4 μm hr^{-1} is reached at $\Delta\phi_{plag}$=29 vol. %, whereas the 1991 Pinatubo G_{plag} for the same $\Delta\phi_{plag}$ is 6.0 μm hr^{-1} and does not reach 27.4 μm hr^{-1} until $\Delta\phi_{plag}\cong$52 vol. % (Fig. 4.4B). Indeed, G_{plag} is more than an order of magnitude higher in the mafic composition for $\Delta\phi_{plag}\lesssim$25%. Our modeled N_{plag} and G_{plag} suggest that although plagioclase nucleates more than an order of magnitude slower in basaltic andesites than in dacites at similar $\Delta\phi_{plag}$ the growth rate G_{plag} in the mafic composition is generally an order of magnitude faster. Significantly, the difference in volumetric growth rate is ~1000 times greater in the basaltic andesite (the linear growth rate G_{plag} raised to the third power). That is, a smaller number of crystals are able to more rapidly grow and thus reduce $\Delta\phi_{plag}$ in the mafic magma as compared to more silicic magmas. This explains the predominance of acicular plagioclase microlites commonly observed in the pyroclasts of mafic explosive eruptions (Constantini et al., 2010; Arzilli et al., 2019; Bamber et al., 2020; Rowe et al., 2021; Marshall et al., 2022a).

4.4.2 Decompression rates

Natural plagioclase CSDs for the Ci are concave upward at the finest size bins (Valdivia et al., 2022). Valdivia et al. (2022) divided Ci CSDs into two segments based on linear regression fitting. Using experimentally derived growth rates of 10^{-4} mm s^{-1} (Arzilli et al., 2019), 2×10^{-5} mm s^{-1} (Arzilli et al., 2015), 10^{-6} mm s^{-1} (Shea and Hammer, 2013), and 10^{-7} mm s^{-1} (Arzilli et al., 2015), they calculated timescales of crystallization from 2 s to 1.2 hr for the smallest size fraction of plagioclase microlites in CSDs, and 8 s to 5.0 hr for the largest size fraction. Here, we use cumulative natural CSDs for fitting to our modeled CSDs (Appendix A) to remove downturns at the smallest size fractions observed by Valdivia et al. (2022).

Using the 1% population of isolated Ci vesicles, Valdivia et al. (2022) calculated average *dP/dt* for the Ci magma of 0.84–1.95 MPa s^{-1} for Unit 1, 0.36 MPa s^{-1} for Unit 2, 2.60 MPa s^{-1} for Unit 3, and 0.55 MPa s^{-1} for Unit 4 using the BND meter of Toramaru (2006), with a minimum average *dP/dt* for the Curacautín eruption of 1.4 MPa s^{-1}. Our average modeled *dP/dt* rates (0.18×10^{-2}–3.9×10^{-2} MPa s^{-1}) are approximately two orders of magnitude slower than the rates calculated by Valdivia et al. (2022) (Fig. 4.7, Table 4.4). The bubble textures investigated by Valdivia et al. (2022) represent two distinct phases of Curacautín magma evolution. The highly tortuous vesicle network of >99% pore volume is indicative of relatively slow ascent (e.g., Marshall et al., 2022b), whereas the small, isolated vesicles likely formed during an episode of homogeneous nucleation very late in ascent or syn-eruptively at low pressures (Mangan and Sisson, 2000) where *dP/dt* are greatest. Conversely, our average *dP/dt* modeled with SNGPlag represent pressures from 10–150 MPa where rates of decompression begin slow and increase over

time (Appendix A). Together, our work and that of Valdivia et al. (2022), suggests that decompression (and therefore ascent) rates increase by up to two orders of magnitude at the shallowest conduit depths (Fig. 4.7).

The low water content of the Ci melt (1.1±0.32%; Schindlbeck et al., 2014) suggests storage at shallower depths, or water undersaturation. We conducted a second, smaller set of experiments (n=50,000) at P_i=15–30 MPa and P_f=3–10 MPa to investigate crystallization over a shorter decompression window to shallower depths. Average *dP/dt* for Unit 1 are 24–59 MPa hr^{-1} (L1), 34–46 MPa hr^{-1} (L4), and 46–61 MPa hr^{-1} (L6). Unit 2 *dP/dt* are 66–75 MPa hr^{-1}. Unit 3 average *dP/dt* are 8–61 MPa hr^{-1}. Finally, average Unit 4 *dP/dt* are 74–80 MPa hr^{-1}. These rates tend to be slower than those modeled for deeper chamber conditions but are generally within the same order of magnitude (Table 4.4). Because Schindlbeck et al. (2014) estimated a chamber depth of ~18 km for the Curacautín magma, the *dP/dt* calculated with P_i up to 150 MPa are likely a more reasonable approximation of Curacautín decompression (Fig. 4.7).

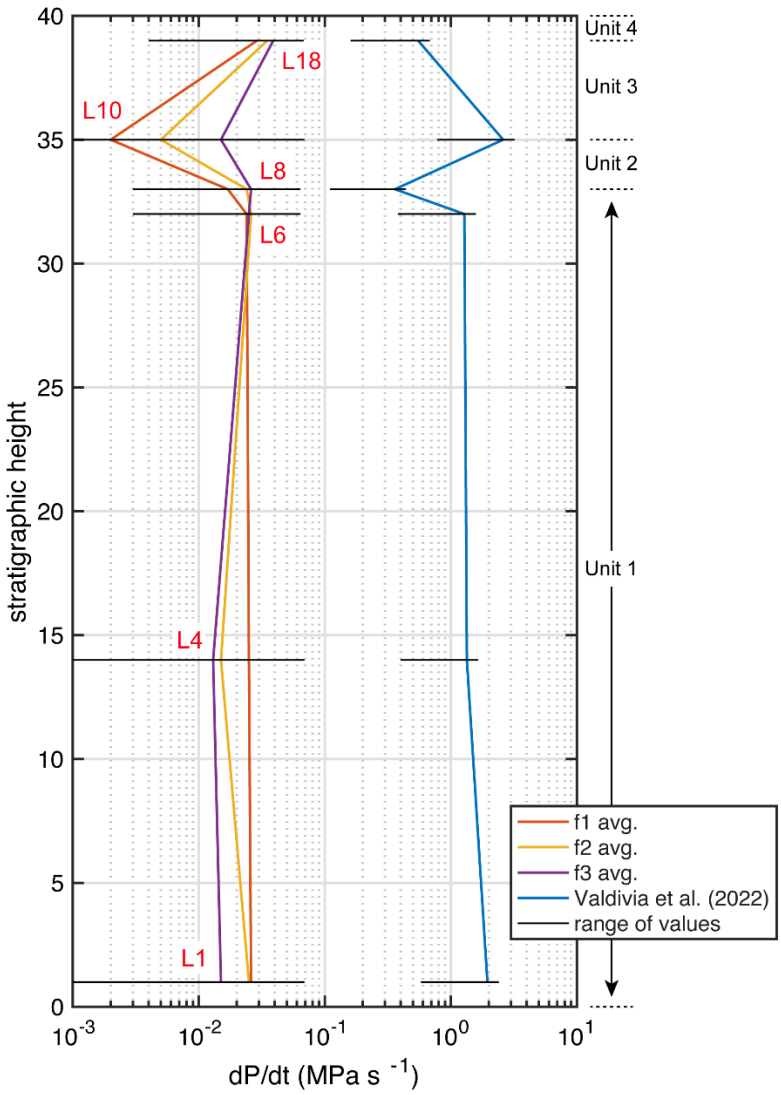

Figure 4.7. Curacautín ignimbrite (Ci) decompression rates (*dP/dt*) modeled using SNGPlag plotted with respect to Ci stratigraphy (m) (Marshall et al., 2022a) along with the *dP/dt* calculated by Valdivia et al. (2022) from x-ray computed microtomography 3D renderings and using the bubble number density rate meter of Toramaru (2006). Sample names are provided in red and associated units are plotted along the right y-axis. SNGPlag curves are provided for all three crystal size distribution fits (see explanation in Table 4.3). *dP/dt* results from this study are those from the 100,000 model run (Table 4.4).

The *dP/dt* modeled here for the Curacautín magma are similar to *dP/dt* calculated or estimated for other mafic eruptions using decompression experiments and diffusion modeling, but are orders of magnitude lower than mafic *dP/dt* calculated from bubble textures (Fig. 4.8). Homogeneous bubble nucleation events create densely packed

networks of bubbles at very shallow depths where rates of *dP/dt* are highest (Mangan and Sisson, 2000), and thus *dP/dt* determined from bubble textures may only reflect very shallow ascent conditions and not be representative of conditions from deeper in the conduit. Conversely, our modeling here reflects ascent rates integrated over the entire conduit and not just the shallowest depths and likely records more of the decompression history, albeit perhaps not the final, shallowest portions.

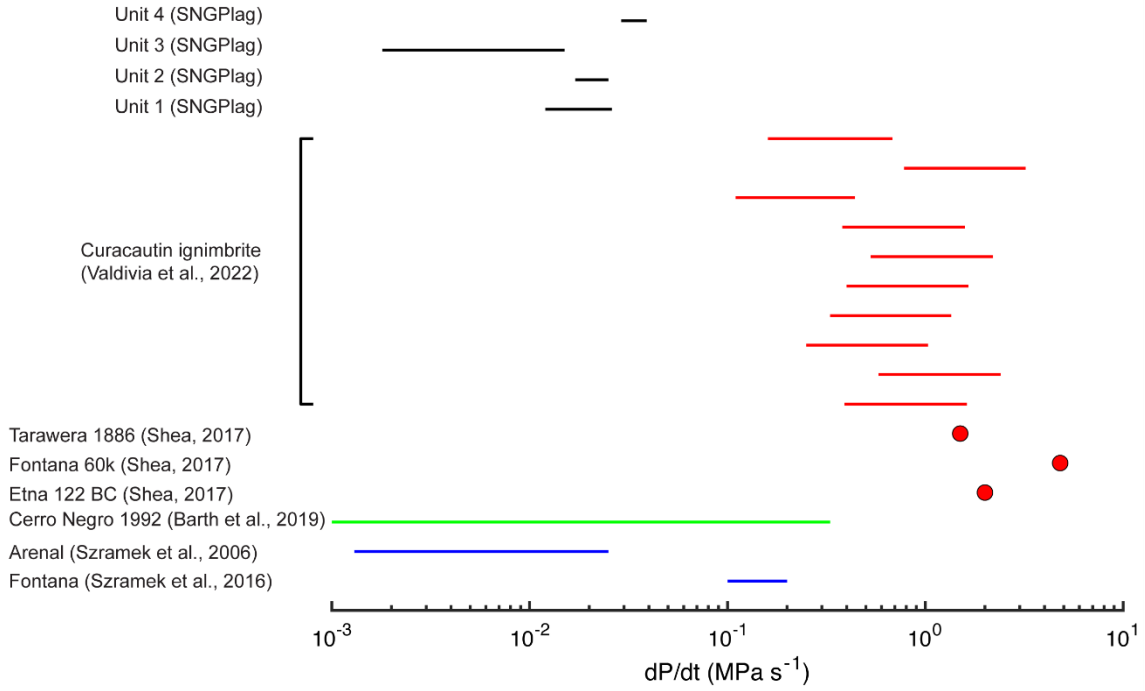

Figure 4.8. The range of decompression rates (*dP/dt*) for mafic magmas estimated using different methods. Blue = decompression experiments. Green = diffusion modeling. Red = bubble number density (BND). Black = SNGPlag. SNGplag modeling has the most overlap with decompression experiments and diffusion modeling. The similarity of our modeled *dP/dt* to decompression experiments is likely due to the way SNGPlag is calibrated using Shea and Hammer (2013) data. *dP/dt* calculated using BND data are consistently orders of magnitude higher. This may be a function of using bubbles from homogeneous nucleation events which occur at very shallow depths and reflect moments of very high *dP/dt* (Mangan and Sisson, 2000).

4.4.3 Magma ascent rates

Decompression rates do not have the same relationship to ascent rate at all volcanoes. This results from differences in lithostatic or magmastatic pressure gradients at different volcanoes, which is impacted by factors such as crustal thickness, country rock compositions and densities, conduit geometry, and elevation. In addition, particular decompression speedometers may be sensitive to the partial pressure of a particular volatile species, not total pressure (P_{total}); SNGPlag is sensitive to P_{H2O}, which is less than P_{total} when the system is water undersaturated or saturated with a mixed volatile phase. Here, we consider two simplified scenarios to derive first order estimates of magma ascent rate from our modeled decompression rates, and then compare those rates with a calculated lithostatic pressure gradient (*dP/dz*) for the crust beneath Llaima.

Our first estimate assumes that $P_{H2O}=P_{total}$ and that there is no other volatile species in our system. This of course is an oversimplification as there would be some amount of P_{CO2} present as well as others volatile species in minor concentrations. If we also assume that a *dP/dz* =90 MPa per every 4 km is reasonable for a mix of mafic lavas and granitic plutons (Naranjo and Moreno 2005), then we obtain average Unit 1 ascent rates for the Ci of 0.66±0.67–1.13±0.78 m s^{-1} for L1, 0.66±0.58–1.10±0.86 m s^{-1} for L4, and 1.07±0.80–1.17±0.80 m s^{-1} for L6. Our Unit 2 (L8) average ascent rates are 0.77±0.37–1.14±0.81 m s^{-1}. Unit 3 (L10) average ascent rates are the slowest at 0.08±0.01–0.68±0.58 m s^{-1}. Conversely, Unit 4 (L18) average ascent rates are the fastest at 1.28±0.09–1.74±0.84 m s^{-1}. Due to our assumptions and simplifications, these rates should be considered a minimum (Fig. 4.9).

Our second calculation combines our modeling parameter space with a chamber depth estimate of 18 km (Schindlbeck et al., 2014). If we assume the Ci magma is water undersaturated, then we can expect the magma resided at a deeper depth prior to decompression. Using a maximum P_i during SNGPlag modeling of 120 MPa, we obtain an effective *dP/dz* in P_{H2O} of 60 MPa per every 9 km. Using these new assumptions, our ascent rates for the Ci magma increase. Average ascent rates for Unit 1 become 2.23±2.27–3.89±2.04 m s^{-1} (L1), 1.90±1.97–3.72±2.90 m s^{-1} (L4), and 3.61±2.68–3.96±2.71 m s^{-1} (L6). Unit 2 average ascent rates are 2.58±1.24–3.86±2.73 m s^{-1}. Unit 3 average ascent rates are 0.27±0.02–2.30±1.97 m s^{-1}. Finally, Unit 4 average ascent rates are 4.31±0.30–5.86±2.85 m s^{-1}. Because this second set of ascent rates assumes the same decompression rates as our first scenario but over a greater depth, they should be considered maximum estimates (Fig. 4.9).

Finally, Schindlbeck et al. (2014) report a *dP/dz* at Llaima of ~20 MPa km^{-1} down to the brittle-ductile transition located at ~14–15 km. Using their σ_v, we calculated ascent rates for Unit 1 of 0.63±0.66–1.32±0.90 m s^{-1}, 0.86±0.41–1.29±0.91 m s^{-1} for Unit 2, 0.09±0.01–0.77±0.66 m s^{-1} for Unit 3, and 1.44±0.10–1.95±0.95 m s^{-1} for Unit 4 (Fig. 4.7). These rates are closer to our lower end approximation. Note that Schindlbeck et al. (2014) estimate a storage depth of 18 km for the Curacautín magma, and thus their *dP/dz* may be a minimum.

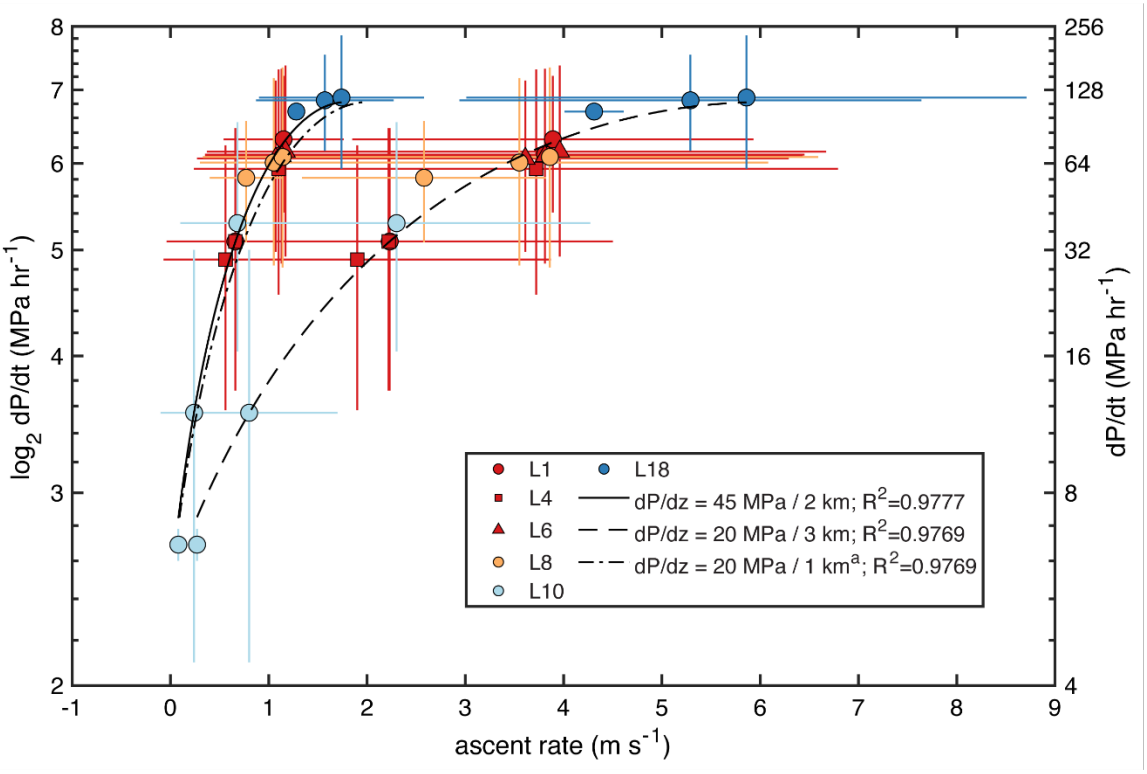

Figure 4.9. Curacautín magma ascent rates (m s^{-1}) versus decompression rate in both $\log_2$ *dP/dt* and *dP/dt* (MPa hr^{-1}). Polynomial fits to our minimum and maximum end-member estimates for lithostatic pressure gradient (*dP/dz*) and that of Schindlbeck et al. (2014) are provided. Points for Schindlbeck et al. (2014) curve are not plotted. Bars are 1σ.

4.4.4 Difficulty of fitting smallest CSD microlites

SNGPlag struggles to fit the smallest crystal sizes in the observed plagioclase CSDs (Appendix A). This may be a result of the tighter 2σ bounds at smaller sizes because the number of crystals exceeding those sizes is large, thus decreasing the uncertainty allowed in the model fits (Fig. 4.3). Alternatively, poor fits at small microlite sizes may result from the range of P values reported in the experiments of Shea and Hammer (2013) and thus used for calibration of SNGPlag N_{plag} and G_{plag} rates (Table 4.1). The lowest P_f used for calibration are 10 and 22 MPa, but these were only two out of the eleven experiments, whereas the other nine were conducted to $42 \leq P_f \leq 100$ MPa

(Shea and Hammer, 2013). Because N_{plag} and G_{plag} are not linear with respect to $\Delta\phi_{plag}$ (Fig. 4.4), they would be higher in experiments conducted at very low P. However, our modeled P_f and calibration P_f stop at 10 MPa, but natural plagioclase textures could continue to record shallower conduit conditions. In this scenario, we would expect crystallization of a higher number of smaller plagioclase microlites, which may have produced the densely crystalline Ci pyroclasts (Marshall et al., 2022a; 2022b; Valdivia et al., 2022).

4.4.5 Interpreting the Curacautín eruption

Rapid magma ascent rates are often invoked to explain mafic Plinian and ignimbrite-forming eruptions (Sable et al., 2006; Sable et al., 2009; Vinkler et al., 2012; Arzilli et al., 2019; Bamber et al., 2020; Marshall et al., 2022a; Valdivia et al., 2022). The resultant supersaturation from rapid ascent supersaturates the melt and drives plagioclase nucleation and crystallization. Our modeling here reveals that N_{plag} in the basaltic andesite Ci is considerably lower than N_{plag} in dacites, but maximum G_{plag} of 7.6×10^{-7} cm s^{-1} is up to 1000X greater than dacite G_{plag} at the same $\Delta\phi_{plag}$. Our G_{plag} is one order of magnitude lower than the ~$3–5\times10^{-6}$ cm s^{-1} measured by Vetere et al. (2021) during basaltic andesite viscosity experiments. Those authors argue for the importance of shear rate being considered in models of magmatic and volcanic processes, which is not something considered in this version of SNGPlag (Table 4.2). Indeed, shear rate and its impact on viscosity would impact our G_{plag} and may help explain recent conduit processes proposed by Marshall et al. (2022b).

Our modeling here suggests that rapid *dP/dt* produced the plagioclase microlite textures observed in Ci pyroclasts (Table 4.3; Marshall et al., 2022a; 2022b; Valdivia et al. 2022). Such extensive crystallization would have increased the magma viscosity to the point that vesicles would begin to distort and wrap around the nucleating and rapidly growing acicular plagioclase. This explains the highly tortuous 99% interconnectivity vesicle population textures identified by Valdivia et al. (2022). Highly tortuous vesicle networks inhibit degassing, which in turn enhances the overpressure necessary for brittle fragmentation.

The three sets of magma ascent rates we estimated here using different *dP/dz* reasonable for the South Central Volcanic Zone of Chile offer a first-order look into the ascent rates that drove the Curacautín eruption (Fig. 4.9). Minimum ascent rates of 0.1–1.7 m s^{-1} using a σ_V of 22.5 MPa km^{-1} are similar to the ascent rates of 0.1–2.0 m s^{-1} we estimated using the σ_V of Schindlbeck et al. (2014). Conversely, a σ_V of 20 MPa per every 3 km yields ascent rates up to 3X faster (Fig. 4.9).

Unit 1 ascent rates are variable between 0.6 and 1.3 m s^{-1} and increase slightly to 0.8–1.3 m s^{-1} in Unit 2. Unit 3 ascent rates drop by an order of magnitude to 0.1–0.8 m s^{-1} and suggests modulation of the magma flux during the Curacautín eruption. Unit 4 has the fastest magma ascent rate of 1.3–2.0 m s^{-1} and represents the final pulse of the Ci eruption. Valdivia et al. (2022) calculated vesicle overpressures necessary to fragment the Ci magma between 3.8 and 5.1 MPa. Such a low fragmentation threshold combined with the rapid *dP/dt* calculated here implies a limited decompression history prior to climatic fragmentation. Because the Ci was produced during a single eruptive event (Marshall et al., 2022a), changes in magma ascent rate did not likely result from changes in shallow

magma storage or magma recharge, but rather changes in vesiculation or conduit/vent geometry during eruption. Discriminating between those different parameters is beyond the scope of the current version of SNGPlag.

Our results reveal that rapidly growing acicular plagioclase morphologies produce highly tortuous vesicle networks that inhibit degassing. Following fragmentation, decompression and ascent rates of the gas-pyroclast mixture are orders of magnitude greater than the original bulk magma and suggest there is little time between fragmentation and eruption. In the case of the Ci, the time period between fragmentation and eruption likely generated the highly crystalline groundmass of l<10 μm plagioclase microlites that overprints sutures between fused domains of heterogeneous vesicle textures. These results help elucidate the still poorly understand conduit processes that impact how mafic magmas can erupt as large, explosive events.

4.5 Conclusions

Plagioclase nucleation and growth rates, N_{plag} and G_{plag}, respectively, differ substantially between mafic and felsic magmas. Those differences can affect eruption style. Modeled maximum N_{plag} for the 12.6 ka basaltic andesite Curacautín eruption are orders of magnitude lower than those for the 1991 Pinatubo dacite (Fig. 4.4); however, G_{plag} is up to 10X greater in mafic magmas than felsic magmas, resulting in volumetric growth rates ~1000X greater in mafic magmas than felsic ones. This result explains the predominately acicular nature of plagioclase microlites in the products of mafic explosive eruptions attributed to rapid ascent rates.

The *dP/dt* modeled here using SNGPlag are between 10^{-3} and 10^{-1} MPa s^{-1} and are similar to *dP/dt* measured experimentally for similar compositions and known eruption styles (e.g., Szramek et al. 2016). We were able to fit the majority of CSD bins to the natural samples. Unlike decompression experiments which must follow some particular decompression pathways (Fig. 4.1), our modeling applies instantaneous N_{plag} and G_{plag} to 150,000 possible decompression pathways to derive the most likely decompression scenario, and thus reflect the total decompression path of the Ci magma. (Appendix A1). Our modeled *dP/dt* are ~2 orders of magnitude lower than those calculated by Valdivia et al. (2022) for the same eruption. This difference reflects time-integrated rates recording most of magma decompression and ascent presented here, whereas those of Valdivia et al. (2022) were calculated using the BND meter of Toramaru (2006) on a homogenous nucleation event from the shallow conduit. Importantly, these two sets of *dP/dt* reveal that decompression (and therefore magma ascent) of the Curacautín magma increased by orders of magnitude following the onset of fragmentation and record the explosive nature of the eruption. Additionally, such a dramatic change in ascent rate would have similar impacts on $\Delta\phi_{plag}$ (Fig. 4.4), resulting in the crystallization of the l<10 μm population of unbroken plagioclase microlites identified by Marshall et al. (2022b) and may explain the rapid τ_c Valdivia et al. (2022) calculated from plagioclase CSDs.

Future work is necessary to fully describe the effects of decompression on crystallization and eruption processes described here. Integrating a viscosity component into SNGPlag would allow us to investigate viscosity's role on ascent dynamics, which has profound impacts on degassing and crystallization and may help explain the textures reported in Marshall et al. (2022b). Additionally, decompression experiments conducted

to very low Pi (and therefore higher melt viscosity) would enhance the calibration parameter space of SNGPlag and allow for the investigation of plagioclase crystallization at the shallowest depths of conduits where microlites are likely to crystallize most extensively.

4.6 References

Andrews BJ, Befus KS (2020) Supersaturation Nucleation and Growth of Plagioclase: a numerical model of decompression-induced crystallization. Contrib Mineral Petrol 175:23. https://doi.org/10.1007/s00410-020-1660-9

Andrews BJ, Gardner JE (2010) Effects of caldera collapse on conduit dimensions and magma decompression rate: an example from the 1800 ^{14}C yr BP eruption of Ksudach Volcano, Kamchatka, Russia. J Volcanol Geotherm Res 198:205–216. https://doi.org/10.1016/j.jvolgeores.2010..08.021

Arzilli F, Agostini C, Landi P, Fortunati A, Mancini L, Carroll M (2015) Plagioclase nucleation and growth kinetics in a hydrous basaltic melt by decompression experiments. Contrib Mineral Petrol 170:55. https://doi.org/10.1007/s00410-015-1205-9

Arzilli F, La Spina G, Burton MR, Polacci, M, Le Gall N, Hartley ME, Di Genova D, Cai B, Vo NT, Bamber EC, Nonni S, Atwood R, Llewellin EW, Brooker RA, Mader HM, Lee PD (2019) Magma fragmentation in highly explosive basaltic eruptions induced by rapid crystallization. Nat Geosci 12:1023–1028. https://doi.org/10.1038/s41561-019-0468-6

Bamber EC, Arzilli F, Polacci M, Hartley ME, Fellowes J, Di Genova D, Chavarría D, Saballos JA, Burton MR (2020) Pre- and *syn*-eruptive conditions of a basaltic Plinian eruption at Masaya Volcano, Nicaragua: The Masaya Triple Layer (2.1 ka). J Volcanol Geotherm Res 392:106761. https://doi.org/10.1016/j.jvolgeores.2019.106761

Barth A, Newcombe M, Plank T, Gonnermann H, Hajimirza S, Soto GJ, Saballos A, Hauri E (2019) Magma decompression rate correlates with explosivity at basaltic volcanoes – Constraints from water diffusion in olivine. J Volcanol Geotherm Res 387:106664. https://doi.org/10.1016/j.jvolgeores.2019.106664

Befus KS, Andrews BJ (2018) Crystal nucleation and growth produced by continuous decompression of Pinatubo magma. Contrib Mineral Petrol 173:92. https://doi.org/10.1007/s00410-018-1519-5

Blundy J, Cashman KV (2008) Petrologic reconstruction of magmatic system variables and processes. In: Putirka KD, Tepley III FJ (eds) Minerals, Inclusions and Volcanic Processes. Rev Mineral Geochem 69(1):179–239. https://doi.org/10.2138/rmg.2008.69.6

Browne B, Gardner JE (2006) The influence of magma ascent path on the texture, mineralogy, and formation of hornblende reaction rims. Earth Planet Sci Lett 246:161–176. https://doi.org/10.1016/j.epsl.2006.05.006

Brugger CR, Hammer JE (2010) Crystal size distribution analysis of plagioclase in experimentally decompressed hydrous rhyodacite magma. Earth Planet Sci Lett 300(3):246–254. https://doi.org/10.1016/j.epsl.2010.09.046

Burgisser A, Gardner JE (2005) Experimental constraints on degassing and permeability in volcanic conduit flow. Bull Volcanol 67: 42–56. https://doi.org/10.1007/s00445-004-0359-5

Cashman KV, Marsh BD (1988) Crystal size distribution (CSD) in rocks and the kinetics and dynamics of crystallization II. Makaopuhi lava lake. Contrib Mineral Petrol 99:292–305. https://doi.org/10.1007/BF00375363

Castro JM, Dingwell DB (2009) Rapid ascent of rhyolitic magma at Chaitén volcano, Chile. Nature 461:780–783. https://doi.org/10.1038/nature08458

Constantini L, Houghton BF, Bonadonna C (2010) Constraints on eruption dynamics of basaltic explosive activity derived from chemical and microtextural study: The example of the Fontana Lapilli Plinian eruption, Nicaragua. J Volcanol Geotherm Res 189:207–224. https://doi.org/10.1016/j.jvolgeores.2009.11.008

Eichelberger JC, Carrigan CR, Westrich HR, Price RH (1986) Non-explosive silicic volcanism. Nature 323:598–602. https://doi.org/10.1038/323598a0

Geschwind C-H, Rutherford MJ (1995) Crystallization of microlites during magma ascent: the fluid mechanics of 1980–1986 eruptions at Mount St. Helens. Bull Volcanol 57:356–370. https://doi.org/10.1007/BF00301293

Ghiorso MS, Gualda GAR (2015) An H2O-CO2 mixed fluid saturated model compatible with rhyolite-MELTS. Contrib Mineral Petrol 169:53. https://doi.org/10.1007/s00410-015-1141-8

Gualda GAR, Ghiorso MS, Lemons. RV, Carley TL (2012) Rhyolite-MELTS: A modified calibration of MELTS optimized for silica-rich, fluid-bearing magmatic systems. J Petrol 53:875–890. https://doi.org/10.1093/petrology/egr080

Hammer JE (2004) Crystal nucleation in hydrous rhyolite: experimental data applied to classical theory. Am Mineral 89(11–12):1673–1679. https://doi.org/10.2138/am-2004-11-1212

Hammer JE, Rutherford MJ (2002) An experimental study of the kinetics of decompression-induced crystallization in silicic melt. J Geophys Res 107(B1). https://doi.org/10.1029/2001JB000281

Jaupart C, Allegre C (1991) Gas content, eruption rate and instabilities of eruption regime in silicic volcanoes. Earth Planet Sci Lett 102:413–429. https://doi.org/10.1016/0012-821X(91)90032-D

La Spina G, Burton M, de' Michieli Vitturi M, Arzilli F (2016) Role of syn-eruptive plagioclase disequilibrium crystallization in basaltic magma ascent dynamics. Nat Commun 7:13402. https://doi.org/10.1038/ncomms13402

Lange RA, Frey HM, Hector J (2009) A thermodynamic model for the plagioclase-liquid hygrometer/thermometer. Am Mineral 94:494–506. https://doi.org/10.2138/am.2009.3011

Liu Y, Anderson AT, Wilson CJN (2007) Melt pockets in phenocrysts and decompression rates of silicic magmas before fragmentation. J Geophys Res 112:B06204. https://doi.org/10.1029/2006JB004500

Lohmar S (2008) Petrologia de las ignimbritas Lican y Pucon (volcan Villarrica) y Curacautin (volcan Llaima) en los Andes del sur de Chile. Dissertation, University of Chile

Mangan M, Sisson T (2000) Delayed, disequilibrium degassing in rhyolitic magma: decompression experiments and implications for explosive volcanism. Earth Planet Sci Lett 183:441–455. https://doi.org/10.1016/S0012-821X(00)00299-5

Marsh BD (1988) Crystal size distribution (CSD) in rocks and the kinetics and dynamics of crystallization: I. Theory. Contrib Mineral Petrol 99:277–291. https://doi.org/10.1007/BF00375362

Marshall AA, Brand BD, Martínez V, Bowers J, Walker M, Wanless VD, Andrews BJ, Manga M, Valdivia P, Giordano G (2022a) The mafic Curacautín ignimbrite of Llaima volcano, Chile. J Volcanol Geotherm Res 421:107418. https://doi.org/10.1016/j.jvolgeores.2021.107418

Marshall AA, Manga M, Brand BD, Andrews BJ (2022b) Autobrecciation and fusing of mafic magma preceding explosive eruptions. Geology 50. https://doi.org/10.1130/G50180.1

Mastin LG, Ghiorso MS (2001) Adiabatic temperature changes of magma-gas mixtures during ascent and eruption. Contrib Mineral Petrol 141:307–321. https://doi.org/10.1007/s004100000210

Mastin LG, Ghiorso MS (2000) A numerical program for steady-state flow of magma-gas mixtures through vertical eruptive conduits. U.S. Geological Survey Open-File Report 2000-209:66 pp. https://doi.org/10/3133/ofr00209

Moran SC, Malone SD, Qamar AI, Thelen WA, Wright AK, Caplan-Auerbach J (2008) Seismicity Associated with Renewed Dome Building at Mount St. Helens, 2004–2005. In: Sherrod DR, Scott WE, Stauffer PH (eds) A Volcano Rekindled: The Renewed Eruption of Mount St. Helens, 2004–2005. U.S. Geological Survey Professional Paper 1750:27–54. https://doi.org/10.3133/pp17502

Murch AP, Cole PD (2019) Using microlites to gain insights into ascent conditions of differing styles of volcanism at Soufrière Hills Volcano. J Volcanol Geotherm Res 384:221–231. https://doi.org/10.1016/j.jvolgeores.2019.07.022

Myers ML, Wallace PJ, Wilson CJN, Morter BK, Swallow EJ (2016) Prolonged ascent and episodic venting of discrete magma batches at the onset of the Huckleberry Ridge supereruption, Yellowstone. Earth Planet Sci Lett 451:285–297. https://doi.org/10.1016/j.epsl.2016.07.023

Myers ML, Wallace PJ, Wilson CJN, Watkins JM, Liu Y (2018) Ascent rates of rhyolitic magma at the onset of caldera-forming eruptions. Am Mineral 103(6):952–965. https://doi.org/10.2138/am-2018-6225

Naranjo JA, Moreno H (1991) Actividad explosiva postglacial en el volcan Llaima, Andes del Sur (38°45'S). Rev Geol Chile 18(1): 69–80. https://dx.doi.org/10.5027/andgeoV18n1-a06

Naranjo JA, Moreno H (2005) Geología del volcán Llaima, Region de la Araucanía. Servicio Nacional de Geología y Minería, Carta Geologíca de Chile, Serie Geología Básica 88:1–33. Escala 1:50,000

Putirka KD (2008) Thermometers and Barometers for Volcanic Systems. Rev Mineral Geochem 69:61–120. https://doi.org/10.2138/rmg.2008.69.3

Rowe MC, Carey RJ, White JDL, Kilgour G, Hughes E, Ellis B, Rosseel J-B, Segovia A (2021) Tarawera 1886: an integrated review of volcanological and geochemical characteristics of complex basaltic eruption. N Z J Geol Geophys. https://doi.org/10.1080/00288306.2021.1914118

Rutherford MJ, Hill PM (1993) Magma ascent rates from amphibole breakdown: an experimental study applied to the 1980–1986 Mount St. Helens eruptions. J Geophys Res 98(B11):19667–19684. https://doi.org/10.1029/93JB01613

Schindlbeck JC, Freundt A, Kutterolf S (2014) Major changes in the post-glacial evolution of magmatic compositions and pre-eruptive conditions at Llaima volcano, Andean Southern Volcanic Zone, Chile. Bull Volcanol 76:830. https://doi.org/10.1007/s00445-014-0830-x

Sable JE, Houghton BF, Del Carlo P, Coltelli M (2006) Changing conditions of magma ascent and fragmentation during the Etna 122 BC basaltic Plinian eruption: Evidence from clast microtextures. J Volcanol Geotherm Res 158:333–354. https://doi.org/10.1016/j.jvolgeores.2006.07.006

Sable JE, Houghton BF, Wilson CJN, Carey RJ (2009) Eruption mechanisms during the climax of the Tarawera 1886 basaltic Plinian eruption inferred from microtextural characteristics of the deposits. In: Thordarson T, Self S, Larsen G, Rowland SK, Hoskuldsson A (eds) Studies in Volcanology: The Legacy of George Walker. Special Publications of IAVCEI 2:129–154. https://doi.org/10.1144/IAVCEI002.7

Shea T, Hammer JE (2013) Kinetics of cooling- and decompression-induced crystallization in hydrous mafic-intermediate magmas. J Volcanol Geotherm Res 260:127–145. https://doi.org/10.1016/j.jvolgeores.2013.04.018

Szramek L, Gardner JE, Larsen J (2006) Degassing and microlite crystallization of basaltic andesite magma erupting at Arenal Volcano, Costa Rica. J Volcanol Geotherm Res 157:182–201. https://doi.org/10.1016/j.jvolgeores.2006.03.039

Thelen WA, Crosson RS, Creagor KC (2008) Absolute and Relative Locations of Earthquakes at Mount St. Helens, Washington, Using Continuous Data: Implications for Magmatic Processes. In: Sherrod DR, Scott WE, Stauffer PH (eds) A Volcano Rekindled: The Renewed Eruption of Mount St. Helens, 2004–2005. U.S. Geological Survey Professional Paper 1750:71–95. https://doi.org/10.3133/pp17504

Toramaru A (2006) BND (bubble number density) decompression rate meter for explosive volcanic eruptions. J Volcanol Geotherm Res 154:303–316. https://doi.org/10.1016/j.jvolgeores.2006.03.027

Toramaru A, Noguchi S, Oyoshihara S, Tsune A (2008) MND (microlite number density) water exsolution rate meter. J Volcanol Geotherm Res 175(1–2):156–167. https://doi.org/10.1016/j.jvolgeores.2008.03.035

Valdivia P, Marshall AA, Manga M, Brand BD, Huber C (2022) Mafic explosive volcanism at Llaima volcano: 3D X-ray microtomography reconstruction of pyroclasts to constrain shallow conduit processes. Bull Volcanol 84(2). https://doi.org/10.1007/s00445-021-01514-8

Vetere F, Petrelli M, Perugini D, Haselbach S, Morgavi D, Pisello A, Iezzi G, Holtz F (2021) Rheological evolution of eruptible Basaltic-Andesite Magmas under dynamic conditions: The importance of plagioclase growth rates. J Volcanol Geotherm Res 420:107411. https://doi.org/10.1016/j.jvolgeores.2021.107411

Vinkler AP, Cashman KV, Giordano G, Groppelli G (2012) volution of the mafic Villa Senni caldera-forming eruption at Colli Albani volcano, Italy, indicated by textural analysis of juvenile fragments. J Volcanol Geotherm Res 235–236:37–54. https://doi.org/10.1016/j.jvolgeores.2012.03.006

Vona A, Romano C, Dingwell DB, Giordano D (2011) The rheology of crystal-bearing basaltic magmas from Stromboli and Etna. Geochim Cosmochim Acta 75:3214–3236. https://doi.org/10.1016/j.gca.2011.03.031

Waters LE, Andrews BJ, Lange RA (2015) Rapid Crystallization of Plagioclase Phenocrysts in Silicic Melts during Fluid-saturated Ascent: Phase Equilibrium and Decompression Experiments. J Petrol 56:981–1006. https://doi.org/10.1093/petrology/egv025

CHAPTER 5: AUTOBRECCIATION AND FUSING OF MAFIC MAGMA PRECEDING EXPLPOSIVE ERUPTIONS

This chapter is a manuscript that was accepted for publication on May 24, 2022, by the Geological Society of America in the journal Geology. The full citation is: Marshall, A.A., Manga, M., Brand, B.D., and Andrews, B.J., 2022, Autobrecciation and fusing of mafic magma preceding explosive eruptions: Geology, v. 50, doi: 10.1130/G50180.1.

5.1 Abstract

Bubble and crystal textures evolve during magma ascent, altering properties that control ascent such as permeability and viscosity. Eruption style results from feedbacks between ascent, bubble nucleation and growth, microlite crystallization, and gas loss, all processes recorded in pyroclasts. We show that pyroclasts of the mafic Curacautín ignimbrite of Llaima volcano, Chile, record a history of repeated autobrecciation, fusing, and crystallization. We identified pyroclasts with domains of heterogeneous vesicle textures in sharp contact with one another that are overprinted by extensive microlite crystallization. Broken crystals with long axes (l) >10 μm record fragmentation events during the eruption. A second population of unbroken microlites with $l \lesssim 10$ μm overprint sutures between fused domains, suggesting the highly crystalline groundmass formed at shallow depths after autobrecciation and fusing. Nearly all pyroclasts contain plutonic

and ancestral Llaima lithics as inclusions, implying that fusing occurs from a few kms depth to as shallow as the surface. We propose that Ci magma autobrecciated during ascent and proto-pyroclasts remained melt-rich enough to fuse together. Lithics from the conduit margins were entrained into the proto-pyroclasts before fusing. Autobrecciation broke existing phenocrysts and microlites; rapid post-fusing crystallization then generated the highly crystalline groundmass. This proposed conduit process has implications for interpreting the products of mafic explosive eruptions.

5.2 Introduction

Researchers analyze the textural properties of erupted magmas and their associated deposits to study conduit ascent dynamics and eruption mechanics, in particular the processes that lead to crystallization, gas loss, and fragmentation. For example, bubble textures in mafic magmas inform on the state of magmatic volatiles at the time of eruption (Valdivia et al., 2022), microlites are used to investigate magma ascent rates and rheological evolution (Vona et al., 2011; Arzilli et al., 2019), broken crystals record fragmentation and healing of melt (Cordonnier et al., 2012; Taddeucci et al., 2021), and deposit granulometry records fragmentation style and efficiency (White and Valentine, 2016). The interplay of bubble and crystallization dynamics, magma ascent, and gas loss gives rise to the diversity of eruption styles (Cassidy et al., 2018).

We examined pyroclast (clast) textures from the mafic Curacautín ignimbrite of Llaima volcano, Chile. We argue that domains of heterogeneous textures and entrained lithic fragments within clasts reflect episodes of autobrecciation and fusing of magma during ascent. In addition, size-restricted fractured plagioclase microlites suggest distinct

episodes of crystallization, which has implications for using crystal size distributions to constrain decompression rates. These textures challenge our understanding of mafic explosive volcanism and impart a need to scrutinize potentially overlooked pyroclast textures.

5.1.1 The Curacautín eruption

The Ci is a 4.0–4.5 km^3 (dense-rock equivalent) unwelded basaltic andesite ignimbrite that erupted ~12.6 ka from Llaima volcano, Chile (Marshall et al., 2022). Ci clasts exhibit two vesicle populations: a polylobate, tortuous vesicle network of 99% pore connectivity and a second population of smaller, μm-scale, isolated vesicles (Fig. 5.1; Valdivia et al., 2022). The groundmass contains high microlite number densities and little glass. Recent studies suggest the Ci eruption is the result of brittle fragmentation of a rapidly ascending, largely non-degassed magma (Marshall et al., 2022; Valdivia et al., 2022).

5.3 Methods

We collected bulk Ci deposits and hand samples in the field and selected sieved clasts for further investigation. We used clast textures to constrain conduit processes during the Ci eruption. High magnification images were acquired using a tabletop scanner, scanning electron microscopy, and X-ray computed microtomography (μCT). Marshall et al. (2022) measured plagioclase microlite number densities, and Valdivia et al. (2022) computed crystal size distributions. We fit regressions to plagioclase crystal

size distributions for size populations with long axes (l) ≤10 μm and >10 μm (extended methods in Supplemental Materials).

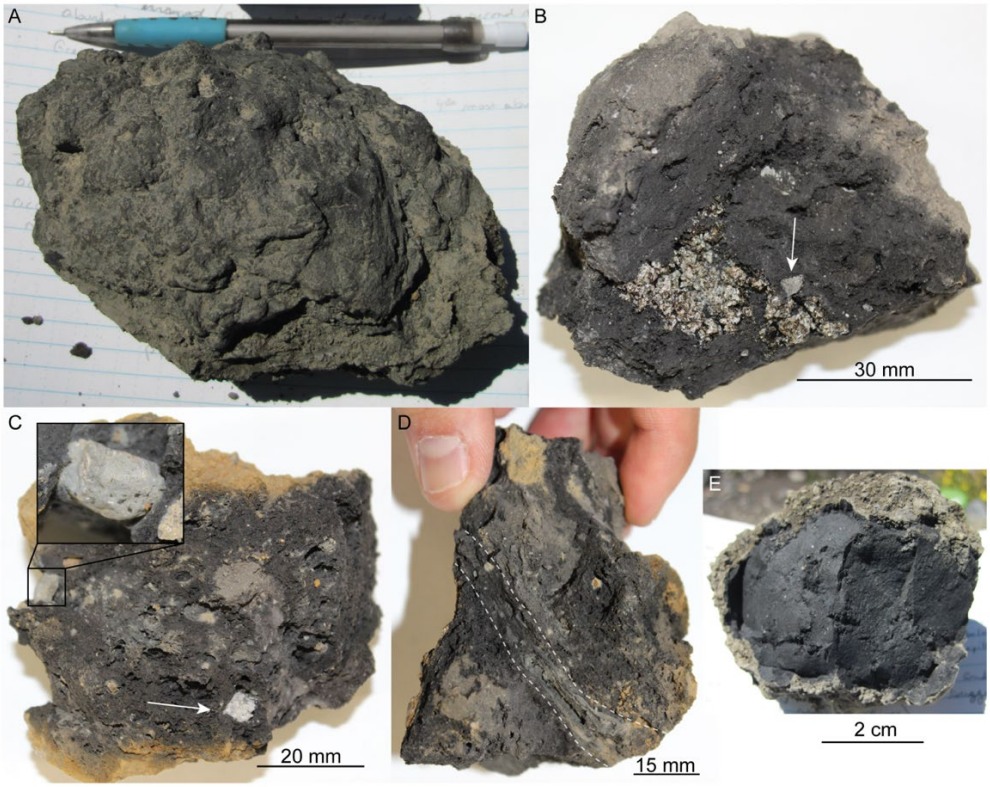

Figure 5.1 Hand samples from the Curacautín ignimbrite (Chile) displaying various macroscale textures. (A) Block consisting of agglomerated pyroclasts (Marshall et al., 2022). (B) Small block that contains crystal mush and intermediate lavas (white arrow). (C) Block with dioritic and intermediate lava lithics. (D) Flow banding between two domains of non-sheared magma (dotted white lines). (E) Dense, jointed clast or cored bomb (Sotilli et al., 2010).

5.4 Results

Domains of heterogeneous vesicle textures exist in all hand samples, 86% of thin sections (54 of 63), and 53% of μCT datasets (25 of 47) (Fig. 5.2A-F). Some domains are separated by void space, but most commonly are in sharp contact with one another. When these domains are in sharp contact, the groundmass across both domains is characterized

by high microlite crystallinities of plagioclase, pyroxene, olivine, and Fe-Ti oxides, and 29–54% glass (Fig. 5.2D-F). We were unable to collect glass compositions across fused domains as the groundmass of all clasts is too microlite-rich. We identified entrained lithics of plutonic rocks and mafic to intermediate lavas in all hand samples and 92% of our thin sections and μCT datasets (101 of 110). Lithics are mostly medium ash to fine lapilli in size (Fig. 5.1B-C, 5.2B-C). We observe broken phenocrysts and microlites at high magnifications (Fig. 5.2G-I).

5.5 Discussion

Crystallization times (τ) inferred from crystal size distributions (Fig. 5.3) suggest disequilibrium crystallization of microlites and, thus, rapid ascent (Valdivia et al., 2022). Increased magma bulk viscosity and the abundant microlites confined bubbles during expansion leading to the convoluted, but mostly connected, vesicle network. Bubble number densities of $1.1–2.3\times10^{3}$ mm^{-3} and permeabilities of $0.3–6\times10^{-12}$ m^{2} (Valdivia et al., 2021) are similar to those of other volatile-driven mafic explosive eruptions, such as the 60 ka Fontana Lapilli Basalt and Masaya Triple Layer eruptions (Nicaragua; Constantini et al., 2009; Bamber et al. 2020), 122 BCE Etna eruption (Italy; Coltelli et al., 1998; Houghton et al., 2004; Sable et al., 2006; Moitra et al., 2013), the 1886 CE Tarawera eruption (New Zealand; Carey et al., 2007; Sable et al., 2009; Schauroth et al., 2016), and mafic ignimbrites of the Roman Magmatic Province (Giordano et al., 2010; Vinkler et al., 2012). Valdivia et al. (2022) estimated a minimum average decompression rate for the Ci eruption of 1.4 MPa s^{-1} in the upper conduit. These results further highlight

the role of rapid ascent for driving explosive mafic volcanism (Szramek et al., 2006; Moitra et al., 2018; Arzilli et al., 2019).

Ci clast textures record repeated episodes of autobrecciation and/or fragmentation, particle recapture and fusing, and further fragmentation within the conduit and during the Ci eruption. The strongest evidence for autobrecciation and recapture are the heterogeneous vesicle domains within clasts (Fig. 5.2). Here, autobrecciation represents the shear-induced tearing of magma as it ascends, analogous to the processes in a'a flows (Fig. 5.4). Fragmentation, the breakup of magma into discrete pieces may occur simultaneously due to gas overpressure and/or localized phreatomagmatic activity (Gonnermann, 2015). Like ash sintering during rhyolitic eruptions (Gardner et al., 2017; Wadsworth et al., 2020), fusing is the welding together of melt-rich particles above the glass transition temperature within the conduit prior to eruption. Unlike sintering, however, fused clasts retain their original porosity. Fused domains exist throughout clasts, suggesting this process occurred when proto-clasts were still melt-rich and hot enough to fully fuse prior to climactic fragmentation. The lack of deformation within fused clasts suggests autobrecciation likely occurred prior to final fragmentation into a turbulent gas-pyroclast mixture; however, we recognize that fusing may have occurred in this zone as well. We identified fused clasts from the μm-scale up to fine block in size, the latter being the upper limit of sizes preserved in accessible Ci deposits, implying this process occurred over a range of spatial scales (Fig. 5.1, 5.2). The ubiquity of fusing suggests that autobrecciation may have extended across the entire conduit (Fig. 5.4).

The contacts between fused domains are overprinted with extensive microlite crystallization (Fig. 5.2, 5.4), indicating that the finest microlite population (long axis

l<10 μm) formed post-fusing and therefore post-initial fragmentation (Fig. 5.3). Additionally, while larger plagioclase microlites are often broken, microlites with l<10 μm are largely intact, further indicating crystallization post-fusing. Subtracting the l<10 μm plagioclase population reduces the plagioclase fraction from 29–44% to 17–29% and increases the glass content from 25–54% to 40–66% (Supplemental Table 1), which may have enabled fusing. This interpretation is further supported by two separate regressions in plagioclase crystal size distributions (Fig. 5.3). The smallest size population likely formed after the cycles of autobrecciation and fusing, perhaps even syneruptively. Rapid microlite crystallization is expected in the shallow conduit where undercooling is highest and would be further enhanced by the increased rate of gas loss following fragmentation (Hammer, 2004, 2008).

The pervasive inclusion of lithics within Ci clasts allows us to constrain the depth of autobrecciation (Fig. 5.4). We suggest that lithics were entrained via a combination of shear-induced erosion, phreatic, and/or phreatomagmatic processes along conduit walls. While phreatic or phreatomagmatic activity may have played a role in fracturing wall rock (e.g., Fig. 15 of Owen et al., 2019), there is no evidence that it played a significant role in the explosivity of the Ci eruption (Marshall et al., 2022). The presence of plutonic lithics and mafic to intermediate lavas within the same clasts suggests that autobrecciation and wall rock rupture and entrainment occurred over depths from 2 km to as shallow as Llaima's ancestral shield (<1 km). The abundance of entrained lithics in nearly all clasts also implies mingling across the entire conduit, a process Bamber et al. (2020) attributes to lateral variations in velocity, implying that fusing is not a localized phenomenon (Fig. 5.4). Alternatively, a narrow conduit from an elongated dike or ring

fracture would increase the surface area to volume ratio, promoting shear across the conduit and thus pervasive autobrecciation and enabling the dispersal of entrained lithics across the conduit.

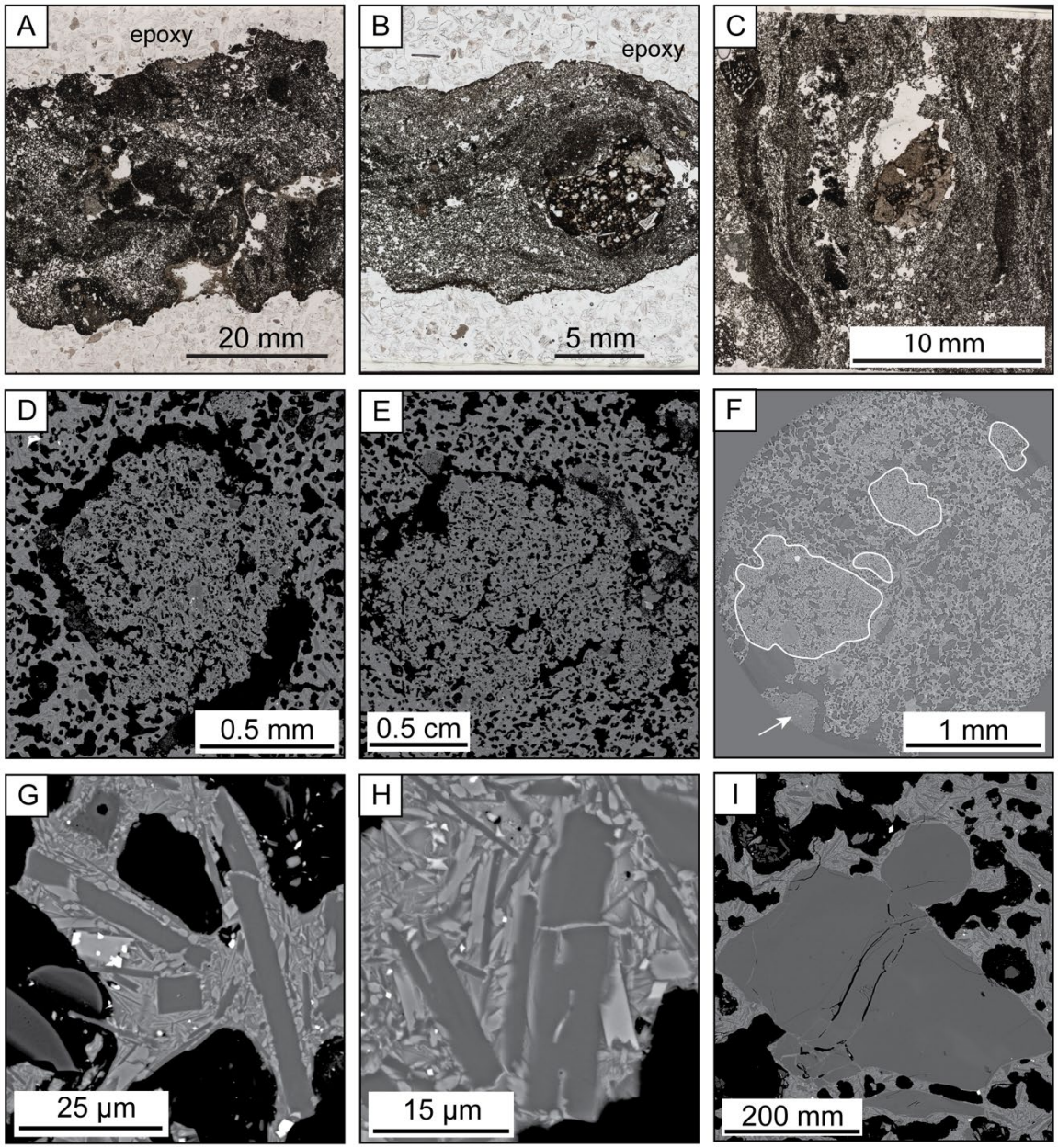

Figure 5.2 Microscale Curacautín ignimbrite (Ci) clast textures. (A) Multiple contrasting vesicle texture domains. (B) Flow banding around a lithic inclusion. (C) Layering of contrasting domains and a lithic inclusion. (D, E) Scanning electron microscopy images of fused clasts. (F) Tomography scan of clast with multiple fused domains (white polygons) and lithic inclusions (arrow). Fused domains are pervasive in Ci clasts and often trapped in the clast interior. (G, H, I) Fractured plagioclase microlites surrounded by smaller, unbroken microlites.

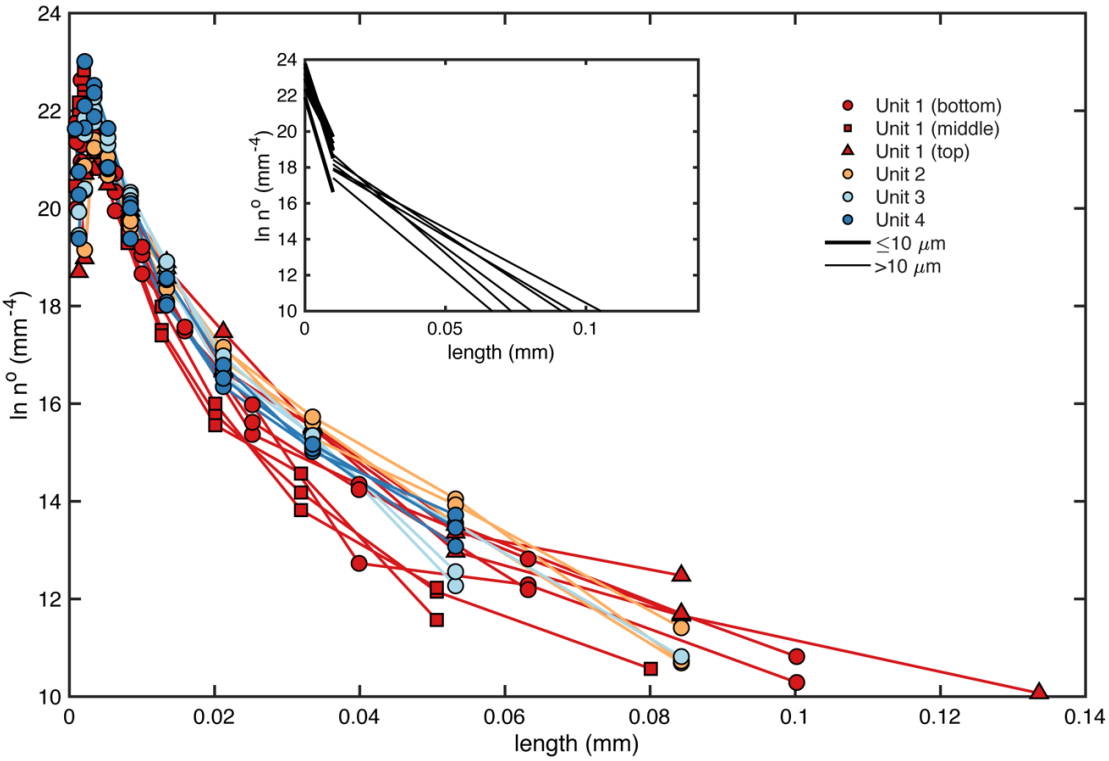

Figure 5.3 Curacautín ignimbrite crystal size distributions from Valdivia et al. (2022) with regressions fit to *l*≤10 µm and *l*>10 µm size populations (inset). Downturns in crystal size distributions are likely due to the difficulty of intersecting small microlites in 2D and not inadequate imaging resolution (Valdivia et al., 2022) and are not included in regressions.

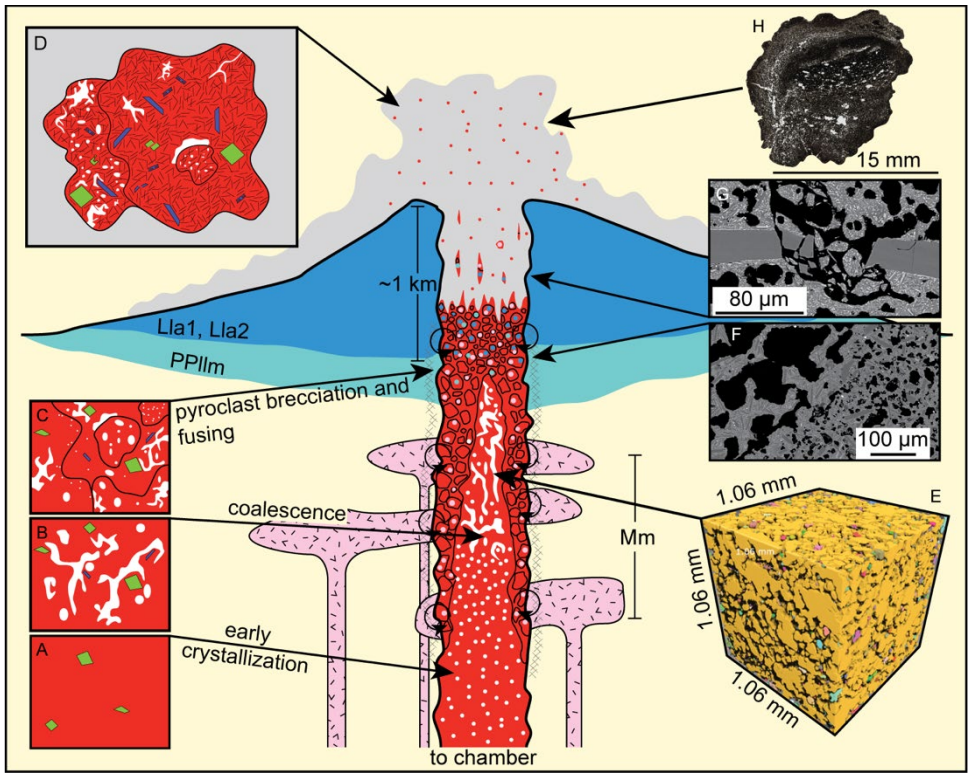

Figure 5.4 Schematic diagram of our conceptual conduit model for the Curacautín (Ci) eruption. (A) Early crystallization in the reservoir generated 1–3.5 vol. % phenocrysts (Marshall et al., 2022). (B) As the Ci magma ascended, bubbles nucleated, grew, and coalesced, and new microlites formed. (C) Magma adjacent to conduit margins autobrecciated and created melt-rich magma particles that were recaptured and fused. Domains of heterogeneous vesicle textures were preserved within individual particles. Miocene plutonic country rocks (Mm), Pliocene basaltic to andesitic lavas (PPllm), and middle Pleistocene ancestral Llaima lavas (Lla1, LLa2; Naranjo and Moreno, 2005) were incorporated into the Ci magma prior to fusing. (D) Following fragmentation, rapid (s to min) microlite crystallization overprinted sutures between fused particles resulting in 84–94% of the total number of plagioclase microlites in erupted Ci clasts. (E) Reconstruction of the Curacautín vesicle network (Valdivia et al., 2022). The yellow domain is a single, interconnected vesicle and additional colors are smaller, isolated vesicles. (F) Suture between domains of contrasting vesicle textures overprinted by microlite crystallization. (G) Shattered phenocryst and microlites from brittle behavior driven by bubble expansion in the shallow conduit. (H) Thin section scan of Ci clast with heterogeneous vesicle domains. The ubiquity of fusing would be favored by dike-shaped conduits. The nucleation zone for the $l \leq 10$ μm plagioclase is not quantified here.

5.4.1 Implications for explosive mafic eruptions

Bulk properties of fused clasts mingle domains of magma with different vesicularity, permeability, and crystallinity. This presents a challenge with the use clast-scale data for eruption interpretation, such as using bubble and crystal data to estimate ascent rates and timescales of crystallization. The incorporation and fusing of both lithics and smaller clasts within larger clasts alters densities, obscuring the true nature of the bulk magma. Fused clasts also alter the pre-fused fragmented grain size distribution, which alters final deposit granulometry (Fig. 5.2; Giachetti et al., 2021).

Our hypothesis that l<10 μm plagioclase microlites formed following fusing have important implications for crystal size distribution interpretation. Valdivia et al. (2022) calculated τ of 2–900 s for the smallest plagioclase size fraction using constant nucleation and growth rates, indicating little time between fragmentation and eruption (Fig. 5.3). Interpreting crystal size distributions with constant nucleation and growth cannot produce reliable time-averaged ascent rates if significant microlite crystallization occurred after fragmentation (e.g., Moore et al., 2022).

While fusing is common in surface flows from effusive mafic eruptions, such as Hawaiian fountains, spatter, or a'a flows, it is not widely documented in the products of highly explosive mafic Plinian and ignimbrite-forming eruptions. Reported instances include the 1886 CE eruption of Tarawera, New Zealand (Sable et al., 2009; Schauroth et al., 2016), the 1918 eruption of Katla, Iceland (Owen et al., 2019), the 11 ka eruption of Tongariro, New Zealand (Heinrich et al., 2020), ignimbrites of the Roman Magmatic Province (Giordano et al., 2010; Vinkler et al., 2012), and perhaps the 2.1 ka Masaya Triple Layer tephra, Nicaragua (Bamber et al., 2020). Heterogeneous textures of

crystalline and glassy domains in clasts of the Croscat eruption, Spain (Cimarelli et al., 2010) are attributed to mingling owing to variable ascent rates across the conduit. Ci clasts, however, lack glassy domains, which we interpret as the complete intermingling across the conduit during fusing while the magma was above the glass transition temperature. Broken crystals surrounded by intact melt are typical in clasts from explosive basaltic eruptions, providing an additional record of fragmentation and healing of fractures (Taddeucci et al., 2021). Concomitant degassing can facilitate decompression-induced microlite crystallization in mafic magmas (e.g., Vinkler et al., 2012) and lithics may serve as nucleation sites for new crystals. Together, those processes increase magma viscosity and promote fragmentation.

5.6 Conclusions

Textures preserved within Ci clasts record autobrecciation and particle fusing within Llaima's conduit prior to final fragmentation and eruption. Fused clasts retain heterogeneous vesicle textures overprinted by post-fusing plagioclase crystallization of $l \leq 10$ μm-sized microlites. Just as sintered obsidian ash records repeated magma brecciation and welding in the conduit, so do fused mafic clasts in the Ci. Lithics excavated from conduit margins are fully incorporated into erupted clasts and suggest that brecciation and fusing can occur from a depth of many kms up to shallow (<1 km) depths. These observations and interpretations provide insights into conduit conditions preceding and during highly explosive mafic eruptions. The process of conduit autobrecciation and role of conduit geometry warrants further exploration through experimental or numerical studies. Care should also be taken when interpreting clast bulk

composition and density, vesicle and crystal textures, and granulometry as heterogeneity from fusing will alter these measurements and hence affect interpretations of conduit processes.

5.7 References

Arzilli, F., La Spina, G., Burton, M.R., Polacci, M., Le Gall, N., Hartley, M.E., Di Genova, D., Cai, B., Vo, N.T., Bamber, E.C., Nonni, S., Atwood, R., Llewellin, E.W., Brooker, R.A., Mader, H.M., and Lee, P.D., 2019, Magma fragmentation in highly explosive basaltic eruptions induced by rapid crystallization: Nature Geoscience, v. 12, p. 1023–1028, doi: 10.1038/s41561-019-0468-6.

Bamber, E.C., Arzilli, F., Polacci, M., Hartley, M.E., Fellowes, J., Di Genova, D., Chavarría, D., Saballos, J.A., and Burton, M.R., 2020, Pre- and *syn*-eruptive conditions of a basaltic Plinian eruption at Masaya Volcano, Nicaragua: The Masaya Triple Layer (2.1 ka): Journal of Volcanology and Geothermal Research, v. 392, p. 1–16, doi: 10.1016/j.jvolgeores.2019.106761.

Carey, R.J., Houghton, B.F., Sable, J.E., and Wilson, C.J.N., 2007, Contrasting grain size and componentry in complex proximal deposits of the 1886 Tarawera basaltic Plinian eruption: Bulletin of Volcanology, v. 69, p. 903–926, doi: 10.1007/s00445-007-0117-6.

Cassidy, M., Manga, M., Cashman, K., and Bachmann, O., 2018, Controls on explosive-effusive volcanic eruption styles: Nature Communications, v. 9, doi: 10.1038/s41467-018-05293-3.

Cimarelli, C., Di Traglia, F., and Taddeucci, J., 2010, Basaltic scoria textures from a zoned conduit as precursors to violent Strombolian activity: Geology, v. 38, 5, p. 439–442, doi: 10.1130.G30720.1.

Coltelli, M., Del Carlo, P., and Vezzoli, L., 1998, Discovery of a Plinian basaltic eruption of Roman age at Etna volcano, Italy: Geology, v. 26, p. 1095–1098, doi: 10.1130/0091-7613(1998)026<1095:DOAPBE>2.3.CO;2.

Constantini, L., Bonadonna, C., Houghton, B.F., and Wehrmann, H., 2009, New physical characterization of the Fontana Lapilli basaltic Plinian eruption, Nicaragua: Bulletin of Volcanology, v. 71, p. 337–255, doi: 10.1007/s00445-008-0227-9.

Cordonnier, B., Caricchi, L., Pistone, M., Castro, J., Hess, K.-U., Gottschaller, S., Manga, M., Dingwell, D.B., and Burlini, L., 2012, The viscous-brittle transition of crystal-bearing silicic melt: Direct observation of magma rupture and healing: Geology, v. 40, 7, p. 611–614, doi: 10.1130/G3914.1.

Gardner, J.E., Llewellin, E.W., Watkins, J.M., and Befus, K.S., 2017, Formation of obsidian pyroclasts by sintering of ash particles in the volcanic conduit: Earth and Planetary Science Letters, v. 459, p. 252–263, doi: 10.1016/j.epsl.2016.11.037.

Giachetti, T., Trafton, K.R., Wiejaczka, J., Gardner, J.E., Watkins, J.M., Shea, T., and Wright, H.M.N, 2021, The products of primary magma fragmentation finally revealed by pumice agglomerates: Geology, v. 49, 11, p. 1307–1311, doi: 10.1130/G48902.1.

Giordano, G., and The Carg Team, 2010, Stratigraphy, volcano tectonics and evolution of the Colli Albani volcanic field, *in* Funiciello, R., and Giordano, G., eds., The Colli Albani Volcano: Geological Society, London, Special Publications of IAVCEI 3, p. 43–97, doi: 10.1144/IAVCEI003.4.

Gonnermann, H., 2015, Magma Fragmentation: Annual Review of Earth and Planetary Sciences, v. 43, p. 431–458, doi: 10.1146/annurev-060614-105206.

Hammer, J.E., 2004, Crystal nucleation in hydrous rhyolite: Experimental data applied to classical theory: American Mineralogist, v. 89, 11–12, p. 1673–1679, doi: 10.2138/am-2004-11-1212.

Hammer, J.E., 2008, Experimental studies of the kinetics and energetics of magma crystallization: Reviews in Mineralogy and Geochemistry, v. 69, 1, p. 9–59, doi: 10.2138/rmg.2008.69.2.

Heinrich, M., Cronin, S.J., Torres-Orozco, R., Colombier, M., Scheu, B., and Pardo, N., 2020, Micro-porous pyroclasts reflecting multi-vent basaltic-andesite Plinian eruptions at Mt. Tongariro, New Zealand: Journal of Volcanology and Geothermal Research, v. 401, 106936, doi: 10.1016/j.jvolgeores.2020.106936.

Houghton, B.F., Wilson, C.J.N., Del Carlo, P., Coltelli, M., Sable, J.E., and Carey, R., 2004, The influence of conduit processes on changes in styles of basaltic Plinian eruptions: Tarawera 1886 and Etna 122 BC: Journal of Volcanology and Geothermal Research, v. 137, p. 1–14, doi: 10.1016/j.jvolgeores.2004.05.009.

Marshall, A.A., Brand, B.D., Martínez, V., Bowers, J.M., Wanless, V.D., Andrews, B.J., Manga, M., Valdivia, P., and Giordano, G., 2022, The mafic Curacautín ignimbrite of Llaima volcano, Chile: Journal of Volcanology and Geothermal Research, v. 421, 107418, doi: 10.1016/j.jvolgeores.2021.107418.

Moitra, P., Gonnermann, H.M., Houghton, B.F., and Tiwary, C.S., 2018, Fragmentation and Plinian eruption of crystallizing basaltic magma: Earth and Planetary Science Letters, v. 500, p. 97–104, doi: 10.1016/j.epsl.2018.08.003.

Moore, H.C., Carey, R.J., Houghton, B.F., Jutzeler, M., and White, J.D.L., 2022, High-temperature oxidation of proximal basaltic pyroclasts, 1886 Tarawera, New Zealand: Bulletin of Volcanology, v. 84, 46, doi: 10.1007/s00445-022-01549-5.

Naranjo, J.A., and Moreno, H., 2005, Geología del volcán Llaima, Región de la Araucanía: Servicio Nacional de Geología y Minería Geológica de Chile, Serie Geología Básica 88, scale 1:50,000, 33 p.

Owen, J., Shea, T., and Tuffen, H., 2019, Basalt, Unveiling Fluid-filled Fractures, Inducing Sediment Intra-void Transport, Ephemerally: Examples from Katla 1918: Journal of Volcanology and Geothermal Research, v. 369, p. 121–144, doi: 10.1016/j.jvolgeores.2018.11.002.

Sable, J., Houghton, B., Del Carlo, P., and Coltelli, M., 2006, Changing conditions of magma ascent and fragmentation during the Etna 122 BC basaltic Plinian eruption: evidence from clast microtextures: Journal of Volcanology and Geothermal Research, v. 158, p. 433–456, doi: 10.1016/j.jvolgeores.2006.07.006.

Sable, J.E., Houghton, B.F., Wilson, C.J.N., and Carey, R.J., 2009, Eruption mechanisms during the climax of the Tarawera 1886 basaltic Plinian eruption inferred from microtextural characteristics of the deposits *in* Thordarson, T., Self, S., Larsen, G., Rowland, S.K., and Hoskuldsson, A., eds., Studies in Volcanology: The Legacy of George Walker: Special Publications of IAVCEI, v. 2, p. 129–154.

Schauroth, J., Wadsworth, F.B., Kennedy, B., von Aulock, F.W., Lavallée, Y., Damby, D.E., Vasseur, J., Scheu, B., and Dingwell, D.B., 2016, Conduit margin heating and deformation during the AD 1886 basaltic Plinian eruption at Tarawera volcano, New Zealand: Bulletin of Volcanology, v. 78, 12, doi: 10.1007/s00445-016-1006-7.

Sottili, G., Taddeucci, J., and Palladino, D.M., 2010, Constraints on magma-wall rock thermal interaction during explosive eruptions from textural analysis of cored bombs: Journal of Volcanology and Geothermal Research, v. 192, p. 27–34, doi: 10.1016/j.jvolgeores.2010.02.003.

Szramek, L., Gardner, J.E., and Larsen, J., 2006, Degassing and microlite crystallization of basaltic andesite magma erupting at Arenal Volcano, Costa Rica: Journal of Volcanology and Geothermal Research, v. 157, p. 182–201, doi: 10.1016/j.jvolgeores.2006.03.039.

Taddeucci, J., Cimarelli, C., Alatorre-Ibargüengoitia, M.A., Delgado-Granados, H., Andronico, D., Del Bello, E., Scarlato, P., and Di Stefano, F., 2021, Fracturing and healing of basaltic magmas during explosive volcanic eruptions: Nature Geoscience, v. 14, p. 248–254, doi: 10.1038/s41561-021-00708-1.

Valdivia, P., Marshall, A.A., Brand, B.D., Manga, M., and Huber, C., 2022, Mafic explosive volcanism at Llaima volcano: 3D X-ray microtomography reconstruction of pyroclasts to constrain shallow conduit processes: Bulletin of Volcanology, v. 84, 2., doi: 10.1007/s00445-021-01514-8.

Vinkler, A.P., Cashman, K.V., Giordano, G., and Groppelli, G., 2012, Evolution of the mafic Villa Senni caldera-forming eruption at Colli Albani volcano, Italy, indicated by textural analysis of juvenile fragments: Journal of Volcanology and Geothermal Research, v. 235–236, p. 37–54, doi: 10.1016/j.jvolgeores.2012.03.006.

Vona, A., Romano, C., Dingwell, D.B., and Giordano, D., 2011, The rheology of crystal-bearing basaltic magmas from Stromboli and Etna: Geochimica et Cosmochimica Acta, v. 75, 11, p. 3214–3236, doi: 10.1016/j.gca.2011.03.031.

Wadsworth, F.B., Llewellin, E.W., Vasseur, J., Gardner, J.E., and Tuffen, H., 2020, Explosive-effusive volcanic eruption transitions caused by sintering: Science Advances, v. 6, doi: eaba7940.

White, J.D.L., and Valentine, G.A., 2016, Magmatic versus phreatomagmatic fragmentation: absence of evidence is not evidence of absence: Geosphere, v. 12, p. 1478–1488, doi: 10.1130/GES01337.1.

5.7 Supplemental Information

5.7.1 Curacautín ignimbrite sample collection

The Curacautín eruption produced extensive ignimbrite deposits radially around the present-day volcano and as far west as the city of Temuco (Naranjo and Moreno, 1991). The Curacautín ignimbrite (Ci) is an unconsolidated coarse ash to fine lapilli tuff of basaltic andesite composition that erupted ~12.6 ka (Marshall et al., 2022). The samples used for this study were collected by Marshall et al. (2022) during three field campaigns from 2016–2020 from exposures to the north, east, and west of Llaima (Fig. S1). While Naranjo and Moreno (1991) state deposits are found up to 100 km from source, we were only able to find reliable exposures up to 30 km from the present-day vent.

Marshall et al. (2022) determined that the Ci consists of four flow units of variable thicknesses. However, identifiable contacts are poorly preserved or not present in most exposures. The best exposure of the flow units is the east side of Llaima (east1, east2, and east3 in Fig. S1); however, the base of the stratigraphically lowest unit is not exposed (Fig. S2). Bulk samples consisting of juvenile ash, lapilli, blocks, and country rock lithics were collected from the eastern stratigraphic section at regular intervals and from other fresh exposures identified around Llaima; charcoal for ^{14}C dating was collected where present (Fig. S1). Ash and lapilli were sieved for granulometric analysis. Up to 100 lapilli-sized pyroclasts were measured for density following the methods of Houghton and Wilson (1989). Componentry was counted for the eastern stratigraphic section down to 1ϕ.

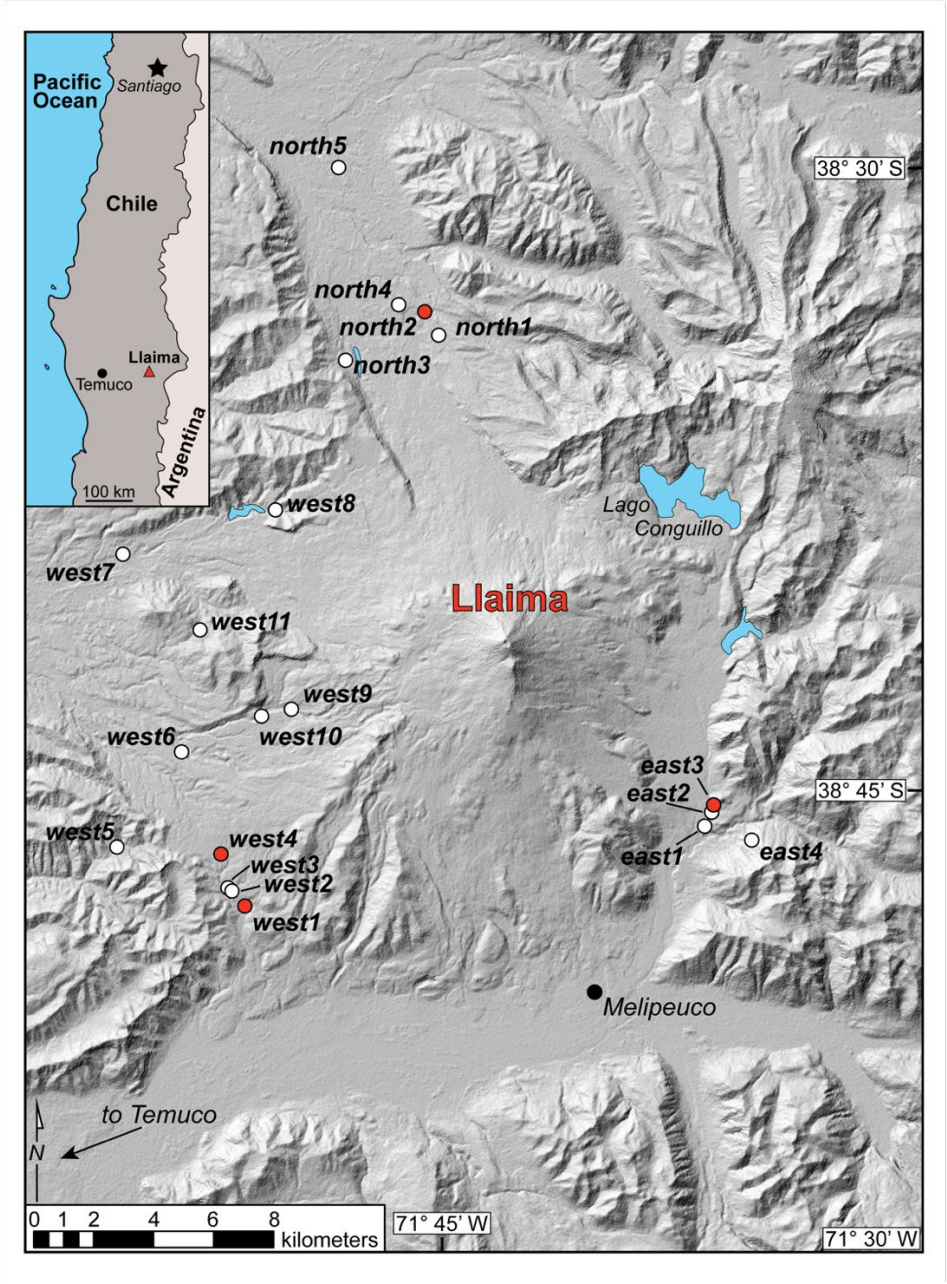

Figure S1 Sample locations from Marshall et al. (2022) (their Fig. 2) for reference with Table S1. Red symbols show locations that contained charcoal for ^{14}C dating.

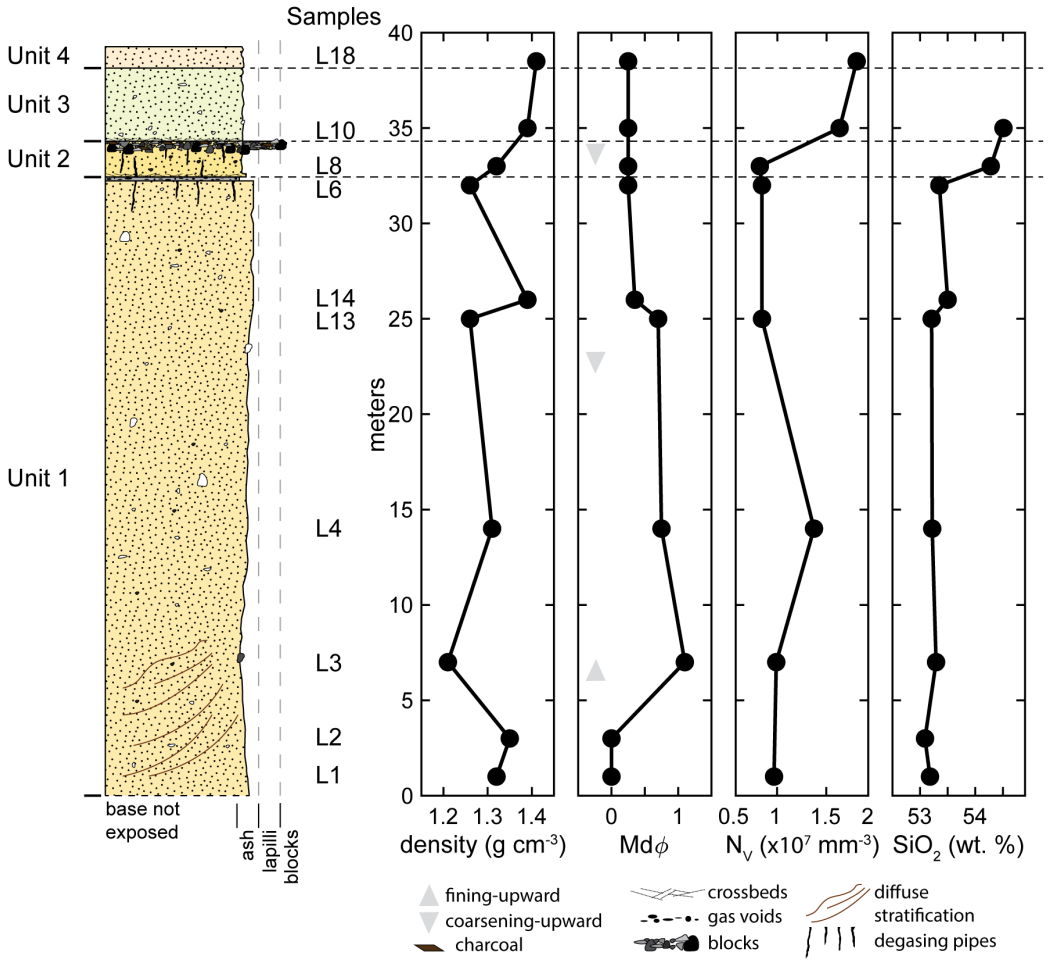

Figure S2 Eastern stratigraphic section reported in Marshall et al. (2022) (their Fig. 4) alongside density, Mdϕ, volumetric microlite number densities (Nv), and SiO_2-content. The stratigraphic column is constructed from samples across exposures east1, east2, and east3 (Fig. S1).

Samples investigated in this study (Table S1) were collected from fresh exposures at various distances from the present-day vent and throughout the four flow units exposed in the eastern outcrops. Lapilli-sized pyroclasts representing the average density and ± one standard deviation were selected for scanning electron microscopy and x-ray tomography.

Clasts selected for scanning electron microscopy (SEM) and x-ray computed microtomography (μCT) were selected based on clast density. SEM images were collected on a Teneo FEI Scanning Electron Microscope at the Boise State University Center for Materials Characterization. Imaging beam current was 6.4 nA and the beam current accelerating voltage was 15 kV. Clast cores 3.3 mm in diameter from the center of clasts were drilled for μCT and imaged at Lawrence Berkeley National Laboratory's Advanced Light Source on beamline 8.3.2 using 25–30 kV monochromatic X-rays, 200 ms exposure times, a PCO edge camera with 5X Mitutoyo lens, and a 50 mm LuAG scintillator. Samples were imaged during 180° continuous sample rotation. The linear voxel size of images is 1.3 μm.

We observed heterogeneous domains of vesicle textures in all size ranges of Ci pyroclasts across all exposures, in 85% of our thin sections, and in 53% of our tomography datasets. Entrained lithics exist in 92% of all thin sections and tomography datasets and in every block-size hand sample we collected. We attribute the lower percentage of tomography datasets containing heterogeneous domains of vesicle textures with the small diameter of cores collected (3.4 mm), which reduces the possibility of intersecting such domains. Additionally, at the time tomography data were collected, the fusing hypothesis presented in this manuscript was not a concept we were investigating and thus was not factored in to how we collected those data.

Table S1 Location information for images in manuscript figures.

Figure	Sample	Unit[a]	Outcrop name[b]	Height above base[c] of unit (m)	Distance from vent[e] (km)
1A	L25	unk	west4	1	16.5
1B	L9	Unit 2	east3	1.5	12
1C	L42	unk	west1	0.1	16.5
1D	L42	unk	west1	0.1	16.5
1E	L23	unk	west9	0.5	10
2A	L10	Unit 3	east3	0.1	12
2B	L21	unk	east4	0.1	13
2C	L25	unk	west4	0.1	16.5
2D	L2	Unit1	east1	3	12
2E	L4	Unit1	east2	14	12
2F	L6	Unit 1	east3	32	12
2G	L3	Unit 1	east1	7	12
2H	L3	Unit 1	east1	7	12
2I	L2	Unit 1	east1	3	12
4E[d]	L4	Unit 1	east2	14	12
4F	L3	Unit 1	east1	7	12
4G	L25	unk	west4	0.1	16.5
4H	L34	unk	north2	0.5	15

[a,b]Unit and outcrop names from Marshall et al. (2022). See Figure S1.
[c]In most cases, the base of the deposit is not exposed, and base here refers to the lowest-most point of the exposure
[d]Valdivia et al. (2022)
[e]Measured in GoogleEarth

Ci crystal size distributions

Plagioclase crystal size distributions (CSDs) were measured and reported in Valdivia et al. (2022) (Fig. S3). Those authors manually traced plagioclase microlites using backscattered electron images collected on a Teneo FEI Field Emission Scanning Electron Microscope at the Boise State University Center for Materials Characterization using a beam current of 6.4 nA and 15 kV accelerating voltage at 1500–2000X magnifications. Microlites were assigned a crystal habit using *CSDslice v.5* (Morgan and Jerram, 2006) and used as inputs for *CSDcorrections v.1.6* (Higgins, 2000) to create plagioclase CSDs. Using linear regression fitting, Valdivia et al. (2022) fit two segment

regressions with high R^2 values (Fig. S3) to the CSDs, and using CSD theory and, following the methods of Bamber et al. (2020), calculated timescales of crystallization of seconds to hours. Due to the difficulty in identifying units outside of the eastern stratigraphic section, the CSD samples are all from the eastern stratigraphic sequence (Figs. S1, S2).

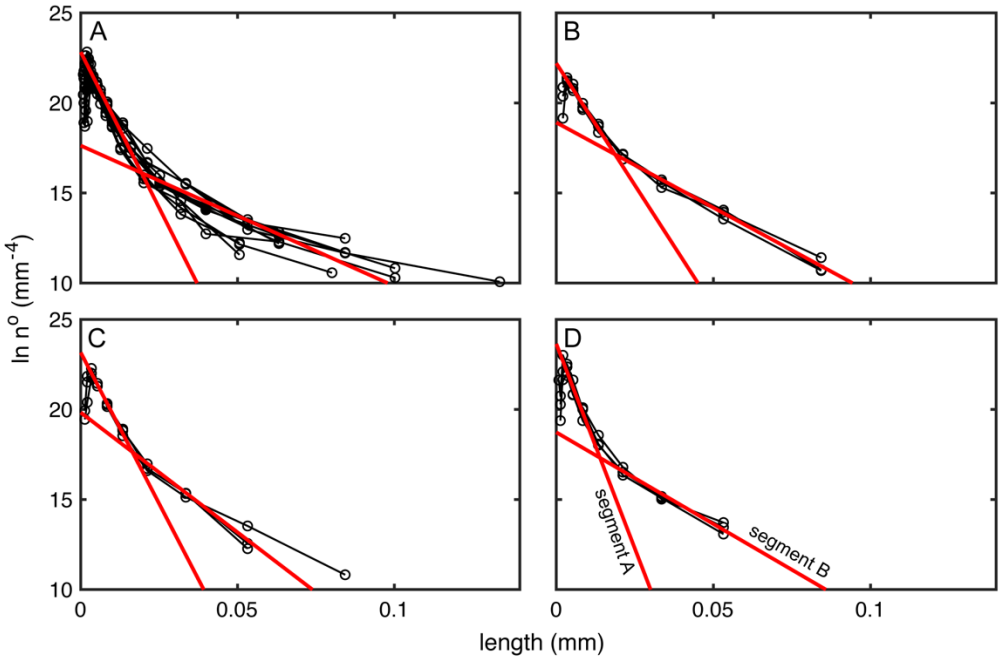

Figure S3 Crystal size distributions (CSDs) with fit regressions based on R^2 values from Valdivia et al. (2022) (their Fig. 4). A) Unit 1. A total of three thin sections were analyzed, one each for the bottom, middle, and top of the unit. B) Unit 2. C) Unit 3. D) Unit 4. Segment A regressions represent late crystallization of smaller microlites whereas segment B regressions are fit to larger crystals produced earlier in ascent. Valdivia et al. (2022) interpret this difference in regression slope as changes in ascent rate of the Curacautín magma prior to eruption.

Table S2 Samples investigated by Valdivia et al. (2022) for plagioclase crystal size distribution analysis. Refer to Figs. S1 and S2 for sample locations. Here, regressions are fit to microlite size populations with long axes (l) >10 μm and l≤10 μm (Fig 5.3). We calculated Pearson coefficients (ρ) for each regression fit. Each CSD is an average of 3 analyzed images; therefore, the value of ρ provided is the average of that total dataset.

Sample	Unit	Outcrop name	Number of images analyzed for CSDs	l >10 μm regression ρ	l≤10 μm regression ρ
L18	4	east3	3	-0.978	-0.987
L10	3	east3	3	-0.989	-0.999
L8	2	east3	3	-0.990	-0.993
L6	1 (top)	east3	3	-0.951	-0.965
L4	1 (middle)	east1	3	-0.975	-0.997
L1	1 (bottom)	east1	3	-0.956	-0.997

[a] $\rho = \frac{n\Sigma xy - \Sigma x \Sigma y}{\sqrt{[n\Sigma x^2 - (\Sigma x)^2][n\Sigma y^2 - (\Sigma y)^2]}}$ where n = number of CSD points

References Cited

Bamber, E.C., Arzilli, F., Polacci, M., Hartley, M.E., Fellowes, J., Di Genova, D., Chavarría, D., Saballos, J.A., and Burton, M.R., 2020, Pre- and *syn*-eruptive conditions of a basaltic Plinian eruption at Masaya Volcano, Nicaragua: The Masaya Triple Layer (2.1 ka): Journal of Volcanology and Geothermal Research, v. 392, p. 1–16, doi: 10.1016/j.jvolgeores.2019.106761.

Higgins, M.D., 2000, Measurement of crystal size distributions: American Mineralogist, v. 85, p. 1105–1116.

Houghton, B.F., and Wilson, C.J.N., 1989, A vesicularity index for pyroclastic deposits: Bulletin of Volcanology, v. 51, p. 451–462, doi: 10.1007/BF01078811.

Marshall, A.A., Brand, B.D., Martínez, V., Bowers, J.M., Wanless, V.D., Andrews, B.J., Manga, M., Valdivia, P., and Giordano, G., 2022, The mafic Curacautín ignimbrite of Llaima volcano, Chile: Journal of Volcanology and Geothermal Research, v. 421, 107418, doi: 10.1016/j.jvolgeores.2021.107418.

Morgan, D.J., and Jerram, D.A., 2006, On estimating crystal shape for crystal size distribution analysis: Journal of Volcanology and Geothermal Research, v. 154, p. 1–7, doi: 10.1016/j.jvolgeeores.2005.09.016.

Naranjo, J.A., and Moreno, H., 1991, Actividad explosiva postglacial en el volcan Llaima, Andes del sur (38°45'S): Revista Geológica de Chile, v. 18, 1, p. 69–80.

Valdivia, P., Marshall, A.A., Brand, B.D., and Manga, M., 2022, Mafic explosive volcanism at Llaima volcano: 3D X-ray microtomography reconstruction of pyroclasts to constrain shallow conduit processes: Bulletin of Volcanology, v. 84, 2, doi: 10.1007/s00445-021-01514-8.

CHAPTER 6: CONCLUSIONS

Mafic magma compositions are among the most abundant magmas erupted on Earth and throughout the Solar System (Parfitt, 2004). Of those eruptions, mafic Plinian and ignimbrite-forming eruptions are rare events that pose significant threats to those living on or near mafic volcanic centers. Uncovering what causes such eruptions is therefore necessary to help inform communities of their risk and improve scientists' ability to forecast similar eruptions in the future. In this dissertation, I investigated the causes and consequences of the mafic Curacautín eruption of Llaima volcano. I accomplished this dissertation using a comprehensive but complementary suite of field work, laboratory work, and numerical modeling. In this way, I combined numerous datasets that allowed me to investigate the Ci and mafic explosive volcanism from the macro to microscale. The work here adds to the growing body of literature whose goal is to unravel the mysteries behind mafic, explosive volcanism.

In Chapter 2, I explored the physical characteristics of the Ci (Marshall et al., 2022a). Using field observations, granulometry, and radiocarbon dating, I determined the Ci is a massive to diffusely stratified, very poorly sorted, coarse ash tuff that was deposited as four individual pulses in valleys and drainages around Llaima during a single eruptive event at ~12,600 years BP. Using field observations, mapping, and measured stratigraphic sections, I revised the tephra volume estimate of the Ci to between 6 and 9 km^3, or 3.5–4.5 km^3 DRE with a total mass of $0.97–1.2\times10^{13}$ kg. This corresponds to an eruption duration of 15–17 hrs. Pyroclast bubble and microlite textures

suggest the Ci was driven by rapid ascent of a moderately vesicular, non-degassed magma with a significantly high viscosity to permit brittle fragmentation. These conclusions support the findings of other studies (e.g., Arzilli et al., 2019; Bamber et al., 2020) that suggest rapid magma ascent and high viscosities as the primary driver of dry, mafic explosive eruptions.

Chapter 3 expanded upon the microlite textural measurements of Chapter 2. I conducted CSD analyses of Ci plagioclase microlites to calculate timescales of plagioclase crystallization, population densities, and nucleation rates. Ci pyroclasts are microlite-rich and glass-poor. Across all units, ϕ_{plag}, ϕ_{anh}, and ϕ_{feti} are 0.29–0.44, 0.17–0.30, and 0.002–0.020, respectively. Glass content varies from 0.25 to 0.54. Average Ci plagioclase N_A and N_V are 4.99–7.32×10^4 mm^{-2} and 0.795–1.84×10^7 mm^{-3}, respectively. CSDs are all concave upward and kinked suggesting changing ascent rates during magma ascent. Using experimentally derived plagioclase growth rates, I calculated timescales of crystallization from seconds to minutes for the smallest size population of plagioclase microlites and between minutes to hours for the largest size population of plagioclase. The smallest size population of microlites is representative of rapid magma ascent in the shallow subsurface or syn-eruptive crystallization, while the largest size population reflects crystallization from deeper in the crust. This work further supports the hypothesis that rapid ascent induces high ΔT and thus extensive microlite crystallization, resulting in rapid increases of viscosity that trap volatiles necessary for brittle fragmentation.

Chapter 4 built upon the SNGPlag model of Befus and Andrews (2018) and Andrews and Befus (2020) by extending the calibration space to include mafic compositions. Using the results of mafic decompression experiments, I found that while

plagioclase microlites nucleate slower in mafic melts than they do in felsic melts, once nucleated they grow at a rate up to ~1000 times greater than in felsic magmas. This helps explain why plagioclase in the products of nearly all explosive mafic deposits are characterized by high number densities of acicular forms. Using these new plagioclase nucleation and growth rates for mafic magmas, I modeled the decompression of Ci magma and found that average decompression rates are between 1.2×10^{-2} and 2.6×10^{-2} MPa s^{-1} for Unit 1, $1.7–2.5\times10^{-2}$ MPa s^{-1} for Unit 2, $0.18–1.5\times10^{-2}$ MPa s^{-1} for Unit 3, and $2.9–3.9\times10^{-2}$ MPa s^{-1} for Unit 4. These rates are approximately two orders of magnitude less than those calculated for the Llaima shallow conduit using the bubble number density rate meter of Toramaru (2006) (Valdivia et al., 2022). Using two sets of assumptions, I calculated first order average ascent rate minima of ~0.1–1.7 m s^{-1} and average maximum ascent rates of ~0.3–5.9 m s^{-1}. Our modeling agrees with mafic decompression experiments and other modeling and confirms that applicability of SNGPlag for simulating mafic magma decompression.

In Chapter 5, I offer a new conceptual model for conduit conditions during the Curacautín eruption from interpretations of pyroclast textures identified in Chapters 2 and 3 (Marshall et al., 2022b). I identified domains of contrasting vesicularity and bubble textures within pyroclasts and hypothesized they formed during autobrecciation and pyroclast fusing within the conduit prior to eruption. Suture zones are overprinted with uniform microlite textures and suggest that proto-pyroclast fusing occurred prior to the majority of groundmass crystallization. The presence of broken microlites >10 μm is further evidence that fragmentation occurred prior to the crystallization of the smallest size population of plagioclase. These unique textures are not discussed extensively in the

literature and may provide insights into conduit processes not previously considered in mafic eruptions but may profoundly impact how these magmas erupt.

The four chapters of this dissertation examined the Ci from the macro to microscale to fully understand the causes and consequences of voluminous, mafic, ignimbrite-forming eruptions. The results here support the findings of other studies that suggest rapid magma ascent and increased viscosity in response to high undercooling drive mafic, explosive volcanism in the absence of external water. An important outcome of this dissertation is the application of the CSD analyses in Chapter 3 and the experimental work of Shea and Hammer (2013) in expanding the calibration of SNGPlag to basaltic andesite compositions. This allows future workers to apply the same methods to investigate mafic magma decompression rates without the need for costly and time-intensive experiments. Finally, the unique textures observed in this work may provide new insights into conduit processes not previously considered in mafic eruptions.

References

Andrews BJ, Befus KS (2020) Supersaturation Nucleation and Growth of Plagioclase: a numerical model of decompression-induced crystallization. Contrib Mineral Petrol 175:23. doi: 10.1007/s00410-020-1660-9

Arzilli F, La Spina G, Burton MR, Polacci, M, Le Gall N, Hartley ME, Di Genova D, Cai B, Vo NT, Bamber EC, Nonni S, Atwood R, Llewellin EW, Brooker RA, Mader HM, Lee PD (2019) Magma fragmentation in highly explosive basaltic eruptions induced by rapid crystallization. Nat Geosci 12:1023–1028. doi: 10.1038/s41561-019-0468-6

Bamber EC, Arzilli F, Polacci M, Hartley ME, Fellowes J, Di Genova D, Chavarría D, Saballos JA, Burton MR (2020) Pre- and *syn*-eruptive conditions of a basaltic Plinian eruption at Masaya Volcano, Nicaragua: The Masaya Triple Layer (2.1 ka). J Volcanol Geotherm Res 392:1–16. doi: 10.1016/j.jvolgeores.2019.106761

Befus KS, Andrews BJ (2018) Crystal nucleation and growth produced by continuous decompression of Pinatubo magma. Contrib Mineral Petrol 173:92. doi: 10.1007/s00410-018-1519-5

Marshall AA, Brand BD, Martínez V, Bowers JM, Walker M, Wanless VD, Andrews BJ, Manga M, Valdivia P, Giordano D (2022a) The mafic Curacautín ignimbrite of Llaima volcano, Chile. J Volcanol Geotherm Res 421:107418. doi: 10.1016/j.jvolgeores.2021.107418

Marshall AA, Manga M, Brand BD, Andrews BJ (2022b) Autobrecciation and fusing of mafic magma preceding explosive eruptions. Geology (in press)

Parfitt E (2004) A discussion of the mechanisms of explosive basaltic eruptions. J. Volcanol Geotherm Res 134:77–107. doi: 10.1016/j.jvolgeores.2004.01.002

Shea T, Hammer JE (2013) Kinetics of cooling- and decompression-induced crystallization in hydrous mafic-intermediate magmas. J Volcanol Geotherm Res 260:127–145. doi: 10.1016/j.jvolgeores.2013.04.018

Toramaru A (2006) BND (bubble number density) decompression rate meter for explosive volcanic eruptions. J Volcanol Geotherm Res 154:303–316. doi: 10.1016/j.jvolgeores.2006.03.027

Valdivia P, Marshall AA, Manga M, Brand BD, Huber C (2022) Mafic explosive volcanism at Llaima volcano: 3D X-ray microtomography reconstruction of pyroclasts to constrain shallow conduit processes. Bull Volcanol 48(2). doi: 10.1007/s00445-021-01415-8

APPENDIX A: SNAGPLAG RESULTS

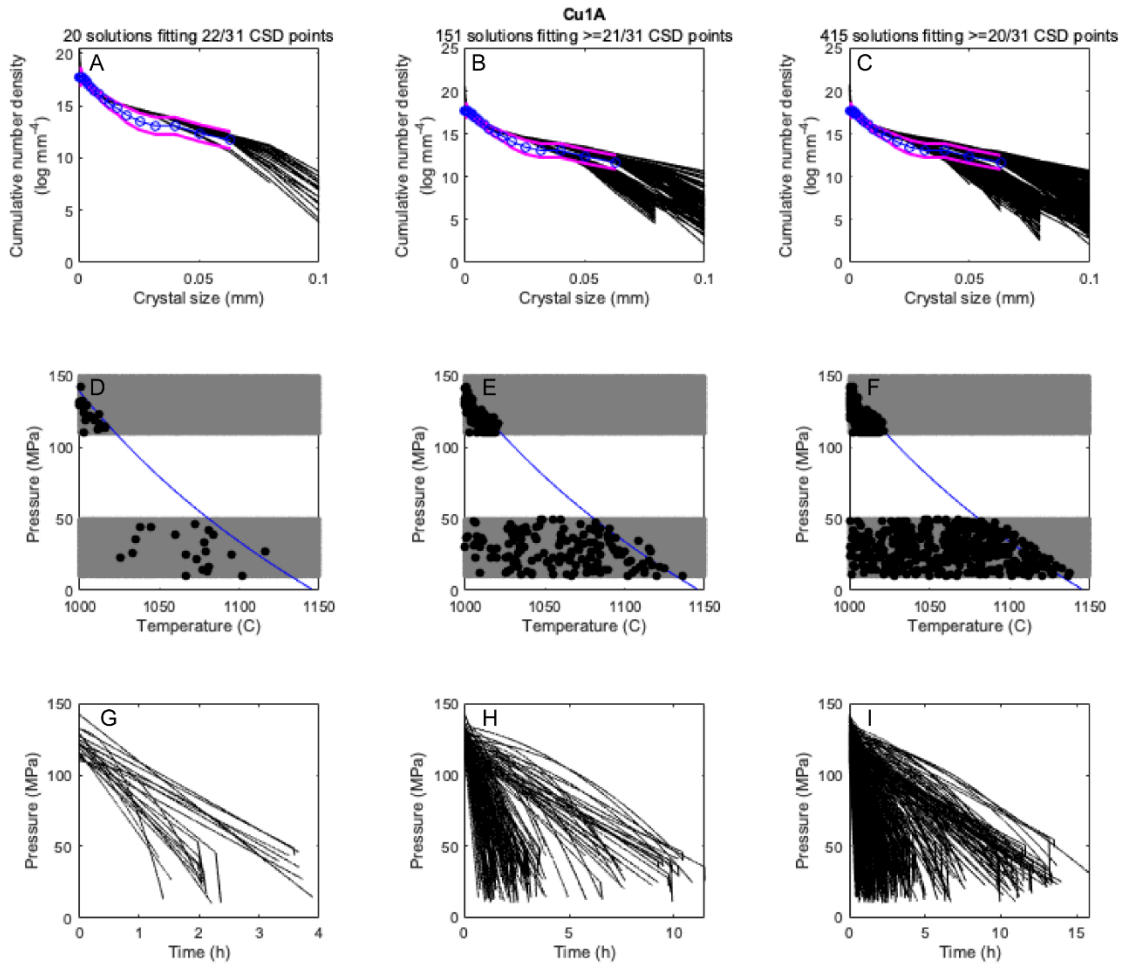

Figure A.1 SNGPlag results for Curacautín sample L1 image A (Cu1A). (A, B, C) Crystal size distributions (CSDs) of model results (black lines), the natural CSD (blue line), and two standard deviations (2σ; pink lines). Above plots A, B, and C are the description of the number of model solutions that match the natural CSD within 2σ and the number of CSD points that are included. Therefore, A is the best fit solutions, B is the second best set of solutions, and C is the third best set of solutions. (D, E, F) The corresponding sampled pressure-temperature space (gray fields), the starting and final P-T points from solutions in A, B, C (black points), and the plagioclase liquidus modeled by MELTS (Gualda and Ghiorso, 2012). (G, E, F) The associated modeled decompression pathways that produced the CSDs in A, B, and C. All plots in Appendix A follow this same format.

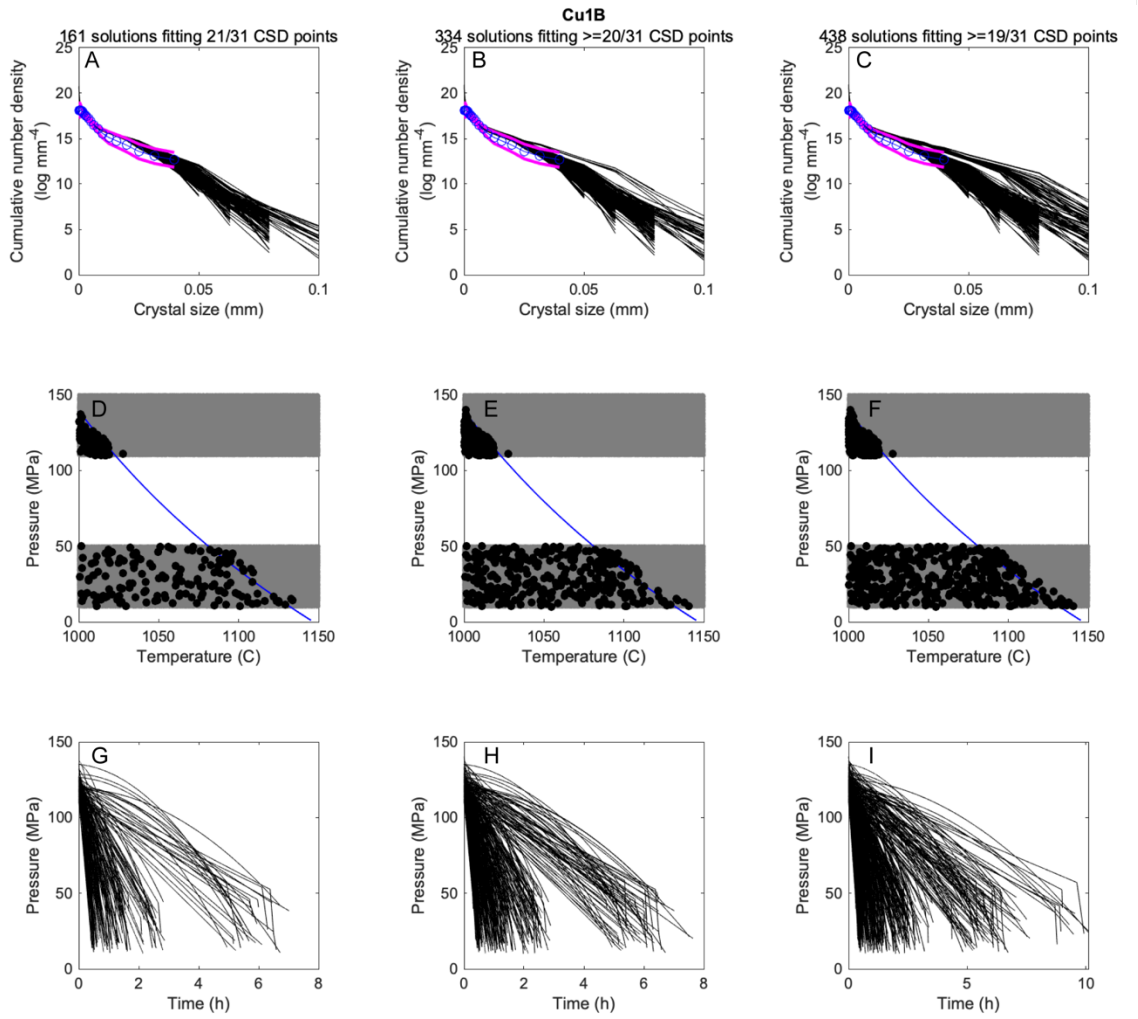

Figure A.2 SNGPlag results for Curacautín sample L1 image B (Cu1B). (A, B, C) Crystal size distributions (CSDs) of model results (black lines), the natural CSD (blue line), and two standard deviations (2σ; pink lines). Above plots A, B, and C are the description of the number of model solutions that match the natural CSD within 2σ and the number of CSD points that are included. Therefore, A is the best fit solutions, B is the second best set of solutions, and C is the third best set of solutions. (D, E, F) The corresponding sampled pressure-temperature space (gray fields), the starting and final P-T points from solutions in A, B, C (black points), and the plagioclase liquidus modeled by MELTS (Gualda and Ghiorso, 2012). (G, E, F) The associated modeled decompression pathways that produced the CSDs in A, B, and C. All plots in Appendix A follow this same format.

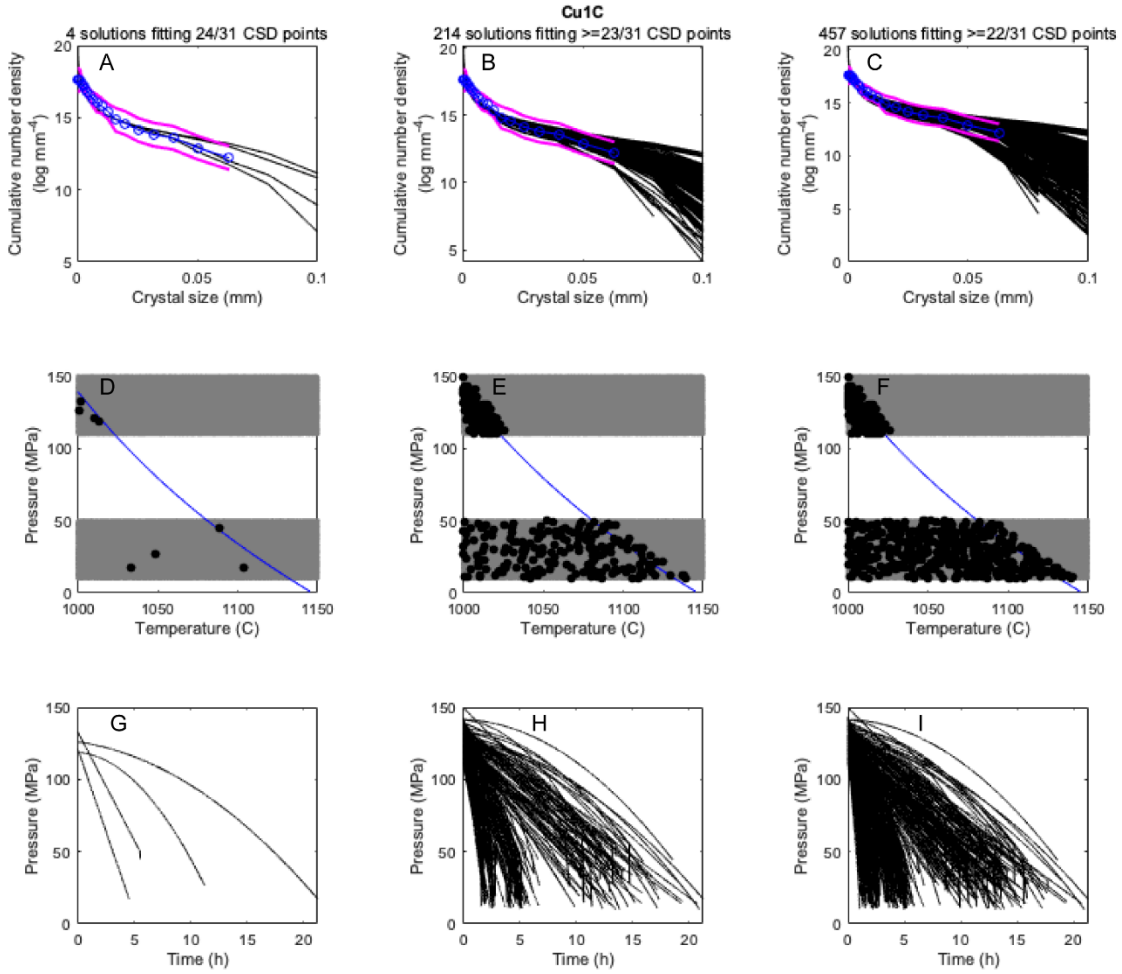

Figure A.3 SNGPlag results for Curacautín sample L1 image C (Cu1C). (A, B, C) Crystal size distributions (CSDs) of model results (black lines), the natural CSD (blue line), and two standard deviations (2σ; pink lines). Above plots A, B, and C are the description of the number of model solutions that match the natural CSD within 2σ and the number of CSD points that are included. Therefore, A is the best fit solutions, B is the second best set of solutions, and C is the third best set of solutions. (D, E, F) The corresponding sampled pressure-temperature space (gray fields), the starting and final P-T points from solutions in A, B, C (black points), and the plagioclase liquidus modeled by MELTS (Gualda and Ghiorso, 2012). (G, E, F) The associated modeled decompression pathways that produced the CSDs in A, B, and C. All plots in Appendix A follow this same format.

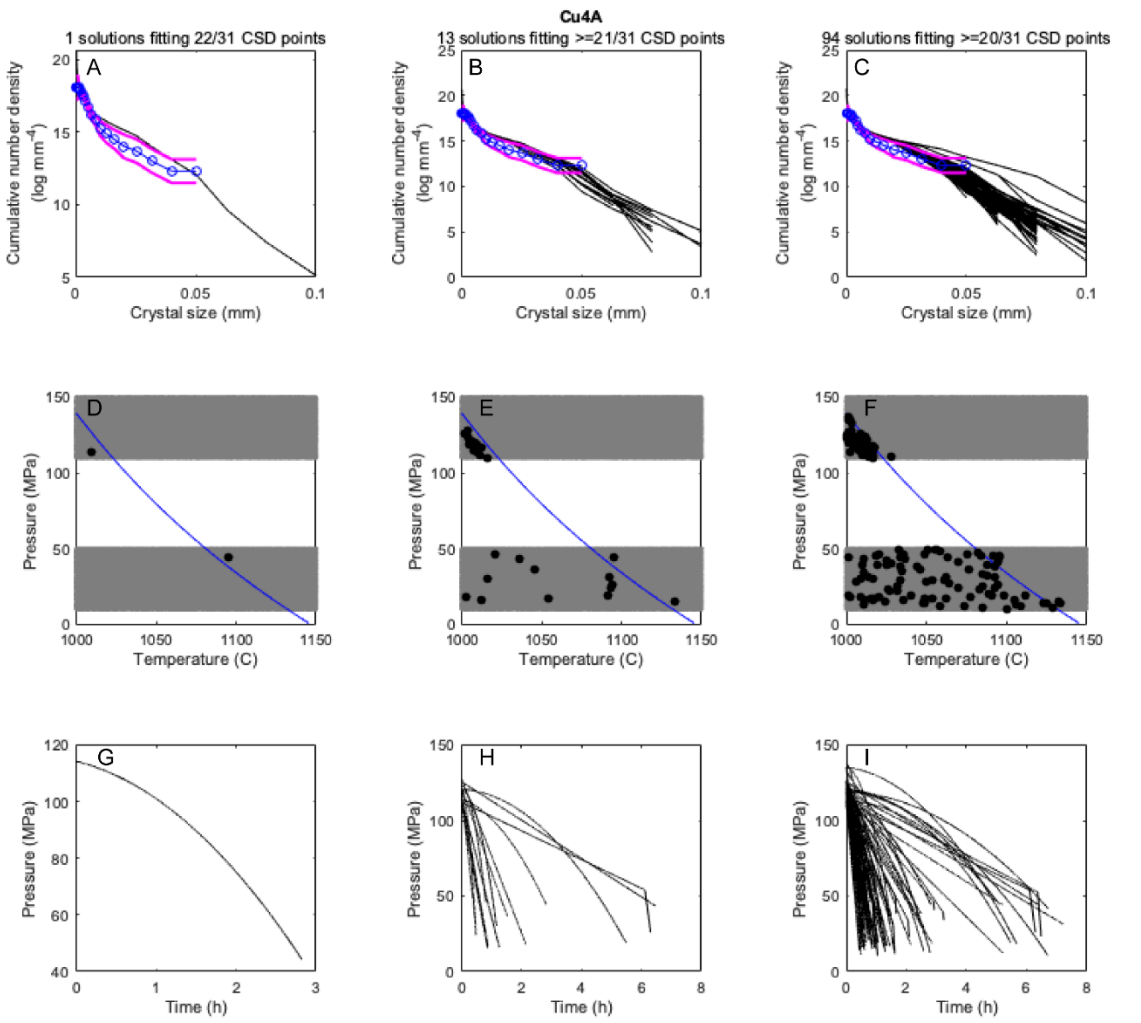

Figure A.4 SNGPlag results for Curacautín sample L4 image A (Cu4A). (A, B, C) Crystal size distributions (CSDs) of model results (black lines), the natural CSD (blue line), and two standard deviations (2σ; pink lines). Above plots A, B, and C are the description of the number of model solutions that match the natural CSD within 2σ and the number of CSD points that are included. Therefore, A is the best fit solutions, B is the second best set of solutions, and C is the third best set of solutions. (D, E, F) The corresponding sampled pressure-temperature space (gray fields), the starting and final P-T points from solutions in A, B, C (black points), and the plagioclase liquidus modeled by MELTS (Gualda and Ghiorso, 2012). (G, E, F) The associated modeled decompression pathways that produced the CSDs in A, B, and C. All plots in Appendix A follow this same format.

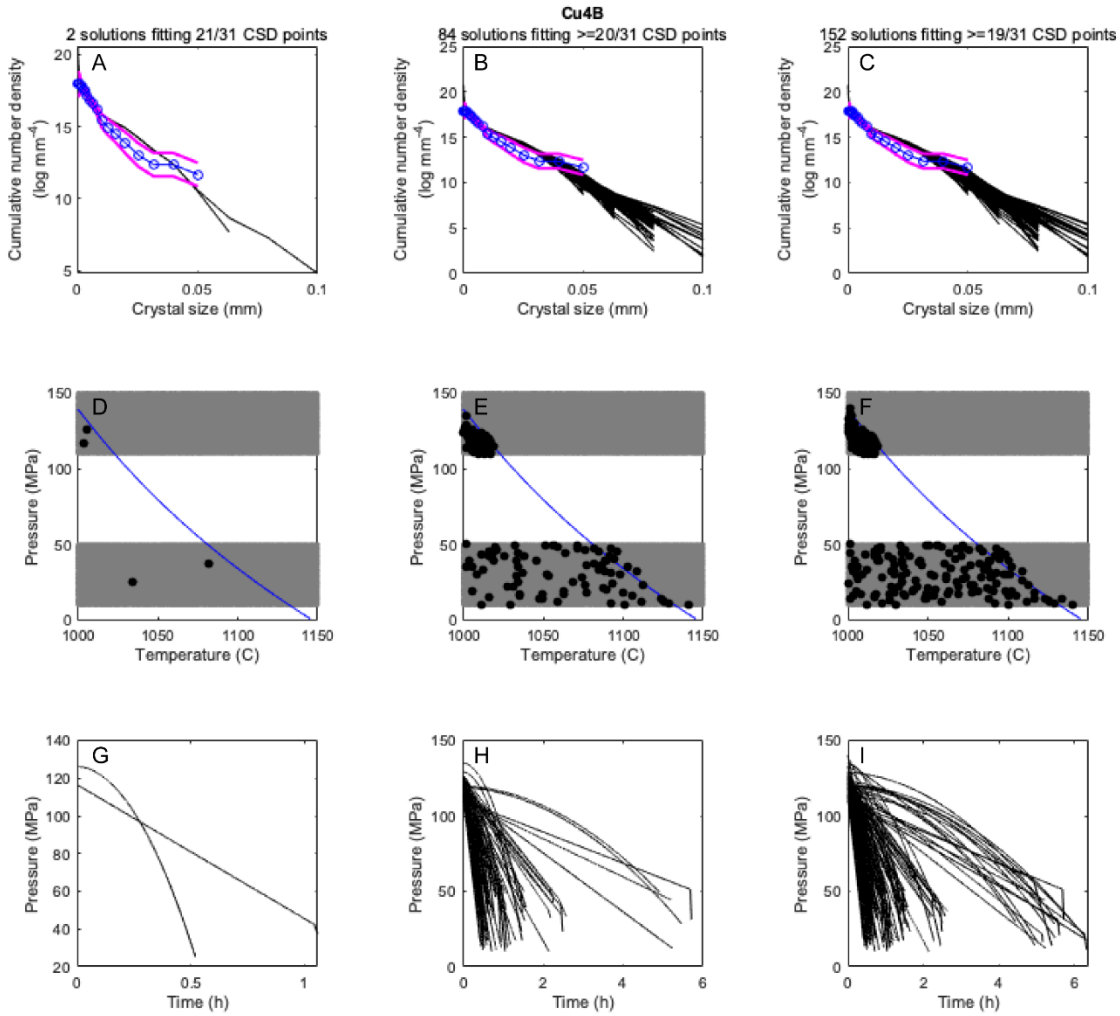

Figure A.5 SNGPlag results for Curacautín sample L4 image B (Cu4B). (A, B, C) Crystal size distributions (CSDs) of model results (black lines), the natural CSD (blue line), and two standard deviations (2σ; pink lines). Above plots A, B, and C are the description of the number of model solutions that match the natural CSD within 2σ and the number of CSD points that are included. Therefore, A is the best fit solutions, B is the second best set of solutions, and C is the third best set of solutions. (D, E, F) The corresponding sampled pressure-temperature space (gray fields), the starting and final P-T points from solutions in A, B, C (black points), and the plagioclase liquidus modeled by MELTS (Gualda and Ghiorso, 2012). (G, E, F) The associated modeled decompression pathways that produced the CSDs in A, B, and C. All plots in Appendix A follow this same format.

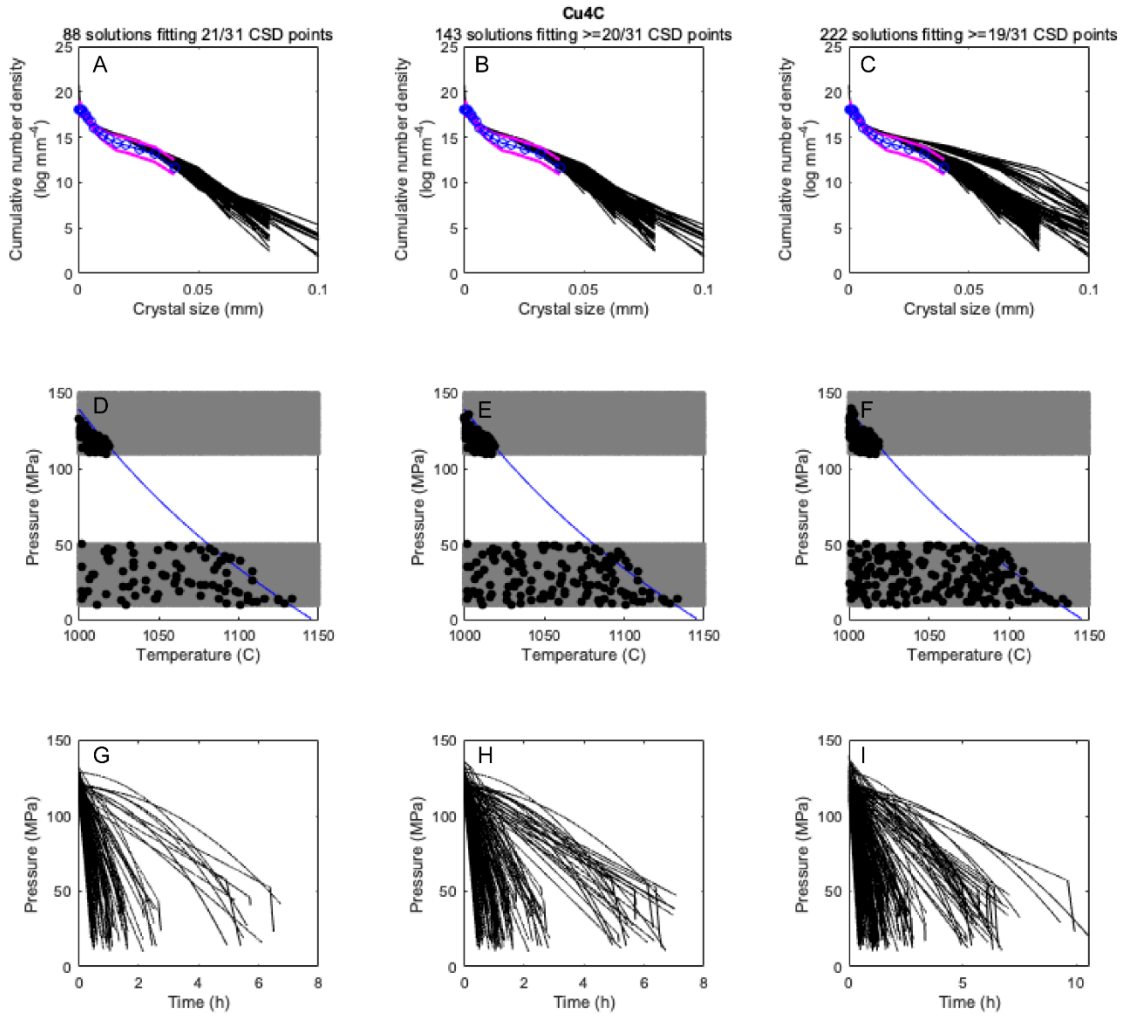

Figure A.6 SNGPlag results for Curacautín sample L4 image C (Cu4C). (A, B, C) Crystal size distributions (CSDs) of model results (black lines), the natural CSD (blue line), and two standard deviations (2σ; pink lines). Above plots A, B, and C are the description of the number of model solutions that match the natural CSD within 2σ and the number of CSD points that are included. Therefore, A is the best fit solutions, B is the second best set of solutions, and C is the third best set of solutions. (D, E, F) The corresponding sampled pressure-temperature space (gray fields), the starting and final P-T points from solutions in A, B, C (black points), and the plagioclase liquidus modeled by MELTS (Gualda and Ghiorso, 2012). (G, E, F) The associated modeled decompression pathways that produced the CSDs in A, B, and C. All plots in Appendix A follow this same format.

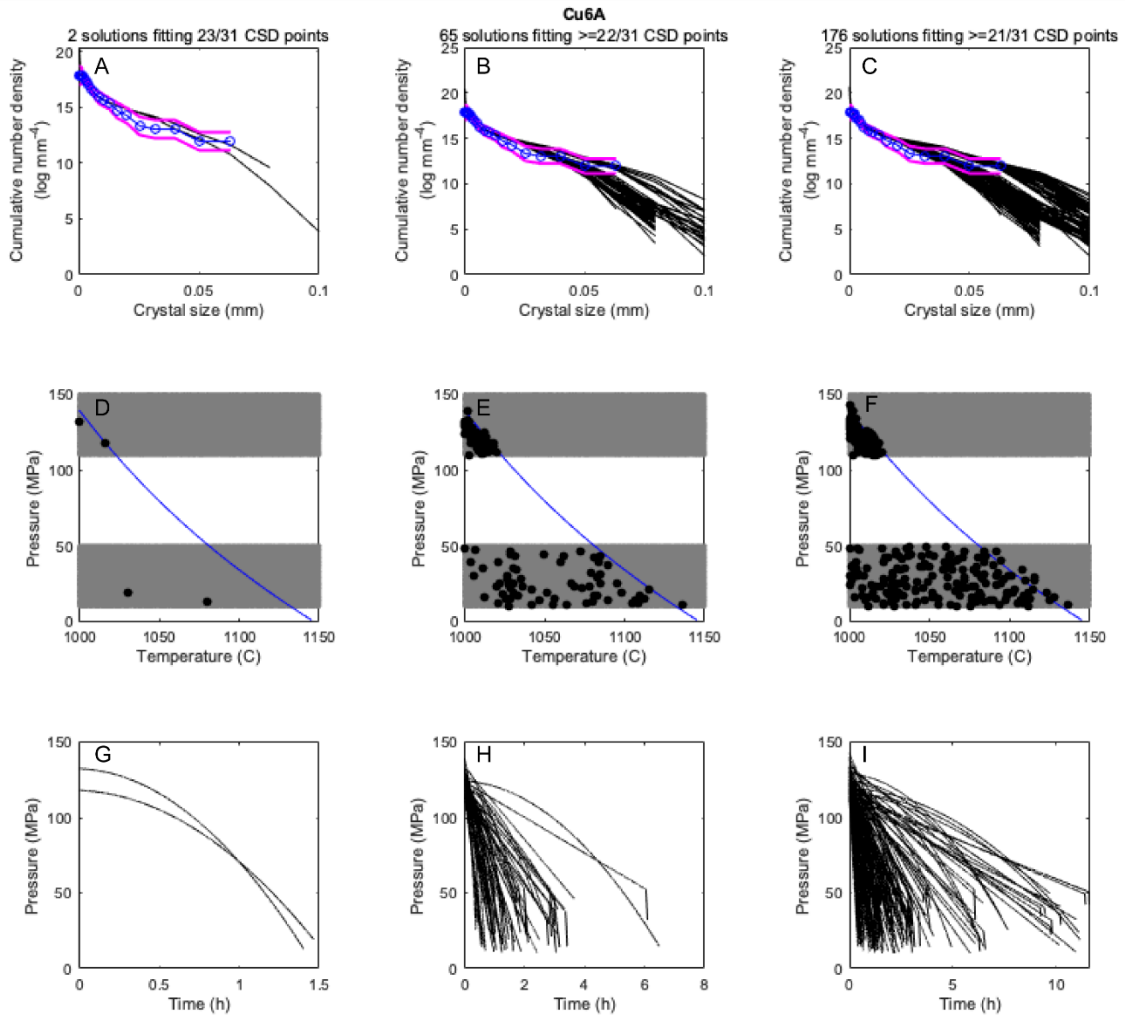

Figure A.7 SNGPlag results for Curacautín sample L6 image A (Cu6A). (A, B, C) Crystal size distributions (CSDs) of model results (black lines), the natural CSD (blue line), and two standard deviations (2σ; pink lines). Above plots A, B, and C are the description of the number of model solutions that match the natural CSD within 2σ and the number of CSD points that are included. Therefore, A is the best fit solutions, B is the second best set of solutions, and C is the third best set of solutions. (D, E, F) The corresponding sampled pressure-temperature space (gray fields), the starting and final P-T points from solutions in A, B, C (black points), and the plagioclase liquidus modeled by MELTS (Gualda and Ghiorso, 2012). (G, E, F) The associated modeled decompression pathways that produced the CSDs in A, B, and C. All plots in Appendix A follow this same format.

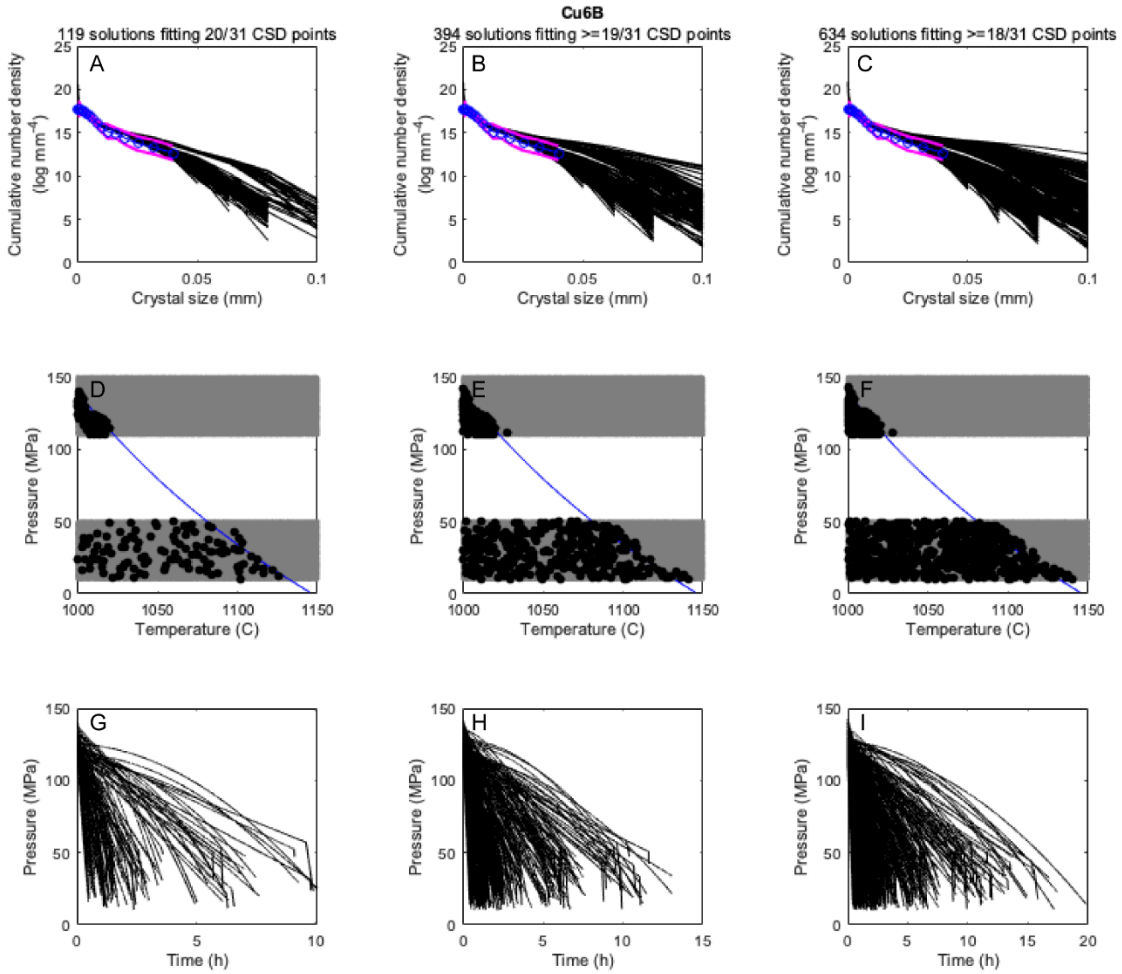

Figure A.8 SNGPlag results for Curacautín sample L6 image B (Cu6B). (A, B, C) Crystal size distributions (CSDs) of model results (black lines), the natural CSD (blue line), and two standard deviations (2σ; pink lines). Above plots A, B, and C are the description of the number of model solutions that match the natural CSD within 2σ and the number of CSD points that are included. Therefore, A is the best fit solutions, B is the second best set of solutions, and C is the third best set of solutions. (D, E, F) The corresponding sampled pressure-temperature space (gray fields), the starting and final P-T points from solutions in A, B, C (black points), and the plagioclase liquidus modeled by MELTS (Gualda and Ghiorso, 2012). (G, E, F) The associated modeled decompression pathways that produced the CSDs in A, B, and C. All plots in Appendix A follow this same format.

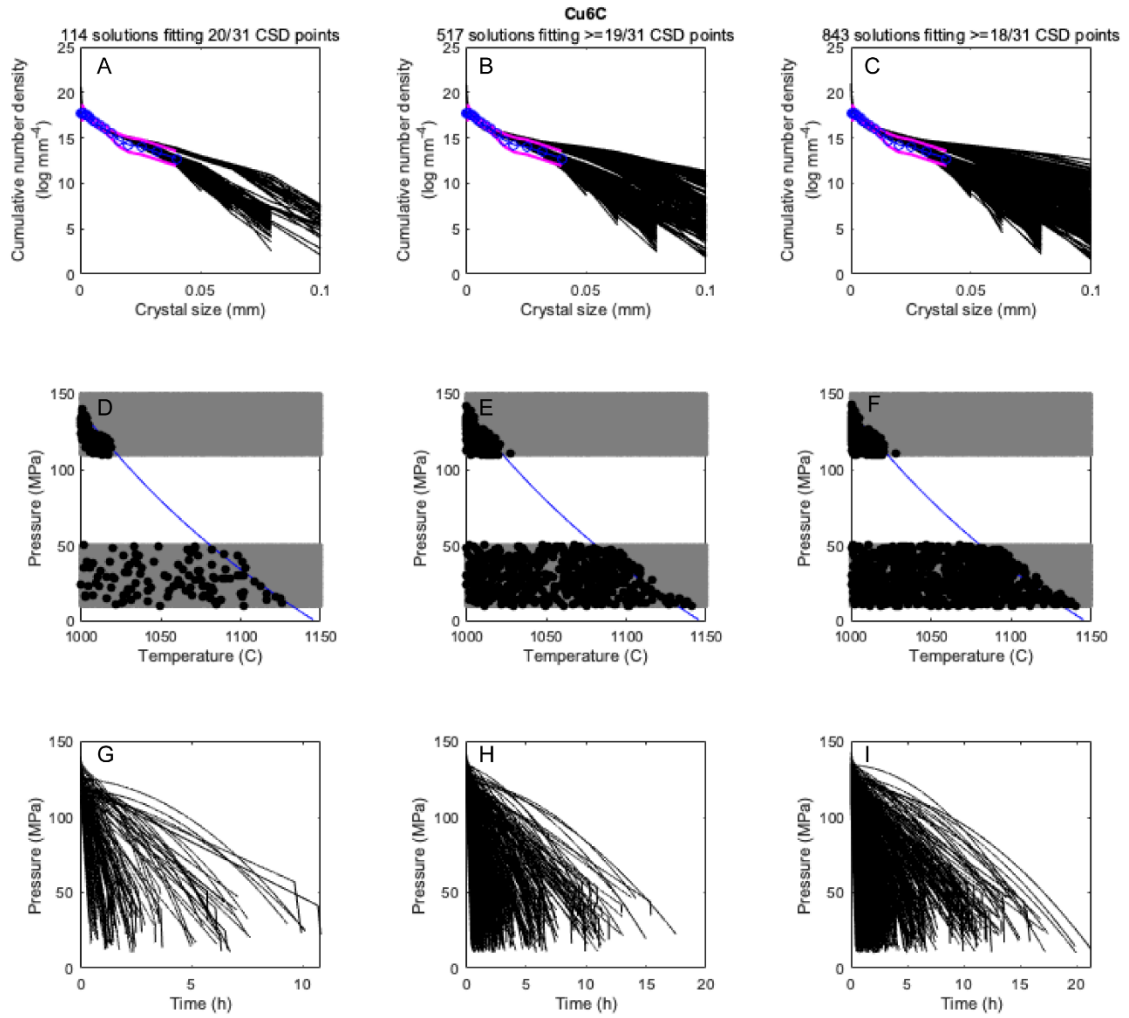

Figure A.9 SNGPlag results for Curacautín sample L6 image C (Cu6C). (A, B, C) Crystal size distributions (CSDs) of model results (black lines), the natural CSD (blue line), and two standard deviations (2σ; pink lines). Above plots A, B, and C are the description of the number of model solutions that match the natural CSD within 2σ and the number of CSD points that are included. Therefore, A is the best fit solutions, B is the second best set of solutions, and C is the third best set of solutions. (D, E, F) The corresponding sampled pressure-temperature space (gray fields), the starting and final P-T points from solutions in A, B, C (black points), and the plagioclase liquidus modeled by MELTS (Gualda and Ghiorso, 2012). (G, E, F) The associated modeled decompression pathways that produced the CSDs in A, B, and C. All plots in Appendix A follow this same format.

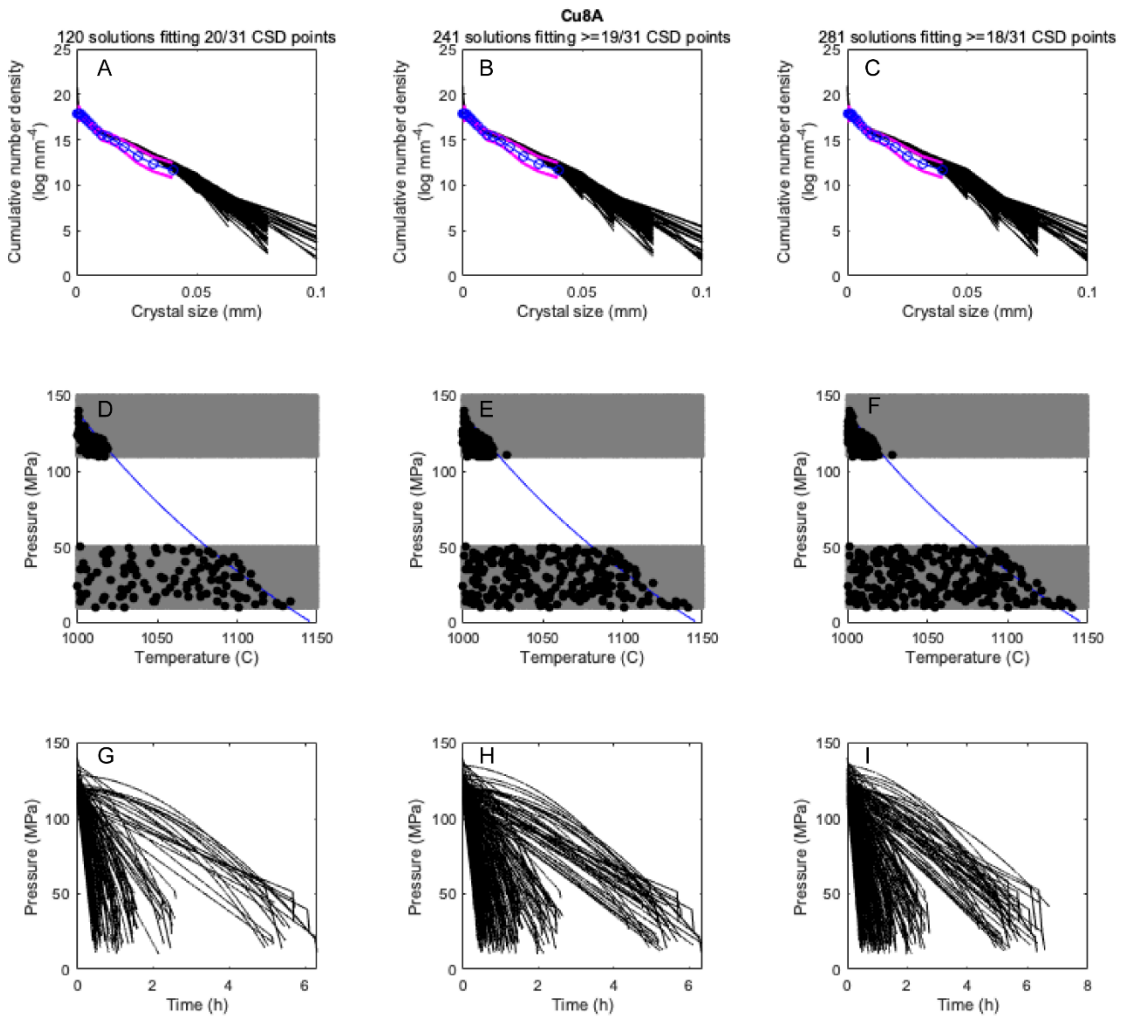

Figure A.10 SNGPlag results for Curacautín sample L8 image A (Cu8A). (A, B, C) Crystal size distributions (CSDs) of model results (black lines), the natural CSD (blue line), and two standard deviations (2σ; pink lines). Above plots A, B, and C are the description of the number of model solutions that match the natural CSD within 2σ and the number of CSD points that are included. Therefore, A is the best fit solutions, B is the second best set of solutions, and C is the third best set of solutions. (D, E, F) The corresponding sampled pressure-temperature space (gray fields), the starting and final P-T points from solutions in A, B, C (black points), and the plagioclase liquidus modeled by MELTS (Gualda and Ghiorso, 2012). (G, E, F) The associated modeled decompression pathways that produced the CSDs in A, B, and C. All plots in Appendix A follow this same format.

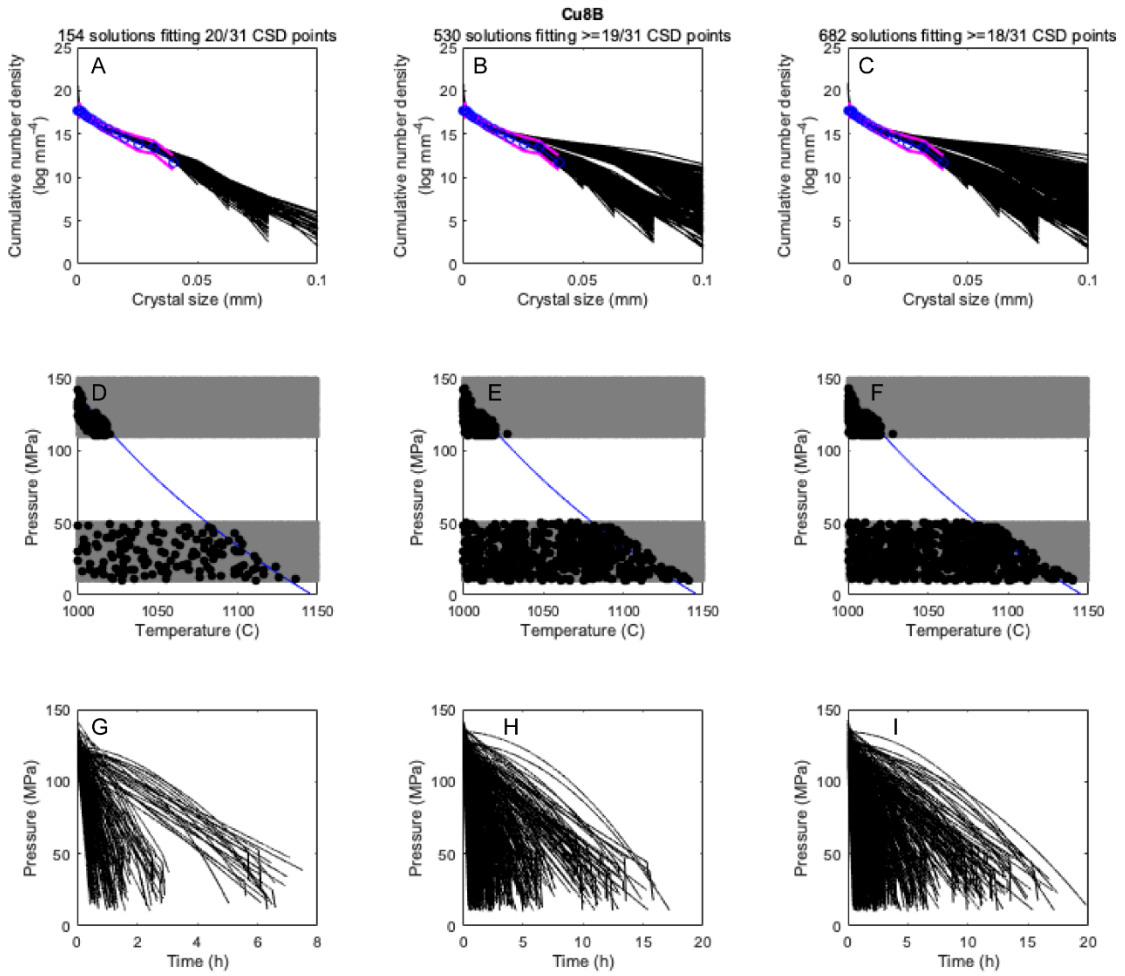

Figure A.11 SNGPlag results for Curacautín sample L8 image B (Cu8B). (A, B, C) Crystal size distributions (CSDs) of model results (black lines), the natural CSD (blue line), and two standard deviations (2σ; pink lines). Above plots A, B, and C are the description of the number of model solutions that match the natural CSD within 2σ and the number of CSD points that are included. Therefore, A is the best fit solutions, B is the second best set of solutions, and C is the third best set of solutions. (D, E, F) The corresponding sampled pressure-temperature space (gray fields), the starting and final P-T points from solutions in A, B, C (black points), and the plagioclase liquidus modeled by MELTS (Gualda and Ghiorso, 2012). (G, E, F) The associated modeled decompression pathways that produced the CSDs in A, B, and C. All plots in Appendix A follow this same format.

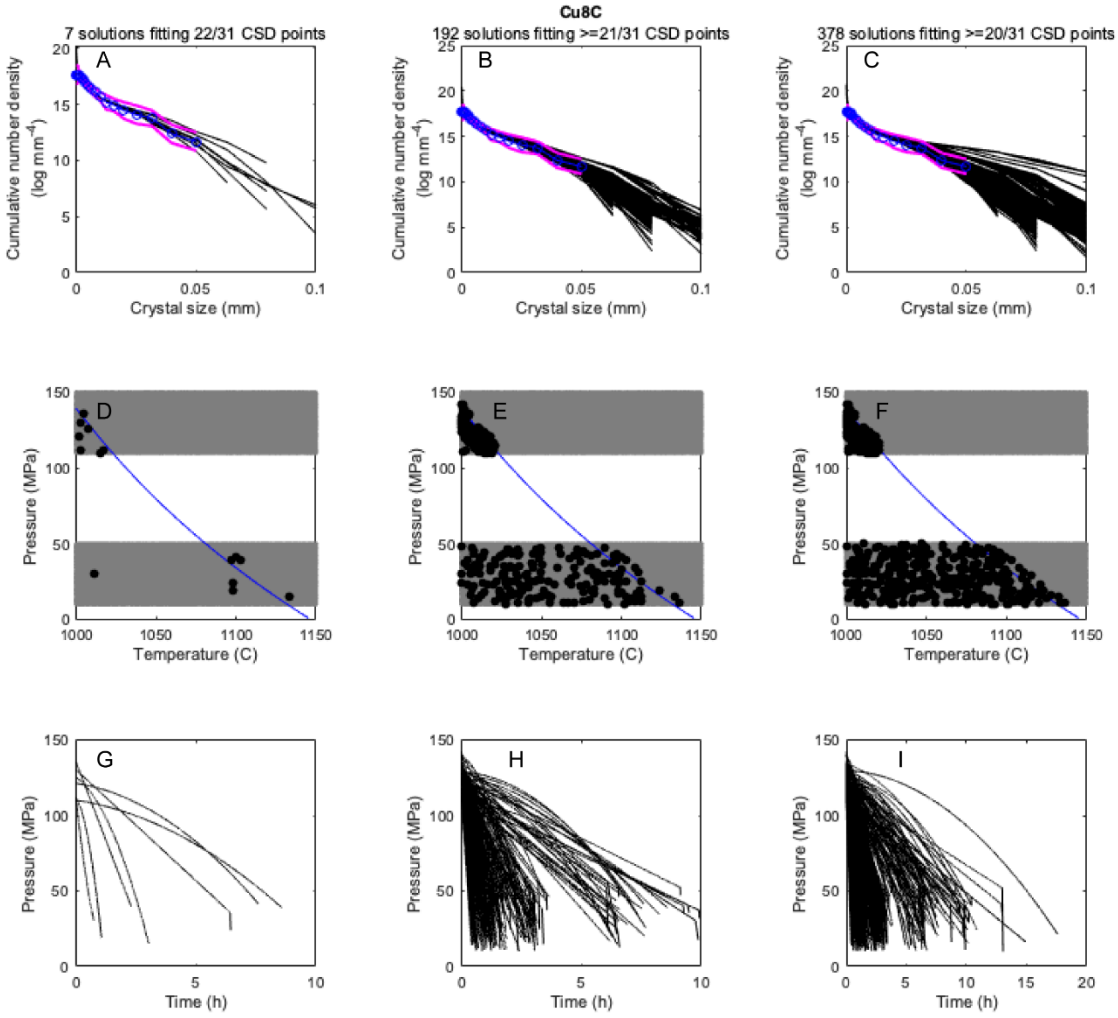

Figure A.12 SNGPlag results for Curacautín sample L8 image C (Cu8C). (A, B, C) Crystal size distributions (CSDs) of model results (black lines), the natural CSD (blue line), and two standard deviations (2σ; pink lines). Above plots A, B, and C are the description of the number of model solutions that match the natural CSD within 2σ and the number of CSD points that are included. Therefore, A is the best fit solutions, B is the second best set of solutions, and C is the third best set of solutions. (D, E, F) The corresponding sampled pressure-temperature space (gray fields), the starting and final P-T points from solutions in A, B, C (black points), and the plagioclase liquidus modeled by MELTS (Gualda and Ghiorso, 2012). (G, E, F) The associated modeled decompression pathways that produced the CSDs in A, B, and C. All plots in Appendix A follow this same format.

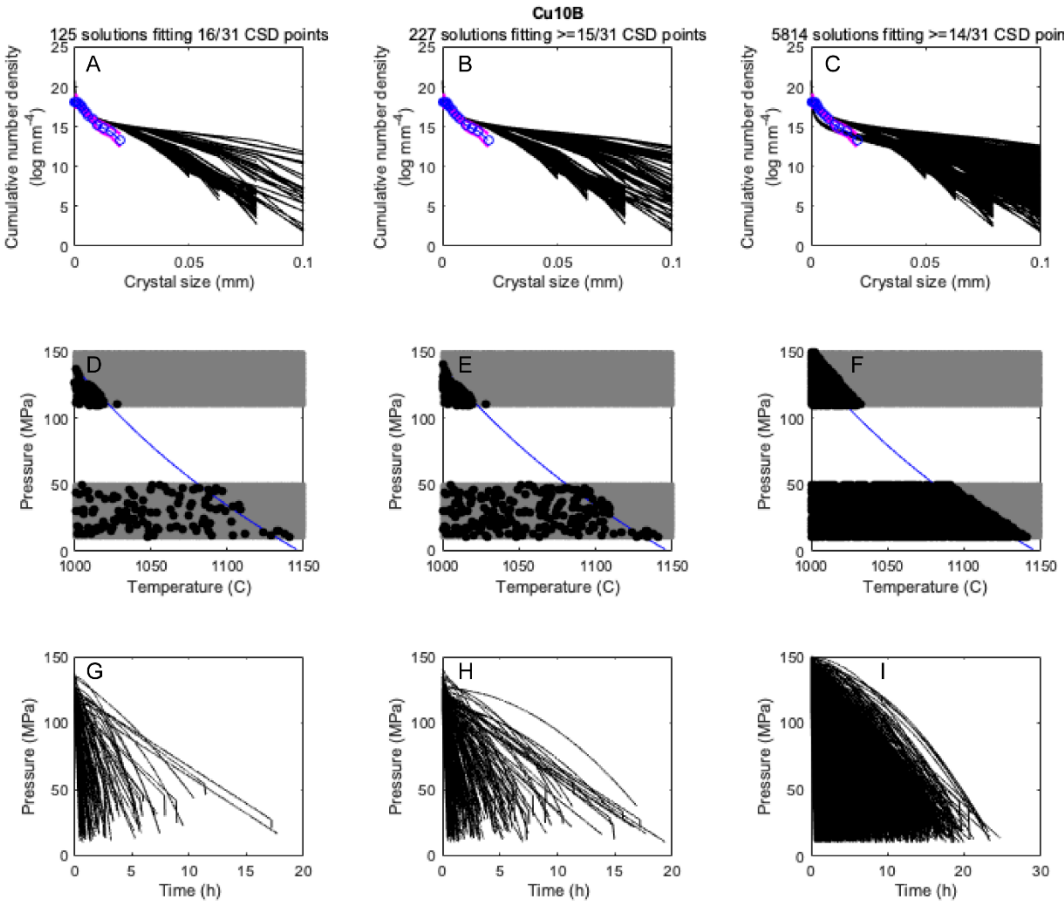

Figure A.13 SNGPlag results for Curacautín sample L10 image A (Cu10A). (A, B, C) Crystal size distributions (CSDs) of model results (black lines), the natural CSD (blue line), and two standard deviations (2σ; pink lines). Above plots A, B, and C are the description of the number of model solutions that match the natural CSD within 2σ and the number of CSD points that are included. Therefore, A is the best fit solutions, B is the second best set of solutions, and C is the third best set of solutions. (D, E, F) The corresponding sampled pressure-temperature space (gray fields), the starting and final P-T points from solutions in A, B, C (black points), and the plagioclase liquidus modeled by MELTS (Gualda and Ghiorso, 2012). (G, E, F) The associated modeled decompression pathways that produced the CSDs in A, B, and C. All plots in Appendix A follow this same format.

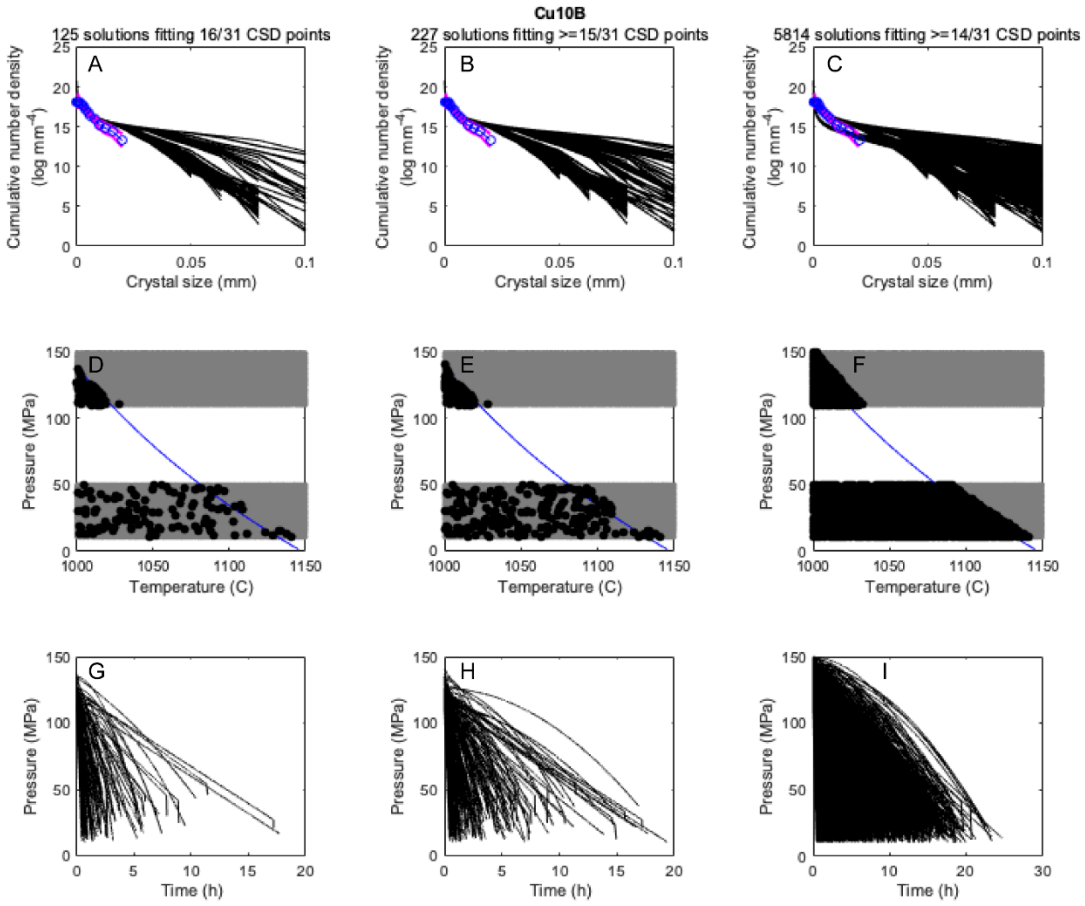

Figure A.14 SNGPlag results for Curacautín sample L10 image B (Cu10B). (A, B, C) Crystal size distributions (CSDs) of model results (black lines), the natural CSD (blue line), and two standard deviations (2σ; pink lines). Above plots A, B, and C are the description of the number of model solutions that match the natural CSD within 2σ and the number of CSD points that are included. Therefore, A is the best fit solutions, B is the second best set of solutions, and C is the third best set of solutions. (D, E, F) The corresponding sampled pressure-temperature space (gray fields), the starting and final P-T points from solutions in A, B, C (black points), and the plagioclase liquidus modeled by MELTS (Gualda and Ghiorso, 2012). (G, E, F) The associated modeled decompression pathways that produced the CSDs in A, B, and C. All plots in Appendix A follow this same format.

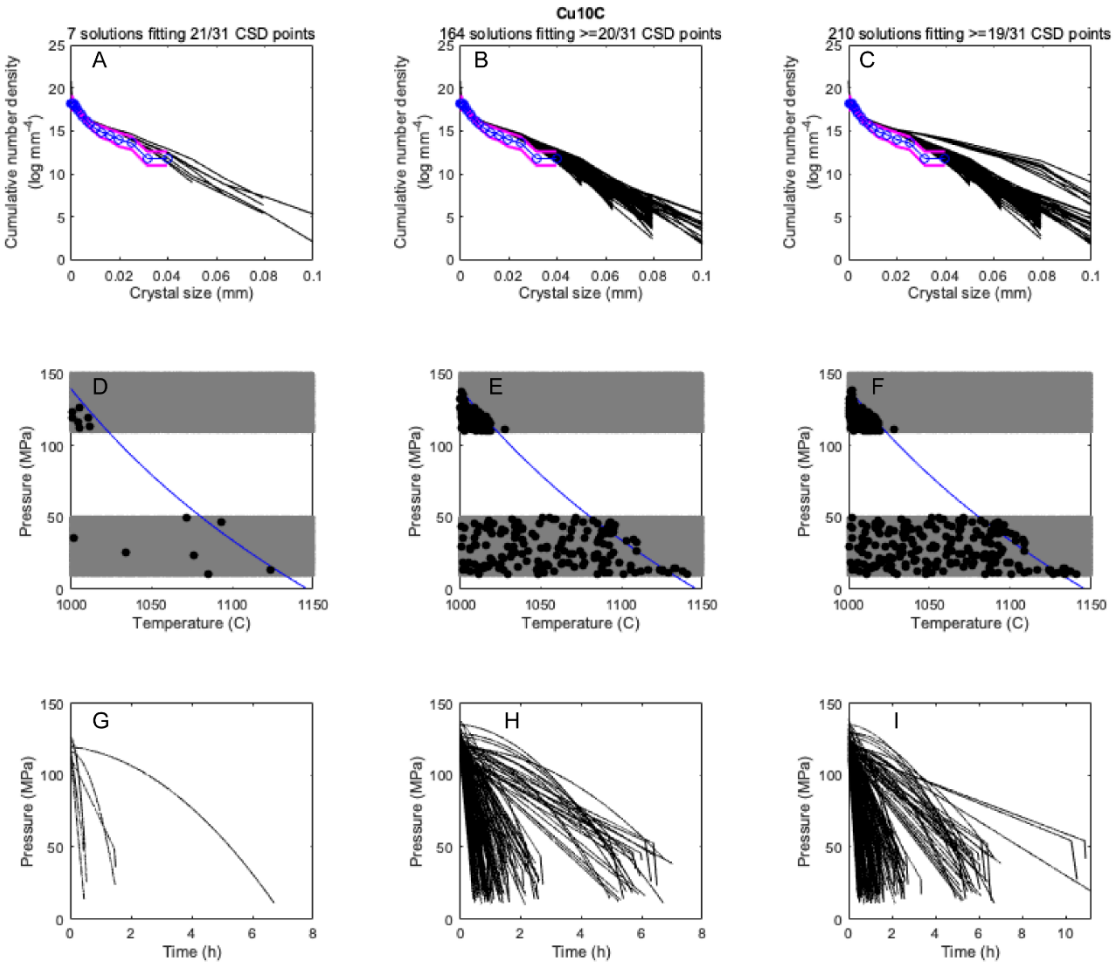

Figure A.15 SNGPlag results for Curacautín sample L10 image C (Cu10C). (A, B, C) Crystal size distributions (CSDs) of model results (black lines), the natural CSD (blue line), and two standard deviations (2σ; pink lines). Above plots A, B, and C are the description of the number of model solutions that match the natural CSD within 2σ and the number of CSD points that are included. Therefore, A is the best fit solutions, B is the second best set of solutions, and C is the third best set of solutions. (D, E, F) The corresponding sampled pressure-temperature space (gray fields), the starting and final P-T points from solutions in A, B, C (black points), and the plagioclase liquidus modeled by MELTS (Gualda and Ghiorso, 2012). (G, E, F) The associated modeled decompression pathways that produced the CSDs in A, B, and C. All plots in Appendix A follow this same format.

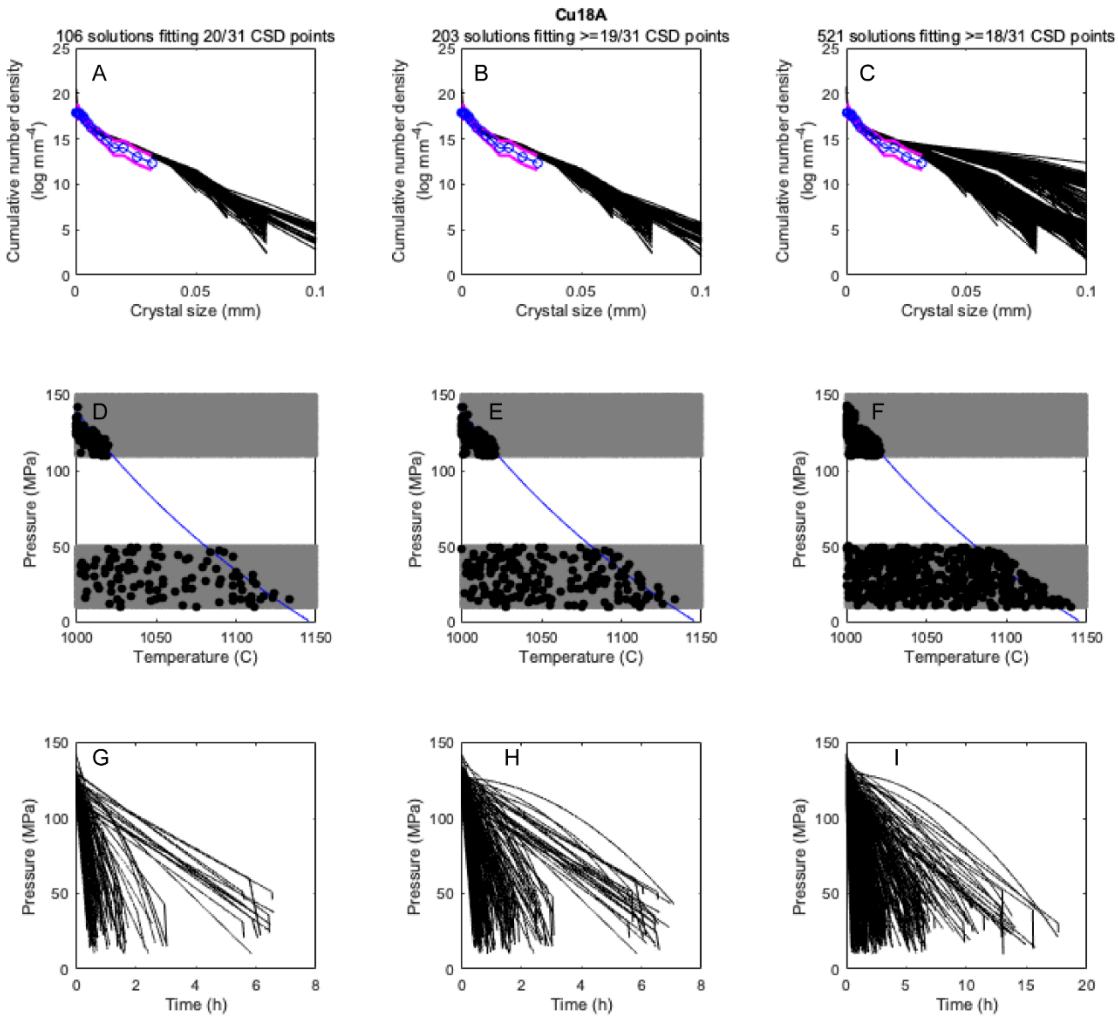

Figure A.16 SNGPlag results for Curacautín sample L18 image A (Cu18A). (A, B, C) Crystal size distributions (CSDs) of model results (black lines), the natural CSD (blue line), and two standard deviations (2σ; pink lines). Above plots A, B, and C are the description of the number of model solutions that match the natural CSD within 2σ and the number of CSD points that are included. Therefore, A is the best fit solutions, B is the second best set of solutions, and C is the third best set of solutions. (D, E, F) The corresponding sampled pressure-temperature space (gray fields), the starting and final P-T points from solutions in A, B, C (black points), and the plagioclase liquidus modeled by MELTS (Gualda and Ghiorso, 2012). (G, E, F) The associated modeled decompression pathways that produced the CSDs in A, B, and C. All plots in Appendix A follow this same format.

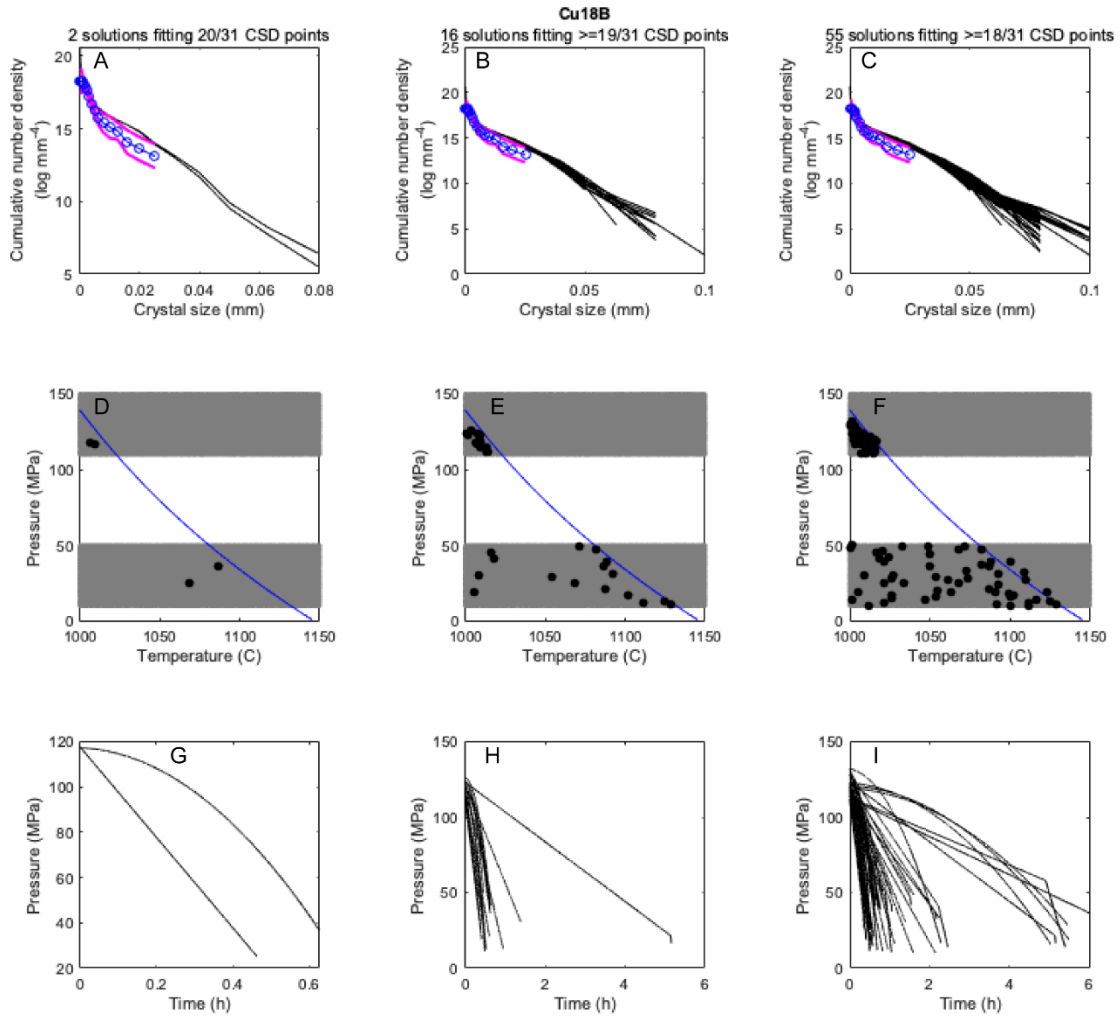

Figure A.17 SNGPlag results for Curacautín sample L18 image C (Cu18B). (A, B, C) Crystal size distributions (CSDs) of model results (black lines), the natural CSD (blue line), and two standard deviations (2σ; pink lines). Above plots A, B, and C are the description of the number of model solutions that match the natural CSD within 2σ and the number of CSD points that are included. Therefore, A is the best fit solutions, B is the second best set of solutions, and C is the third best set of solutions. (D, E, F) The corresponding sampled pressure-temperature space (gray fields), the starting and final P-T points from solutions in A, B, C (black points), and the plagioclase liquidus modeled by MELTS (Gualda and Ghiorso, 2012). (G, E, F) The associated modeled decompression pathways that produced the CSDs in A, B, and C. All plots in Appendix A follow this same format.

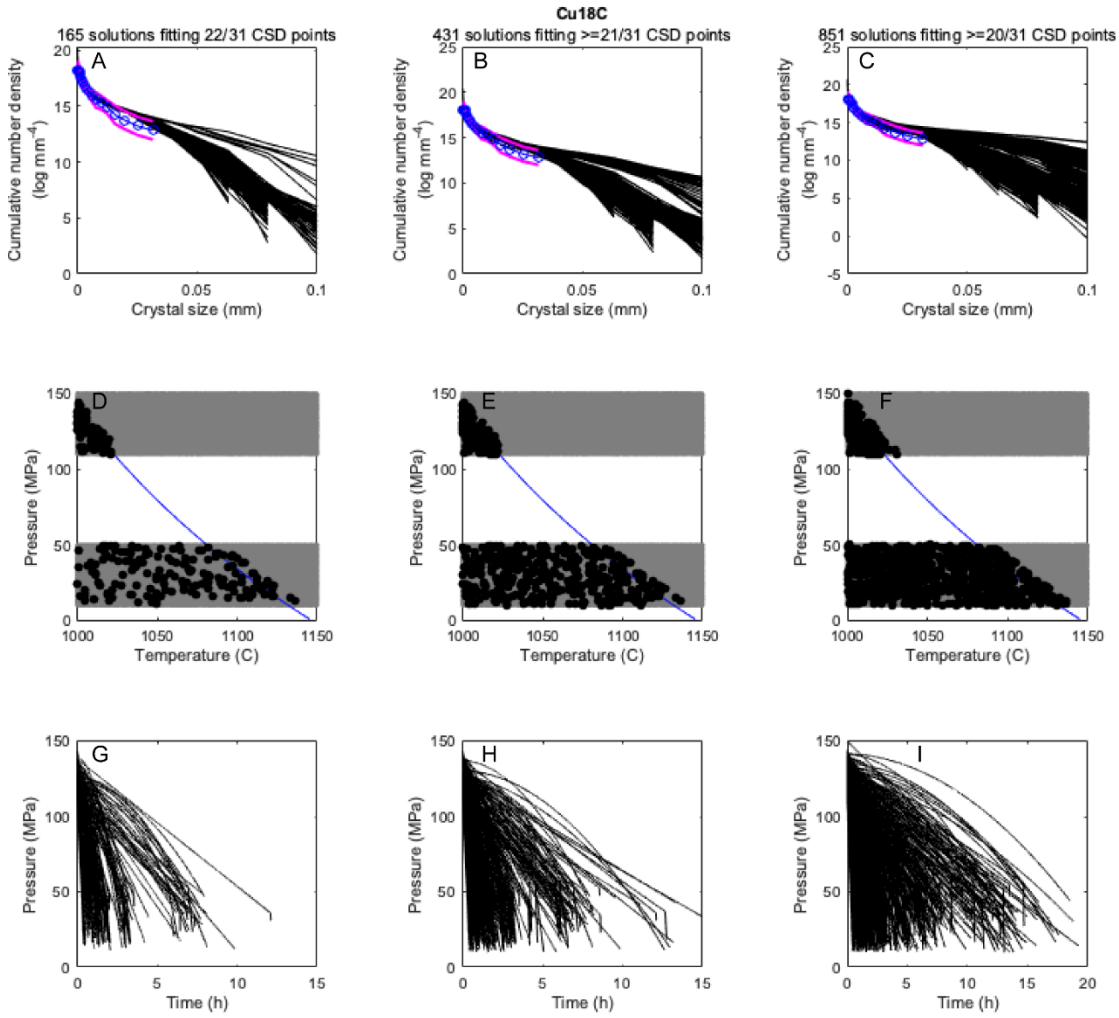

Figure A.18 SNGPlag results for Curacautín sample L18 image C (Cu18C). (A, B, C) Crystal size distributions (CSDs) of model results (black lines), the natural CSD (blue line), and two standard deviations (2σ; pink lines). Above plots A, B, and C are the description of the number of model solutions that match the natural CSD within 2σ and the number of CSD points that are included. Therefore, A is the best fit solutions, B is the second best set of solutions, and C is the third best set of solutions. (D, E, F) The corresponding sampled pressure-temperature space (gray fields), the starting and final P-T points from solutions in A, B, C (black points), and the plagioclase liquidus modeled by MELTS (Gualda and Ghiorso, 2012). (G, E, F) The associated modeled decompression pathways that produced the CSDs in A, B, and C. All plots in Appendix A follow this same format.

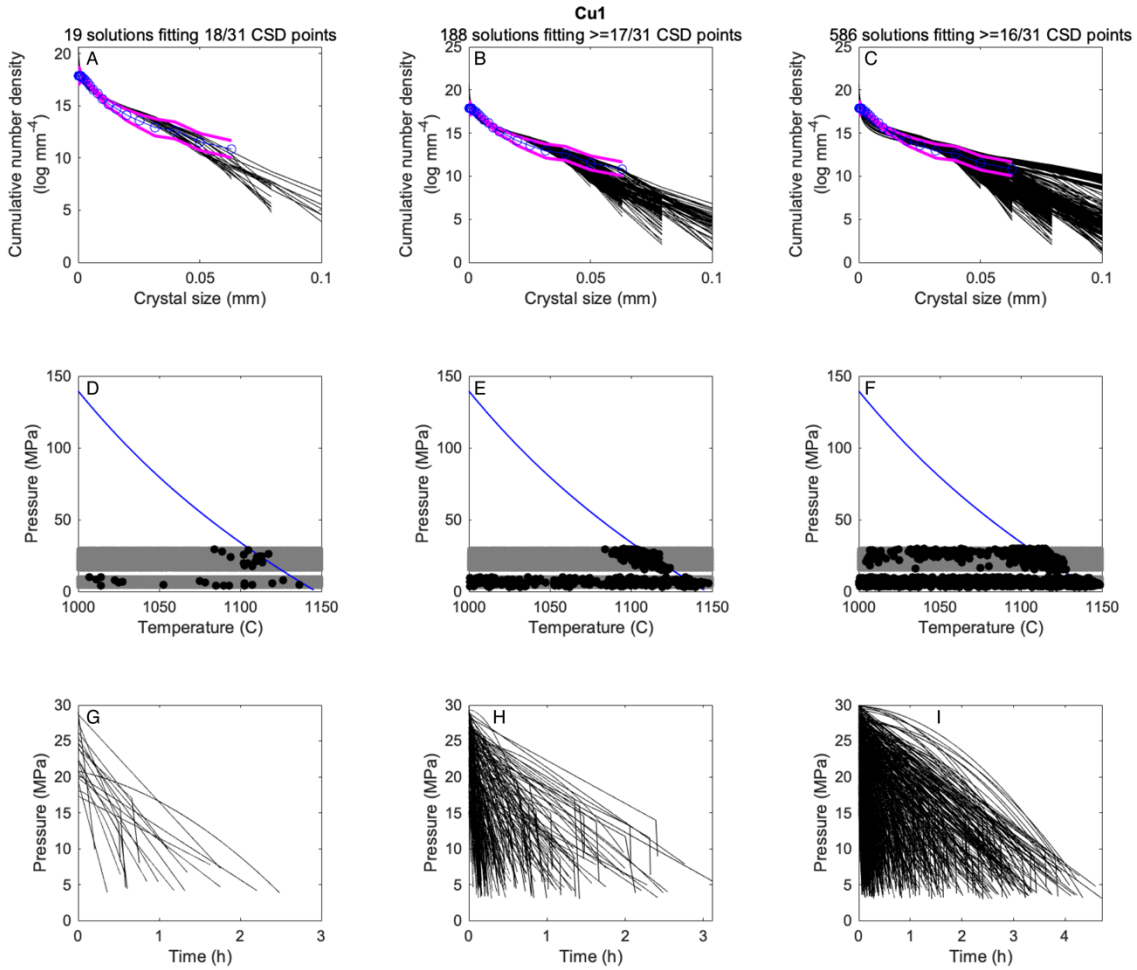

Figure A.19 SNGPlag results for Curacautín sample L1 run at P_i=15–30 MPa and P_f=3–10 MPa. (A, B, C) Crystal size distributions (CSDs) of model results (black lines), the natural CSD (blue line), and two standard deviations (2σ; pink lines). Above plots A, B, and C are the description of the number of model solutions that match the natural CSD within 2σ and the number of CSD points that are included. Therefore, A is the best fit solutions, B is the second best set of solutions, and C is the third best set of solutions. (D, E, F) The corresponding sampled pressure-temperature space (gray fields), the starting and final P-T points from solutions in A, B, C (black points), and the plagioclase liquidus modeled by MELTS (Gualda and Ghiorso, 2012). (G, E, F) The associated modeled decompression pathways that produced the CSDs in A, B, and C. All plots in Appendix A follow this same format.

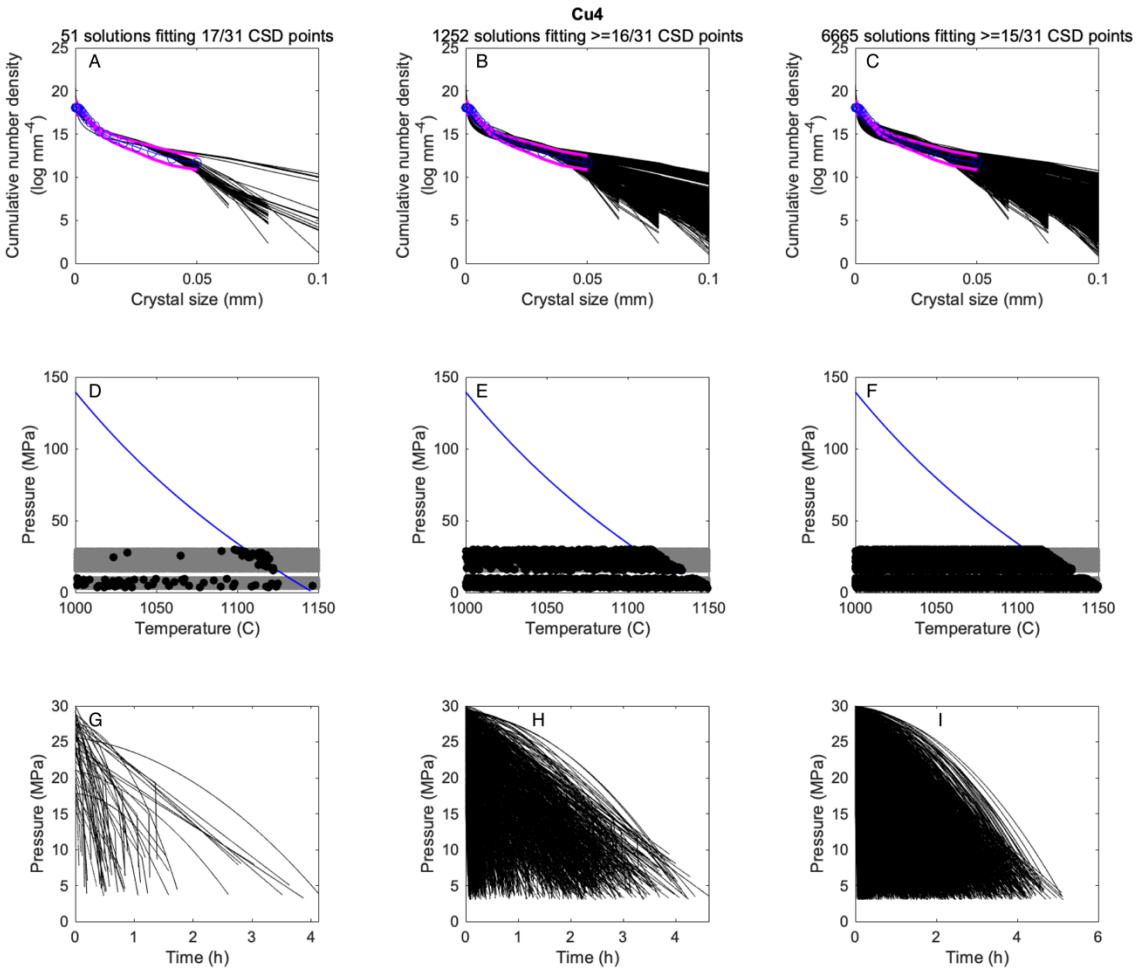

Figure A.20 SNGPlag results for Curacautín sample L4 run at P_i=15–30 MPa and P_f=3–10 MPa. (A, B, C) Crystal size distributions (CSDs) of model results (black lines), the natural CSD (blue line), and two standard deviations (2σ; pink lines). Above plots A, B, and C are the description of the number of model solutions that match the natural CSD within 2σ and the number of CSD points that are included. Therefore, A is the best fit solutions, B is the second best set of solutions, and C is the third best set of solutions. (D, E, F) The corresponding sampled pressure-temperature space (gray fields), the starting and final P-T points from solutions in A, B, C (black points), and the plagioclase liquidus modeled by MELTS (Gualda and Ghiorso, 2012). (G, E, F) The associated modeled decompression pathways that produced the CSDs in A, B, and C. All plots in Appendix A follow this same format.

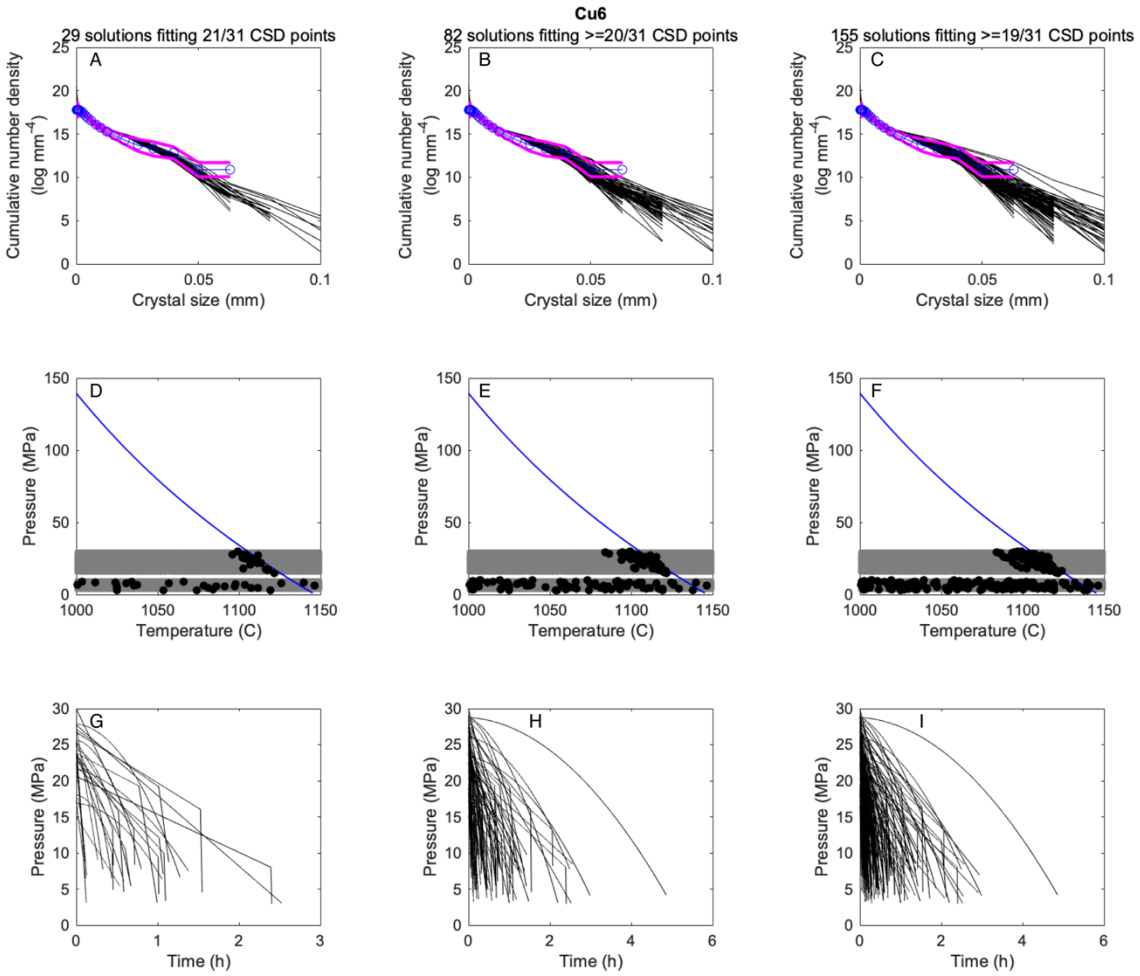

Figure A.21 SNGPlag results for Curacautín sample L6 run at P_i=15–30 MPa and P_f=3–10 MPa. (A, B, C) Crystal size distributions (CSDs) of model results (black lines), the natural CSD (blue line), and two standard deviations (2σ; pink lines). Above plots A, B, and C are the description of the number of model solutions that match the natural CSD within 2σ and the number of CSD points that are included. Therefore, A is the best fit solutions, B is the second best set of solutions, and C is the third best set of solutions. (D, E, F) The corresponding sampled pressure-temperature space (gray fields), the starting and final P-T points from solutions in A, B, C (black points), and the plagioclase liquidus modeled by MELTS (Gualda and Ghiorso, 2012). (G, E, F) The associated modeled decompression pathways that produced the CSDs in A, B, and C. All plots in Appendix A follow this same format.

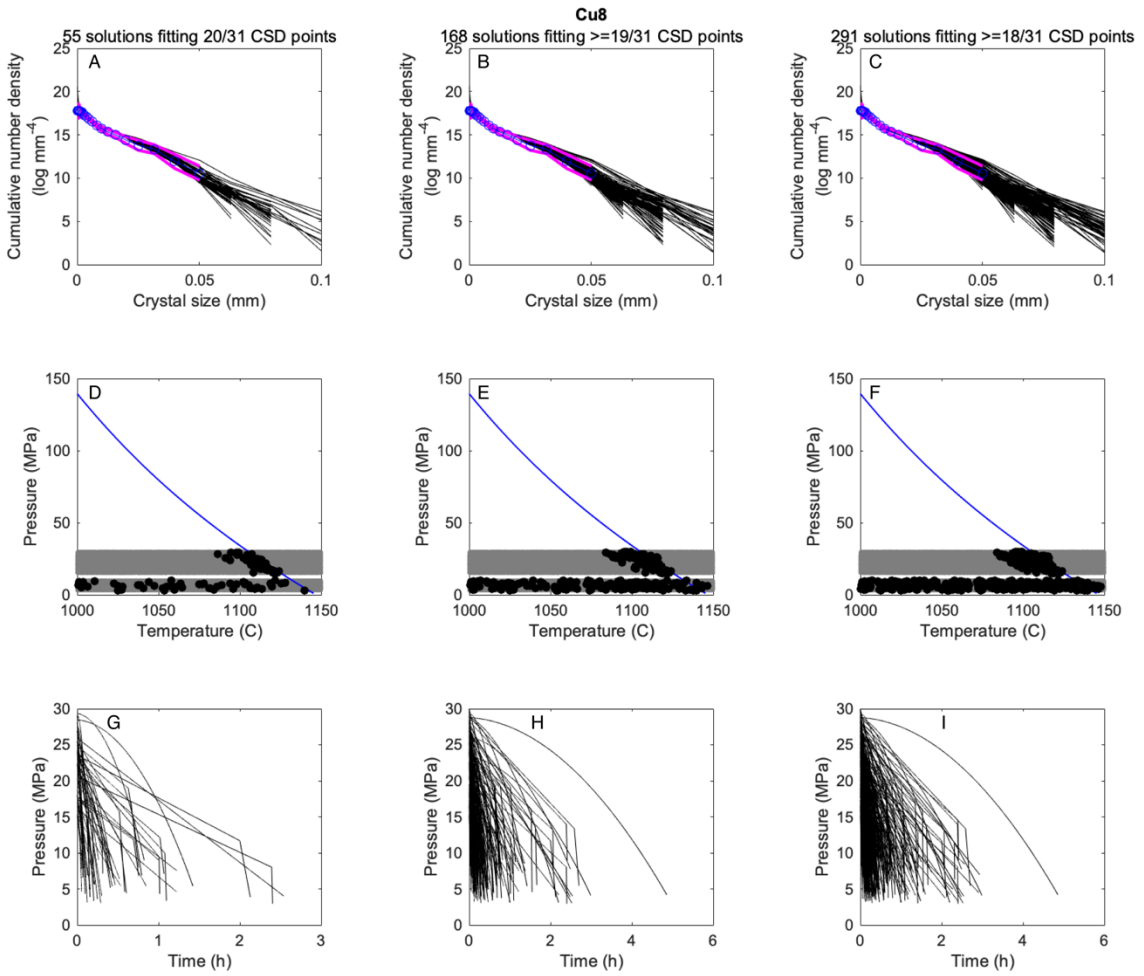

Figure A.22 SNGPlag results for Curacautín sample L8 run at P_i=15–30 MPa and P_f=3–10 MPa. (A, B, C) Crystal size distributions (CSDs) of model results (black lines), the natural CSD (blue line), and two standard deviations (2σ; pink lines). Above plots A, B, and C are the description of the number of model solutions that match the natural CSD within 2σ and the number of CSD points that are included. Therefore, A is the best fit solutions, B is the second best set of solutions, and C is the third best set of solutions. (D, E, F) The corresponding sampled pressure-temperature space (gray fields), the starting and final P-T points from solutions in A, B, C (black points), and the plagioclase liquidus modeled by MELTS (Gualda and Ghiorso, 2012). (G, E, F) The associated modeled decompression pathways that produced the CSDs in A, B, and C. All plots in Appendix A follow this same format.

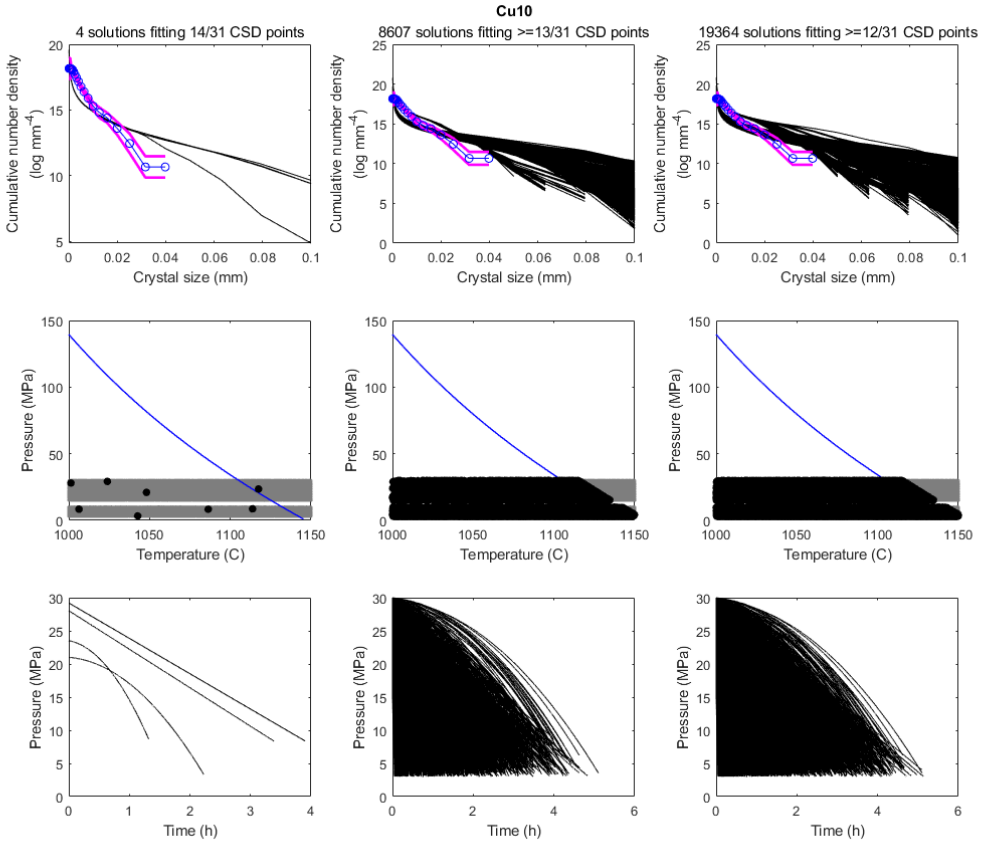

Figure A.23 SNGPlag results for Curacautín sample L10 run at P_i=15–30 MPa and P_f=3–10 MPa. (A, B, C) Crystal size distributions (CSDs) of model results (black lines), the natural CSD (blue line), and two standard deviations (2σ; pink lines). Above plots A, B, and C are the description of the number of model solutions that match the natural CSD within 2σ and the number of CSD points that are included. Therefore, A is the best fit solutions, B is the second best set of solutions, and C is the third best set of solutions. (D, E, F) The corresponding sampled pressure-temperature space (gray fields), the starting and final P-T points from solutions in A, B, C (black points), and the plagioclase liquidus modeled by MELTS (Gualda and Ghiorso, 2012). (G, E, F) The associated modeled decompression pathways that produced the CSDs in A, B, and C. All plots in Appendix A follow this same format.

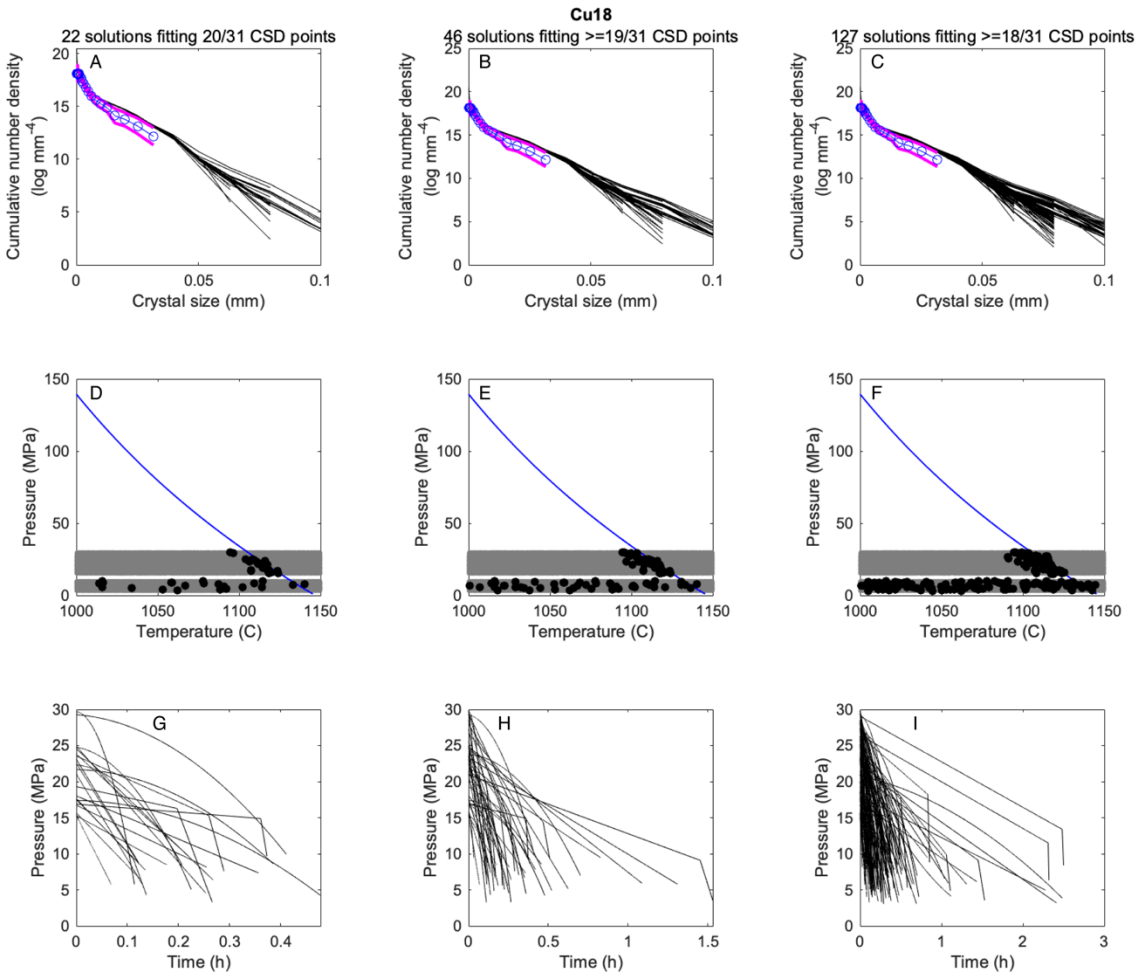

Figure A.24 SNGPlag results for Curacautín sample L18 run at P_i=15–30 MPa and P_f=3–10 MPa. (A, B, C) Crystal size distributions (CSDs) of model results (black lines), the natural CSD (blue line), and two standard deviations (2σ; pink lines). Above plots A, B, and C are the description of the number of model solutions that match the natural CSD within 2σ and the number of CSD points that are included. Therefore, A is the best fit solutions, B is the second best set of solutions, and C is the third best set of solutions. (D, E, F) The corresponding sampled pressure-temperature space (gray fields), the starting and final P-T points from solutions in A, B, C (black points), and the plagioclase liquidus modeled by MELTS (Gualda and Ghiorso, 2012). (G, E, F) The associated modeled decompression pathways that produced the CSDs in A, B, and C. All plots in Appendix A follow this same format.

APPENDIX B: MATLAB SCRIPTS

SNGplag_RateFinderPar.m

```
      % SNGPlag_RateFinder.m

      % 1) SNGPlag_RateFinder is a parallelized .m-file that explores
      % parameter space for plagioclase nucleation and growth rates

      % 2) Saves outputs that include rate parameters, crystal geometry
      % parameters, Nv, Sn, and 95% max length for final and applicable
      % intermediate steps

      % 3) inputs are equilibrium crystal fraction as function of P and
T,
      % decompression rate, decompression style (CD, MSD, SSD), quench
      % pressures (for CD) or times (for SSD)
      %
      % rate equations (R) are lognormal distributions:
      % R=k/(x*sqrt(2 pi)) * exp(-(ln x - mu)^2/(2 sigma^2))
      % where x = b*exp(1) * Dfplag, where Dfplag = disequilibrium
fraction
      % plag program will loop through the 4 parameters (each) for Rnuc
and
      % Rgrow to make rates, then use those rates to run a modified
SNGPlag
      % to get final (and potentially intermediate) Nv and Sn values
for >1
      % um and total CSD

      % 1) define the composition, and get the appropriate Plag(P,T)
file
      % 2) define the decompression paths -- these should be grouped
into
      % common series (ones with same final pressure but different
dwell
      % times)

      % 3) define the growth geometry
      % 4) define the range of parameters for nucleation and growth
search
      % 5) run the first simulation and give a time estimate for
completion
      % of entire run
      % 6) give prompt asking to proceed
      % 7) start looping through the parameters

      %%%%
      %%%%
      %%%%
      % Need to vectorize the program - rather than a grid search, do
this as
      % a randomized search for all conditions:

      % Specify the total number of iterations iterN, then run this as:

      iterN=100000;
```

```
      nk=zeros(iterN,1);
      nmu=nk;
      nsigma=nk;
      nb=nk;
      gk=nk;
      gmu=nk;
      gsigma=nk;
      gb=nk;
      sizermat=zeros(iterN,11);
      outXtal=sizermat;
      outNv=sizermat;
      outSn=sizermat;
      outL95=sizermat;
      outXtal1=sizermat;
      outNv1=sizermat;
      outSn1=sizermat;
      outL951=sizermat;

      SaveName='MAS22NucGrowthOutput.mat';

      VolTot=1; % declare the experiment volume (cubic m)

      NumExp=5; % number of experiments, defined as range of final
pressures
      NumExp11=11;

      % define the hard coded values for plag crystallinity as
f(P,T,fO2)
      XtalEQB=zeros(1,NumExp); % values in order of Pf given below
      XtalEQB=[0.0357 0.2405 0.2657 0.3654 0.4841];
      XtalInit=0.005;

      % Define the decompression paths
      % prompt asking for the number of decompression series (defined
as
      % having same initial P-T and either same rate for CD or same Pf
for
      % SSD)
      % make the defaults be the S&H values
      PathType=ones(1,NumExp); % set 0 for CD and 1 for SSD
      Pi=PathType.*150; % initial P in MPa
      Pf=PathType;
      Ti=Pf;
      Tf=Pf;

      % tdwell=PathType
      Pf=[100, 65, 42, 22, 10]; % final pressures
      tdwell=[12, 24, 48]; % dwell times in hours
      Ti=1025.*Ti; % initial temperature
      Tf=Ti; % isothermal experiments

      numsteps=2500; % number of steps to perform in each run
      tdur=max(tdwell).*3600;
```

```
      % make tstep adaptive - initial steps are very short, final steps
are
      % long
      tstepmax=2.*tdur./numsteps;
      tstepslope=tstepmax./2500;
      tstep=zeros(numsteps,1);
      tcum=tstep;
      tstep(1)=tstepslope;
      tcum(1)=tstep(1);
      for i=2:numsteps
          tstep(i)=i.*tstepslope;
          tcum(i)=tcum(i-1)+tstep(i);
      end
      t12=find(tcum>12.*3600,1)+1;
      t24=find(tcum>24.*3600,1)+1;
      t48=numsteps+1;

      % declare phenocrysts - these sizes are estimates from looking at
MAS-
      % 22
      % BSE images
      XPheno=XtalInit; % volume fraction phenocrysts at start
      SPhenoa=200.*1E-6; % a-axis length(s) in m
      SPhenob=300.*1E-6; % b-axis length(s) in m
      SPhenoc=500.*1E-6; % c-axis length(s) in m
      FPheno=1; % specific volume fractions within phenocrysts group
      FPheno=FPheno./sum(FPheno);

      % Define the growth geometry
      % Follow the functional form from Andrews and Befus (2020), make
      % default be Andrews and Befus (2020) values - follow functional
form
      % Jx=(1+Df*mx)Jc, where mx is negative (-3 and -2 for a and b
axes) as
      % crystals become increasingly anisotropic
      ma=-3;
      mb=-2;

      %%%%%%%%%%%%%%%%%%%%%%%%%%
      % Define the range of parameters for nucleation and growth search
      % Prompt with 8 rows prepopulated with the Rnuc and Rgrow values
      % Rnuck=[2:10]; scaling for nucleation, gives 3 orders of
magnitude
      % more range than previous rhyolite version (was originally 1:11)
      % Rnuck=10.^(Rnuck./2+8); this should give a scaling range of
~10^9 per
      % m^3 per second to 10^13

      % Rnuck=[10.^9 10.^13];
      % Rnucmu=[0.1 1.5];
      % Rnucsigma=[0.5 2];
      % Rnucb=1;
      % Rgrowk=[2:10]; %scaling for growth
      % Rgrowk=10.^(Rgrowk./2-10); scaling factor in m/s - high end
should be
```

```
      % order of um/s - so 1E-5 m/s - current range should be ~0.001
um/s
      % to ~10 um/s
      % Rgrowk=[10.^-10 10.^-5];
      % Rgrowmu=[0.1 1.5];
      % Rgrowsigma=[0.5 2];
      % Rgrowb=1;

      %%%%%%%%%%%%%%%%%%%%%%%%%%%%%%%%%%%

      %
sizerMat=[Nnuck,Nnucmu,Nnucsigma,Nnucb,Ngrowk,Ngrowmu,Ngrowsigma,
      % Ngrowb,11]; vector giving matrix size for save variables
      % Declare matrices for Xtal, Nv, Sn, L95, Xtal1, Nv1, Sn1, L951
(the
      % "1"denotes greater than 1 micron and no 1 means all crystals)-
final
      % 11 is the number of experiments

      % start looping through the parameters
      % variables to save for each iteration are the rate parameters,
the
      % geometry parameters, then the P-t paths with full and >1 um Nv
and Sn
      % and 95% max size values
      % rate equations (R) are lognormal distributions:
      % R=k/(x*sqrt(2 pi)) * exp(-(ln x - mu)^2/(2 sigma^2))
      % where x = b*exp(1) * Dfplag where Dfplag is disequilibrium
fraction
      % plag

      % Declaration of parallelization, the outermost loop is
parallelized
      % for speed. No variables defined outside the outermost loop can
be
      % changed.

      % These include Nxtal, Vxtal, Xtalinity, La, Lb, Lc. Outermost
      % occurences renamed wit A- prefix (e.g., ANxtal) as temporary
      % variables

      % initialize matrices for Xtalinity, Nxtal, a-, b-, c-sizes
      AXtalinity=zeros(numsteps+1,1); % Xtalinity through time
      ANxtal=zeros(numsteps+1,numsteps+length(FPheno)); % number of
crystals
      % for each class through time
      AVxtal=ANxtal; % volume of each crystal class through time
      ALa=ANxtal; % a lengths through time
      ALb=ANxtal; % b lengths through time
      ALc=ANxtal; % c lengths through time

      ALa(1,1:length(FPheno))=SPhenoa;
      ALb(1,1:length(FPheno))=SPhenob;
      ALc(1,1:length(FPheno))=SPhenoc;
      AVxtal(1,1:length(FPheno))=ALa(1,1:length(FPheno))...
```

```
        .*ALb(1,1:length(FPheno)).*ALc(1,1:length(FPheno));
    AXtalinity(1)=XtalInit;
    ANxtal(1,1:length(FPheno))=AXtalinity(1).*FPheno...
        ./AVxtal(1,1:length(FPheno));

    xDf=0:1000;
    xDf=xDf./1000;
    tic
    figure(1);
    clf;

    c=parcluster;
    c.AdditionalProperties.AdditionalSubmitArgs=' -o log_slurm.o%j -p
shortq ';
    parpool(c,27);

    parfor iiter=1:iterN
        iiter
        nk(iiter)=10.^(8+rand(1).*7);
        nmu(iiter)=rand(1).*1.4+.1;
        nsigma(iiter)=rand(1).*1.5+0.5;
        nb(iiter)=1;
        gk(iiter)=10.^(rand(1).*8-9);
        gmu(iiter)=rand(1).*1.4+.1;
        gsigma(iiter)=rand(1).*1.5+0.5;
        gb(iiter)=1;


        % calculate nucleation rate
        Iln=zeros(1,1001);
        for iDf=0:1000
            x=nb(iiter).*exp(1).*(iDf./1000);
            Iln(iDf+1)=nk(iiter)./(x.*sqrt(2.*3.14159))...
                .*exp((-(log(x)-
nmu(iiter)).^2)./(2.*nsigma(iiter).^2));
        end

        %calculate growth rate
        Gln=zeros(1,1001);
        for iDf=0:1000
            x=gb(iiter).*exp(1).*(iDf./1000);
            Gln(iDf+1)=gk(iiter)./(x.*sqrt(2.*3.14159))...
                .*exp((-(log(x)-
gmu(iiter)).^2)./(2.*gsigma(iiter).^2));
        end

        outX=zeros(1,NumExp11);
        outN=zeros(1,NumExp11);
        outS=zeros(1,NumExp11);
        outL=zeros(1,NumExp11);
        outX1=outX;
        outN1=outN;
        outS1=outS;
        outL1=outL;
```

```
          for ex=1:NumExp
              % apply the nucleation and growth rates to decompression
path,
              % save the crystallinity, Nv, Sn, L95 parameters to the
various
              % values in the outVAR matrices

              % zero out the matrices
              Xtalinity=0.*AXtalinity;
              Nxtal=0.*ANxtal;
              Vxtal=0*AVxtal;
              La=0.*ALa;
              Lb=0.*ALb;
              Lc=0.*ALc;
              La(1,1:length(FPheno))=SPhenoa;
              Lb(1,1:length(FPheno))=SPhenob;
              Lc(1,1:length(FPheno))=SPhenoc;
              Vxtal(1,1:length(FPheno))=La(1,1:length(FPheno))...
                  .*Lb(1,1:length(FPheno)).*Lc(1,1:length(FPheno));
              Xtalinity(1)=XtalInit;
              Nxtal(1,1:length(FPheno))=floor(Xtalinity(1)...
                  .*FPheno./Vxtal(1,1:length(FPheno)));

              for t=1:numsteps
                  P=Pf(ex);
                  disEQB=XtalEQB(ex)-Xtalinity(t); % determine
disequilibrium
                  I=interp1(xDf,Iln,disEQB); % nucleation rate
                  Jc=interp1(xDf,Gln,disEQB); % growth rate for c-axis
                  Ja=(1+disEQB*ma).*Jc; % a-axis growth rate
                  Jb=(1+disEQB*mb).*Jc; % b-axis growth rate
                  if Ja<0.1.*Jc
                      Ja=0.1.*Jc;
                  end
                  if Jb<0.1.*Jc
                      Jb=0.1.*Jc;
                  end

                  % add growth to existing crystals
                  La(t+1,1:t+length(FPheno)-1)=La(t,1:t+length(FPheno)-
1)...
                      +Ja.*tstep(i);
                  Lb(t+1,1:t+length(FPheno)-1)=Lb(t,1:t+length(FPheno)-
1)...
                      +Jb.*tstep(i);
                  Lc(t+1,1:t+length(FPheno)-1)=Lc(t,1:t+length(FPheno)-
1)...
                      +Jc.*tstep(i);

                  % calculate crystal volume
                  Vxtal(t+1,1:t+length(FPheno)-
1)=La(t+1,1:t+length(FPheno)-1)...
                      .*Lb(t+1,1:t+length(FPheno)-1).*Lc(t+1,1:t...
                      +length(FPheno)-1);

                  % add new nucleii
```

```
Nxtal(t+1,1:t+length(FPheno))=Nxtal(t,1:t+length(FPheno));
                    if t<numsteps
                        Nxtal(t+1,t+length(FPheno))=floor(I.*tstep(i));
                    end

                    % calculate the crystalinity
                    Xtalinity(t+1)=sum(Vxtal(t+1,1:t+length(FPheno))...
                        .*Nxtal(t+1,1:t+length(FPheno)));
                end

                % need to subtract phenocryst contribution from below
                if ex<4

                    % save variables at 12, 24, 48 hours
                    ex12=ex.*3-2;
                    ex24=ex.*3-1;
                    ex48=ex.*3;
                    outX(1,ex12)=Xtalinity(t12)-XtalInit;
                    outX(1,ex24)=Xtalinity(t24)-XtalInit;
                    outX(1,ex48)=Xtalinity(t48)-XtalInit;
                    outN(1,ex12)=sum(Nxtal(t12,2:end));
                    outN(1,ex24)=sum(Nxtal(t24,2:end));
                    outN(1,ex48)=sum(Nxtal(t48,2:end));
                    outS(1,ex12)=((Xtalinity(t12)-XtalInit)...
                        ./sum(Nxtal(t12,2:end))).^(1/3);
                    outS(1,ex24)=((Xtalinity(t24)-XtalInit)...
                        ./sum(Nxtal(t24,2:end))).^(1/3);
                    outS(1,ex48)=((Xtalinity(t48)-XtalInit)...
                        ./sum(Nxtal(t48,2:end))).^(1/3);

                    % find the 95% crystal size, then take its max length
                    LLL=Lc(t12,2:end);
                    NNN=Nxtal(t12,2:end);
                    NNNcum=NNN;
                    NNNcum(1)=sum(NNN);
                    for j=2:length(NNN)
                        NNNcum(j)=NNNcum(j-1)-NNN(j);
                    end

                    % find the 95% value
                    NNNcum=NNNcum./NNNcum(1);
                    f95=find(NNNcum<0.95,1);
                    if isempty(f95)==0
                        f95=f95-1;
                        outL(1,ex12)=LLL(f95);
                    end

                    LLL=Lc(t24,2:end);
                    NNN=Nxtal(t24,2:end);
                    NNNcum=NNN;
                    NNNcum(1)=sum(NNN);
                    for j=2:length(NNN)
                        NNNcum(j)=NNNcum(j-1)-NNN(j);
                    end
```

```
                    % find the 95% value
                    NNNcum=NNNcum./NNNcum(1);
                    f95=find(NNNcum<0.95,1);
                    if isempty(f95)==0
                        f95=f95-1;
                        outL(1,ex24)=LLL(f95);
                    end

                    LLL=Lc(t48,2:end);
                    NNN=Nxtal(t48,2:end);
                    NNNcum=NNN;
                    NNNcum(1)=sum(NNN);
                    for j=2:length(NNN)
                        NNNcum(j)=NNNcum(j-1)-NNN(j);
                    end

                    % find the 95% value
                    NNNcum=NNNcum./NNNcum(1);
                    f95=find(NNNcum<0.95,1);
                    if isempty(f95)==0
                        f95=f95-1;
                        outL(1,ex48)=LLL(f95);
                    end

                    % find the crystals with c-axis >1 um
                    LLc=Lc(t12,2:end);
                    LLc(LLc<1E-6)=0;
                    LLc(LLc>0)=1;

outX1(1,ex12)=sum(LLc.*Vxtal(t12,2:end).*Nxtal(t12,2:end));
                    outN1(1,ex12)=sum(LLc.*Nxtal(t12,2:end));

outS1(1,ex12)=(sum(LLc.*Vxtal(t12,2:end).*Nxtal(t12,2:end))...
                        ./sum(LLc.*Nxtal(t12,2:end))).^(1/3);

                    %find the 95% crystal size, then take
                    %its max length (c-axis length) --
outL951=zeros(sizerMat);
                    LLL=Lc(t12,2:end);
                    NNN=Nxtal(t12,2:end);
                    NNN(LLL<1E-6)=0;
                    LLL(LLL<1E-6)=0;
                    NNNcum=NNN;
                    NNNcum(1)=sum(NNN);
                    for j=2:length(NNN)
                        NNNcum(j)=NNNcum(j-1)-NNN(j);
                    end

                    % find the 95% value
                    NNNcum=NNNcum./NNNcum(1);
                    f95=find(NNNcum<0.95,1);
                    if isempty(f95)==0
                        f95=f95-1;
                        outL1(1,ex12)=LLL(f95);
                    end
```

```
                    LLc=Lc(t24,2:end);
                    LLc(LLc<1E-6)=0;
                    LLc(LLc>0)=1;

outX1(1,ex24)=sum(LLc.*Vxtal(t24,2:end).*Nxtal(t24,2:end));
                    outN1(1,ex24)=sum(LLc.*Nxtal(t24,2:end));

outS1(1,ex24)=(sum(LLc.*Vxtal(t24,2:end).*Nxtal(t24,2:end))...
                        ./sum(LLc.*Nxtal(t24,2:end))).^(1/3);
                    % find the 95% crystal size, then take
                    % its max length (c-axis length)
                    LLL=Lc(t24,2:end);
                    NNN=Nxtal(t24,2:end);
                    NNN(LLL<1E-6)=0;
                    LLL(LLL<1E-6)=0;
                    NNNcum=NNN;
                    NNNcum(1)=sum(NNN);
                    for j=2:length(NNN)
                        NNNcum(j)=NNNcum(j-1)-NNN(j);
                    end

                    % find the 95% value
                    NNNcum=NNNcum./NNNcum(1);
                    f95=find(NNNcum<0.95,1);
                    if isempty(f95)==0
                        f95=f95-1;
                        outL1(1,ex24)=LLL(f95);
                    end

                    LLc=Lc(t48,2:end);
                    LLc(LLc<1E-6)=0;
                    LLc(LLc>0)=1;

outX1(1,ex48)=sum(LLc.*Vxtal(t48,2:end).*Nxtal(t48,2:end));
                    outN1(1,ex48)=sum(LLc.*Nxtal(t48,2:end));

outS1(1,ex48)=(sum(LLc.*Vxtal(t48,2:end).*Nxtal(t48,2:end))...
                        ./sum(LLc.*Nxtal(t48,2:end))).^(1/3);

                    % find the 95% crystal size, then take
                    % its max length (c-axis length)
                    LLL=Lc(t48,2:end);
                    NNN=Nxtal(t48,2:end);
                    NNN(LLL<1E-6)=0;
                    LLL(LLL<1E-6)=0;
                    NNNcum=NNN;
                    NNNcum(1)=sum(NNN);
                    for j=2:length(NNN)
                        NNNcum(j)=NNNcum(j-1)-NNN(j);
                    end

                    % find the 95% value
                    NNNcum=NNNcum./NNNcum(1);
                    f95=find(NNNcum<0.95,1);
                    if isempty(f95)==0
```

```
                    f95=f95-1;
                    outL1(1,ex48)=LLL(f95);
                end

            else

                % save variables at 48 hours
                ex482210=6+ex; %for 48 hour run at 22 MPa Pf or 10
MPa
                outX(1,ex482210)=Xtalinity(t48)-XtalInit;
                outN(1,ex482210)=sum(Nxtal(t48,2:end));
                outS(1,ex482210)=((Xtalinity(t48)-XtalInit)...
                    ./sum(Nxtal(t48,2:end))).^(1/3);

                %find the 95% crystal size, then take
                %its max length (c-axis length) --
outL95=zeros(sizerMat);
                LLL=Lc(t48,2:end);
                NNN=Nxtal(t48,2:end);
                NNNcum=NNN;
                NNNcum(1)=sum(NNN);
                for j=2:length(NNN)
                    NNNcum(j)=NNNcum(j-1)-NNN(j);
                end

                % find the 95% value
                NNNcum=NNNcum./NNNcum(1);
                f95=find(NNNcum<0.95,1);
                if isempty(f95)==0
                    f95=f95-1;
                    outL(1,ex482210)=LLL(f95);
                end

                %find the crystals with c-axis >1 um
                LLc=Lc(t48,2:end);
                LLc(LLc<1E-6)=0;
                LLc(LLc>0)=1;

outX1(1,ex482210)=sum(LLc.*Vxtal(t48,2:end).*Nxtal(t48,2:end));
                outN1(1,ex482210)=sum(LLc.*Nxtal(t48,2:end));
                outS1(1,ex482210)=(sum(LLc.*Vxtal(t48,2:end)...

.*Nxtal(t48,2:end))./sum(LLc.*Nxtal(t48,2:end))).^(1/3);

                % find the 95% crystal size, then take
                % its max length (c-axis length) --
outL951=zeros(sizerMat);
                LLL=Lc(t48,2:end);
                NNN=Nxtal(t48,2:end);
                NNN(LLL<1E-6)=0;
                LLL(LLL<1E-6)=0;
                NNNcum=NNN;
                NNNcum(1)=sum(NNN);
                for j=2:length(NNN)
                    NNNcum(j)=NNNcum(j-1)-NNN(j);
                end
```

```
                % find the 95% value
                NNNcum=NNNcum./NNNcum(1);
                f95=find(NNNcum<0.95,1);
                if isempty(f95)==0
                    f95=f95-1;
                    outL1(1,ex482210)=LLL(f95);
                end
            end
        end
        outXtal(iiter,:)=outX;
        outNv(iiter,:)=outN;
        outSn(iiter,:)=outS;
        outL95(iiter,:)=outL;
        outXtal1(iiter,:)=outX1;
        outNv1(iiter,:)=outN1;
        outSn1(iiter,:)=outS1;
        outL951(iiter,:)=outL1;
    end

    toc
    save(SaveName,'nk','nmu','nsigma','nb','gk','gmu','gsigma','gb','
iterN','NumExp','XtalInit','XtalEQB','Pi','Ti','Pf','Tf','tdwell',...
    'numsteps','tdur','tstep','VolTot','PathType','ma','mb','outXtal'
,...
    'outXtal1','outNv','outNv1','outSn','outSn1','outL95','outL951');
    toc
```

CalibratedPlotTest.m

```
    % % CalibratedPlotTest.m

    SheaHammerOut=load('SheaHammerOld.txt');
    load('MAS22NucGrowthOutput_6b.mat');

    % generate weighting factors
    SaveName='OutputView_6_weights.mat';
    Nsim=10000;
    for i=1:Nsim
        weight1(i)=10.^(rand(1).*2);
        weight2(i)=10.^(rand(1).*2);
        weight3(i)=10.^(rand(1).*2);
        weight4(i)=10.^(rand(1).*2);
    end
    save(SaveName,'weight1','weight2','weight3','weight4');
    load(SaveName);

    % loads and converts experimental data from Shea and Hammer
(2013)
    SHoutOld=SheaHammerOut;
    SheaHammerOut=SHoutOld(1:11,:);
    SheaHammerOut(2,:)=SHoutOld(4,:);
    SheaHammerOut(3,:)=SHoutOld(7,:);
    SheaHammerOut(4,:)=SHoutOld(2,:);
```

```
SheaHammerOut(5,:)=SHoutOld(5,:);
SheaHammerOut(6,:)=SHoutOld(8,:);
SheaHammerOut(7,:)=SHoutOld(3,:);
SheaHammerOut(8,:)=SHoutOld(6,:);
SheaHammerOut(9,:)=SHoutOld(9,:);
SheaHammerOut(10,:)=SHoutOld(10,:);
SheaHammerOut(11,:)=SHoutOld(11,:);

weight=ones(11,1);

outXtal(outXtal<0)=0.01;
CompXtal=outXtal;
CompXtal1=outXtal1;
CompNv=outNv;
CompNv1=outNv1;
CompL95=outL95;
CompL951=outL951;

for i=1:length(SheaHammerOut);
    CompXtal(:,i)=outXtal(:,i)./SheaHammerOut(i,1);
    CompXtal1(:,i)=outXtal1(:,i)./SheaHammerOut(i,1);
    CompNv(:,i)=outNv(:,i)./SheaHammerOut(i,3);
    CompNv1(:,i)=outNv1(:,i)./SheaHammerOut(i,3);
    CompL95(:,i)=outL95(:,i)./SheaHammerOut(i,4);
    CompL951(:,i)=outL951(:,i)./SheaHammerOut(i,4);
end

% weighting experiments
SquareCompXtal=CompXtal;
SquareCompXtal1=CompXtal1;
SquareCompL95=CompL95;
SquareCompL951=CompL951;
SquareCompNv=CompNv;
SquareCompNv1=CompNv1;

for i=1:length(SquareCompXtal)
    for j=1:length(SheaHammerOut)
        if SquareCompXtal(i,j)<1
            SquareCompXtal(i,j)=1./SquareCompXtal(i,j);
        end
        if SquareCompXtal1(i,j)<1
            SquareCompXtal1(i,j)=1./SquareCompXtal1(i,j);
        end

        if SquareCompL95(i,j)<1
            SquareCompL95(i,j)=1./SquareCompL95(i,j);
        end
        if SquareCompL951(i,j)<1
            SquareCompL951(i,j)=1./SquareCompL951(i,j);
        end

        if SquareCompNv(i,j)<1
            SquareCompNv(i,j)=1./SquareCompNv(i,j);
        end
        if SquareCompNv1(i,j)<1
```

```
                SquareCompNv1(i,j)=1./SquareCompNv1(i,j);
            end
        end
    end

    SqCompXtal=abs(SquareCompXtal);
    SqCompXtal1=abs(SquareCompXtal1);
    SqCompNv=abs(SquareCompNv);
    SqCompNv1=abs(SquareCompNv1);
    SqCompL95=abs(SquareCompL95);
    SqCompL951=abs(SquareCompL951);

    weightOld=weight;
    listW(length(weight1))=0;
    listW=listW.*0;
    listInd=listW;

    for iW=1:length(weight1)
        weight(1:3)=weight1(iW);
        weight(4:6)=weight2(iW);
        weight(7:9)=weight3(iW);
        weight(10:11)=weight4(iW);

        for i=1:length(SheaHammerOut);
            SqCompXtal(:,i)=SqCompXtal(:,i).*weight(i);
            SqCompXtal1(:,i)=SqCompXtal1(:,i).*weight(i);
            SqCompNv(:,i)=SqCompNv(:,i).*weight(i);
            SqCompNv1(:,i)=SqCompNv1(:,i).*weight(i);
            SqCompL95(:,i)=SqCompL95(:,i).*weight(i);
            SqCompL951(:,i)=SqCompL951(:,i).*weight(i);

            SquareCompXtal(:,i)=SquareCompXtal(:,i).*weight(i);
            SquareCompXtal1(:,i)=SquareCompXtal1(:,i).*weight(i);
            SquareCompNv(:,i)=SquareCompNv(:,i).*weight(i);
            SquareCompNv1(:,i)=SquareCompNv1(:,i).*weight(i);
            SquareCompL95(:,i)=SquareCompL95(:,i).*weight(i);
            SquareCompL951(:,i)=SquareCompL951(:,i).*weight(i);
        end


SumSqCompXtal=sum(SqCompXtal,2)./sum(weight./length(SheaHammerOut));

SumSqCompXtal1=sum(SqCompXtal1,2)./sum(weight./length(SheaHammerOut));

SumSqCompNv=sum(SqCompNv,2)./sum(weight./length(SheaHammerOut));

SumSqCompNv1=sum(SqCompNv1,2)./sum(weight./length(SheaHammerOut));

SumSqCompL95=sum(SqCompL95,2)./sum(weight./length(SheaHammerOut));

SumSqCompL951=sum(SqCompL951,2)./sum(weight./length(SheaHammerOut));


minX=min((SumSqCompXtal(:).*SumSqCompNv(:)).^2+(SumSqCompXtal(:)...
```

```
.*SumSqCompL95(:)).^2+(SumSqCompNv(:).*SumSqCompL95(:)).^2);
          listW(iW)=minX;
          listInd(iW)=find((SumSqCompXtal(:).*SumSqCompNv(:)).^2+...
              (SumSqCompXtal(:).*SumSqCompL95(:)).^2+(SumSqCompNv(:)...
              .*SumSqCompL95(:)).^2==minX,1);

          SquareCompXtal=CompXtal;
          SquareCompXtal1=CompXtal1;
          SquareCompL95=CompL95;
          SquareCompL951=CompL951;
          SquareCompNv=CompNv;
          SquareCompNv1=CompNv1;

          for i=1:length(SquareCompXtal);
              for j=1:length(SheaHammerOut);
                  if SquareCompXtal(i,j)<1;
                      SquareCompXtal(i,j)=1./SquareCompXtal(i,j);
                  end
                  if SquareCompXtal1(i,j)<1;
                      SquareCompXtal1(i,j)=1./SquareCompXtal1(i,j);
                  end

                  if SquareCompL95(i,j)<1;
                      SquareCompL95(i,j)=1./SquareCompL95(i,j);
                  end
                  if SquareCompL951(i,j)<1;
                      SquareCompL951(i,j)=1./SquareCompL951(i,j);
                  end
                  if SquareCompNv(i,j)<1;
                      SquareCompNv(i,j)=1./SquareCompNv(i,j);
                  end
                  if SquareCompNv1(i,j)<1;
                      SquareCompNv1(i,j)=1./SquareCompNv1(i,j);
                  end
              end
          end

          SqCompXtal=abs(SquareCompXtal);
          SqCompXtal1=abs(SquareCompXtal1);
          SqCompNv=abs(SquareCompNv);
          SqCompNv1=abs(SquareCompNv1);
          SqCompL95=abs(SquareCompL95);
          SqCompL951=abs(SquareCompL951);
      end

      % create plots of test data
      figure(1)
      subplot(3,1,1);
      plot(outXtal,'.');
      ylabel('Xtalinity')
      hold on
      subplot(3,1,2);
      plot(outNv,'.');
      ylabel('Nv');
      set(gca, 'YScale', 'log')
```

```
        hold on
        subplot(3,1,3);
        plot(outL95,'.');
        ylabel('L95')
        hold on

        sortedlistW=sort(listW,'ascend');
        slW=sortedlistW([1:100]);
        for iW=1;
            minminX=slW(iW);
            ffx=find(listW==minminX);
            fX=listInd(ffx);
            for i=1;
                Iln=zeros(1,1001);
                Gln=zeros(1,1001);
                for iDf=0:1000;
                    x=nb(fX(i)).*exp(1).*(iDf./1000);
                    Iln(iDf+1)=nk(fX(i))./(x.*sqrt(2.*3.14159)).*exp((-
(log(x)-...
                        nmu(fX(i))).^2)./(2.*nsigma(fX(i)).^2));
                    Gln(iDf+1)=gk(fX(i))./(x.*sqrt(2.*3.14159)).*exp((-
(log(x)-...
                        gmu(fX(i))).^2)./(2.*gsigma(fX(i)).^2));
                end

                xx=0:1000;
                xx=xx./1000;
                figure(2);
                subplot(2,1,1);
                hold on
                plot(xx.*100,Iln./1000000.*3600);
                ylabel('Nucleation Rate (cm{^-}{^3}hr^{-1})');
                subplot(2,1,2);
                hold on
                plot(xx.*100,Gln.*1000000.*3600);
                ylabel('Growth Rate (\mum hr{^-}^{1})');
                xlabel('\Delta\phi_p_l_a_g (vol. %)');

                figure(3);
                xp=[1:11];
                xp=xp+((iW-1).*length(SheaHammerOut))+iW-1;
                subplot(3,1,1);
                plot(xp,outXtal(fX(1),:),'.');
                ylabel('Xtalinity')
                hold on
                subplot(3,1,2);
                plot(xp,outNv(fX(1),:),'.');
                ylabel('Nv');
                hold on
                subplot(3,1,3);
                plot(xp,outL95(fX(1),:),'.')
                ylabel('L95')
                hold on

                figure(4);
                hold on
```

```
        plot(xx.*100+(iW./10),Iln./1000000.*3600);
        ylabel('Nucleation Rate (cm{^-}{^3}hr^{-1})');

        figure(5);
        hold on
        plot(xx.*100+(iW./10),Gln.*1000000.*3600);
        ylabel('Growth Rate (\mum hr{^-}^{1})');
    end
end

figure(6);
for iW=1:(length(slW));
    xp=[1:11];
    xp=xp+((iW-1).*length(SheaHammerOut))+iW-1;

    subplot(3,1,1);
    plot(xp,SheaHammerOut(:,1),'o');
    ylabel('Xtalinity')
    hold on
    subplot(3,1,2);
    plot(xp,SheaHammerOut(:,3),'o');
    ylabel('Nv');
    set(gca, 'YScale', 'log')

    hold on
    subplot(3,1,3);
    plot(xp,SheaHammerOut(:,4),'o')
    ylabel('L95')
    hold on
end
```

SNGPlag_Par_Inverse_v1c.m

```
% SNGPlag_Par_Inverse_v1c.m

% last updated 5 Nov 2021 by Aaron Marshall

% change log
% wrt v1 - hard coding parameters - AM, 25 Oct. 2021
% wrt v1b - finalizing for paralllelization - AM, 26 Oct. 2021
% wrt v1c - change tempSizeStack=zeros(Nbracket,sizer(2)),...
%   tempNStack=tempSizeStack, Lstack=sizer(2) location - AM, 4 Nov. 2021
% wrt v1d - added randomized population of antecrysts (volum fraction can
%vary), size populations of antecrysts and phenocrysts varies within
%specified range
% wrt v1e - size populations of antecrysts and phenocrysts are now evenly
% sampled in log space on randomly skewed interval, decreased lower bound of
% Antestack

% program that etimates likely decompression paths given: magma
% composition, initial conditions, and observed CSD

% 1) All parameters are hard coded in
% 2) Change line 55 (Nsim= ) to number of runs
% 3) Output files are SNGPlag_Par_Inverse.mat and
```

```
%    SNGPlag_Par_Inverse_Output.mat

% Decompress_PTt_Function_v0() -- inputs are: t series, T series, P series,
% EQB series, Input plag sizes and numbers,
% -- outputs are CSD, sizes and numbers matrices, xtalinity, Nvd
tic
% load in the nucleation and growth rates
load('NucGrowthRateBASnew.mat'); % basaltic andesite nucleation, growth rates
IlnBAS=Iln;
GlnBAS=Gln;
f=find(isnan(IlnBAS)==1);
IlnBAS(f)=0;
GlnBAS(f)=0;
load('NucGrowthRatenew.mat'); % dacite nucleation and growth rates
IlnRHY=Iln;
GlnRHY=Gln;
f=find(isnan(IlnRHY)==1);
IlnBAS(f)=0;
GlnBAS(f)=0;

NewRun=1; %1-New; 2-Existing; 3-Quit
Decomp=2; % ask if there will be new compositional data
InputFile='Cura1_Input.mat'; % change for Ci_Input_file %%%%
load(InputFile);

% parameters
NAME='SNGPlag_Par_Inverse';
Pinitstack=[110 150]; % initial pressure in MPa
Pinitstack(Pinitstack>PspaceMax)=PspaceMax;
Pfinalstack=[10 50]; % final pressure in MPa
Pfinalstack(Pfinalstack>240)=240;
Tstack=[1000 1150]; % starting temperature in Celsius
Tfinalstack=[1000 1150]; % final temperature in Celsius
Prate=[5 250]; % decompression rates
Pstepstack=0; % 0=steady, 1=single step, 2=multistep
Antestack=(0.05); % 5 vol. % starting antecrysts
Phenostack=1; % 0=no phenocrysts, 1=start with phenocrysts
saveall=1;
HR=2; % 0=Befus and Andrews (2018), 1=Hammer and Rutherford,  %%%%
% 2=Marshall and Andrews (2021)
Nsim=100000; % number of simulations, change to 100000 for R2
pawsRange=[40 120]; % pressure range for pause during ascent
pawsDur=[.1 20]; % time range for duration of pause (hours)
pawsAcc=[.05 50]; % acceleration range  (1=linear)
Prate2step1=[5 100]; % dP/dT range before pause
Prate2step2=[50 750]; % dP/dT range after pause
Pfrag=[20 60]; % pressure at point of fragmentation (=0 if not 2-step)
pathFrac=[.4 .3 .3]; % what fraction is linear accelerating 2-step  %%%%  (50 linear, 50
accel, 0 2-stp)
pawsFrac=[0 0 0]; % what fraction paused (lin accel 2-step)        %%%% (within each
group, what fraction = pause, each number 0<n<1, sum can be >1)
pathFrac=pathFrac./sum(pathFrac);
% pawsFrac=pawsFrac./sum(pawsFrac);
Tcrash=60; % max T drop, Mastin and Ghiorso (2001)
growthfactors=[.5 .25];
cgrowth2=growthfactors(1);
```

```
        cgrowth3=growthfactors(2);
        SrangeAA=[300 10]; %size range big then small in microns
        SrangeAA=SrangeAA./1E6; % set to units of meters
        SrangePP=[300 10]; %size range big then small in microns
        SrangePP=SrangePP./1E6; % set to units of meters
        NantecrystA=length(SrangeAA);
        NphenocrystP=length(SrangePP);

        Nprob=1E5;
        ddist=ellipser(cgrowth2, cgrowth3,Nprob); % function that determines the elliptical
projection of crystals thereby reducing apparent crystal size
        probddist=zeros(Nprob,3);
        probddist(:,1)=[1:Nprob]./Nprob;
        probddist(:,2)=sort(ddist(:,6)); %long axis of randomly positioned ellipse
        probddist(:,3)=sort(ddist(:,11)); %long axis of ellipse through centroid

        fileInCSD='Ci_CSDin_v2_5.mat'; % change to Ci_CSD_input %%%%
        load(fileInCSD);

        % save the inputs:
        saveName=[NAME datestr(now,'mm-dd-yyyy HH-MM') '.mat'];
        save(saveName,'TTM','PPM','PlagM','Pinitstack','Pfinalstack',...
            'Tstack','Tfinalstack','Antestack','Phenostack','Prate','HR',...
            'growthfactors','SrangeAA','SrangePP','NantecrystA','NphenocrystP',...
            'InputFile','Nsim','pathFrac','pawsFrac','Prate2step1',...
            'Prate2step2','Pfrag','Tcrash','probddist','fileInCSD');

        CSDbinsHammer=CSDbins; %still in mm
        CSDinHammerDiff=CSDinHammer.*CSDbins;
        HammerSize=size(CSDinHammer);
        NHammer=HammerSize(1);
        for i=1:100;
            for j=1:NHammer;
                CSDinHammerDiff(j,i)=CSDinHammer(j,i).*CSDbinsHammer(i)-
CSDinHammer(j,i+1).*CSDbinsHammer(i+1);
            end
        end
        CSDinHammerDiff=1E9.*CSDinHammerDiff;
        CSDbinsm=CSDbinsHammer; %./1000;
        CSDinHammerV=CSDbinsm.^3.*growthfactors(1).*growthfactors(2); %volume per crystal
in m^3
        CSDinHammerVfrac=CSDinHammerV.*CSDinHammerDiff; %volume fraction per cubic
meter
        CSDinHammerN=CSDinHammerVfrac./CSDinHammerV;
        % growr=1E-5;
        % CSDbinsmg=CSDbinsm-growr;
        % CSDbinsmg(CSDbinsmg<=0)=0;
        % CSDinHammerVg=CSDbinsmg.^3.*growthfactors(1).*growthfactors(2); %volume per
crystal in m^3
        % CSDinHammerVfracg=CSDinHammerVg.*CSDinHammerDiff; %volume fraction per
cubic meter


        %generate the FXplagNew function
        FXplagNew=scatteredInterpolant(TTM,PPM,PlagM,'natural');
        if HR==0
```

```
    GROWRATE=GlnRHY; %input the growth rate - RHYOLITE
    NUCRATE=IlnRHY; %input the nucleation rate - RHYOLITE
elseif HR==2
    GROWRATE=GlnBAS; %input the growth rate - BASALTIC ANDESITE
    NUCRATE=IlnBAS; %input the nucleation rate - BASALTIC ANDESITE
end

pathFraccum=pathFrac;
for j=2:3
    pathFraccum(j)=sum(pathFrac(1:j));
end

Nbracket=Nsim;
InitParam=zeros(Nbracket,11);
XtalStack=zeros(Nbracket,1);
XtalStackInit=zeros(Nbracket,1);
NVDStack=zeros(Nbracket,1);
NVDStack1=zeros(Nbracket,1);
CSD50Stack=zeros(Nbracket,1);
CSDbinStack=zeros(1,101);
CSDcumStack=zeros(Nbracket,101);
CSDcumeStack=zeros(Nbracket,101);
CSD50eStack=0.*CSD50Stack;
CSDcume0Stack=zeros(Nbracket,101);
CSD50e0Stack=0.*CSD50Stack;


tic
for iSim=1:Nsim
    DPi=abs(Pinitstack(2)-Pinitstack(1));
    DPf=abs(Pfinalstack(2)-Pfinalstack(1));
    DTi=abs(Tstack(2)-Tstack(1));
    DTf=abs(Tfinalstack(2)-Tfinalstack(1));
    DPrate=max(log10(Prate))-min(log10(Prate));

    dPdt=0;
    DPrate1=max(log10(Prate2step1))-min(log10(Prate2step1));
    DPrate2=max(log10(Prate2step2))-min(log10(Prate2step2));
    DPfrag=Pfrag(2)-rand(1).*(Pfrag(2)-Pfrag(1));

    Pi=min(Pinitstack)+rand(1).*DPi;
    Pf=min(Pfinalstack)+rand(1).*DPf;

    if DPfrag<Pf+5
        DPfrag=Pf+5;
    end

    Ti=min(Tstack)+rand(1).*DTi;
    Tf=min(Tfinalstack)+rand(1).*DTf;
    r1=rand(1);
    r2=rand(1);

    if r1<=pathFraccum(1)
        dPdt=min(log10(Prate))+rand(1).*DPrate;
        dPdt=10.^dPdt;
        accel=1;
```

```
            dPdt1=0;
            dPdt2=0;
            Pfr=0;

            if r2>pawsFrac(1)
               pauseP=0;
               pauseDur=0;
            else
               pauseP=pawsRange(2)-rand(1).*(pawsRange(1)-pawsRange(2));
               pauseDur=rand(1).*log10(pawsDur(2)./pawsDur(1))+...
                  log10(pawsDur(1));
               pauseDur=10.^pauseDur;
            end

         elseif r1<=pathFraccum(2)
            dPdt=min(log10(Prate))+rand(1).*DPrate;
            dPdt=10.^dPdt;
            accel=(max(pawsAcc)-min(pawsAcc)).*rand(1)+min(pawsAcc);
            dPdt1=0;
            dPdt2=0;
            Pfr=0;

            if r2>pawsFrac(2)
               pauseP=0;
               pauseDur=0;
            else
               pauseP=pawsRange(2)-rand(1).*(pawsRange(1)-pawsRange(2));
               pauseDur=rand(1).*log10(pawsDur(2)./pawsDur(1))+...
                  log10(pawsDur(1));
               pauseDur=10.^pauseDur;
            end

         elseif r1>pathFraccum(2)
            dPdt1=min(log10(Prate2step1))+rand(1).*DPrate1;
            dPdt1=10.^dPdt1;
            dPdt2=min(log10(Prate2step2))+rand(1).*DPrate2;
            dPdt2=10.^dPdt2;
            while dPdt2<dPdt1;
               dPdt2=min(log10(Prate2step2))+rand(1).*DPrate2;
               dPdt2=10.^dPdt2;
            end
            accel=0;
            Pfr=DPfrag;
            pauseP=0;
            pauseDur=0;
         end
         InitParam(iSim,:)=[Pi Pf Ti Tf dPdt pauseP pauseDur accel dPdt1...
            dPdt2 Pfr];
      end
      Tcrasher=zeros(Nsim,4);
      NantecrystA=length(SrangeAA);
      NphenocrystP=length(SrangePP);
      sizer=[5001 5040];
      % nRun=0;
      % tempSizeStack=zeros(Nbracket,sizer(2));
      % tempNStack=tempSizeStack;
```

```
% Lstack=sizer(2);

% c=parcluster;
% c.AdditionalProperties.AdditionalSubmitArgs=' -o log_slurm.o%j -p shortq ';
% parpool(c,27);

AntestackOut=zeros(Nsim,1);
growrstackOut=AntestackOut;
iCSDstack=AntestackOut;
AnteFracsOut=zeros(Nsim,20);
PhenoFracsOut=zeros(Nsim,20);
SrangeAStack=zeros(Nsim,20);
SrangePStack=zeros(Nsim,20);
Nantecryst=20;
Nphenocryst=20;
NStack=zeros(Nsim,5040);
SizeStack=zeros(Nsim,5040);

CSDbinstemp=CSDbins;
% parfor below at 250
parfor i=1:Nsim
% for i=1;
   [i Nsim]
   CSDbinstemp=CSDbins;
   tempSizeStack=zeros(Nbracket,sizer(2));
   tempNStack=tempSizeStack;
   Lstack=sizer(2);
   Pi=InitParam(i,1);
   Pf=InitParam(i,2);
   Ti=InitParam(i,3);
   Tf=InitParam(i,4);
   dPdt=InitParam(i,5);
   pauseP=InitParam(i,6);
   pauseDur=InitParam(i,7);
   accel=InitParam(i,8);
   dPdt21=InitParam(i,9);
   dPdt22=InitParam(i,10);
   P2frag=InitParam(i,11);
   tempTcrasher=zeros(1,4);

   [tt,Pt,Tt]=PauseAccelerate2StepInverse(Pi,Pf,Ti,Tf,dPdt,pauseP,...
      pauseDur,accel,dPdt21,dPdt22,P2frag);
   try Tcr=Tcrash;
      if Tcrash>0
         fcrash=find(Pt<=P2frag,1);
         stepcrash=length(Pt)-fcrash;
         stepTcrash=rand(1).*Tcrash./stepcrash;

         for iTcr=1:stepcrash
            Tt(fcrash+iTcr)=Tt(fcrash+iTcr)-iTcr.*stepTcrash;
         end

         tempTcrasher(1,1)=fcrash;
         tempTcrasher(1,2)=stepcrash;
         tempTcrasher(1,3)=stepTcrash.*stepcrash;
         tempTcrasher(1,4)=stepTcrash;
```

```
            end
        end
        Tcrasher(i,:)=tempTcrasher(1,:);

        EQBt=FXplagNew(Tt,Pt); % EQB xtalinity series
        fP=find(Pt<20);
        if isempty(fP)==0;
            fP20=find(Pt>=20,1,'last');
            EQBt(fP)=EQBt(fP20);
        end


            %randomly select the particular CSD to look at:
        iCSD=ceil(rand(1).*NHammer);
        iCSDstack(i)=iCSD;
        %%%%%%%%%%%%%%%%%%
        growr=5.*10^(-6+rand(1).*1.6); %amount of growth expected 5-200 um
        growrstackOut(i)=growr;
        CSDbinsmg=CSDbinsm-growr;
        PhenoInDef=CSDbins(18:37);

PhenoInV=CSDinHammerDiff(iCSD,18:37).*CSDbins(18:37).^3.*growthfactors(1).*growthfactors(
2);
        PhenoInDef=flip(PhenoInDef);
        PhenoInV=flip(PhenoInV);


        CSDbinsmg(CSDbinsmg.*CSDinHammerDiff(iCSD,:)<=0)=0;
        CSDinHammerVg=CSDbinsmg(:).^3.*growthfactors(1).*growthfactors(2); %volume per
crystal in m^3
        CSDinHammerVfracg=CSDinHammerVg.*CSDinHammerN(iCSD,:)'; %%%
CSDinHammerDiff(iCSD,:)'; %volume fraction per cubic meter
        fmtemp=find(CSDbinsmg>0);
        fmltemp=length(fmtemp);
        AnteFracs=zeros(20,1);
        SrangeA=AnteFracs;
        if fmltemp>=20;
            SrangeA=CSDbinsmg(fmtemp(1:20));
            AnteFracs=CSDinHammerVfracg(fmtemp(1:20));
        elseif fmltemp==0;
            SrangeA=CSDbinsmg(1:20);
            AnteFracs=0.*SrangeA;
        elseif fmltemp<20;
            SrangeA(1:fmltemp-1)=CSDbinsmg(fmtemp(1:fmltemp-1));
            AnteFracs(1:fmltemp-1)=CSDinHammerVfracg(fmtemp(1:fmltemp-1));
            SrangeA(fmltemp:20)=CSDbinsmg(fmtemp(fmltemp));
            AnteFracs(fmltemp:20)=CSDinHammerVfracg(fmtemp(fmltemp))./(21-fmltemp);
        end

        %add random component to the Antecryst fraction:
    %     AnteFracs=2.^(4-5.*rand(1)).*AnteFracs;
    %     AnteFracs=2.^(3-2.*rand(1)).*AnteFracs; %first integer is the maximum increase
(power of 2) and first minus second gives lower bound (power of 2)
        AntestackOut(i)=sum(AnteFracs);
        SrangeP=SrangeA;
        PhenoFracs=AnteFracs;
```

```
%%%%%%%%%%%%%%
SrangeA=flip(SrangeA);
SrangeP=flip(SrangeP);
SrangeAStack(i,:)=SrangeA;
SrangePStack(i,:)=SrangeP;
AnteFracs=flip(AnteFracs);
AnteFracsOut(i,:)=AnteFracs;
PhenoFracsOut(i,:)=PhenoFracs;

%     Nantecryst=length(SrangeA);
%     Nphenocryst= length(SrangeP);

[SizeXtal,NXtal,Xtalinity,NVDfinal,NVDfinal1,CSD50,CSDbinstemp,CSDcum, CSD50e,
CSDcume, CSD50e0,
CSDcume0]=Decompress_PTt_Function_v41(tt,Pt,Tt,EQBt,AntestackOut(i),Phenostack,dPdt,Sra
ngeA,SrangeP,Nantecryst,Nphenocryst,HR,NUCRATE,GROWRATE,growthfactors,probddist,Ant
eFracs,PhenoFracs,PhenoInDef,PhenoInV);

%     [SizeXtal,NXtal,Xtalinity,NVDfinal,NVDfinal1,CSD50,CSDbins,...
%         CSDcum]=Decompress_PTt_Function_v3(tt,Pt,Tt,EQBt,AntestackOut(i),...
%         Phenostack,dPdt,SrangeA,SrangeP,Nantecryst,Nphenocryst,HR,...
%         NUCRATE,GROWRATE,growthfactors);

XtalStack(i)=Xtalinity(end);
XtalStackInit(i)=Xtalinity(1);
NVDStack(i)=NVDfinal(end);
NVDStack1(i)=NVDfinal1(end);
CSD50Stack(i)=CSD50(end);
CSDcumStack(i,:)=CSDcum;
CSD50eStack(i)=CSD50e(end);
CSDcumeStack(i,:)=CSDcume;
CSD50e0Stack(i)=CSD50e0(end);
CSDcume0Stack(i,:)=CSDcume0;


if i==1
   CSDbinStack(i,:)=CSDbinstemp;
end

try
   tempSizeStack(i,:)=SizeXtal(end,:);
   tempNStack(i,:)=NXtal(end,:);
catch
   L2=length(SizeXtal(end,:));
   if L2<Lstack
      tempSizeStack(i,1:L2)=SizeXtal(end,:);
      tempNStack(i,1:L2)=NXtal(end,:);
   elseif L2>Lstack
      Ldiff=L2-Lstack;
      Zdiff=zeros(Nbracket,Ldiff);
      tempSizeStack=[tempSizeStack Zdiff];
      tempNStack=[tempNStack Zdiff];
      tempSizeStack(i,:)=SizeXtal(end,:);
      tempNStack(i,:)=NXtal(end,:);
```

```
                Lstack=L2;
            end
        end
        NStack(i,:)=tempNStack(1,:);
        SizeStack(i,:)=tempSizeStack(1,:);
    end

    % saveName2=[NAME datestr(now,'mm-dd-yyyy HH-MM') '_Output.mat'];
    saveName2=saveName;
    saveName2(end-3:end)=[];
    saveName2=[saveName2 '_Output.mat'];
    save(saveName2,'CSDcumStack','CSD50Stack','CSDcumeStack','CSD50eStack','CSDc
ume0Stack','CSD50e0Stack','Nbracket','CSDbinStack','InitParam',...
        'FXplagNew','Antestack', 'Phenostack', 'SrangeAA','SrangePP',...
        'Nantecryst', 'Nphenocryst', 'HR', 'NUCRATE', 'GROWRATE',...
        'growthfactors','LIQUIDUS','PspaceMax','TspaceMin', 'TspaceMax',...

'Tcrasher','AntestackOut','SrangeAStack','SrangePStack','XtalStackInit','growrstackOut','AnteFrac
sOut','PhenoFracsOut','XtalStack','iCSDstack');
    toc
```

SNGPlag_Inverse_Banana_v3.m

```
    % SNGPlag_Inverse_Banana_v3

    % try cd(folderIn)
    % catch
        folderstart=pwd;
        folderIn=uigetdir(' ','select folder that contains the input or target CSDs');
        cd(folderIn)
    %     fileIn=uigetfile('*.mat','select .mat file that contains the input or target CSD(s)');
        fileIn='Ci_CSDin_v2_5.mat';
        load(fileIn);
        InputFile='Cura1_Input.mat';
        load(InputFile);
        cd(folderstart);
        folderMC=uigetdir(' ','select folder that contains the Monte Carlo output file for
comparison');
        cd(folderMC);
        fileMC=uigetfile('*.mat','select .mat file that contain the Monte Carlo SNG outputs');
        load(fileMC);
        sizerCSD=size(CSDcumStack);
        Nsim=sizerCSD(1);
        try
        CSDcumStackOld=CSDcumeStack;
        catch
            CSDcumeStack=CSDcumStack;
            CSDcumStackOld=CSDcumeStack;
        end
        CSDcumStackOld=CSDcumeStack;
    % end
    CSDbins=CSDbinStack(1,:).*1000;
    %     find the difference between the CSDcumInLog and the various runs;

    % CSDcumStack=CSDin;
```

```
Nbracket=Nsim;
% 'CSDcumStack','Nbracket','CSDbinStack','InitParam');
% fclean=find(CSDbins>1E-4);

CSDcumStack=CSDcumStackOld; %.*1000;
% CSDcumStack=CSDcumeStack;

% Tranges=[865-13 865+13; 858-21.5 858+21.5; 862.75-27 862.75+27; 860-31 860+31];

liqP=1:PspaceMax;
   liqT=0.*liqP;
   for k=1:PspaceMax;

liqT(k)=LIQUIDUS(1).*liqP(k).^3+LIQUIDUS(2).*liqP(k).^2+LIQUIDUS(3).*liqP(k)+LIQUIDUS(4);
   end

corrf=1E0;
   fitter=2;

Tfloor=floor(min([InitParam(:,3);InitParam(:,4)]));
Tceil=ceil(max([InitParam(:,3);InitParam(:,4)]));

fpass=SNGPlagFiltering(InitParam,liqT,liqP,Nsim);
for iSuper=1:2; %:NCSD=24;

%    fT=find(InitParam(:,3)<Tranges(iSuper,1) | InitParam(:,3)>Tranges(iSuper,2));
%    CSDcumStack(fT,:)=0;

   ctsDiff=CSDinCts(iSuper,2:end)-CSDinCts(iSuper,1:end-1);
   ctsDiff2=CSDinCharCts(iSuper,:);
   %    ctsDiff2(1:end-1)=CSDinCts(iSuper,1:end-1)-CSDinCts(iSuper,2:end);
   CSDinErr2=sqrt(ctsDiff2)./ctsDiff2;
   CSDinErr2(isnan(CSDinErr2)==1)=0;
   CSDinErr2(CSDinErr2>0.5)=0.5;
   CSDinErr2(CSDinErr2==0)=0.5;

   binLow=find(ctsDiff<0,1);
   binLow=find(CSDbins>=1E-5,1);
   binHigh=find(ctsDiff<0,1,'last');
   binHigh=find(CSDbins==0.1);
   binNum=binHigh-binLow+1;
   CSDinErr2(1:binLow-1)=0;
   CSDinErr2(binHigh+1:end)=0;
   %    binHigh=max(binHigh);
   %get rid of any of the CSD information for crystals coarser than
   %binHigh in CSDcumStack
   binChop=CSDcumStack(:,binHigh+1);
   for ii=1:Nsim;
      CSDcumStack(ii,:)=CSDcumStack(ii,:)-binChop(ii);
   end
   CSDcumStack(CSDcumStack<0)=0;

   CSDcumIn=CSDinHammer(iSuper,:).*CSDbins.^2;

%    CSDcumIn=CSDinChar(iSuper,:);
   %    CSDcumIn(fclean)=0;
```

```
            % CSDcumIn
            CSDbinIn=CSDbins;
            CSDcumInLog=log(CSDcumIn./(CSDbinIn));
            CSDcumInLog(CSDcumInLog<0)=0;

            CSDcumErr=zeros(Nsim,length(CSDbins));
            for i=1:length(CSDbins);
               %        f=find(CSDcumStack(:,i)>(1-6.*CSDinErr2(i)).*CSDcumIn(i) &
CSDcumStack(:,i)<(1+6.*CSDinErr2(i)).*CSDcumIn(i)); %5 sigma
               %        if isempty(f)==0;
               %           CSDcumErr(f,i)=1;
               %        end
               %        f=find(CSDcumStack(:,i)>(1-4.*CSDinErr2(i)).*CSDcumIn(i) &
CSDcumStack(:,i)<(1+4.*CSDinErr2(i)).*CSDcumIn(i)); %4 sigma
               %        if isempty(f)==0;
               %           CSDcumErr(f,i)=2;
               %        end
               %        f=find(CSDcumStack(:,i)>(1-3.*CSDinErr2(i)).*CSDcumIn(i) &
CSDcumStack(:,i)<(1+3.*CSDinErr2(i)).*CSDcumIn(i)); %3 sigma
               %        if isempty(f)==0;
               %           CSDcumErr(f,i)=3;
               %        end
               x3=5;
               x2=3;
               x1=2;
               f=find(log(CSDcumStack(:,i))>log(CSDcumIn(i))-x3.*log(1+CSDinErr2(i)) &
log(CSDcumStack(:,i))<log(CSDcumIn(i))+x3.*log(1+CSDinErr2(i))); %5 sigma
               if isempty(f)==0;
                  CSDcumErr(f,i)=1;
               end
               f=find(log(CSDcumStack(:,i))>log(CSDcumIn(i))-x2.*log(1+CSDinErr2(i)) &
log(CSDcumStack(:,i))<log(CSDcumIn(i))+x2.*log(1+CSDinErr2(i))); %3 sigma
               if isempty(f)==0;
                  CSDcumErr(f,i)=2;
               end
               f=find(log(CSDcumStack(:,i))>log(CSDcumIn(i))-x1.*log(1+CSDinErr2(i)) &
log(CSDcumStack(:,i))<log(CSDcumIn(i))+x1.*log(1+CSDinErr2(i))); %2 sigma
               if isempty(f)==0;
                  CSDcumErr(f,i)=3;
               end
            end

            CSDcumErr2=CSDcumErr;
            CSDcumErr2(:,1:binLow-1)=0;
            CSDcumErr2(:,binHigh+1:end)=0;

            %find how the calculations compare with the natural sample. Fit index
            %has 3 columns - each row is a simulation, and the columns are the
            %number of bin sizes that the fit falls within 3, 2, or 1 sigma of
            %natural
            CSDfitIndex=zeros(Nsim,3);
            for i=1:Nsim;
               tempRow=CSDcumErr2(i,:);
               tempRow(tempRow>1)=1;
               CSDfitIndex(i,1)=sum(tempRow);
               tempRow=CSDcumErr2(i,:);
```

```
            tempRow(tempRow<2)=0;
            tempRow(tempRow>=2)=1;
            CSDfitIndex(i,2)=sum(tempRow);
            tempRow=CSDcumErr2(i,:);
            tempRow(tempRow<3)=0;
            CSDfitIndex(i,3)=sum(tempRow)./3;
        end
        %plot the values that have at least 5 CSD bins that agree
        fitmax=max(CSDfitIndex(:,fitter));
        f1=find(CSDfitIndex(:,fitter)==fitmax); %best fit
        f2=find(CSDfitIndex(:,fitter)>=fitmax-1); %second best
        f3=find(CSDfitIndex(:,fitter)>=fitmax-2); %third best
        %apply filter to f1, f2, f3
        gmap=gray(100);

        fig1=figure; %subplots to be 3x3 (each column is a sigma range, rows are CSD, P-T
space, decompression path)
        subplot(3,3,4)
        plot(InitParam(:,3),InitParam(:,1),'.','Color',gmap(50,:));
        hold on
        plot(InitParam(:,4),InitParam(:,2),'.','Color',gmap(50,:));
        try
            plot(liqT, [1:PspaceMax],'b','LineWidth',1);
        end
        xlabel('Temperature (C)');
        ylabel('Pressure (MPa)');
        xlim([Tfloor Tceil])
        ylim([0 150])

        subplot(3,3,5)
        plot(InitParam(:,3),InitParam(:,1),'.','Color',gmap(50,:));
        hold on
        plot(InitParam(:,4),InitParam(:,2),'.','Color',gmap(50,:));
        try
            plot(liqT, [1:PspaceMax],'b','LineWidth',1);
        end
        xlabel('Temperature (C)');
        ylabel('Pressure (MPa)');
        xlim([Tfloor Tceil])
        ylim([0 150])
        subplot(3,3,6)
        plot(InitParam(:,3),InitParam(:,1),'.','Color',gmap(50,:));
        hold on
        plot(InitParam(:,4),InitParam(:,2),'.','Color',gmap(50,:));
        try
            plot(liqT, [1:PspaceMax],'b','LineWidth',1);
        end
        xlabel('Temperature (C)');
        ylabel('Pressure (MPa)');
        xlim([Tfloor Tceil])
        ylim([0 150])
        if isempty(f1)==0;
            subplot(3,3,1);
            plot(CSDbins,log(CSDcumStack(f1,:)'./CSDbins'),'k');
            hold on
            subplot(3,3,4);
```

```
            plot(InitParam(f1,3),InitParam(f1,1),'ok','MarkerSize',5,'MarkerFaceColor','k');
            plot(InitParam(f1,4),InitParam(f1,2),'ok','MarkerSize',5,'MarkerFaceColor','k');
            subplot(3,3,7)
            for ii=1:length(f1);
                fmm=f1(ii);
                try
                    [ttF, PtF, TtF]=PauseAccelerate2StepInverse(InitParam(fmm,1),
InitParam(fmm,2), InitParam(fmm,3), InitParam(fmm,4), InitParam(fmm,5), InitParam(fmm,6),
InitParam(fmm,7), InitParam(fmm,8), InitParam(fmm,9), InitParam(fmm,10), InitParam(fmm,11));
                catch
                    [ttF, PtF, TtF]=PauseAccelerate2StepInverse(InitParam(fmm,1),
InitParam(fmm,2), InitParam(fmm,3), InitParam(fmm,4), InitParam(fmm,5), InitParam(fmm,6),
InitParam(fmm,7), InitParam(fmm,8), 0, 0, 0);
                end
                plot(ttF./3600,PtF,'k');
                hold on
            end
            xlabel('Time (h)');
            ylabel('Pressure (MPa)');
        end
        if isempty(f2)==0;
            subplot(3,3,2);
            plot(CSDbins,log(CSDcumStack(f2,:)'./CSDbins'),'k');
            hold on
            subplot(3,3,5);
            plot(InitParam(f2,3),InitParam(f2,1),'ok','MarkerSize',5,'MarkerFaceColor','k');
            plot(InitParam(f2,4),InitParam(f2,2),'ok','MarkerSize',5,'MarkerFaceColor','k');
            subplot(3,3,8)
            for ii=1:length(f2);
                fmm=f2(ii);
                try
                    [ttF, PtF, TtF]=PauseAccelerate2StepInverse(InitParam(fmm,1),
InitParam(fmm,2), InitParam(fmm,3), InitParam(fmm,4), InitParam(fmm,5), InitParam(fmm,6),
InitParam(fmm,7), InitParam(fmm,8), InitParam(fmm,9), InitParam(fmm,10), InitParam(fmm,11));
                catch
                    [ttF, PtF, TtF]=PauseAccelerate2StepInverse(InitParam(fmm,1),
InitParam(fmm,2), InitParam(fmm,3), InitParam(fmm,4), InitParam(fmm,5), InitParam(fmm,6),
InitParam(fmm,7), InitParam(fmm,8), 0, 0, 0);
                end
                plot(ttF./3600,PtF,'k');
                hold on
            end
            xlabel('Time (h)');
            ylabel('Pressure (MPa)');
        end
        if isempty(f3)==0;
            subplot(3,3,3);
            plot(CSDbins,log(CSDcumStack(f3,:)'./CSDbins'),'k');
            hold on
            subplot(3,3,6);
            plot(InitParam(f3,3),InitParam(f3,1),'ok','MarkerSize',5,'MarkerFaceColor','k');
            plot(InitParam(f3,4),InitParam(f3,2),'ok','MarkerSize',5,'MarkerFaceColor','k');
            subplot(3,3,9)
            for ii=1:length(f3);
                fmm=f3(ii);
                try
```

```
                    [ttF, PtF, TtF]=PauseAccelerate2StepInverse(InitParam(fmm,1),
InitParam(fmm,2), InitParam(fmm,3), InitParam(fmm,4), InitParam(fmm,5), InitParam(fmm,6),
InitParam(fmm,7), InitParam(fmm,8), InitParam(fmm,9), InitParam(fmm,10), InitParam(fmm,11));
                catch
                    [ttF, PtF, TtF]=PauseAccelerate2StepInverse(InitParam(fmm,1),
InitParam(fmm,2), InitParam(fmm,3), InitParam(fmm,4), InitParam(fmm,5), InitParam(fmm,6),
InitParam(fmm,7), InitParam(fmm,8), 0, 0, 0);
                end
                plot(ttF./3600,PtF,'k');
                hold on
            end
            xlabel('Time (h)');
            ylabel('Pressure (MPa)');
        end
        %plot the natural CSDs
        subplot(3,3,1)
        plot(CSDbinIn,log(CSDcumIn./CSDbinIn),'b')
        plot(CSDbinIn,log(CSDcumIn)-x1.*log(1+CSDinErr2)-log(CSDbinIn),'m','LineWidth',2)
        plot(CSDbinIn,log(CSDcumIn)+x1.*log(1+CSDinErr2)-log(CSDbinIn),'m','LineWidth',2)

plot(CSDbinIn(binLow:binHigh),log(CSDcumIn(binLow:binHigh)./CSDbinIn(binLow:binHigh)),'bo')
        xlabel('Crystal size (mm)')
        ylabel({'Cumulative number density', '(log mm^{-4})'})
        title(' ',{[num2str(length(f1)) ' solutions fitting ' num2str(fitmax) '/' num2str(binNum) '
CSD points']});
        subplot(3,3,2)
        plot(CSDbinIn,log(CSDcumIn./CSDbinIn),'b')
        plot(CSDbinIn,log(CSDcumIn)-x1.*log(1+CSDinErr2)-log(CSDbinIn),'m','LineWidth',2)
        plot(CSDbinIn,log(CSDcumIn)+x1.*log(1+CSDinErr2)-log(CSDbinIn),'m','LineWidth',2)

plot(CSDbinIn(binLow:binHigh),log(CSDcumIn(binLow:binHigh)./CSDbinIn(binLow:binHigh)),'bo')
        title(sheetnames{iSuper},{[num2str(length(f2)) ' solutions fitting >=' num2str(fitmax-1) '/'
num2str(binNum) ' CSD points']});
        xlabel('Crystal size (mm)')
            ylabel({'Cumulative number density', '(log mm^{-4})'})


        subplot(3,3,3)
        plot(CSDbinIn,log(CSDcumIn./CSDbinIn),'b')
        plot(CSDbinIn,log(CSDcumIn)-x1.*log(1+CSDinErr2)-log(CSDbinIn),'m','LineWidth',2)
        plot(CSDbinIn,log(CSDcumIn)+x1.*log(1+CSDinErr2)-log(CSDbinIn),'m','LineWidth',2)

plot(CSDbinIn(binLow:binHigh),log(CSDcumIn(binLow:binHigh)./CSDbinIn(binLow:binHigh)),'bo')
        title(' ',{[num2str(length(f3)) ' solutions fitting >=' num2str(fitmax-2) '/' num2str(binNum) '
CSD points']});
        xlabel('Crystal size (mm)')
        ylabel({'Cumulative number density', '(log mm^{-4})'})

    % create fig name
    % add line to save fig, save in .fig; saveAs(fig1,figname)
    % add line to close fig; close fig1
    figname=([sheetnames{iSuper} '.fig']);
    saveas(fig1,figname);
    close(fig1);
    %     fig2=figure;
    %     for ii=1:length(f3);
```

```
%       fmm=f3(ii);
%       try
%          [ttF, PtF, TtF]=PauseAccelerate2StepInverse(InitParam(fmm,1),
InitParam(fmm,2), InitParam(fmm,3), InitParam(fmm,4), InitParam(fmm,5), InitParam(fmm,6),
InitParam(fmm,7), InitParam(fmm,8), InitParam(fmm,9), InitParam(fmm,10), InitParam(fmm,11));
%       catch
%          [ttF, PtF, TtF]=PauseAccelerate2StepInverse(InitParam(fmm,1),
InitParam(fmm,2), InitParam(fmm,3), InitParam(fmm,4), InitParam(fmm,5), InitParam(fmm,6),
InitParam(fmm,7), InitParam(fmm,8), 0, 0, 0);
%       end
%       stepcrash=Tcrasher(fmm,2);
%       stepTcrash=Tcrasher(fmm,4);
%       fcrash=Tcrasher(fmm,1);
%       for iTcr=1:stepcrash
%          TtF(fcrash+iTcr)=TtF(fcrash+iTcr)-iTcr.*stepTcrash;
%       end
%       plot(ttF./3600, TtF,'k');
%       hold on
%    end
%       xlabel('Time (h)');
%       ylabel('Temperature (^oC)');



if length(f1)<5;
   ff1=f2;
else
   ff1=f1;
end

dP=InitParam(ff1,1)-InitParam(ff1,2);
dt=0.*dP;
for i=1:length(ff1);
   fmm=ff1(i);
          [ttF, PtF, TtF]=PauseAccelerate2StepInverse(InitParam(fmm,1),
InitParam(fmm,2), InitParam(fmm,3), InitParam(fmm,4), InitParam(fmm,5), InitParam(fmm,6),
InitParam(fmm,7), InitParam(fmm,8), InitParam(fmm,9), InitParam(fmm,10), InitParam(fmm,11));
dt(i)=max(ttF)./3600;
end
dPdt=dP./dt
dt
dt2=InitParam(ff1,1)./dPdt;

% Sind=[1; 8; 6; 4];
% SSS(Sind(iSuper),9)=min(InitParam(ff1,2));
% SSS(Sind(iSuper),10)=max(InitParam(ff1,1));
% SSS(Sind(iSuper),11)=min(dPdt);
% SSS(Sind(iSuper),12)=max(dPdt);
% SSS(Sind(iSuper),13)=mean(dPdt);
% SSS(Sind(iSuper),14)=min(dt);
% SSS(Sind(iSuper),15)=max(dt);
% SSS(Sind(iSuper),16)=mean(dt);
% SSS(Sind(iSuper),17)=min(dt2);
% SSS(Sind(iSuper),18)=max(dt2);
% SSS(Sind(iSuper),19)=mean(dt2);
```

```
end

%%

figure(3);clf;
plot(liqT,liqP,'k','linewidth',1.5);
set(gca,'FontSize',12,'LineWidth',1);
xlim([900 1150]);
ylim([0 275]);
xlabel('temperature (degrees C)');
% ylim([0.935 0.957]);
ylabel('pressure (MPa)');
```